ABSTRACT

Title of dissertation: LOSS IN SUPERCONDUCTING QUANTUM DEVICES FROM NON-EQUILIBRIUM QUASIPARTICLES AND INHOMOGENEITY IN ENERGY GAP

Rui Zhang, Doctor of Philosophy, 2021

Dissertation directed by: Professor Frederick C. Wellstood
Department of Physics

Dr. Benjamin S. Palmer
Laboratory for Physical Sciences

This dissertation describes energy dissipation and microwave loss due to non-equilibrium quasiparticles in superconducting transmon qubits and titanium nitride coplanar waveguide resonators. During the measurements of transmon T_1 relaxation time and resonator quality factor Q_I, I observed reduced microwave loss as the temperature increased from 20 mK to approximately $T_c/10$ at which the loss takes on a minimum value. I argue that this effect is due to non-equilibrium quasiparticles.

I measured the temperature dependence of the relaxation time T_1 of the excited state of an Al/AlO_x/Al transmon and found that, in some cases, T_1 increased by almost a factor of two as the temperature increased from 30 mK to 100 mK with a best T_1 of 0.2 ms. I present an argument showing this unexpected temperature dependence occurs due to the behavior of non-equilibrium quasiparticles in devices in which one electrode in the tunnel junction has a smaller volume, and

slightly smaller superconducting energy gap, than the other electrode. At sufficiently low temperatures, non-equilibrium quasiparticles accumulate in the electrode with the smaller gap, leading to a relatively high density of quasiparticles at the junction and a short T_1. Increasing the temperature gives the quasiparticles enough thermal energy to occupy the higher gap electrode, reducing the density at the junction and increasing T_1. I present a model of this effect, extract the density of quasiparticles and the two superconducting energy gaps, and discuss implications for increasing the relaxation time of transmons.

I also observed a similar phenomenon in low temperature microwave studies of titanium nitride coplanar waveguide resonators. I report on loss in a resonator at temperatures from 20 mK up to 1.1 K and with the application of infrared pair breaking radiation ($\lambda = 1.55$ μm). With no applied IR light, the internal quality factor increased from Q_I = 800,000 at $T < 70$ mK up to $Q_I = (2 \times 10^6)$ at 600 mK. The resonant frequency f_0 increased by 2 parts per million over the same temperature range. Above 600 mK both Q_I and f_0 decreased rapidly, consistent with the increase in the density of thermally generated quasiparticles. With the application of IR light and for intensities below 1 aW μm^{-2} and $T < 400$ mK, Q_I increased in a similar way to increasing the temperature before beginning to decrease with larger intensities. I show that a model involving non-equilibrium quasiparticles and two regions of different superconducting gaps can explain this unexpected behavior.

LOSS IN SUPERCONDUCTING QUANTUM DEVICES FROM NON-EQUILIBRIUM QUASIPARTICLES AND INHOMOGENEITY IN ENERGY GAP

by

Rui Zhang

Dissertation submitted to the Faculty of the Graduate School of the
University of Maryland, College Park in partial fulfillment
of the requirements for the degree of
Doctor of Philosophy
2021

Advisory Committee:
Professor Frederick C. Wellstood, Chair/Co-Advisor
Dr. Benjamin S. Palmer, Co-Advisor
Dr. Christopher J. K. Richardson
Professor Christopher J. Lobb
Professor Ichiro Takeuchi, Dean's Representative

Dedicated to my family.

Acknowledgments

During my years at the University of Maryland and Laboratory for Physical Sciences, there were many people that I want to express my gratitude to.

First of all, I want to thank my advisors Benjamin Palmer and Frederick Wellstood, for introducing me to research and guiding me through my works with their knowledge, insights, scrupulous approach and bold ideas. I also thank them for their careful proofread and detailed comments on my manuscripts. I am really grateful to Ben's patience at teaching me cryogenic, microwave and fabrication skills. His enthusiasm and persistence at tackle problems has greatly inspired me. His questioning on the prevailingly accepted explanations and the attitude of never willing to compromise on the details have led to new understanding on the underlying physics, as well as unveiled new perspective on problems. His intuition on problems had guided me through the difficulties in research. I am also greatly benefited from Prof Wellstood's expertise and insights during our weekly discussions; his ability to pinpoint the core of problem from intricate phenomena, to devise quick yet effective schemes to verify postulations.

I am grateful to Dr. Christopher Richardson and Professor Christopher Lobb for being members of my dissertation committee, and Professor Ichiro Takeuchi for being the Dean's representative for the committee.

Through collaboration in research, I also received numerous devices, samples, materials and help from Dr. Richardson, Dr. Kevin Osborn and Dr. Shane Cybart, as well as advises from Professor Lobb. Here I take the chance to express my gratitude to them.

I am thankful to Prof Steven Anlage, Prof Sarah Eno, Prof Kara Hoffman and Prof Alberto Belloni for the guidance I received from them in my early year as their teaching assistant.

I am thankful to my seniors – Jen-Hao Yeh and Shavindra Premaratne, who walked me through step by step on how to perform operations and measurements on transmon qubits, as well as showed me the fabrication procedures and techniques. I am thankful to Sergey Novikov, Baladitya Suri, and Zaeill Kim, for the previous works they have done, upon which my works are built on. I am also thankful to the help and discussions from my lab-mates – Zachary Steffen, Tamin Tai, Yizhou Huang and Jay Lefebvre. I also thank Cody Ballard, Sudeep Dutta, Kungang Li and Ashish Alexander, with whom my research projects were collaborated.

I appreciate the help and company I received from the scientists and my friends at LPS – Joyce Coppock, Wan-Ting Liao, Luke Robertson, Neda Forouzani, Chih-Chiao Hung, Tim Kohler, Dr. Yaniv Rosen, Dr. Victor Yun, Dr. Donghun Park, Dr. Yongzhang Leng, Dr. Bahman Sarabi and Dr. Bruce Kane.

I thank the LPS cleanroom, research, and administrative staff members – Steve Brown, Toby Olver, Curt Walsh, Jim Fogleboch, Paul Hannah, Dan Hinkel, David Gutierrez, Doug Ketchum, Warren Berk, Debtanu Basu, Dave Bowen, Jonas Wood, Niquinn Fowler, Althia Kirlew and Cynthia Evans, who trained me on safety measures, cleanroom procedures and machinery operations, and were always there to help when I had problems. I thank the machinists at LPS – Donald Crouse, Ruben Brun, John Sugrue and Bill Donaldson, who fabricated the all the machinery parts in my projects. I thank Greg Latini and Mark Thornton, for their helps with issues on electronics or computers.

Last but not least, I thank my family and Jiashun who supported me all the while.

Table of Contents

List of Tables

List of Figures

List of Abbreviations

RSA – Rivest-Shamir-Adleman

NMR – nuclear spin magnetic resonance

TiN – titanium nitride

Al – aluminum

CPW – coplanar waveguide

DC – direct current

AC – alternating current

BCS – Bardeen-Cooper-Schrieffer

GR – Gittleman and Rosenblum

FFF – free-flux-flow

CC – Coffey-Clem

TLS – two-level system

EM – electromagnetic

LC – inductor-capacitor

CPB – Cooper pair box

CQE – cavity quantum electrodynamics

cQED – circuit quantum electrodynamics

QND – quantum non-demolition

RWA – rotating wave approximation

AS – air-to-substrate

SC – substrate-to-conductor

CA – conductor-to-air

MKID – microwave kinetic inductance detector

TEM – transverse electromagnetic

RF – radio frequency

PAMBE – plasma-assisted molecular beam epitaxy

SMA – SubMiniature version A

CAD – computer-aided design

BBQ – *black box quantization*

FGMRES – flexible generalized minimal residual

LPS – Laboratory for Physical Sciences

SEM – scanning electron microscope

ESD – electrostatic discharge

IPA – isopropyl alcohol

DI – deionized water

PPE – personal protective equipment

VNA – vector network analyzer

OVC – outer vacuum can

IVC – inner vacuum can

MXC – *mixing chamber*

DUT – device under test

HEMT – high-electron-mobility transistor

AWG – arbitrary waveform generators

SSG – synthesized signal generator

IR – infrared

DCM – diameter correction method

STEM – scanning transmission electron microscopy

STM – scanning tunneling microscopy

RIE – reactive ion etch

CHAPTER 1

Introduction

In principle, quantum computing possesses some advantages over classical computing for certain classes of problems that can exploit quantum entanglement, superposition, interference, and parallelism. Among which, finding patterns via interference gives rise to an exponential speedup over classical computing [1]. Due to its potential, quantum computing has been a hot topic since the late 1990s.

1.1. A Brief History of Quantum Computation

The idea of a quantum computer dates back to the 1970's, when physicist Paul Benioff began theoretical research on the feasibility of performing computation using quantum formalisms. In 1980, Benioff published a paper on the quantum mechanical model of the Turing machine [2], where he showed reversible computing [3] via the Schrödinger equation. In the same year, motivated by Benioff's work, Yuri Manin and Richard Feynman independently described how a quantum computer could in principle outperform a classical computer [4][5]. The first model for a universal quantum computer was described by David Deutsch in 1985 [6]. Deutsch showed that a universal quantum computer could simulate any quantum computer, with at most a polynomial

slowdown. In 1988, Kazuhiro Igeta and Yoshihisa Yamamoto proposed using atoms and photons as a physical platform for constructing a quantum computer [7].

In the subsequent decade of 1990s, David Deutsch and Richard Jozsa proposed a deterministic quantum algorithm that can efficiently solve a specific computational problem that no deterministic classical algorithm can solve efficiently [8], proving the capability for a quantum computer to surpass classical computer. In 1994 came Peter Shor's quantum algorithm [9] for prime factorization of integers, providing the potential to break RSA-encrypted communications [10]. This important application for quantum computing brought about a burst of interest in constructing physical realizations of quantum computers.

The first quantum logic gate, proposed by Ignacio Cirac, and Peter Zoller, was realized by Christopher Monroe and David Wineland in 1995 via trapped ions [11][12]. Since then, physical realizations of quantum computing have expanded enormously. In 1997, quantum logic gates based on bulk nuclear spin magnetic resonance (NMR) were reported by David Cory, Amr Fahmy and Timothy Havel [13], and independently by Neil Gershenfeld and Isaac L. Chuang [14], although it was later realized that this approach was not feasible because it required exponentially many preparation steps. In the same year, Alexei Kitaev proposed topological quantum computation to mitigate decoherence [15]. In the following year, Grover's algorithm was executed on an NMR quantum computer [16] and Bruce Kane proposed a quantum computer based on nuclear spins in silicon [17]. In 1999, Yasunobu Nakamura, Yuri Pashkin and Jaw-Shen Tsai demonstrated the first working superconducting quantum bit, or qubit, based on the Cooper Pair Box [18]. In 2001, Emanuel Knill, Raymond Laflamme and Gerard Milburn invented linear optical quantum computing [19].

Technical progress in quantum computing has persisted at rapid pace for the last two decades, during which the trapped ion, NMR, quantum dot, superconducting, and linear optical qubits further evolved into subspecies, high fidelity control [20]-[25] with quantum error correction [26]-[29] was achieved, and the scale of the quantum processors expanded to ~ 50 qubits [30]. An exhaustive listing of achievements is beyond the scope of this thesis, but we note that 2016 opened a new page in quantum computing with IBM releasing an online interface to their superconducting quantum processors [31], providing the general public access to a programmable quantum computer.

Early in the 1990s, a list of minimal ingredients for an efficient quantum computer was put forth by David P. DiVincenzo [32]: (1) A scalable physical system with well-characterized qubits; (2) ability to initialize the state of the qubits to a simple fiducial state; (3) qubit coherence times that are much longer than gate operation times; (4) a universal set of quantum gates; and (5) a reliable technique to measure the state of the qubits with high fidelity. Figure 1. 1 shows an illustration for the hierarchy of the criteria in order of technical complexity. The work presented in the rest of the dissertation is focused on the second step in this hierarchy – understanding and extending the superconducting qubit relaxation time T_1.

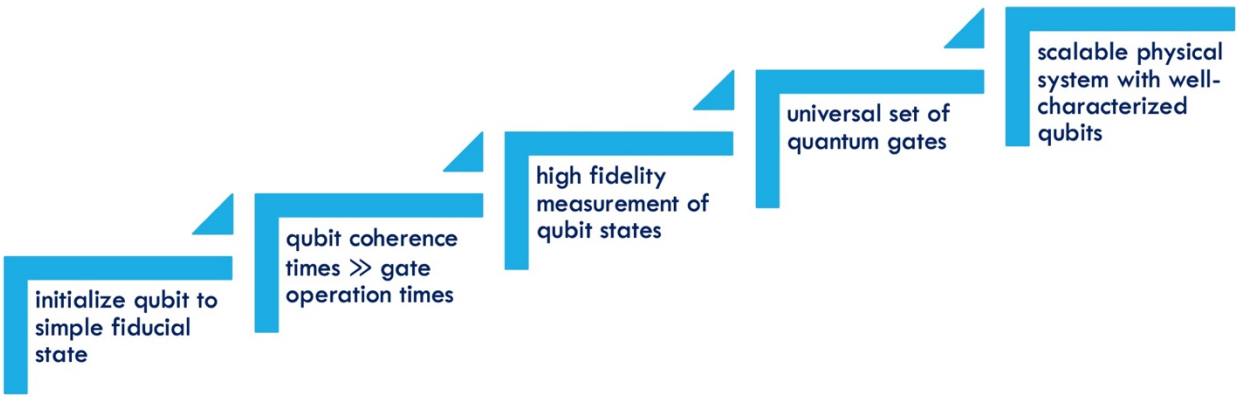

Figure 1. 1 Illustration for the hierarchy of the David P. DiVincenzo criteria in order of technical complexity. Each progress in the steps requires loose mastery of the previous step.

1.2. Increasing Qubit Lifetime

The word qubit [33] for a quantum bit was first coined by Benjamin Schumacher. A qubit is a physical system that is the quantum analog of a classical binary bit, in which information is stored in the quantum state of the system. The coherence time of a qubit measures the lifetime of the logic state and is a metric within which the logic gate operations need to be completed. Decoherence has two contributions: energy relaxation and dephasing. Ultimately, decoherence is a result of entanglement between the qubit and its environment, where information contained in the qubit is lost to the environment. The environment, in this case, could be control or measurement lines, radiation out to free space, and coupling to atomic-scale systems. Since absolute physical isolation from the environment is infeasible, mitigation of these effect is sought after.

My dissertation is concerned with superconducting qubits, a leading candidate in demonstrating quantum supremacy/advantage [34]-[36] over conventional supercomputers. Superconducting qubits [18][37], due to their construction from circuit elements, have evolved into a variety of subspecies. Figure 1. 2 shows how the relaxation time T_1 and coherence time T_2 have grown over the years [18][38]-[60]. Significant prolongation of the coherence times has been achieved via three major strategies: (1) physical improvement of the qubits and other hardware [39]-[56][61][62], (2) implementation of error correction protocols [26]-[29][63], and (3) bosonic encoding [28][57]-[60].

My work pertains to understanding the relaxation time T_1 due to non-equilibrium quasiparticles. The studies I conducted were on a 3D aluminum transmon [46][64] and a titanium nitride (TiN) superconducting coplanar waveguide (CPW) resonator [65][66]. Measurements on both of these devices showed a decrease in the loss (*i.e.* increase in T_1 or Q_I) when the temperature of the device was increased from 20 mK to about one-tenth of the critical temperature of the

superconductors. I argue that this behavior is due to inhomogeneities in the superconducting gap [67] leading to non-equilibrium quasiparticles being trapped in the low gap region in a location that presents the device with extra loss. By increasing the temperature, the quasiparticle density in this region decreases and hence reducing the loss. Based on this mechanism, I create a model to explain and extract key parameters from the measured data. This new understanding opens up possible improvements in transmon T_1 to 200 μs and beyond [62].

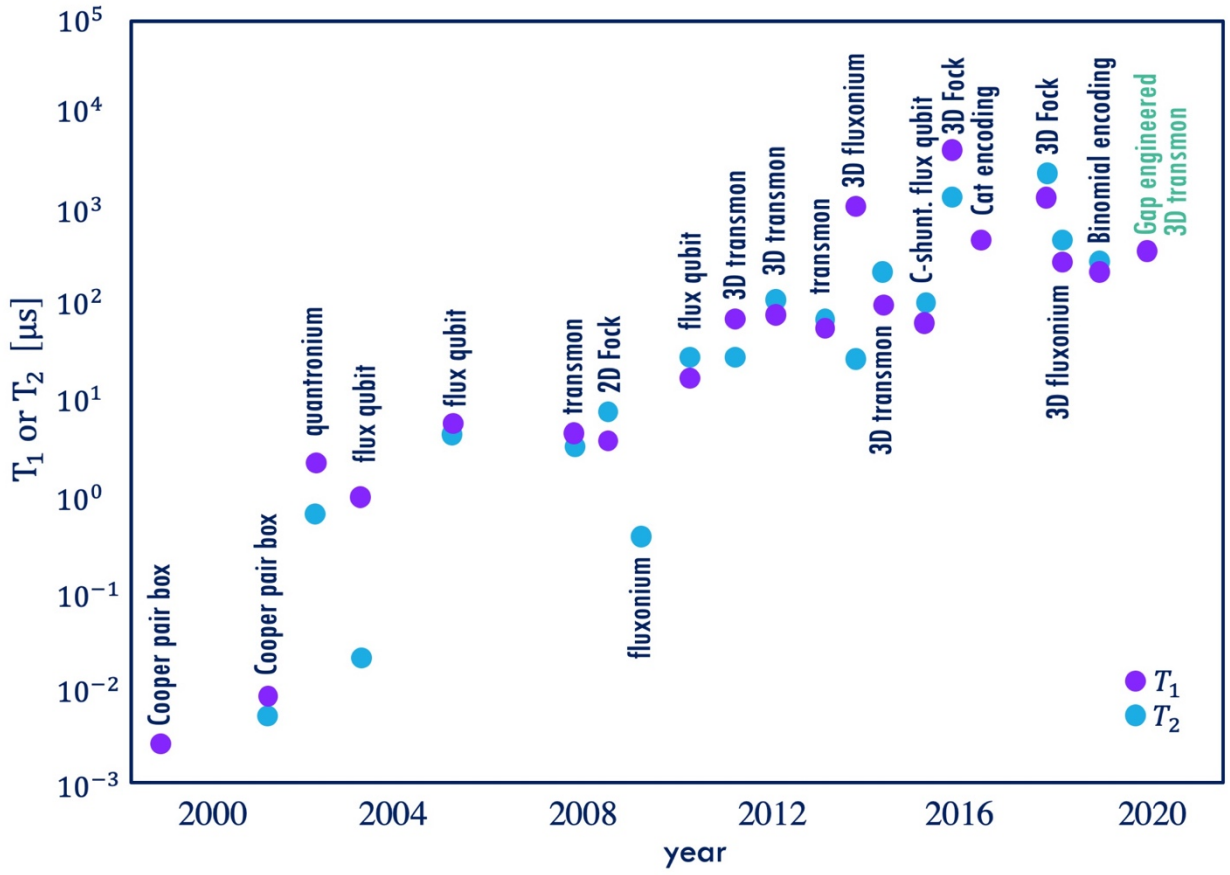

Figure 1. 2 Plot of coherence times attained in superconducting qubits versus year [18][38]-[60], adapted from M. Kjaergaard, *et al.* [38].

1.3. Overview of the Dissertation

The underlying theory and theoretical models are discussed in the next 4 chapters of the dissertation. Chapter 2 opens with a review of the various energy dissipation mechanisms in superconducting thin films. In Chapter 3 and 4, I provide an introduction to the transmons and superconducting coplanar waveguide (CPW) resonators, respectively. The key focus of the dissertation – the redistribution of non-quasiparticles in superconducting thin-film devices with energy gap inhomogeneity is explained in Chapter 5, where the manifestations of the phenomenon in transmon and coplanar resonator are explained and derived.

The experimental aspects are presented in the rest of the dissertation. The device fabrication, experimental setup and characterization can be found in Chapter 6, 7 and 8, respectively. Chapter 9 and 10 proceeds by presenting the experimental results and discussions for the Al 3D transmon qubit and the TiN superconducting coplanar waveguide (CPW) resonator. Chapter 11 provides a summary of my main results and conclude with some insights into the future research.

CHAPTER 2

Microwave Dissipation Mechanisms in Superconducting Thin Films

Superconductivity was discovered in 1911 by Heike Kamerlingh Onnes in mercury [68]. This was just 3 years after he succeeded in liquefying helium [69], which provided his lab the ability to cool to temperatures of a few Kelvins. The key features of superconductivity are the abrupt vanishing of DC electrical resistance and the expulsion of magnetic flux below the characteristic critical temperature T_c of the material at atmospheric pressure. In the subsequent decades, similar transitions were observed in many other elements and compounds. The T_c and year of discovery of some well-known superconductors are summarized in Figure 2. 1.

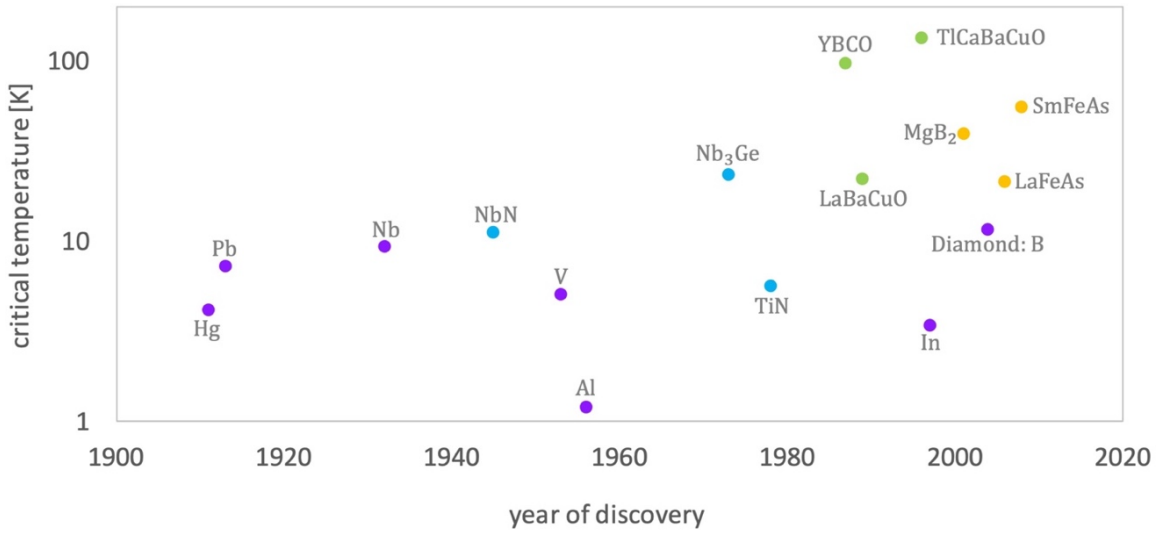

Figure 2. 1 Semi-log plot of superconducting transition temperature T_c of some elements and compounds discovered over the decades [68]-[85].

It was first argued by Herbert Frohlich in 1950 and further described by Leon Cooper in 1956, that the carriers of supercurrent are electron pairs. Leon Cooper later developed a microscopic theory of the pairing in 1956, where the Cooper pairs are formed due to electron-phonon interaction. The Bardeen-Cooper-Schrieffer (BCS) theory of superconductivity was published in 1957 [86], which depicts the many-body wave function of the condensate as a linear combination of single-electron states with correlation among electrons of opposite momenta and spin. The correlation persists over a coherence length

$$\xi_0 = \hbar v_F / \pi \Delta_0 \,, \tag{2.1}$$

where v_F is the Fermi velocity and $\Delta_0 = \Delta(T = 0)$ is the energy gained per electron due to formation of Cooper pair at zero temperature. The condensation energy is given by the difference between the superconducting energy $U_s(0)$ and normal state energy $U_n(0)$.

$$U_s(0) - U_n(0) = -\frac{1}{2} N_0 \Delta^2(0) \,, \tag{2.2}$$

where $N_0 = 3n_e/4\varepsilon_F$ is the single-spin density of electron states in the normal state at the Fermi level, n_e is the density of conduction electrons, and ε_F is the Fermi energy. A handy BCS relation gives the energy gap at zero temperature as [87]

$$\Delta_0 \equiv \Delta(0) = \frac{\hbar\omega_D}{\sinh(U_0 N_0)^{-1}} \approx 1.764 k_B T_c \,, \tag{2.3}$$

where ω_D is the Debye frequency and U_0 is the interaction energy between electrons. For empirical convenience, $\Delta(T)$ can be approximated for various temperature ranges as [87][88]

$$\Delta(T) \simeq \begin{cases} \Delta_0 \sqrt{1-\left(\frac{T}{T_c}\right)^4} & \text{, for } T > T_c \\ 1.735\Delta_0 \sqrt{1-\frac{T}{T_c}} & \text{, for } T \sim T_c \\ \Delta_0 e^{-\frac{2\pi k_B T}{\Delta_0}} e^{-\frac{\Delta_0}{k_B T}} & \text{, for } T \ll T_c \end{cases} . \quad (2.4)$$

In *type I* superconductors [87], typically found in clean pure metals, presence of a sufficiently strong magnetic field H_c destroys superconductivity and returns a material to its normal state. This critical magnetic field depends on the temperature as [89]

$$H_c(T) \cong H_c(0)\left(1-\frac{T^2}{T_c^2}\right). \quad (2.5)$$

Below the critical value, magnetic field decays exponentially from the surface to the interior of the superconductor. The distance from the surface where the magnetic field decays to e^{-1} of its value defines the London penetration depth λ_L [90]. In the local limit where $\xi_0 \ll \lambda_L$, the penetration depth λ_L varies with temperature as

$$\frac{1}{\lambda_L^2(T)} = \frac{1}{\lambda_{L0}^2}\left(1 + 2\int_{\Delta(T)}^{\infty} dE \, \frac{\partial f(E)}{\partial E} \frac{E}{\sqrt{E^2-\Delta(T)^2}}\right), \quad (2.6)$$

where $\lambda_{L0} \equiv \lambda_L(0) = \sqrt{m_q/\mu_0 n_s q^2}$, n_s is the density of Cooper pairs, m_q is the mass of a Cooper pair, and $q = 2e$ is the charge of a Cooper pair. Empirical approximations [87][91] give

$$\frac{\lambda_L(T)}{\lambda_{L0}} \simeq \begin{cases} \left(1-\left(\frac{T}{T_c}\right)^4\right)^{-\frac{1}{2}} & , \quad \text{for } T/T_c > 0.8 \\ \sqrt{\frac{\pi\Delta}{2k_B T}} e^{-\frac{\Delta}{k_B T}} + 1 & , \quad \text{for } T/T_c < 0.5 \end{cases} . \quad (2.7)$$

2.1. Quasiparticle Loss

When a superconductor absorbs a phonon or photon with energy $> 2\Delta$, a Copper pair breaks into two single-particle excitations (see Figure 2. 2). These excitations are called quasiparticles. Quasiparticles moving in a superconductor behave much like electrons in a normal metal and give rise to dissipation at high frequencies. Two quasiparticles can recombine into a Cooper pair, emitting a phonon with energy $\sim 2\Delta$. When the quasiparticle creation rate balances with the recombination rate, an equilibrium quasiparticle density is achieved.

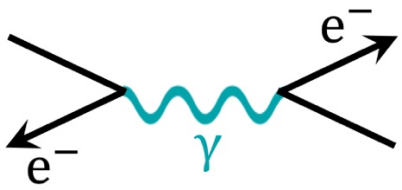

Figure 2. 2 Illustration of a Cooper pair as two electrons e^{-1} exchange a phonon γ. When a pair absorbs a phonon or photon with energy $> 2\Delta$, the pair breaks into two quasiparticles.

2.1.1. Thermal Quasiparticles

The equilibrium thermal quasiparticle density [87] can be calculated from

$$n_{thqp} = \int_{-\infty}^{\infty} dE\, D(E) f(E)\,, \tag{2. 8}$$

where $f(E)$ is the Fermi distribution and $D(E)$ is the quasiparticle density of states given by

$$D(E) = \begin{cases} 2N_0 \dfrac{|E|}{\sqrt{E^2 - \Delta(T)^2}} & ,\text{for} |E| > \Delta \\ 0 & ,\text{for} |E| \leq \Delta \end{cases}. \tag{2. 9}$$

Adopting the semiconductor model of a superconductor and setting the chemical potential to $\mu = 0$, which is equivalent to assuming that the energy E of the quasiparticles is measured from the Fermi energy that lies midway between the valence band and conduction band (as illustrated in Figure 2. 3, (2. 8) can be evaluated as

$$n_{thqp}(T) = 4N_0 \int_{\Delta}^{\infty} dE \, \frac{E}{\sqrt{E^2 - \Delta^2}} \frac{1}{1 + e^{E/k_B T}} \tag{2.10}$$

$$= 4N_0 \int_{\Delta}^{\infty} dE \, \frac{E}{\sqrt{E^2 - \Delta^2}} e^{-E/k_B T} \sum_{n=0}^{\infty} (-1)^n e^{-nE/k_B T} \, ,$$

where a Taylor series expansion has been applied to $\left(1 + e^{E/k_B T}\right)^{-1}$. In the limit $E \sim \Delta \gg k_B T$ where my devices were studied, one finds

$$n_{thqp} \simeq 4N_0 k_B T \int_{\frac{\Delta}{k_B T}}^{\infty} dx \, \frac{x e^{-x}}{\sqrt{x^2 - (\Delta/k_B T)^2}}$$

$$= 4N_0 k_B T e^{-\Delta/k_B T} \int_0^{\infty} dy \, \frac{(y + \Delta/k_B T) e^{-y}}{\sqrt{(y + \Delta/k_B T)^2 - (\Delta/k_B T)^2}}$$

$$= 4N_0 k_B T e^{-\Delta/k_B T} \left(\int_0^{\infty} dy \, \frac{y^{1/2} \, e^{-y}}{\sqrt{y + 2\Delta/k_B T}} + \frac{\Delta}{k_B T} \int_0^{\infty} dy \, \frac{y^{-1/2} \, e^{-y}}{\sqrt{y + 2\Delta/k_B T}} \right) \tag{2.11(a)}$$

For $2\Delta/k_B T \gg 1$, this gives

$$n_{thqp} \simeq \frac{4N_0 (k_B T)^{3/2} e^{-\Delta/k_B T}}{\sqrt{2\Delta}} \left(\int_0^{\infty} dy \, y^{1/2} \, e^{-y} + \frac{\Delta}{k_B T} \int_0^{\infty} dy \, y^{-1/2} \, e^{-y} \right)$$

$$\simeq \frac{4N_0 (k_B T)^{3/2} e^{-\Delta/k_B T}}{\sqrt{2\Delta}} \left(\Gamma\left(\frac{3}{2}\right) + \frac{\Delta}{k_B T} \Gamma\left(\frac{1}{2}\right) \right)$$

$$= \frac{4N_0 (k_B T)^{3/2} e^{-\Delta/k_B T}}{\sqrt{2\Delta}} \left(\frac{\sqrt{\pi}}{2} + \frac{\Delta}{k_B T} \sqrt{\pi} \right) , \tag{2.11(b)}$$

where Γ is the gamma function. Again using $\Delta \gg k_B T$ gives

$$n_{thqp} \simeq \frac{4N_0(k_BT)^{3/2}e^{-\Delta/k_BT}}{\sqrt{2\Delta}}\left(\frac{\Delta}{k_BT}\sqrt{\pi}\right)$$

$$= 2\sqrt{2\pi k_B T \Delta} N_0 e^{-\Delta/k_BT}\,. \qquad (2.11(c))$$

We note that (2.11(c)) is commonly used, but (2.11(b)) is a much better approximation.

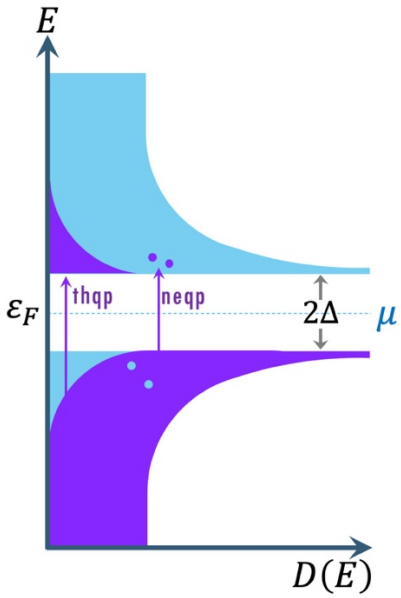

Figure 2. 3 Semiconductor model of a superconductor with $\mu = 0$, which is equivalent to assuming that the energy E of the quasiparticles is measured from the Fermi energy, which lies midway between the valence band and conduction band. Purple represent occupied states and blue represent unoccupied state.

2.1.2. Non-equilibrium Quasiparticles

Figure 2. 4 shows a log plot of the expected density of thermal quasiparticles in aluminum versus temperature using $\Delta_0 = 1.67 \times 10^{-4}$ eV, and $N_0 = 4.53 \times 10^{47}$ eV μm^{-3} [92]. At typical cryogenic temperatures of 20 mK, we would expect $n_{thqp} \sim 7 \times 10^{-37}$ μm^{-3}, which is an

exceedingly small density (for reference the volume of Earth's moon is $\sim 2 \times 10^{37}$ μm^3) and approximately 10^{37} times smaller than typical observed densities [93]-[100]. The observed excess density, which are referred to as the non-equilibrium quasiparticle density n_{neqp}, could arise from infrared radiation from stages of the dilution refrigerator that are at higher temperatures [101], photons traveling through the transmission lines [102], stray cosmic radiation [103], or background radioactivity [103]. In the steady state, the rate of excess quasiparticle production will be balanced by recombination and trapping (*e.g.* from vortices) so that the quasiparticles reach a constant average density n_{neqp}. If trapping dominates over recombination, the total quasiparticle density obeys $n_{qp} = n_{neqp} + n_{thqp}$.

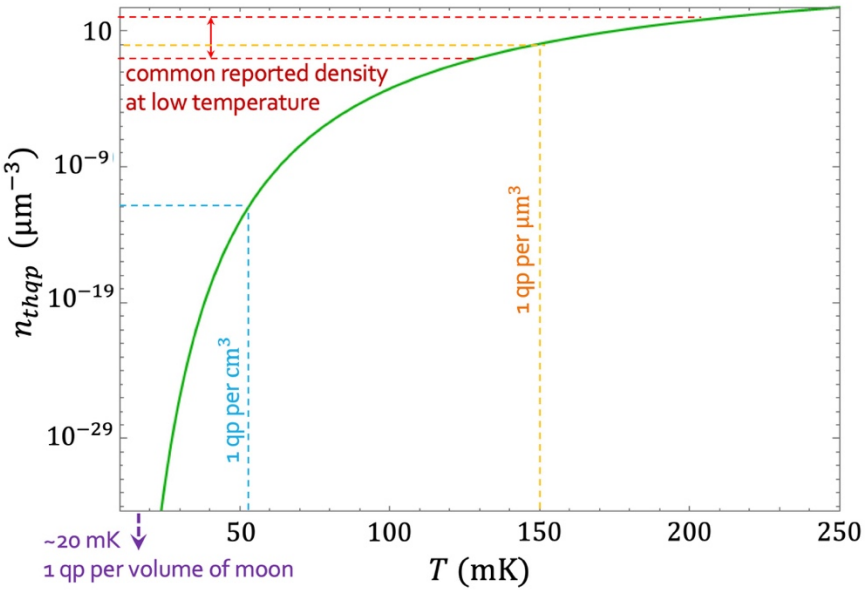

Figure 2. 4 Log plot of the expected density of thermal quasiparticles in aluminum versus temperature using $\Delta_0 = 1.67 \times 10^{-4}$ eV, and $N_0 = 4.53 \times 10^{47}$ eV μm^{-3}.

2.1.2.1. Effective Chemical Potential Representation

In 1972, C.S. Owen and D.J. Scalapino introduced a model for the non-equilibrium quasiparticles that uses an effective chemical potential μ^* [104] in the Fermi distribution, such that

$$f(E,T) \to f(E-\mu^*,T)\,. \tag{2.12}$$

With this approach, the total quasiparticle density can still be obtained from

$$n_{qp} = 4N_0 \int_0^\infty D(\epsilon)\frac{d\epsilon}{1+e^{\beta(\epsilon-\mu^*)}}, \tag{2.13}$$

where $\epsilon = \sqrt{E^2+\Delta^2}$ and $\beta = (k_B T)^{-1}$.

In the limit of low temperature ($T \lesssim \frac{1}{10}T_c$), the non-equilibrium quasiparticle density can be approximated as

$$\begin{aligned} n_{neqp} &= 4N_0 \int_0^\infty D(\epsilon)\frac{d\epsilon}{1+e^{\beta(\epsilon-\mu^*)}} - 4N_0 \int_0^\infty D(\epsilon)\frac{d\epsilon}{1+e^{\beta(\epsilon)}} \\ &= 4N_0 \int_\Delta^\infty dE\ \frac{E}{\sqrt{E^2-\Delta^2}}\frac{1-e^{\beta\mu^*}}{1+e^{\beta\mu^*}+e^{-\beta E}+e^{\beta\mu^*}e^{\beta E}} \\ &\simeq 2N_0\sqrt{2\Delta}\frac{1-e^{\beta\mu^*}}{e^{\beta\mu^*}}e^{-\beta\Delta}\int_\Delta^\infty dE\ \left(\frac{1}{\sqrt{E-\Delta}}+\frac{3}{4\Delta}\sqrt{E-\Delta}\right)e^{-\beta(E-\Delta)} \\ &\simeq 2N_0\sqrt{\frac{2\pi\Delta}{\beta}}\left(1+\frac{3}{8\Delta\beta}\right)\frac{1-e^{\beta\mu^*}}{e^{\beta\mu^*}}e^{-\beta\Delta} \\ &\simeq 2N_0\sqrt{\frac{2\pi\Delta}{\beta}}e^{-\beta(\Delta-\mu^*)}\,. \end{aligned} \tag{2.14}$$

From this relation, the effective chemical potential can be calculated as

$$\mu^* \simeq k_B T ln\left(\frac{n_{neqp}}{2N_0\sqrt{2\pi k_B T\Delta}}\right)+\Delta\ . \tag{2.15}$$

Figure 2. 5 shows a plot of the effective chemical potential for a constant non-equilibrium quasiparticle density of $n_{neqp} = 7 \times 10^{-37}$ μm^{-3}(purple), 1 cm^{-3} (blue), 1 μm^{-3} (orange), 10^{-1} to 10^{2} μm^{-3} (red region) corresponding to the plot in Figure 2. 4. This effective chemical potential model is one way to account for a non-equilibrium quasiparticle density and has been applied to Cooper pair box [105] as well as superconducting coplanar resonators [106].

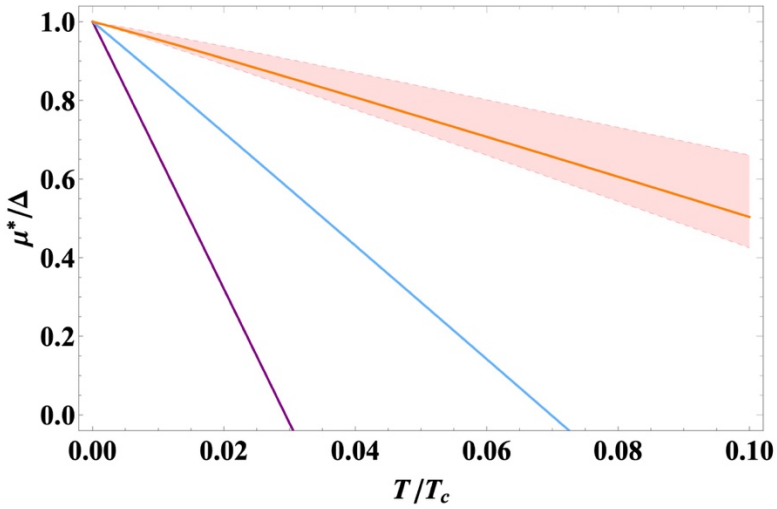

Figure 2. 5 Plot of effective chemical potential for non-equilibrium densities of $n_{neqp} = 7 \times 10^{-37}$ μm^{-3}(purple), 1 cm^{-3} (blue), 1 μm^{-3} (orange), and the range 10^{-1} to 10^{2} μm^{-3} (red region), corresponding to the plot in Figure 2. 4.

2.1.2.2. Effective Temperature Representation

In 1975, W. H. Parker proposed an alternative representation for describing non-equilibrium effects in the quasiparticle distribution via an elevated effective temperature T^* [107] such that

$$f(E,T) \rightarrow f(E,T^*)\,, \tag{2.16}$$

where $T^* > T$ is given implicitly by the equation

$$\left(\frac{n_{qp}}{n_{thqp}}\right)^2 \cong \left(\frac{T^*}{T}\right)^3 \left(\int_{X_G^*}^{\infty} \frac{x^2 dx}{e^x - 1} \Big/ \int_{X_G}^{\infty} \frac{x^2 dx}{e^x - 1}\right) \tag{2.17}$$

for $X_G^* = \frac{2\Delta(T^*)}{k_B T^*}$ and $X_G = \frac{2\Delta(T)}{k_B T}$.

In my system, excess energy from non-equilibrium quasiparticles leaves the system by phonons. The Parker model can be used to describe non-equilibrium quasiparticles generated from high-energy phonons ($E > 2\Delta$) by considering the Rothwarf and Taylor rate equations [108] given by

$$\frac{dn_{qp}}{dt} = I_0 + \frac{2n_\omega}{\tau_B} - Rn_{qp}^2 \tag{2.18}$$

$$\frac{dn_\omega}{dt} = \frac{Rn_{qp}^2}{2} - \frac{n_\omega}{\tau_B} - \frac{n_\omega - n_{\omega T}}{\tau_\gamma}, \tag{2.19}$$

where I_0 is the volume rate of creation of quasiparticles by an external mechanism, $\tau_B^{-1}$is the mean rate at which a phonon creates quasiparticles, R is a recombination coefficient, τ_γ^{-1} is the rate at which phonons of energy $> 2\Delta$ disappear by processes other than quasiparticle creation, n_ω is the density of phonons with energy $> 2\Delta$, and $n_{\omega T}$ is the thermal equilibrium density of phonons with energy $> 2\Delta$.

For non-equilibrium quasiparticles created by optical illumination, incorporating T^* into the Rothwarf and Taylor equations gives [107]

$$P = \frac{2n_{\omega T} V}{\tau_\gamma} \frac{\bar{E}(n_{qp}, T^*)}{F(n_{qp}, T^*)} \left[n_{qp}^2 - 1\right], \tag{2.20}$$

where P is the power absorbed from optical illumination, V is the volume of the superconductor, $\bar{E}(n_{qp}, T^*)$ is mean energy of quasiparticles given by

$$\bar{E}\left(n_{qp}, T^*\right) = \int_{\Delta}^{\infty} dE \, \frac{E^2}{\sqrt{E^2 - \Delta^2(T^*)}} f(E, T^*) \Big/ \int_{\Delta}^{\infty} dE \, \frac{E}{\sqrt{E^2 - \Delta^2(T^*)}} f(E, T^*) \,, \qquad (2.21)$$

and $F\left(n_{qp}, T^*\right) = (1 + R(T^*))^{-1}$ is the fraction of the absorbed energy that is shared among the non-equilibrium quasiparticles.

2.1.3. Gorter-Casimir Two-Fluid Model

For temperatures below T_c, a superconductor contains a mixture of Cooper pairs and quasiparticles. The Gorter-Casimir two-fluid model from 1933 [109] considers a superconductor as a superconducting inductive channel in parallel to a normal resistive channel associated with quasiparticles; analogous to an electric circuit with an inductor connected in parallel to a resistor. In the DC limit, the inductive channel shorts out the resistive channel and results in zero resistance. In the AC case, charge carriers flow in the parallel channels, and for sinusoidal field $\vec{E}(t) = \overrightarrow{E_0} e^{i\omega t}$ and current $\vec{J}(t) = \overrightarrow{J_0} e^{i\omega t}$, the complex conductivity σ is defined by

$$\vec{J} \equiv \sigma(\omega)\vec{E} \,. \qquad (2.22)$$

If there was no normal channel one finds $\sigma(\omega) = q^2 n_c \backslash i\omega m_c$, where q, n_c, and m_c are the charge, density and mass of the charge carriers (Cooper pairs).

Adopting the empirical approximation for the density of charge carrier in the superconducting channel as $n_s \sim 1 - \left(\frac{T}{T_c}\right)^4$, and in the normal channel as $n_n \sim \left(\frac{T}{T_c}\right)^4$, gives the complex conductivity as

$$\begin{aligned}\sigma(\omega) &= \frac{n_n e^2}{m_e}\frac{\tau_n}{1+i\omega\tau_n} + \frac{n_s e^2}{m_e}\frac{\tau_s}{1+i\omega\tau_s} \\ &= \frac{n_n e^2 \tau_n}{m} + \frac{\pi n_s e^2}{2m}\delta(\omega) - i\frac{n_s e^2}{m\omega},\end{aligned} \tag{2.23}$$

where e and m_e are the charge and mass of an electron, $\tau_n \ll 1/\omega$ for my experiments, and $\tau_s \to \infty$ are the relaxation time of the normal and "superconducting electrons" respectively.

2.1.4. Mattis-Bardeen Complex Conductivity

In 1958, D. C. Mattis and J. Bardeen [110], and independently A. A. Abrikosov, L. P. Gor'kov and I. M. Khalatnikov [111], reported theories of the surface impedance for superconductors based on the BCS theory. Mattis-Bardeen theory describes the non-local relation between the current density $\vec{J}$ and the vector potential $\vec{A}$ as

$$\vec{J}(\vec{r}) = \frac{3\Delta_0}{4\pi\xi_0\lambda_{L0}^2}\int_V d\vec{r}' \frac{\vec{R}\vec{R}\cdot\vec{A}(\vec{r}')I(\omega,R,T)e^{-R/l}}{R^4}, \tag{2.24}$$

with the kernel $I(\omega, R, T)$, an extension to nonzero frequencies of the BCS kernel [86], given by

$$I(\omega,R,T) = -i\pi \int_{\Delta-\hbar\omega}^{\Delta} dE\ \big(1-2f(E+\hbar\omega)\big)\big(g(E)\cos\alpha\Delta_2 - i\sin\alpha\Delta_2\big)e^{i\alpha\Delta_1}$$
$$-i\pi \int_{\Delta}^{\infty} dE\ \big(1-2f(E+\hbar\omega)\big)\big(g(E)\cos\alpha\Delta_2 - i\sin\alpha\Delta_2\big)e^{i\alpha\Delta_1} \qquad (2.25)$$
$$+i\pi \int_{\Delta}^{\infty} dE\ \big(1-2f(E)\big)\big(g(E)\cos\alpha\Delta_1 + i\sin\alpha\Delta_1\big)e^{-i\alpha\Delta_2}\ ,$$

where $\Delta_1 = \begin{cases} \sqrt{E^2-\Delta^2}\ , & |E|<\Delta \\ i\sqrt{\Delta^2-E^2}\ , & |E|<\Delta \end{cases}$, $\Delta_2 = \sqrt{(E^2+\hbar\omega)^2-\Delta^2}$, $g(E) = \frac{E^2+\Delta^2+\hbar\omega E}{\Delta_1\Delta_2}$, $\alpha = \frac{R}{\hbar v_0}$, $\vec{R} = \vec{r}\,' - \vec{r}$, and l is the mean free path. The factor $e^{-R/l}$ accounts for the effect of scattering by random scattering centers.

In the extreme anomalous limit where the penetration depth λ_L is small relative to ξ_0, an approximation $\alpha \sim 0$ can be made. The ratio of the superconducting complex conductivity $\sigma_s = \sigma_1 - i\sigma_2$ to the normal conductivity σ_n can then be expressed by [110]

$$\frac{\sigma_1 - i\sigma_2}{\sigma_n} = \frac{I(\omega,R,T)}{-i\pi\hbar\omega} \qquad (2.26)$$

$$\frac{\sigma_1}{\sigma_n} = \frac{2}{\hbar\omega}\int_{\Delta}^{\infty} dE\ \big(f(E)-f(E+\hbar\omega)\big)g(E) + \frac{1}{\hbar\omega}\int_{\Delta-\hbar\omega}^{-\Delta} dE\ \big(1-2f(E+\hbar\omega)\big)g(E) \qquad (2.27)$$

$$\frac{\sigma_2}{\sigma_n} = \frac{1}{\hbar\omega}\int_{\Delta-\hbar\omega,-\Delta}^{\Delta} dE\ \frac{[1-2f(E+\hbar\omega)](E^2+\Delta^2+\hbar\omega E)}{\sqrt{\Delta^2-E^2}\sqrt{(E+\hbar\omega)^2-\Delta^2}}dE\ . \qquad (2.28)$$

The second term in (2.27) vanishes except for $\hbar\omega > 2\Delta$, in which case the lower integration limit is $-\Delta$ instead of $\Delta - \hbar\omega$.

In the extreme anomalous limit, an effective penetration depth can be obtained with [110]

$$\lambda_{eff} = \mathrm{Re}\left[\frac{\sqrt{3}}{2}K_{\infty}\left(\xi_0, l_{mf}, T\right)^{-\frac{1}{3}}\right], \tag{2.29}$$

where l_{mf} is the mean free path, and K_{∞} is the asymptote of the one-dimensional Mattis-Bardeen kernel in Fourier space.

2.1.4.1. Simplifications from Adopting Parker's T^* Model

If I take $\hbar\omega < 2\Delta$ and adopt the effective temperature T^* representation of non-equilibrium quasiparticles (see Section 2.1.2.2), the Mattis-Bardeen conductivity $\sigma_s = \sigma_1 + i\sigma_2$ in (2.27) and (2.28) can be expressed as

$$\frac{\sigma_1}{\sigma_n} = \frac{2}{\hbar\omega}\int_{\Delta}^{\infty}\frac{[f(E,\Delta,T^*) - f(E+\hbar\omega,\Delta,T^*)](E^2+\Delta^2+\hbar\omega E)}{\sqrt{E^2-\Delta^2}\sqrt{(E+\hbar\omega)^2-\Delta^2}}dE \tag{2.30}$$

$$\frac{\sigma_2}{\sigma_n} = \frac{1}{\hbar\omega}\int_{\Delta-\hbar\omega}^{\Delta}\frac{[1-2f(E+\hbar\omega,\Delta,T^*)](E^2+\Delta^2+\hbar\omega E)}{\sqrt{\Delta^2-E^2}\sqrt{(E+\hbar\omega)^2-\Delta^2}}dE\ . \tag{2.31}$$

For $\hbar\omega \ll \Delta$, $k_BT \ll \Delta$, $e^{-E/k_BT^*} \ll 1$, the Mattis-Bardeen conductivity can be simplified to [106]

$$\frac{\sigma_1}{\sigma_n} = \frac{4\Delta}{\hbar\omega}e^{-\Delta/k_BT^*}\sinh(\xi)K_0(\xi) \tag{2.32}$$

$$\frac{\sigma_2}{\sigma_n} = \frac{\pi\Delta}{\hbar\omega}[1-2e^{-\Delta/k_BT^*}e^{-\xi}I_0(\xi)\,], \tag{2.33}$$

where $\xi = \hbar\omega/2k_BT^*$.

The quasiparticle distribution in Parker's model, as expressed in (2.16) predicts a density of quasiparticles that decreases approximately exponentially as temperature decreases until $T < T^*$, at which point the density of quasiparticles approaches a constant value given by $n_{qp} \simeq 2N_0\sqrt{2\pi k_B T^* \Delta}\, e^{-\Delta/k_B T^*}$. Expressing T^* as a function of n_{qp} gives

$$\frac{\sigma_1}{\sigma_n} \simeq \frac{2\Delta}{\hbar\omega}\frac{n_{qp}}{N_0\sqrt{2\pi k_B T^* \Delta}}\sinh(\xi)K_0(\xi) \tag{2.34}$$

$$\frac{\sigma_2}{\sigma_n} \simeq \frac{\pi\Delta}{\hbar\omega}\left[1 - \frac{n_{qp}}{N_0\sqrt{2\pi k_B T^* \Delta}}e^{-\xi}I_0(\xi)\right]. \tag{2.35}$$

The surface impedance Z_s for thin film with thickness $t < \lambda_{eff}$ can be written as

$$\begin{aligned} Z_s \equiv R_s + i\omega L_{sur} &= \frac{E_x(0)}{\int_0^t J_x(z)dz} \simeq \frac{E_x(0)}{\int_0^t J_x(0)dz} = \frac{E_x(0)}{\int_0^t \sigma E_x(0)dz} = \frac{1}{(\sigma_1 - i\sigma_2)t} \\ &= \sigma_1 t|Z_s|^2 + i\sigma_2 t|Z_s|^2, \end{aligned} \tag{2.36}$$

where z is parallel to the surface normal, and $E_x(0)$ is the electric field in the direction of the current flow. The surface inductance is then given by

$$L_{sur} = \frac{\sigma_2 t}{\omega}|Z_s|^2, \tag{2.37}$$

and the surface resistance is given by

$$R_s = \sigma_1 t|Z_s|^2. \tag{2.38}$$

2.1.5. Realistic Quasiparticle Distribution Under Drive

In the previous discussion, both the effective chemical potential and the effective temperature representations of non-equilibrium quasiparticles assume a smooth Fermi-like distribution $f(E,T)$. A more rigorous examination into the situation finds that this is not true in general. Nevertheless, both effective μ and T^* representations are good approximations of $f(E,T)$ for low energy quasiparticles. Taking into consideration the absorption of photons at frequency v_p by the quasiparticles produces spikes in the distribution $f(E,T)$ corresponding to the photon energy hv_p and subsequent phonons emitted from scattering of non-equilibrium quasiparticles with energies $> 3\Delta$ are expected. In 2012, D. J. Goldie and S. Withington [112] described the dynamics of the coupled quasiparticle and phonon system with the following rate equations:

$$\begin{aligned}\frac{df(E)}{dt} = I_{qp}(E, v_p)\\ &-\frac{1}{\tau_0(k_B T_c)^3}\int_0^{\infty} d\Omega\, \Omega^2 \rho(E+\Omega)\left(1-\frac{\Delta^2}{E(E+\Omega)}\right)\\ &\times\{f(E)[1-f(E+\Omega)]n(\Omega)-[1-f(E)]f(E+\Omega)[n(\Omega)+1]\}\\ &-\frac{1}{\tau_0(k_B T_c)^3}\int_0^{E-\Delta} d\Omega\, \Omega^2 \rho(E-\Omega)\left(1-\frac{\Delta^2}{E(E-\Omega)}\right)\\ &\times\{f(E)[1-f(E-\Omega)][n(\Omega)+1]-[1-f(E)]f(E-\Omega)n(\Omega)\}\\ &-\frac{1}{\tau_0(k_B T_c)^3}\int_{E+\Delta}^{\infty} d\Omega\, \Omega^2 \rho(\Omega-\mathrm{E})\left(1+\frac{\Delta^2}{E(\Omega-E)}\right)\\ &\times\{f(E)f(\Omega-E)[n(\Omega)+1]-[1-f(E)][1-f(\Omega-E)]n(\Omega)\},\end{aligned} \tag{2.39}$$

$$\frac{dn(\Omega)}{dt} = -\frac{n(\Omega) - n(\Omega, T_b)}{\tau_l}$$
$$-\frac{2}{\pi\tau_0^{\phi}\Delta_0}\int_{\Delta}^{\infty} dE\ \rho(E)\rho(E+\Omega)\left(1-\frac{\Delta^2}{E(E+\Omega)}\right)$$
$$\times\{f(E)[1-f(E+\Omega)]n(\Omega) - [1-f(E)]f(E+\Omega)[n(\Omega)+1]\} \quad (2.40)$$
$$-\frac{2}{\pi\tau_0^{\phi}\Delta_0}\int_{\Delta}^{\Omega-\Delta} dE\ \rho(E)\rho(\Omega-E)\left(1+\frac{\Delta^2}{E(\Omega-E)}\right)$$
$$\times\{[1-f(E)][1-f(\Omega-E)]n(\Omega) - f(E)f(\Omega-E)[n(\Omega)+1]\}.$$

Here τ_0 and τ_0^{ϕ} are the characteristic quasiparticle and phonon lifetimes [113], respectively. τ_l is the energy-independent lifetime of the emitted phonons. $\rho(E,\Delta) = E/\sqrt{E^2-\Delta^2}$ is the normalized quasiparticle density of states. $n(\Omega)$ is the Bose distribution of the phonons at energy Ω and $n(\Omega, T_b)$ is $n(\Omega)$ evaluated at the bath temperature T_b. The term $I_{qp}(E, v_p)$ accounts for an external source of photons at energy E that generates quasiparticles. The energy gap Δ, shifted from the equilibrium value due to the presence of non-equilibrium quasiparticles, can be determined by the self-consistent equation

$$\frac{1}{N_0 V_{BCS}} = \int_{\Delta}^{\infty} dE\ \frac{1-2f(E)}{\sqrt{E^2-\Delta^2}}, \quad (2.41)$$

where V_{BCS} is the BCS interaction parameter. In the steady state under external drive,

$$\frac{df(E)}{dt} = \frac{dn(\Omega)}{dt} = 0. \quad (2.42)$$

G.M. Eliashberg showed in 1972 [114] that for sub-gap photons, *i.e.* $hv_p < 2\Delta$, $I_{qp}(E, v_p)$ takes the form

$$I_{qp}(E,v_p) = 2B\left\{\rho(E+hv_p,\Delta)\left(1+\frac{\Delta^2}{E(E+hv_p)}\right)[f(E+hv_p)-f(E)]\right.$$
$$\left.-\rho(E-hv_p,\Delta)\left(1+\frac{\Delta^2}{E(E-hv_p)}\right)[f(E)-f(E-hv_p)]\right\}, \tag{2.43}$$

where B is a rate coefficient that needs to be determined. For uniform absorption, the power absorbed per unit volume of material can be calculated as [112]

$$P_{abs} = 4N_0\int_{\Delta}^{\infty} dE\; I_{qp}(E,v_p)E\rho(E,\Delta). \tag{2.44}$$

B can be obtained numerically by writing $I_{qp}(E,v_p) = BK_{qp}(E,v_p)$ and solving

$$\delta P \equiv 4N_0B\int_{\Delta}^{\infty} dE\; K_{qp}(E,v_p)E\rho(E,\Delta) - P_{abs} = 0. \tag{2.45}$$

The power transfer from quasiparticles to phonons (see Figure 2. 6) per unit volume of the film is

$$P_{qp-\phi} = 4N_0\int_{\Delta}^{\infty} dE\; I_{qp-\phi}(E,v_p)E\rho(E,\Delta). \tag{2.46}$$

A corresponding error term can be defined by the fraction

$$\xi_{qp-\phi} \equiv \frac{P_{abs}-P_{qp-\phi}}{P_{abs}}. \tag{2.47}$$

The power transfer from the phonons to the substrate per unit volume of the film can be written as

$$P_{\phi-b} = \sum_{br} N_{ion}\int_0^{\infty} d\Omega\, D(\omega)\Omega\frac{n(\Omega)-n(\Omega,T_b)}{\tau_l}, \tag{2.48}$$

where $D(\omega) = 3\Omega^2/\Omega_D^3$ is the Debye density of states for Debye energy Ω_D, and N_{ion} is the density of ions per phonon dissipation channel branch. A corresponding error term can be defined by the fraction

$$\xi_{\phi-b} \equiv \frac{P_{abs} - P_{\phi-b}}{P_{abs}}. \tag{2.49}$$

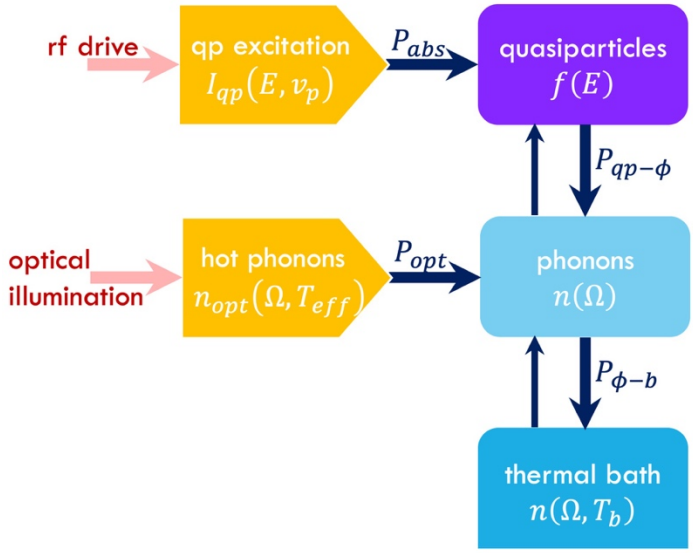

Figure 2. 6 Illustration of power transfer between quasiparticles, phonons and bath. Adapted from ref.[186].

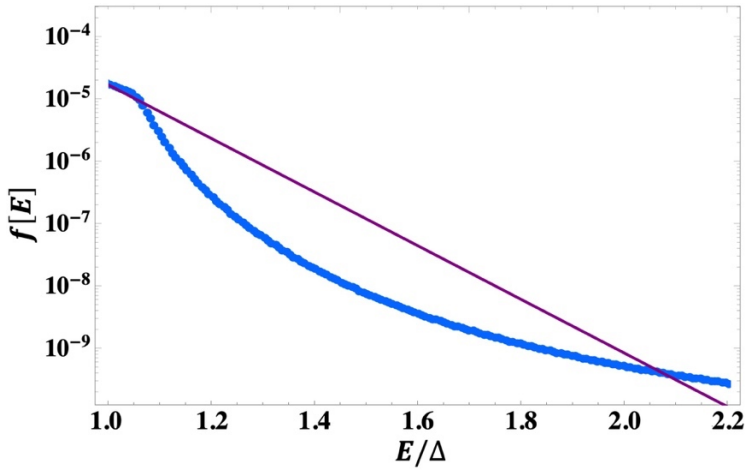

Figure 2. 7 Example of quasiparticle distribution numerically solved from (2.39) and (2.40) for $hv_p \sim 2.5\Delta$, $\Delta \sim 215\mu eV$ (blue). For comparison, $f(E,T)$ is plotted for $T \sim 226mK$ (purple).

2.1.6. Quasiparticle Recombination

Solving (2.39) and (2.40) for the steady state with $dn/dt = 0$ and $df/dt = 0$ gives steady state values about which the instantaneous densities fluctuate. Time fluctuations in the number of quasiparticle excitations introduces a possible source of noise in superconducting devices. The origin of the fluctuations could come from a combination of noises in quasiparticle generation, trapping and recombination, among which fluctuations in recombination and trapping should show a distinctive dependence on n_{qp}.

2.1.6.1. Recombination Mechanism

Whether quasiparticle recombination or trapping dominates depends on the density of quasiparticles compared with the density of trapping sites. In 1976, S. B. Kaplan *et al.* obtained the expected lifetimes of quasiparticles for near equilibrium conditions [113] by using the Eliashberg formulation [114]. The recombination rate $\tau_r(\varepsilon)$ for a quasiparticle with energy ε can be written as

$$\frac{\tau_0}{\tau_r(\varepsilon)} = \frac{1}{(k_B T_c)^3 (1-f(\varepsilon))} \int_\Delta^\infty dE\ (E+\varepsilon)^2 Re\left(\frac{E}{\sqrt{E^2+\Delta^2}}\right)\left(1+\frac{\Delta^2}{\varepsilon E}\right)(n(E+\varepsilon)+1)f(E)\,, \qquad (2.50)$$

where $f(\varepsilon)$ is the Fermi distribution, $n(E+\varepsilon)$ is the Bose-Einstein distribution, and τ_0 is a characteristic recombination time associated with the specific metal under consideration.

In the limit $T \ll T_c$ and in thermal equilibrium, this yields

$$\frac{\tau_0}{\tau_r(\Delta,T)} \simeq \sqrt{\pi}\left(\frac{2\Delta}{k_B T_c}\right)^{\frac{5}{2}} \sqrt{\frac{T}{T_c}} e^{-\Delta/k_B T} \simeq \frac{(2\Delta)^2}{(k_B T_c)^3} \frac{n_{thqp}}{2N_0}\,. \qquad (2.51)$$

Since the empirically observed non-equilibrium quasiparticle density at millikelvin temperatures generally exceeds the thermal density, （2.51） will not be valid. Instead, consider a single quasiparticle moving with speed v_{qp} in a superconductor with quasiparticle density n_{qp} and suppose each quasiparticle has an associated interaction cross-section $\sigma_{int} = \pi r_{int}^2$ of radius r_{int} measured from its location such that quasiparticles with overlapped cross-sections will recombine. In time dt, it will sweep out an interaction volume of $\pi(2r_{int})^2 v_{qp} dt$ containing $n_{qp}\pi(2r_{int})^2 v_{qp} dt$ quasiparticles. This yields on expected change in quasiparticle density as

$$dn_{qp} = -2\frac{n_{qp}}{2} n_{qp}\pi(2r_{int})^2 v_{qp} dt = -4\pi n_{qp}^2 r_{int}^2 v_{qp} dt\,. \tag{2.52}$$

It follows that

$$\frac{dn_{qp}}{dt} = -4\pi n_{qp}^2 r_{int}^2 v_{qp} \equiv -\frac{n_{qp}}{\tau_r}, \tag{2.53}$$

where $\tau_r = \left(4\pi r_{int}^2 v_{qp} n_{qp}\right)^{-1}$ is an effective recombination time constant with an inverse proportionality to n_{qp} analogous to the result of （2.51） in the thermal limit [113].

In 2011, R. Barends *et al.* [101] incorporated non-equilibrium quasiparticles into the Rothwarf-Taylor equations [108], and modelled the rate equation of the total quasiparticle density as

$$\frac{\delta n_{qp}}{\delta t} = \frac{P}{V\Delta} + \frac{G}{V} - RVn_{qp}^2\,, \tag{2.54}$$

where V is the volume of the superconductor, P is the absorbed power of photons with energy $\hbar\omega > 2\Delta$, G is the thermal generation term due to pair breaking by phonons, R is the material specific recombination constant, and trapping has been ignored. For example, Aluminum, with a

gap frequency of ~ 88 GHz, can absorb 96% of the power from a black body at 4.2 K. Solving (2.54) in steady state with $G = 0$ gives $n_{neqp} \propto \sqrt{P/\Delta}$.

2.1.6.2. Recombination Noise

In 2003, C. M. Wilson and D. F. Prober [115] described quasiparticle fluctuations due to generation and recombination using the master equation

$$\frac{\partial P(N,t|k,0)}{\partial t} = -\big(g(N) + r(N)\big) \cdot P(N,t|k,0) + g(N-\delta N) \cdot P(N-\delta N,t|k,0) + r(N+\delta N) \cdot P(N+\delta N,t|k,0). \tag{2.55}$$

$P(N,t|k,0)$ is the *conditional* probability of N quasiparticles present at time t given that k quasiparticles were present at $t = 0$. $g(N)dt$ and $r(N)dt$ are the probability of a generation or recombination event occurring in the time interval dt when N quasiparticles are present, respectively. δN is the change in quasiparticles number, which equals to 2 for one recombination event. In steady state, (2.55) gives the expectation value

$$\langle g(N) \rangle = \langle r(N) \rangle . \tag{2.56}$$

Taylor expansion of $g(N)$ and $r(N)$ around an equilibrium N^0 to second order gives

$$g(N^0) + \frac{1}{2} g''(N^0) \langle \Delta N^2 \rangle = r(N^0) + \frac{1}{2} r''(N^0) \langle \Delta N^2 \rangle , \tag{2.57}$$

where $\langle \Delta N^2 \rangle = \langle (N - N^0)^2 \rangle$ is the variance of N. Assuming generation and recombination balance in equilibrium gives $g(N^0) \simeq r(N^0)$. On the other hand, multiplying the steady state master equation by N^2 and sum over all N gives [115]

$$\left\langle \left(N + \frac{\delta N}{2} \right) \cdot g(N) \right\rangle = \left\langle \left(N - \frac{\delta N}{2} \right) \cdot r(N) \right\rangle . \tag{2.58}$$

Taylor expansion of *(2.58)* around N^0 to second order and comparing with (2.56) gives

$$\langle \Delta N^2 \rangle = \delta N \frac{r(N^0)}{r'(N^0) + g'(N^0)} . \tag{2.59}$$

The autocorrelation function [116] between time $t = 0$ to t_{lag} is defined as

$$\Phi(t_u) \equiv \langle N(0) N(t_{lag}) \rangle = \sum_k \sum_j k \cdot j \cdot P(k, 0 \cap j, t_{lag}) , \tag{2.60}$$

where $P(k, 0 \cap j, t_{lag})$ is the *joint* probability of k quasiparticles present at $t = 0$ and j quasiparticles at $t = t_{lag}$. Evaluating the sum over j yields

$$\Phi(t_u) \equiv \sum_k k \cdot P(k, 0) \sum_j j \cdot P(j, t_{lag} | k, 0) = \sum_k k \cdot \langle N \rangle_k \cdot P(k, 0) , \tag{2.61}$$

where $\langle N \rangle_k$ is the expectation value of N given that k quasiparticles were present at $t = 0$. From the master equation it can be shown that [115]

$$\frac{d\langle N \rangle_k}{dt_{lag}} = \delta N (\langle g(N) \rangle - \langle r(N) \rangle) . \tag{2.62}$$

Taylor expansion of (2.62) around N^0 gives

$$\frac{d}{dt_{lag}}\langle \Delta N\rangle_{k-N^0} = -\frac{\langle \Delta N\rangle_{k-N^0}}{\tau_{eff}}, \tag{2.63}$$

$$\tau_{eff} = \frac{1}{\delta N}\frac{1}{r'(N^0) - g'(N^0)}, \tag{2.64}$$

where τ_{eff} is an effective relaxation time constant. Inserting the solution of $\langle \Delta N\rangle_{k-N^0}$ into the autocorrection function and take the Fourier transform gives the power spectrum of quasiparticle number fluctuations as

$$S_N(\omega) = \frac{4\langle \Delta N^2\rangle\, \tau_{eff}}{1+\omega^2\tau_{eff}^2}. \tag{2.65}$$

In the limit $\tau_{eff} = \tau_r$ where quasiparticle recombination is dominant, comparing equations (2.63), (2.64), (2.65) with the rate equation (2.53) in the previous section gives

$$g(n_{qp}) = \frac{P}{2\Delta} + \frac{G}{2} \quad ; \quad r(n_{qp}) = \frac{R}{2}n_{qp}^2, \tag{2.66}$$

$$\langle \Delta N^2\rangle = N^0. \tag{2.67}$$

Note that (2.67) is just what one expects from Poisson statistics, and the same result would be obtained if trapping dominated. Finally, the spectrum of noise is simply

$$S_{n_{qp}}(\omega) = \frac{4n_{qp}\tau_r}{1+\omega^2\tau_r^2} = \frac{8Rn_{qp}^2}{4R^2n_{qp}^2+\omega^2}. \tag{2.68}$$

2.2. Trapping and Loss from Vortex Motion

For quasiparticle limited systems, trapping of quasiparticles due to pinned vortices should also be considered. Thin films of *type I* superconductors such as aluminum commonly exhibit *type II* behavior [117], because the coherence length tends to be reduced by scattering from impurities on the film surface. For a *type II* superconductor, Abrikosov vortices [118] of trapped flux form when cooling through the superconducting phase transition in the presence of a strong enough magnetic field B. These vortices can be pinned in the film and be present for temperatures far below T_c.

Each magnetic vortex carries a single flux quantum $\Phi_0 = h/2e$. The superconducting order parameter reduces to zero in the vortex core over a length scale of ξ_0, while the magnetic flux extends beyond the core over a length scale of λ_L. Works from Stan *et al*. in 2004 gave a very rough value for the expected number of vortices as

$$N = \frac{A}{2\Phi_0}(B - B_m) \qquad \text{, for } B > B_m \tag{2.69}$$

in a strip of superconducting thin film with width W and area A, where $B_m \sim \Phi_0/W^2$ is the critical cooldown field beyond which vortices start to be trapped in the film.

2.2.1. Gittleman and Rosenblum (GR) Model

Vortices can move in a superconductor when acted upon by a Lorentz force from currents, causing dissipation. When the Lorentz force is balanced by viscous drag, vortices experience free-flux-flow (FFF), giving rise to the flux flow resistivity

$$\rho_{fff} = (B - B_m)\frac{\Phi_0}{\eta} \sim n_v \frac{\Phi_0^2}{\eta}, \tag{2.70}$$

where η is the vortex viscosity, and n_v is the areal density of vortices.

Defects, thickness variation and local inhomogeneity could induce the *strong vortex pinning* [119][120] in a thin film. Driving an AC current through the film causes a pinned vortex to oscillate in its pinning potential U approximated by $\nabla U(\vec{v}) \simeq k_p \vec{v}/i\omega$ with (de)pinning angular frequency $\omega_p = k_p/\eta$, where k_p is the pinning constant, $\vec{v}$ is the velocity of vortex motion and $\vec{v}/i\omega$ is the vortex displacement. Without considering thermal and Hall effects, Jonathan I. Gittleman and Bruce Rosenblum wrote the vortex motion resistivity as [121]

$$\rho_{vm,GR} = (B - B_m)\frac{\Phi_0}{\eta}\frac{1}{1 - i\frac{\omega_p}{\omega}}. \tag{2.71}$$

This reduces to the free-flux-flow resistivity ρ_{fff} in the high frequency limit $\omega \gg \omega_p$.

2.2.2. Coffey-Clem (CC) Model

Mark W. Coffey and John R. Clem incorporated thermal effects in the vortex motion. Assuming a uniform periodic pinning potential U with height U_0, they obtained a vortex resistivity [122][123]

$$\rho_{vm,CC} = (B - B_m)\frac{\Phi_0}{\eta}\frac{\epsilon_c + i\frac{\omega}{\omega_0}}{1 + i\frac{\omega}{\omega_0}}, \tag{2.72}$$

where $\epsilon_c = \left(\mathrm{I}_0(u/2)\right)^{-2}$ is a thermal creep factor, $\omega_0 = \omega_p \frac{1}{1-\epsilon} \frac{\mathrm{I}_1(u/2)}{\mathrm{I}_0(u/2)}$, and $u = \frac{U_0}{k_B T}$ is the normalized energy barrier height. I_0 and I_1 are the *modified* Bessel function of the first kind with order 0 and 1 respectively. Near T_c, $\epsilon_c \to 1$ and the effect of pinning is washed out, giving $\rho_{vm,CC} \to \rho_{fff}$.

2.2.3. A Universal Expression

The GR model and the CC model, along with the Brandt model [124] and the two-mode approach [125][126], which were not discussed here, can all be casted into a common analytical form [127]

$$\rho_{vm} = (B - B_m)\frac{\Phi_0}{\eta_{eff}} \frac{\epsilon_{c,eff} + i\omega\tau_{eff}}{1 + i\omega\tau_{eff}}, \tag{2.73}$$

where τ_{eff} is an effective time constant associated with the vortex oscillation, and $\epsilon_{c,eff}$ measures the relative strength of the thermal creep. As a side note, the Hall effect can also be incorporated into ρ_{vm} [128].

2.3. Two Level System Loss

A two-level system (TLS) model of defects in amorphous solids was introduced independently in 1972 by William A. Phillips [129] and P. W. Anderson [130]. The model describes the thermal, acoustic, and dielectric properties of amorphous solids with a broad spectrum of tunneling states, each treated as a quantum particle in double-well potential, with elastic and electric dipole moments that can be coupled to stress and electric fields. TLS are

abundant in amorphous dielectrics such as native aluminum oxide. They have often been identified as the main factor causing energy loss in superconducting devices, with the most deleterious TLS believed to be residing in metal-substrate and substrate-air interfaces [131]-[141].

In the position basis, the Hamiltonian of a tunneling TLS can be written as

$$H_0 = \Delta\sigma_z + \Delta_0\sigma_x \,, \tag{2.74}$$

where Δ is the asymmetry energy difference between the two sides of the double-well potential, Δ_0 is the tunneling energy term, and σ_x, σ_y, and σ_z are the Pauli matrices. This gives eigenenergies $\pm\varepsilon/2$, where $\varepsilon = \sqrt{\Delta^2 + \Delta_0^2}$ corresponds to eigenstates

$$\psi_1 = \phi_1\cos\theta + \phi_2\sin\theta \,, \tag{2.75}$$

$$\psi_2 = \phi_1\sin\theta - \phi_2\cos\theta \,, \tag{2.76}$$

with $\tan 2\theta = \frac{\Delta_0}{\Delta}$. For a broad distribution $P(\Delta, \Delta_0)$ of tunneling states, the TLS density of states P_0 is given by

$$P(\Delta, \Delta_0)d\Delta d\Delta_0 = \frac{P_0}{\Delta_0} d\Delta d\Delta_0 \,, \tag{2.77}$$

where Δ takes a uniform distribution and Δ_0 takes a log uniform distribution.

When subjected to an external electric field $\vec{E}$, the perturbation in Δ is the dominant effect, while the changes in Δ_0 are usually neglected. The Hamiltonian of the system with an applied electric field is given by

$$H_{TLS} = H_0 + H_{int}^e \,. \tag{2.78}$$

The interaction Hamiltonian H_{int}^{e} is given by

$$H_{int}^{e} = \left(\frac{\Delta}{\varepsilon}\sigma_z + \frac{\Delta_0}{\varepsilon}\sigma_x\right)\overrightarrow{d_0}\cdot\vec{E} \equiv \left(\frac{1}{2}\sigma_z\overrightarrow{d'} + \sigma_x\vec{d}\right)\cdot\vec{E}\,, \tag{2.79}$$

where $\overrightarrow{d'} = 2\frac{\Delta}{\varepsilon}\overrightarrow{d_0}$ is the permanent electric dipole moment and $\vec{d} = \frac{\Delta_0}{\varepsilon}\overrightarrow{d_0}$ is the transition electric dipole moment.

Analogous to spins in a magnetic field [142], the Hamiltonian in (2.79) can be treated by introducing an electric susceptibility tensor $\boldsymbol{\chi}_{res}(\omega)$ for the resonance and $\boldsymbol{\chi}_{rel}(\omega)$ for the relaxation, such that

$$\boldsymbol{\chi}_{res}(\omega) = -\frac{\langle\sigma_z^0\rangle}{\hbar}\left(\frac{1}{\omega_\varepsilon - \omega + iT_2^{-1}} + \frac{1}{\omega_\varepsilon + \omega - iT_2^{-1}}\right)\vec{d}\vec{d} \tag{2.80}$$

$$\boldsymbol{\chi}_{rel}(\omega) = -\frac{d\langle\sigma_z^{eq}(\varepsilon)\rangle}{d\varepsilon}\frac{1 - i\omega T_1}{1 + \omega^2 T_1^2}\overrightarrow{d'}\,\overrightarrow{d'} \tag{2.81}$$

$$\langle\vec{d}\rangle = \boldsymbol{\chi}_{res}(\omega)\cdot\vec{E} \tag{2.82}$$

$$\langle\overrightarrow{d'}\rangle = \boldsymbol{\chi}_{rel}(\omega)\cdot\vec{E}\,, \tag{2.83}$$

where

$$\langle\sigma_z^{eq}(\varepsilon)\rangle = -tanh\left(\frac{\varepsilon}{2k_BT}\right) \tag{2.84}$$

$$\langle\sigma_z^0(\varepsilon)\rangle = \frac{1 + (\omega_\varepsilon - \omega)^2T_2^2}{1 + \Omega^2T_1T_2 + (\omega_\varepsilon - \omega)^2T_2^2}\sigma_z^{eq}(\varepsilon)\,, \tag{2.85}$$

$\omega_\epsilon = \frac{\varepsilon}{\hbar}$ and $\Omega = 2\vec{d} \cdot \frac{\vec{E}}{\hbar}$ is the Rabi frequency. T_1 and T_2 are the longitudinal and transverse relaxation times respectively.

At microwave frequencies and low temperatures, relaxation from (2.83) is typically negligible. The resonance (2.82) yields an isotropic dielectric function given by

$$\epsilon_{TLS}(\omega) = \iiint d\Delta d\Delta_0 d\hat{d}\, (\hat{e} \cdot \boldsymbol{\chi}_{res}(\omega) \cdot \hat{e}) \frac{P}{\Delta_0} \equiv \epsilon'_{TLS}(\omega) - i\epsilon''_{TLS}(\omega)\,. \tag{2.86}$$

2.3.1. Temperature Dependence – Weak Field

In weak electric field and under the condition $\Omega^2 T_1 T_2 \ll 1$, (2.86) can be simplified [143] to

$$\begin{aligned}\epsilon_{TLS}(\omega, T) &= \int_0^{\varepsilon_{max}} d\varepsilon\, \frac{P d_0^2}{3\hbar} tanh\left(\frac{\varepsilon}{2k_B T}\right)\left(\frac{1}{\omega_\varepsilon - \omega + iT_2^{-1}} + \frac{1}{\omega_\varepsilon + \omega - iT_2^{-1}}\right) \\ &= -\frac{2Pd_0^2}{3}\left[\Psi\left(\frac{1}{2} - \frac{\hbar\omega - i\hbar T_2^{-1}}{2i\pi k_B T}\right) - log\frac{\varepsilon_{max}}{2\pi k_B T}\right],\end{aligned} \tag{2.87}$$

where ε_{max} is the maximum energy splitting of TLS and Ψ is the complex digamma function.

The corresponding dielectric loss tangent is given by

$$\delta_{TLS}(\omega, T) = -\frac{Im\,\epsilon_{TLS}(\omega)}{\epsilon} = \delta_{TLS}^0 \tanh\left(\frac{\hbar\omega}{2k_B T}\right), \tag{2.88}$$

where ϵ is the intrinsic dielectric constant of the material, $\delta_{TLS}^0 = \frac{\pi P d_0^2}{3\epsilon}$ is the TLS-induced loss tangent at zero temperature in weak field. It should be noted that only TLSs close to the resonance contribute significantly to δ_{TLS}.

2.3.2. Power Dependence – Strong Field

In a strong electric field, the power affects the dielectric response of two level systems. From [143] one finds

$$\epsilon_{TLS}(\omega, T, \bar{\Omega}) \tag{2.89}$$
$$= \int_0^{\varepsilon_{max}} d\varepsilon \, \frac{P d_0^2}{3} tanh\left(\frac{\varepsilon}{2k_B T}\right)\left(\frac{1+(\omega_\varepsilon-\omega)^2 T_2^2}{1+\bar{\Omega}^2 T_1 T_2+(\omega_\varepsilon-\omega)^2 T_2^2}\right)\left(\frac{1}{\omega_\varepsilon-\omega+iT_2^{-1}}+\frac{1}{\omega_\varepsilon+\omega-iT_2^{-1}}\right),$$

where $\bar{\Omega} = \frac{2d_0|\vec{E}|}{\sqrt{3}\hbar}\frac{\Delta_0}{\varepsilon}$ is the modified Rabi frequency accounting for the orientation integral.

In the high power limit, the imaginary part of the TLS dielectric constant can be evaluated to [143]

$$\delta_{TLS}\left(\omega, T, \left|\vec{E}\right|\right) = -\frac{Im\,\epsilon_{TLS}(\omega)}{\epsilon} = \delta_{TLS}^0 \frac{\tanh\left(\frac{\hbar\omega}{2k_B T}\right)}{\kappa} \simeq \delta_{TLS}^0 \frac{\tanh\left(\frac{\hbar\omega}{2k_B T}\right)}{\sqrt{1+\left|\frac{\vec{E}}{E_c}\right|^2}}, \tag{2.90}$$

where $\kappa = \sqrt{1+\bar{\Omega}^2 T_1 T_2}$ is the power broadening factor of the Lorentzian absorption profile. $E_c = \frac{\sqrt{3}\hbar}{2d_0|\vec{E}|\sqrt{T_{1,min}T_2}}$ is the critical saturation field of TLS.

The real part of the TLS dielectric constant can be approximated to [143]

$$Re\,\frac{\epsilon_{TLS}(\kappa)-\epsilon_{TLS}(0)}{\epsilon} = \delta_{TLS}^0(1-\kappa)\,\mathrm{sech}^2\left(\frac{\hbar\omega}{2k_B T}\right)\frac{\hbar T_2^{-1}}{2k_B T} + \delta_{TLS}^0 \tanh\left(\frac{\hbar\omega}{2k_B T}\right)\frac{1-\kappa^2}{\kappa}\frac{T_2^{-1}}{2\omega}, \tag{2.91}$$

which typically gives a very small power dependence for $\kappa\hbar T_2^{-1} \ll k_B T$ and $\kappa T_2^{-1} \ll \omega$.

2.4. Dielectric Loss and Participation Ratio

On the macro scale, the microscopic phenomenon of TLS is manifested as the macroscopic property of dielectric dissipation of the material. The magnitude of this dissipation can be described by the ratio of imaginary part of the material's intrinsic dielectric constant ϵ to the real part, given by [144]

$$tan\ \delta = -\frac{Im\ \epsilon}{Re\ \epsilon}. \tag{2.92}$$

The intrinsic quality factor of the material can be calculated as

$$Q = \frac{1}{tan\ \delta}. \tag{2.93}$$

When electromagnetic (EM) waves propagate in a superconducting structure deposited on a dielectric substrate, the effective intrinsic quality factor Q_I of the structure can be written as

$$\frac{1}{Q_I} = \sum_k \frac{P_k}{Q_k} = \sum_k P_k\ tan\ \delta_k\ , \tag{2.94}$$

where P_k is the participation ratio, defined as the fraction of EM energy stored in the volume of the k^{th} material with intrinsic quality factor Q_k and loss tangent $tan\ \delta_k$. The P_k and Q_k pertain to the specific geometry and material of transmon and coplanar resonator will be discussed in later chapters.

CHAPTER 3

The Architecture of Transmon

Built upon the idea of a simple quantum harmonic LC-oscillator, superconducting qubits have evolved into one of the leading candidates towards achieving scalable quantum computing over the past decades.

3.1. Quantum Harmonic LC-Oscillator

A simple harmonic LC-oscillator circuit can be constructed by connecting an inductor with inductance L across a capacitor with capacitance C, hence allowing oscillatory transfer of energy between the two circuit elements. The Hamiltonian for such an LC-oscillator circuit can be written as

$$\hat{H}_{QHO} = \frac{\hat{Q}^2}{2C} + \frac{\hat{\Phi}^2}{2L}. \tag{3.1}$$

Here, the charge operator $\hat{Q}$ and flux operator $\hat{\Phi}$ are canonically conjugate variables such that

$$\hat{Q} = -i\hbar\frac{\partial}{\partial\Phi} \quad \text{and} \quad \left[\hat{\Phi}, \hat{Q}\right] = -i\hbar. \tag{3.2}$$

Expressin (3.1) in terms of the number of Cooper pairs $\hat{n} = \hat{Q}/2e$ and phase of superconducting order parameter $\hat{\phi} = 2\pi\hat{\Phi}/\Phi_0$ yields

$$\hat{H}_{QHO} = 4e^2 \frac{\hat{n}^2}{2C} + \frac{\Phi_0^2}{4\pi^2} \frac{\hat{\phi}^2}{2L}, \tag{3.3}$$

where $\Phi_0 = \frac{h}{2e}$ is the flux quantum.

From (3.3), the ladder operators [145] can be constructed using

$$\hat{a} = \sqrt{\frac{C\omega_0}{2\hbar}} \left(\frac{\Phi_0}{2\pi} \hat{\phi} + i \frac{2e}{C\omega_0} \hat{n} \right) \tag{3.4}$$

$$\hat{a}^\dagger = \sqrt{\frac{C\omega_0}{2\hbar}} \left(\frac{\Phi_0}{2\pi} \hat{\phi} - i \frac{2e}{C\omega_0} \hat{n} \right) \tag{3.5}$$

where $\hat{a}$ and $\hat{a}^\dagger$ are the annihilation and creation operators respectively, $\omega_0 = 1/\sqrt{LC}$ is the angular resonance frequency. Rewriting the Hamiltonian in terms of $\hat{a}$ and $\hat{a}^\dagger$ gives

$$\hat{H}_{QHO} = \hbar\omega_0 \left(\hat{a}^\dagger \hat{a} + \frac{1}{2} \right) = \hbar\omega_0 \left(\hat{\mathcal{N}} + \frac{1}{2} \right), \tag{3.6}$$

where $\hat{\mathcal{N}} = \hat{a}^\dagger \hat{a}$ is the number operator. The eigenstates of $\hat{\mathcal{N}}$ are called Fock states [146]. The eigenstates of the $\hat{a}$ and $\hat{a}^\dagger$ operators are superpositions of Fock states, and are known as coherent states [147]. Coherent states are important when dissipation is present and the system is driven by an external field.

If nonlinearity is introduced into the LC-oscillator circuit, the system acts as an artificial atom with unequally spaced energy levels. This is essential for allowing manipulation of just two energy levels for use as a qubit. For superconducting qubits, nonlinearity is achieved by incorporating a Josephson junction [148][149], which acts like a nonlinear inductor in the circuit.

3.2. Josephson Junction

Named after B. D. Josephson in 1962, the DC Josephson effect [148][149] is a quantum relation between the phase ϕ across a junction of weak link and the supercurrent I_s through the link due to the tunneling of Cooper pairs:

$$I_s = I_c \sin \phi \,, \tag{3.7}$$

where I_c is the critical current that can flow through the junction before inducing a voltage drop. The AC Josephson relation connects the rate at which the phase ϕ changes due to the voltage across the junction:

$$V_J = \frac{\hbar}{2e}\frac{d\phi}{dt}. \tag{3.8}$$

Applying a constant voltage V_J across the junction induces an AC current

$$I_{s,0} = I_c \sin\left(\frac{2eV_J}{\hbar}t\right) \tag{3.9}$$

with a well-defined frequency $f_J = 2eV_J/h$.

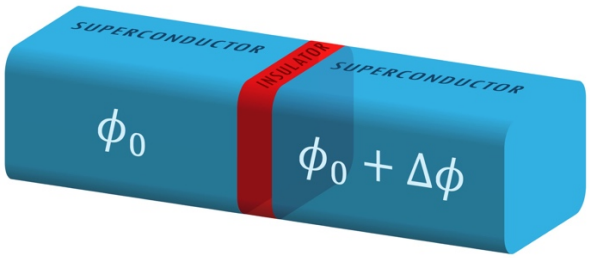

Figure 3. 1 S-I-S weak link junction made from a thin insulating layer (red) sandwiched between two superconducting electrodes (blue).

Consider an S-I-S weak link junction made from a thin insulating layer sandwiched between two superconducting electrodes (see Figure 3. 1). Taking the derivative of （3. 7） and plugging $d\phi/dt$ into （3. 8）, the current versus voltage relation can be written as

$$V_J = \pm\left(\frac{\hbar}{2e}\frac{1}{\sqrt{I_c^2 - I_s^2}}\right)\frac{dI_s}{dt} = \left(\frac{\hbar}{2e}\frac{1}{I_c\cos\phi}\right)\frac{dI_s}{dt} \equiv L_J\frac{dI_s}{dt}, \tag{3.10}$$

where L_J is the Josephson inductance. A typical value for L_J in my transmons is ~10 nH, as to compare with the geometrical inductance of ~10 pH. The corresponding mean stored energy is $-E_J\cos\phi$, where the Josephson energy is defined by

$$E_J \equiv \frac{\hbar}{2e}I_c. \tag{3.11}$$

The geometry of the sandwiched structure of the S-I-S junction also introduces a junction capacitance C_J, and stores mean capacitive energy given by $\frac{1}{2}C_J V_J^2$.

Additional perspective on the Josephson effect can be obtained from consideration of Andreev reflection effect [150]. When electrons from a normal conduction region are incident on a superconducting region, scattering occurs at the normal-to-superconducting (N-S) interface [151]. An incident electron with energy less than the superconducting energy gap Δ can form a Cooper pair in the superconducting region accompanied by the retroreflection of a hole of equal momentum but opposite spin and velocity. Due to time-reversal symmetry, the same goes for an incident hole (see Figure 3. 2). In a Josephson junction, constructive interference of the Andreev reflections at the two N-S interfaces creates Andreev bound states [152] with an energy in the superconducting gap. These subgap states in the junction support the coherent transport of Cooper pairs and incoherent transport of quasiparticles.

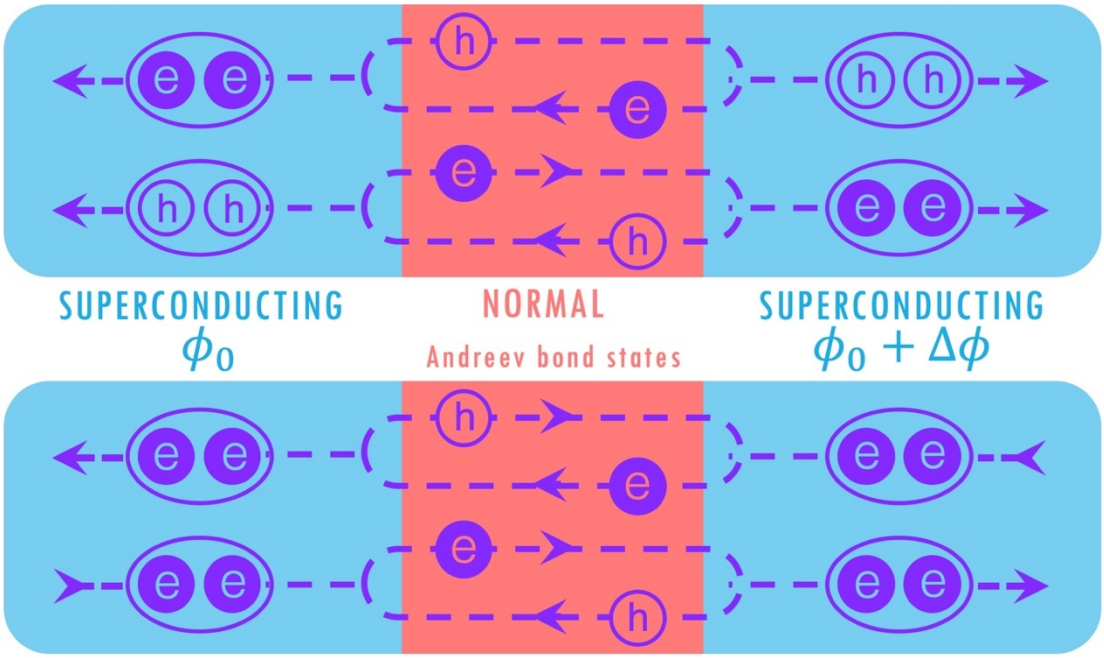

Figure 3. 2 (Upper) Incident electron from normal region (red) with energy less than the superconducting energy gap Δ forms a Cooper pair in the superconducting region (blue) accompanied by the retroreflection of a hole of opposite spin and velocity. Due to time-reversal symmetry, the same goes for an incident hole. At the Josephson junction, constructive interference of the Andreev reflections forms Andreev bound states. (Lower) Equivalent electron representation of the retroreflected holes.

Typically, transmons have Josephson junction made of an insulating barrier [153] of thickness less than the coherence length ξ_0. The junction can be modeled as a collection of N parallel conduction channels, each with transmission coefficient τ_i and a spin-degenerate Andreev doublet at energy

$$\varepsilon_{Ai} = \Delta\sqrt{1 - \tau_i \sin^2(\phi/2)}. \tag{3.12}$$

The current corresponding to the i^{th} conduction channel can be evaluated from Hamilton's equation of motion with the conjugate variables of the phase difference ϕ and number of charge carriers transported, yielding

$$I_{Ai} = -\frac{2e}{h}\frac{d\varepsilon_{Ai}}{d\phi} = \frac{e\Delta}{2h}\frac{\tau_i \sin\phi}{\sqrt{1-\tau_i \sin^2(\phi/2)}}. \tag{3.13}$$

The total current through the Josephson junction is given by the sum $I_s = \sum_{i=1}^{N} I_{Ai}$. For relatively opaque S-I-S Josephson junctions, one has $\tau \ll 1$ and

$$I_s \cong \sum_{i=1}^{N} \frac{e\Delta}{2h}\tau_i \sin\phi. \tag{3.14}$$

Comparing mesoscopic picture (3.14) with the macroscopic relation (3. 7) gives

$$I_c = \sum_{i=1}^{N} \frac{e\Delta}{2h}\tau_i \equiv \frac{e\Delta}{2h}\bar{\tau}\frac{A}{\left(\frac{\lambda_F}{2}\right)^2} = \frac{\pi\Delta}{2eR_n}, \tag{3.15}$$

where $\bar{\tau}$ is the average channel transparency, A is the junction area, and λ_F is the Fermi wavelength. $R_n = \frac{h}{2e^2}\frac{(\lambda_F/2)^2}{A\bar{\tau}}$ is the normal state junction resistance from the Landauer formula [154] for the single electron quantum of resistance $R_q = h/2e^2$. The expression for I_c in (3.15) agrees with the zero-temperature limit of the Ambegaokar-Baratoff relation [155]

$$I_c = \frac{\pi}{2eR_n}\Delta(T)\tanh\frac{\Delta(T)}{2k_BT}. \tag{3.16}$$

3.3. Cooper Pair Box to Transmon

First described in 1997 by A. Shnirman [156] and realized in 1998 by Vincent Bouchiat, *et al.* [37], the Cooper pair box (CPB) is a prototypical charge qubit [157] formed by a

superconducting island coherently coupled to a grounded reservoir via a Josephson junction (see Figure 3. 3). A gate voltage V_g is applied to a gate capacitance C_g to tune the polarization charge on the island. The number of Cooper pairs on the island is the relevant degree of freedom for describing the physics of this simple system.

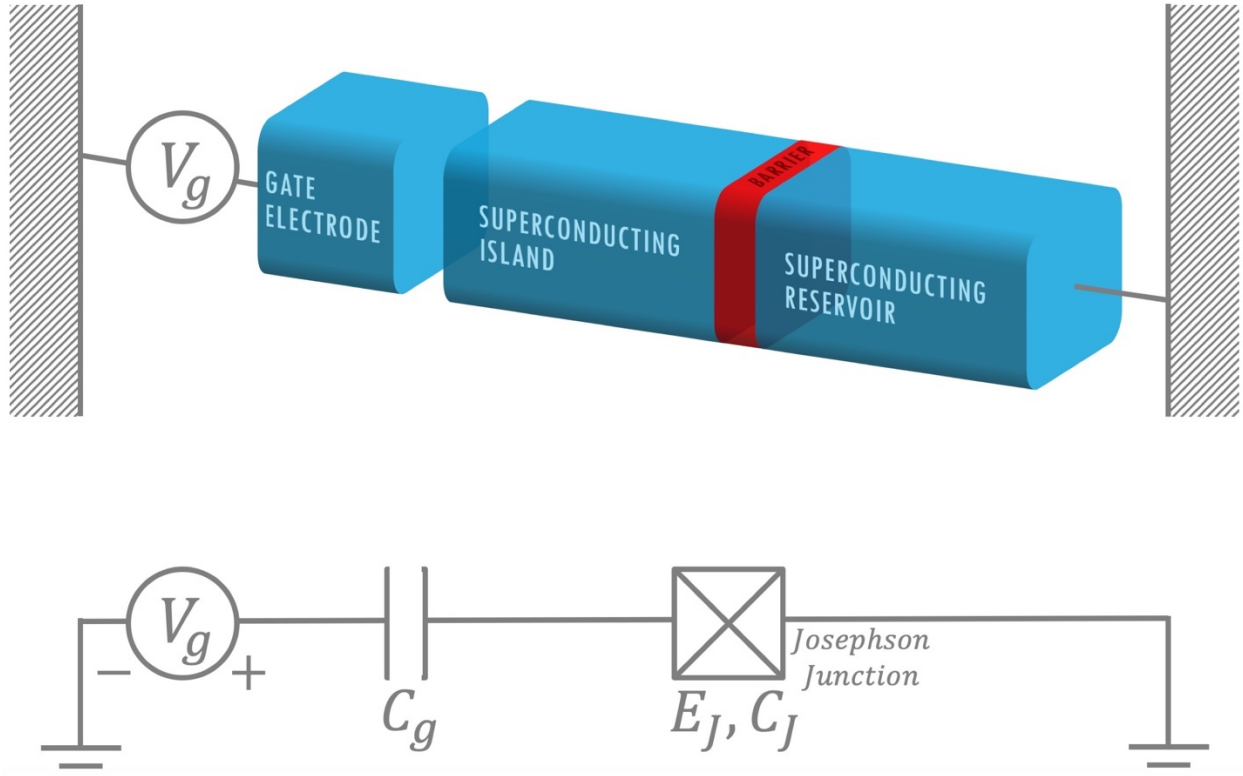

Figure 3. 3 Illustration of Cooper pair box (CPB), a charge qubit formed by a superconducting island coupled to grounded reservoir via a Josephson junction. A gate voltage V_g applied to bias the island via a gate capacitance C_g (between gate electrode and island).

The Hamiltonian for a Cooper pair box can be obtained by replacing the inductive element in （3. 3） with a Josephson junction inductance L_J and corresponding stored inductive energy E_J in （3.10） to obtain

$$\mathcal{H}_{CPB} = 4E_C\left(\hat{n} - n_g\right)^2 - E_J \cos\hat{\phi}\,, \tag{3.17}$$

where $E_C = e^2/2C_J$ is the charging energy, $\hat{n}$ is the operator for excess number of Cooper pairs that tunnel onto the island, $n_g = C_g V_g/2e$ is the reduced gate charge, and $\hat{\phi}$ is the operator for the superconducting phase difference across the Josephson junction.

Using the canonical conjugate relation

$$\hat{n} = -i\frac{\partial}{\partial\hat{\phi}} \qquad \text{and} \qquad \left[\hat{\phi}, \hat{n}\right] = -i\,, \tag{3.18}$$

the Hamiltonian for the Cooper pair box can be expressed in the phase basis as

$$\mathcal{H}_{CPB} = 4E_C\left(-i\frac{\partial}{\partial\hat{\phi}} - n_g\right)^2 - E_J\cos\hat{\phi}. \tag{3.19}$$

This is in the same form as the Schrödinger equation for a particle in periodic potential, with n_g taking the role of a Bloch wavevector. The dependence on n_g of the resulting energy spectrum resembles a band structure. The exact solutions [158] can be written in the form of Mathieu functions as

$$E_m\left(n_g\right) = E_C M_A\left((m+1)\ mod\ 2 + 2(-1)^m n_g, -\frac{E_J}{2E_C}\right), \tag{3.20}$$

where $M_A(r, q)$ is the characteristic value for the even Mathieu functions with characteristic exponent r and parameter q.

The energies from (3.20) are plotted in Figure 3. 4 for various E_J/E_C ratios. From the plot, it can be seen that as E_J/E_C increases, $E_m\left(n_g\right)$ flattens at the expense of reduced anharmonicity in the energy levels. For the typical operating regime of charge qubit, we have $E_J \ll$

E_C and the energy levels are strongly dependent on the offset charge n_g. Unfortunately, quasiparticle tunneling and ubiquitous $1/f$ charge noise [159] are quite significant and cause unwanted fluctuations in n_g. This causes decoherence due to large fluctuations in the qubit transition frequency. For this reason, charge qubits are no longer being pursued as viable qubits.

Whereas raising the E_J/E_C ratio suppresses the charge sensitivity of a Cooper pair box exponentially, the tradeoff involves a reduction in the selectiveness in driving the qubit to particular states due to reduced anharmonicity. For $E_J/E_C \sim 1$, the system transits to a charge-flux qubit [160]. For $E_J/E_C \gg 1$, the $-E_J \cos\hat{\phi}$ term in (3.19) dominates and the system acts like a particle in a periodic potential. The perturbation of the quantum harmonic oscillator comes from the higher order terms in the Taylor expansion of $\cos\phi \sim 1 - \phi^2/2 + O(\phi^4)$. In this regime, the relative anharmonicity is approximately

$$\frac{E_{12} - E_{01}}{E_{01}} \sim -\sqrt{\frac{E_C}{8E_J}}. \tag{3.21}$$

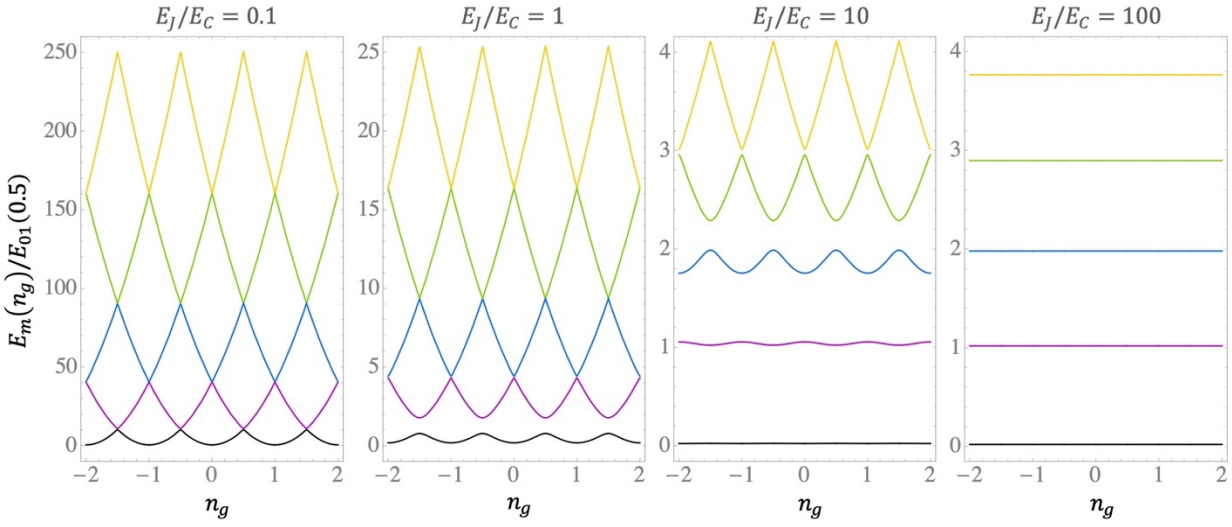

Figure 3. 4 The energies $E_m(n_g)$ normalized by $E_{01}(0.5) \equiv E_1(0.5) - E_0(0.5)$ are plotted for various E_J/E_C ratios. $E_m(n_g)$ flattens and anharmonicity is reduced for higher values of E_J/E_C.

For better protection from charge noise, a large E_J/E_C ratio is desired, but not too large such that the anharmonicity becomes too small. This can be achieved practically by increasing the effective junction capacitance via connecting a shunting capacitance $C_B \gg C_J$ in parallel to the Josephson junction (see Figure 3. 5) as in phase qubits. Following through on this idea yields a simple and elegant qubit design – the transmon.

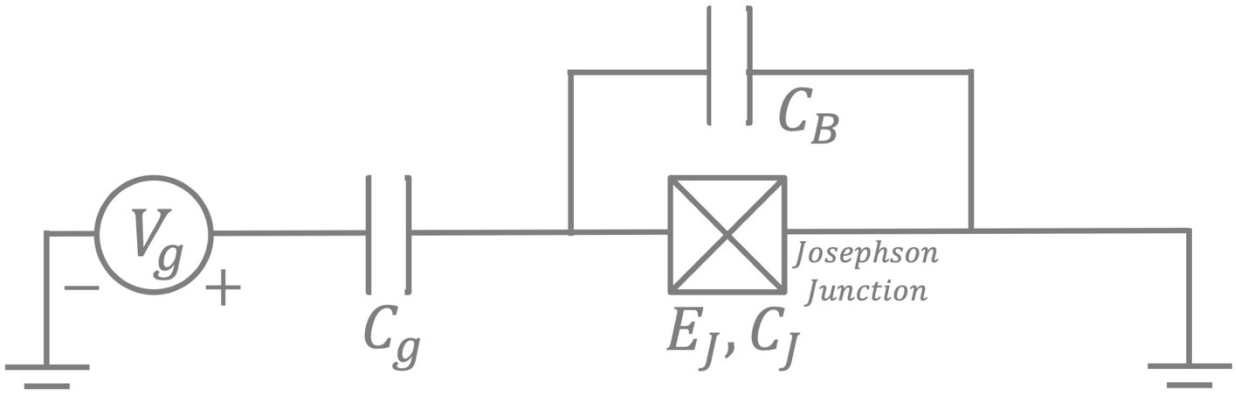

Figure 3. 5 To create a large E_J/E_C ratio, the Josephson junction is shunted with a large capacitance $C_B \gg C_J$.

3.4. Transmon

Named from an abbreviation for *transmission line shunted plasma oscillation qubit*, the transmon was invented by Robert J. Schoelkopf, Michel Devoret, and Steven M. Girvin in 2007 [161]. Their path to the transmon was as a variation of the superconducting charge qubit, initially used to realize the cQED scheme. To avoid the charge qubit limit and the typical phase qubit regime, the capacitance and Josephson junction critical current were designed to achieve $1 \ll E_J/E_C \ll 200$. From perturbation theory [162], the transmon Hamiltonian can be approximated by

$$\mathcal{H}_{trans} = \hbar\omega_p\left(\hat{b}^\dagger\hat{b} + \frac{1}{2}\right) - \frac{E_C}{4}\left(2\hat{b}^\dagger\hat{b}\hat{b}^\dagger\hat{b} + 2\hat{b}^\dagger\hat{b} + 1\right) - E_J\,, \tag{3.22}$$

where $\omega_p = \sqrt{8E_JE_C}/\hbar$ is the plasma frequency of the transmon, $\hat{b}$ and $\hat{b}^\dagger$ are the corresponding annihilation and creation operators, respectively. The frequency $\omega_m = E_m/\hbar$ can be defined for the m^{th} energy level such that

$$\mathcal{H}_{trans} = \sum_{m=0}^{\infty} \hbar\omega_m\,|m\rangle\langle m|. \tag{3.23}$$

The asymptotic expressions for the m^{th} eigenenergy E_m, absolute anharmonicity α_{abs} and relative anharmonicity α_{rel} of the transmon can be obtain as [161][163]

$$E_m = \sqrt{8E_JE_C}\left(m + \frac{1}{2}\right) - \frac{E_C}{4}(2m^2 + 2m + 1) - E_J, \tag{3.24}$$

$$\alpha_{abs} = (E_{m+2} - E_{m+1}) - (E_{m+1} - E_m) = -E_C, \tag{3.25}$$

$$\alpha_{rel} = \alpha_{abs}/E_0 = -\sqrt{E_C/8E_J}. \tag{3.26}$$

3.5. Circuit Quantum Electrodynamics

To implement the control and readout for a transmon, the device is typically capacitively coupled to a microwave resonator. This scheme allows circuit quantum electrodynamics (cQED) techniques to be applied, analogous to cavity quantum electrodynamics (CQE) techniques. In CQE, an atom is placed in a cavity that is nearly resonant with one of the energy levels of the atom [164] (see Figure 3. 6). The advantages of the cQED scheme includes: (1) isolation of the qubit from

direct coupling to the external electromagnetic environment; (2) allows quantum non-demolition microwave measurements (QND) [165]; (3) can be used as a quantum bus [166] for entangling multiple qubits.

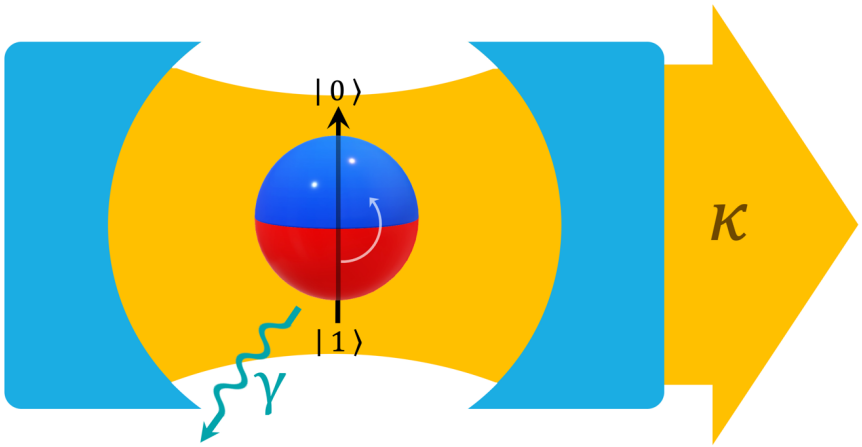

Figure 3. 6 Illustration of cQED. An atom interacts with light inside a cavity. The light inside cavity leaks out at a rate κ. Relaxation of qubit state from $|1\rangle$ to $|0\rangle$ emits a photon γ.

3.5.1. Jaynes-Cummings Hamiltonian

Developed in 1963 by Edwin T. Jaynes and Frederick W. Cummings [167], the Jaynes-Cummings Hamiltonian describes the interaction of a two-level atom with a *single mode* of a quantum electromagnetic field. This formalism can be applied to the case of a qubit coupled to a single-mode cavity, giving a Hamiltonian

$$\mathcal{H}_{JC} = \hbar\omega_r \left(\hat{a}^\dagger \hat{a} + \frac{1}{2}\right) + \frac{1}{2}\hbar\omega_q \sigma_z + \hbar g(\hat{a}\sigma^+ + \hat{a}^\dagger \sigma^-)\,, \tag{3.27}$$

where ω_r is the resonator frequency, ω_q is the qubit transition frequency, σ_z and $\sigma^\pm$ are the Pauli matrix in z-axis and the ladder operators for the qubit. $\hat{a}$ and $\hat{a}^\dagger$ are the annihilation and creation

operators, respectively, for the photon and g is the rate of photon exchange between the qubit and resonator if $\omega_r = \omega_q$.

For a multi-level system such as the transmon, the Jaynes-Cummings Hamiltonian can be generalized to [163]

$$\mathcal{H}_{JC}^{(gen)} = \hbar\omega_r \hat{a}^\dagger \hat{a} + \sum_j \hbar\omega_j |j\rangle\langle j| + \hbar g_{ge}\left(\hat{a}\hat{b}^\dagger + \hat{a}^\dagger \hat{b}\right) \tag{3.28}$$

$$= \hbar\omega_r \hat{a}^\dagger \hat{a} + \sum_j \hbar\omega_j |j\rangle\langle j| + \sum_j \hbar g_{j,j+1}\left(\hat{a}|j+1\rangle\langle j| + \hat{a}^\dagger |j\rangle\langle j+1|\right) \tag{3.29}$$

for $j \geq 2$, where $g_{j,j+1} \simeq g_{ge}\sqrt{j}$ denotes the coupling coefficient for the j-photon manifold in the transmon-cavity system. The notation $\{g, e, f, h, \ldots\}$ refers to the $\{ground, 1^{st}\ excited, 2^{nd}\ excited, 3^{rd}\ excited, \ldots\}$ qubit states.

In the *dispersive regime* with large detuning between the cavity resonance and qubit transition such that $|\omega_r - \omega_{ge}| \gg g_{ge} \gg \gamma, \kappa$, (3.29) can be approximately diagonalized. Truncating the transmon to the lowest two levels (qubit levels $|g\rangle$ and $|e\rangle$) yields [163][168]

$$\mathcal{H}_{JC}^{(disp)} = \hbar\tilde{\omega}_r \hat{a}^\dagger \hat{a} + \frac{1}{2}\hbar\tilde{\omega}_{ge}\sigma_z + \hbar\chi \hat{a}^\dagger \hat{a}\sigma_z\,, \tag{3.30}$$

where $\chi = \chi_{ge} - \chi_{ef}/2$, $\tilde{\omega}_{ge} = \omega_{ge} + \chi_{ge}$, $\tilde{\omega}_r = \omega_r + \chi_{ef}/2$. The transition frequencies $\omega_{j,j+1}$, detuning $\Delta_{j,j+1}$, and dispersive shift $\chi_{j,j+1}$ are defined as

$$\omega_{j,j+1} \equiv \omega_{j+1} - \omega_j \tag{3.31}$$

$$\Delta_{j,j+1} \equiv \omega_{j,j+1} - \omega_r \tag{3.32}$$

$$\chi_{j,j+1} \equiv g_{j,j+1}^2/\Delta_{j,j+1}. \tag{3.33}$$

The effect of the dispersive shifts is illustrated for the case $\omega_{ge} \ll \omega_r$ in Figure 3. 7. The bare cavity frequency ω_r (solid black) shifts to $\omega_r - \chi_{ge}$ (purple) if the transmon is in $|g\rangle$ state. When the transmon is in the $|e\rangle$ state, the cavity resonance shifts down by 2χ (blue). This frequency shift provides a way to measure the state of the qubit.

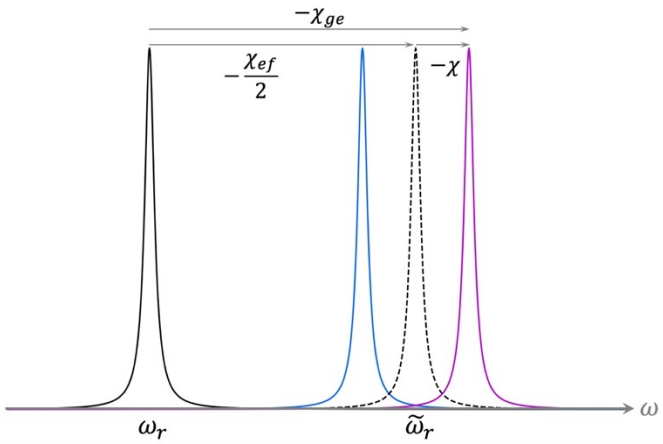

Figure 3. 7 Dispersive shifts of cavity resonance for the case $\omega_{ge} \ll \omega_r$. Dressed cavity frequency $\tilde{\omega}_r$ for transmon $|g\rangle$ state (purple) and transmon $|e\rangle$ state (blue).

3.5.2. Hamiltonian of the Driven System

Electromagnetic drive at microwave frequencies are implemented to manipulate the state of the transmon and perform logic gates. The transmon states $|g\rangle$ and $|e\rangle$ are commonly adopted as the analogue to classical binary logic bit 0 and 1. To simplify the discussion, in this section, I will restrict transmon to the qubit space formed by the states $|g\rangle$ and $|e\rangle$.

Suppose the qubit is associated with an electric dipole moment operator [169]

$$\hat{\vec{d}} = \langle g|\vec{d}|e\rangle(|g\rangle\langle e| + |e\rangle\langle g|) = \langle g|\vec{d}|e\rangle(\sigma^- + \sigma^+). \tag{3.34}$$

Consider an applied qubit drive given by the electric field

$$\vec{E}(t) = \vec{\varepsilon}E_0 \cos\omega_d t = \frac{1}{2}\vec{\varepsilon}E_0\left(e^{i\omega_d t} + e^{-i\omega_d t}\right) \tag{3.35}$$

with the polarization vector $\vec{\varepsilon}$, drive amplitude E_0, and drive frequency ω_d. The qubit interaction Hamiltonian is given by

$$\mathcal{H}_{int} = -\hat{\vec{d}} \cdot \vec{E} \tag{3.36}$$

$$= \frac{E_0}{2}\langle g|\vec{\varepsilon}\cdot\vec{d}|e\rangle(\sigma^- + \sigma^+)\left(e^{i\omega_d t} + e^{-i\omega_d t}\right). \tag{3.37}$$

Applying the rotating wave approximation (RWA) [170] to average out the fast counter-rotating terms results in

$$\mathcal{H}_{int} \simeq \frac{E_0}{2}\langle g|\vec{\varepsilon}\cdot\vec{d}|e\rangle\left(\sigma^- e^{i\omega_d t} + \sigma^+ e^{-i\omega_d t}\right) \tag{3.38}$$

$$\equiv \frac{\hbar\Omega_q}{2}\left(\sigma^- e^{i\omega_d t} + \sigma^+ e^{-i\omega_d t}\right), \tag{3.39}$$

where Ω_q is the Rabi frequency [171] for the atom interacting with the external field identified as

$$\Omega_q = -\frac{E_0}{\hbar}\langle g|\vec{\varepsilon}\cdot\vec{d}|e\rangle. \tag{3.40}$$

By replacing the qubit operators in （3.39） with the resonator ladder operators [145], the interaction Hamiltonian for the resonator can be obtained as

$$\mathcal{H}_{int}^{(res)} = \frac{\hbar\Omega_r}{2}\left(\hat{a}e^{i\omega_d t} + \hat{a}^\dagger e^{-i\omega_d t}\right), \tag{3.41}$$

where Ω_r is the effective Rabi drive frequency for the resonator. Thus, the driven dispersive Jaynes-Cummings Hamiltonian can be constructed as

$$\begin{aligned}\widetilde{\mathcal{H}} &= \mathcal{H}_{JC}^{(disp)} + \mathcal{H}_{int} + \mathcal{H}_{int}^{(res)} \\ &= \hbar\tilde{\omega}_r \hat{a}^\dagger \hat{a} + \frac{\hbar}{2}\left(\tilde{\omega}_{ge} + 2\chi \hat{a}^\dagger \hat{a}\right)\sigma_z + \frac{\hbar\Omega_q}{2}\left(\sigma^- e^{i\omega_d t} + \sigma^+ e^{-i\omega_d t}\right) \\ &\quad + \frac{\hbar\Omega_r}{2}\left(a e^{i\omega_d t} + a^\dagger e^{-i\omega_d t}\right).\end{aligned} \tag{3.42}$$

A unitary transformation to the rotating frame of drive can be applied to remove the time dependence [163][168], yielding

$$\mathcal{H} = \hbar\Delta_r \hat{a}^\dagger \hat{a} + \frac{\hbar}{2}\left(\Delta_{ge} + 2\chi \hat{a}^\dagger \hat{a}\right)\sigma_z + \frac{\hbar\Omega_q}{2}(\sigma^- + \sigma^+) + \frac{\hbar\Omega_r}{2}(a + a^\dagger)\,, \tag{3.43}$$

where $\Delta_r = \tilde{\omega}_r - \omega_d$, and $\Delta_{ge} = \tilde{\omega}_{ge} - \omega_d$.

3.6. Density Matrix and Master Equation Formalism

3.6.1. Bloch Sphere Representation

Introduced by Felix Bloch in 1946 [172], the Bloch sphere is a geometrical representation of the pure quantum state space of a TLS or qubit. It is analogous to the Poincaré sphere [173] representation of polarization states in optics. The pure quantum state of a qubit can be expressed in Dirac notation as

$$|\psi\rangle = \cos\frac{\theta}{2}|g\rangle + e^{i\phi}\sin\frac{\theta}{2}|e\rangle\,, \tag{3.44}$$

where the normalized magnitude of the state vector and the two angles θ and ϕ span a two-dimensional surface of a sphere (see Figure 3. 8).

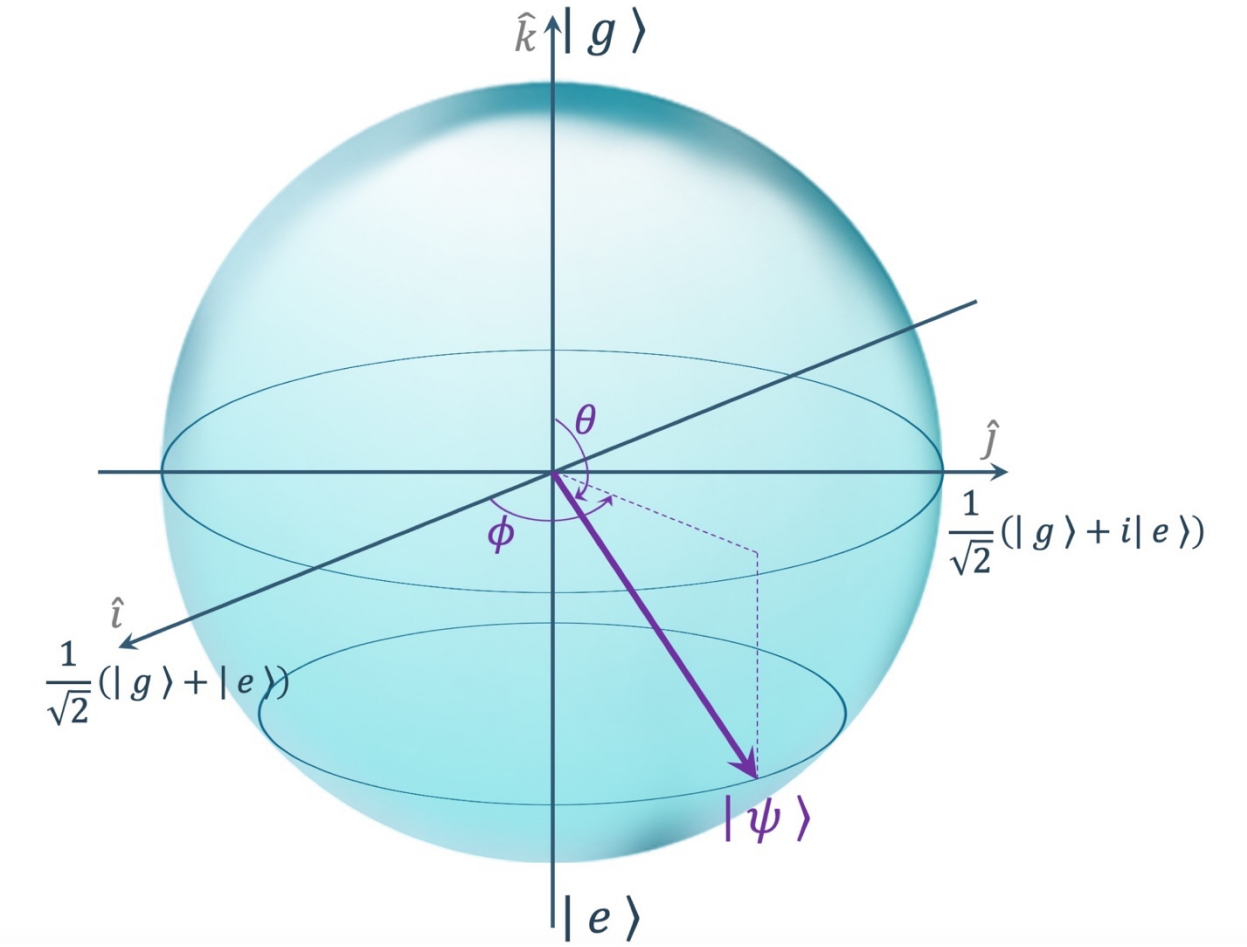

Figure 3. 8 The Bloch sphere is a geometrical representation of the pure quantum state space of a TLS or qubit, where normalized magnitude of the state vector and the two angles θ and ϕ span a two-dimensional surface of spherical space.

To depict mixed states of a qubit, an additional parameter is required to capture the *state purity* [174]. This can be done by defining the *state purity* as the magnitude of the Bloch vector [172]

$$\vec{\sigma}_{Bloch} = \langle \hat{\sigma}_x \rangle \hat{\imath} + \langle \hat{\sigma}_y \rangle \hat{\jmath} + \langle \hat{\sigma}_z \rangle \hat{k} \,, \tag{3.45}$$

which spans a three-dimensional spherical space.

3.6.2. Density Matrix

The density matrix operator $\hat{\rho}$ [175][176] provides a representation for the statistical ensemble of quantum states. The density matrix for a quantum state $|\psi\rangle$ can be defined as the outer product of the wave function and its conjugate,

$$\hat{\rho}(t) = |\psi\rangle\langle\psi| \,, \tag{3.46}$$

such that the integral $\langle\alpha_i|\hat{\rho}|\alpha_i\rangle$ gives the probability of finding the system in the state $|\alpha_i\rangle$. For a system described by

$$|\psi(t)\rangle = \sum_i c_i(t)|\alpha_i\rangle \,. \tag{3.47}$$

The expectation value of a time-dependent operator $\hat{\mathcal{A}}(t)$ can be calculated as

$$\langle\hat{\mathcal{A}}(t)\rangle = \sum_{i,j} c_i(t)c_j^*(t)\,\langle\alpha_j|\hat{\mathcal{A}}|\alpha_i\rangle \tag{3.48}$$

$$= \sum_{i,j} \mathcal{A}_{ji}\rho_{ij}(t) \equiv \mathrm{Tr}\big[\hat{\mathcal{A}}\hat{\rho}(t)\big] \,, \tag{3.49}$$

where the density matrix operator is defined explicitly by the density elements ρ_{ij} as

$$\hat{\rho}(t) \;= \sum_{i,j} c_i(t)c_j^*(t)|\alpha_i\rangle\langle\alpha_j| \equiv \sum_{i,j} \rho_{ij}(t)|\alpha_i\rangle\langle\alpha_j|. \tag{3.50}$$

For an isolated system described by the Hamiltonian $\mathcal{H}$ evolving according to the Schrödinger equation [177], the evolution of $\hat{\rho}$ can be described by the Liouville-Von Neumann equation [178]

$$i\hbar \frac{\partial \hat{\rho}}{\partial t} = -[\hat{\rho}, \mathcal{H}] \equiv \mathcal{H}\hat{\rho} - \hat{\rho}\mathcal{H}. \tag{3.51}$$

The solution is given formally by

$$\hat{\rho}(t) = U\hat{\rho}(0)U^{\dagger}, \tag{3.52}$$

where U is the *time evolution operator* [169].

Finally, I note that the density matrix has the following properties:

(1) Hermiticity: $\rho_{ij}^{*} = \rho_{ji}$

(2) Non-negative diagonal elements: $\rho_{ii} \geq 0$

(3) Normalization: $\mathrm{Tr}(\hat{\rho}) = 1$

(4) $\mathrm{Tr}(\hat{\rho}^2)\begin{cases} = 1 & \text{for pure state} \\ < 1 & \text{for mixed state} \end{cases}$

3.6.3. Lindblad-Kossakowski Master Equation

The general case of (3.51) is where the system of qubit(s) $\mathcal{H}_S$ is entangled with an external bath $\mathcal{H}_B$, such that the full Hilbert space is $\mathcal{H} = \mathcal{H}_S \otimes \mathcal{H}_B$. The evolution of the combined system can be described by

$$\hat{\rho}(t) = U(\hat{\rho}_S \otimes |0\rangle\langle 0|_B)U^{\dagger}, \tag{3.53}$$

where the evolution of the density matrix $\hat{\rho}_S$ of the qubit system can be obtained via a partial trace over B as

$$\hat{\rho}_S(t) = Tr_B\big(\hat{\rho}(t)\big) = \sum_i \langle \alpha_i|U|0\rangle\, \hat{\rho}_S(0) \langle 0|U^{\dagger}|\alpha_i\rangle. \tag{3.54}$$

Typically, it is impractical to calculate the evolution of the combined system of the qubits and environment, whereas restricting the system of interest to the ensemble of qubits introduces decoherence channels from ubiquitous noise and leads to non-unitary evolution of the qubit states. A pragmatic approach is to think of the environment as a sufficiently large reservoir that undergoes little change due to entanglement with the qubit system and remains in thermal equilibrium.

Since the Schrödinger equation is meant to describe the time evolution of a coherent system, to take into account decoherence, an additional ingredient is required – the Markov approximation [179]. A non-unitary quantum evolution can be captured by differential equations if and only if the evolution is Markovian – *i.e.* local in time. In particular, $\hat{\rho}(t+dt)$ has to be completely determined by $\hat{\rho}(t)$. This criterion implies that the reservoir retains no memory of its interaction with the qubit system, thus information can only flow from the qubit system to the reservoir but not vice versa. Thus, the reservoir can be traced out to obtain a reduced system of the qubit ensemble. The Liouville-Von Neumann equation in (3.51) can be generalized to Markovian non-unitary evolution to obtain the Lindblad-Kossakowski master equation [180][181]

$$i\hbar \frac{\partial \hat{\rho}}{\partial t} = -[\hat{\rho}, \mathcal{H}] + \mathcal{L}[\hat{\rho}]\,, \tag{3.55}$$

in which the non-Hermitian evolution is captured in the Liouvillian

$$\mathcal{L}[\hat{\rho}] = \sum_i \Gamma_i \mathcal{D}[\hat{\mathcal{A}}_i]\hat{\rho} = \sum_i \Gamma_i \left(\hat{\mathcal{A}}_i \hat{\rho} \hat{\mathcal{A}}_i^\dagger - \frac{1}{2} \hat{\mathcal{A}}_i^\dagger \hat{\mathcal{A}}_i \hat{\rho} - \frac{1}{2} \hat{\rho} \hat{\mathcal{A}}_i^\dagger \hat{\mathcal{A}}_i \right), \tag{3.56}$$

where $\mathcal{D}$ are the dissipators, Γ_i is the decoherence rate, and $\hat{\mathcal{A}}_i$ is the Lindblad operator [182] corresponding to the i^{th} decoherence channel.

Applying the Lindblad-Kossakowski master equation to the driven transmon-cavity system described in (3.43) yields

$$i\hbar \frac{\partial \hat{\rho}}{\partial t} = -[\hat{\rho}, \mathcal{H}] + \kappa \mathcal{D}[a]\hat{\rho} + \Gamma \mathcal{D}[\sigma^-]\hat{\rho} + \frac{\gamma}{2}\mathcal{D}[\sigma_z]\hat{\rho}\,, \tag{3.57}$$

where κ is the relaxation rate of the cavity (see Section 3.8.1), Γ is the relaxation rate of the transmon (see Section 3.7.2), and γ is the dephasing rate of transmon (see Section 3.7.1). The following section reviews the decoherence channels for the transmons.

3.7. Decoherence Channels

Decoherence posts a critical and pressing challenge towards realization of practical quantum computer made from superconducting qubits. It sets the time limit within which logic gates and measurements need to finish. In general, the desired qubit lifetime rises with the scale and complexity of the quantum computer. The population and coherence of the quantum system reside in the diagonal and off-diagonal matrix elements of the density operator $\hat{\rho}$, respectively. Typical decoherence channels in a transmon can be grouped into two categories – dephasing channels that randomize ϕ, and relaxation channels that affect θ. The rate of information loss can be quantified by the relaxation and decoherence rates corresponding to the various channels.

3.7.1. Dephasing Time T_ϕ

In this section I will consider a dephasing channel that acts only on the phase ϕ. First consider the situation when there is no dephasing, the time evolution of the superposition state in

(3.44) can then be obtained by applying the time evolution operator U, yielding

$$|\psi(t)\rangle = \cos\frac{\theta}{2}e^{-iE_g t/\hbar}|g\rangle + e^{i\phi_0}\sin\frac{\theta}{2}e^{-iE_e t/\hbar}|e\rangle$$
$$= \cos\frac{\theta}{2}\Big|g\rangle + \left(e^{i(\phi_0-\omega_{ge}t)}\right)\sin\frac{\theta}{2}\Big|e\rangle\,. \tag{3.58}$$

The time evolution of the quantum state causes precession of the phase ϕ around the $\hat{k}$-axis of the Bloch sphere as

$$\phi(t) = \phi_0 - \omega_{ge}t\,. \tag{3.59}$$

If the qubit transition frequency fluctuates as [183][184]

$$\omega_{ge}(t) = \langle\omega_{ge}\rangle - \delta\omega_{ge}(t)\,, \tag{3.60}$$

where $\delta\omega_{ge}(t)$ is the fluctuation at time t, the phase at time t becomes

$$\phi(t) = \phi_0 - \langle\omega_{ge}\rangle t - \int_0^t \delta\omega_{ge}(t')dt'. \tag{3.61}$$

From (2.60), the autocorrelation function $\Phi(t)$ [116] then can be written as

$$\Phi(t) \equiv \langle\delta\omega_{ge}(0)\delta\omega_{ge}(t)\rangle = \frac{1}{2\pi}\int_{-\infty}^{\infty} S_{\omega_{ge}}(\omega)e^{-i\omega t}d\omega\,, \tag{3.62}$$

where $S_{\omega_{ge}}(\omega)$ is the power spectrum of the fluctuations.

To gain insight into the time evolution for the ensemble average of the phase fluctuation, consider the function defined by

$$\mathrm{F}(t) \equiv \langle e^{-i\int_0^t \delta\omega_{ge}(t')dt'}\rangle \tag{3.63}$$

Using the relation $\langle e^{i\Delta\varphi}\rangle = e^{-\frac{1}{2}\langle\Delta\varphi^2\rangle}$ for free induction decay, (3.63) can be written as

$$\mathrm{F}(t) = \exp\left(-\frac{1}{2}\int_0^t dt_1 \int_0^t dt_2\, \langle\delta\omega_{ge}(t_1)\delta\omega_{ge}(t_2)\rangle\right) \tag{3.64}$$

$$= \exp\left(-\frac{1}{4\pi}\int_{-\infty}^{\infty} d\omega\, S_{\omega_{ge}}(\omega)\int_0^t dt_1 \int_0^t dt_2\, e^{-i\omega(t_1-t_2)}\right)$$

$$= \exp\left(-\frac{|t|}{2\pi}\int_{-\infty}^{\infty} d\left(\frac{\omega t}{2}\right) S_{\omega_{ge}}(\omega)\,\mathrm{sinc}^2(\omega t/2)\right). \tag{3.65}$$

The $\mathrm{sinc}^2(\omega t/2)$ term in (3.65) weights the noise with respect to ω, leading to higher dephasing at lower noise frequencies. By relating $\mathrm{F}(t)$ to $S_{\omega_{ge}}(\omega)$, (3.65) has been used to examine some standard types of noise [183][184].

Start by consider the case of Gaussian white noise, which has a flat noise power spectral $S_{\omega_{ge}}(\omega) = S_0$. (3.65) can be evaluated to find

$$\mathrm{F}(t) = \mathrm{e}^{-|t|S_0/2}. \tag{3.66}$$

This means that phase decay is exponential with a characteristic dephasing time constant

$$\mathrm{T}_\phi = \frac{2}{S_0}. \tag{3.67}$$

Next examine the case of ubiquitous $1/f$ noise, which has $S_{\omega_{ge}}(\omega) \propto 1/|\omega|^\mu$ with μ~1. For $\mu = 1$, one finds [183]

$$\mathrm{F}(t) \propto \mathrm{e}^{-t^2/2\sigma^2}. \tag{3.68}$$

The phase decays with a Gaussian envelope. $1/f$ critical current and charge noise could be present in Josephson junction due to reconfiguration of ions inside the tunnel barrier [185]. Noise in I_c is superimposed on E_J and hence on ω_{ge}. Since $\omega_{ge} \propto \sqrt{I_c}$, the variance in ω_{ge} is given by [186]

$$\langle \delta\omega_{ge}^2 \rangle = \left(\frac{\partial \omega_{ge}}{\partial I_c} \right)^2 \langle I_c^2 \rangle \simeq \left(\frac{\omega_{ge}}{2I_c} \right)^2 \langle I_c^2 \rangle. \tag{3.69}$$

The corresponding dephasing time constant can be obtained as [187]

$$T_\phi \propto \frac{2}{\omega_{ge}}. \tag{3.70}$$

Charge noise enters in an analogous form and one finds [186]

$$\langle \delta\omega_{ge}^2 \rangle = \left(\frac{\partial \omega_{ge}}{\partial n_g} \right)^2 \langle n_g^2 \rangle. \tag{3.71}$$

For my typical transmon E_J/E_c values, $\partial\omega_{ge}/\partial n_g$ is small by design, rendering dephasing from charge noise negligible. However, it can be important if E_J/E_c is at the low end of the transmon range or if other sources of dephasing are not present.

Fluctuations of the photon number ($N = \hat{a}^\dagger \hat{a}$) in the microwave cavity can also cause dephasing, due to coupling between qubit and cavity mode. This can pose serious limitations to the coherence of transmons [188][189]. In particular, *transverse coupling* [190] between a transmon and cavity mode as in (3.27) induces a 2χ shift in ω_{ge} per cavity photon. In 2006, A. A. Clerk and D. Wahyu Utami [191] showed that dephasing from cavity photons could be written as

$$\frac{1}{T_\phi} \equiv \Gamma_\phi = \frac{\kappa}{2}\mathrm{Re}\left[\sqrt{\left(1+\frac{2i\chi}{\kappa}\right)^2 + \frac{8i\bar{n}_{th}\chi}{\kappa}} - 1\right], \tag{3.72}$$

where κ is the cavity decay rate, and $\bar{n}_{th}$ is the average number of thermal photons in the cavity.

3.7.2. Relaxation Time T_1

The relaxation time T_1 is the mean lifetime for an un-driven qubit to decay from the excited state to the steady-state occupancy. The relaxation rate can be written as [192]

$$\frac{1}{T_1} = \Gamma_{e\to g} + \Gamma_{g\to e}\,, \tag{3.73}$$

where $\Gamma_{e\to g}$ is the rate at which the excited state $|e\rangle$ relaxes back to the ground state $|g\rangle$, and $\Gamma_{g\to e}$ is the rate at which the qubit is excited from $|g\rangle$ to $|e\rangle$. A dissipation channel can be modeled as an arbitrary admittance $Y(\omega)$ connected in parallel to the transmon. The characteristic decay RC time constant of the transmon is then given by [193][194]

$$T_1 = \frac{C_\Sigma}{\mathrm{Re}\, Y(\omega_{ge})}, \tag{3.74}$$

where $C_\Sigma = C_B + C_J$ is the total capacitance of the shunting capacitor and the Josephson junction.

Common relaxation mechanisms include the Purcell effect, dielectric loss and quasiparticles. In subsequent sections of this chapter I provide brief discussions of the known dissipation mechanisms in the transmon. The overall relaxation rate Γ_1 is given by

$$\Gamma_1 = \frac{1}{T_1} = \sum_i \frac{1}{T_{1,i}}, \tag{3.75}$$

where $1/T_{1,i}$ is the relaxation rate from the i^{th} relaxation channel. Typically, the different dissipation mechanisms should be of different order of magnitudes, such that only one dominant channel of loss limits T_1. Of course this need not be true and in fact there has been serious disagreement about the dominant source of loss in different transmons.

3.8. Dissipation Mechanisms in Transmon

Over the last two decades, better understandings on the causes of relaxation in superconducting devices has led to remarkable improvements in T_1 [195][196]. In this section, I provide brief reviews of the Purcell effect and dielectric TLS loss, followed by a discussion on the main theme of this dissertation – quasiparticle induced relaxation.

3.8.1. Purcell Effect

Discovered in 1946 by Edward M. Purcell, the Purcell effect [197] describes the enhancement of the spontaneous emission rate of atoms in resonant cavity. From Fermi's golden rule [198], the transition rate for an atom in vacuum is proportional to the density of final states. For an atom in cavity, the density of final photon states is much smaller than the density of states in free space, except near cavity resonance. For *transverse coupling* [190] between a transmon and a *single-mode* cavity, the contribution to relaxation from the Purcell effect is given by

$$\frac{1}{T_{1,\text{Purcell}}} = \left(\frac{g_{ge}}{\Delta_d}\right)^2 \kappa, \tag{3.76}$$

where $\Delta_d \equiv \omega_r - \omega_q$ is the detuning between the cavity and the qubit. It should be noted that this formula is only valid if the detuning is not too small compared to decoupling g_{ge}. The spontaneous emission rate of the atom can be increased in the case of resonance, or diminished in the case of far detuning. In the Purcell limit, the transmon relaxation depends on the cavity decay rate κ, and hence on the cavity photon lifetime. Due to coupling of the qubit to the higher order cavity modes, additional Purcell contributions will be present. An efficient way to reduce the Purcell loss is to increase Δ_d. However, since the cavity is also used to read out the qubit state, increasing Δ_d causes reduction in *signal-to-noise ratio* in the read-out. A Purcell filter [199], which impedes microwave propagation at the qubit frequency with bandpass filtering, is another way to suppress qubit relaxation from the Purcell effect while maintaining the measurement rate.

3.8.2 Dielectric Loss

Dielectric loss comes from the interaction of the stored electric field with nearly resonant two-level systems (ionic defects) in or on the surface of dielectrics. It has been identified as a key factor limiting the T_1 of transmons [61][200][201]. By using a single-crystal Al_2O_3 tunnel barrier in a phase qubit with a relatively large area, in 2006 S. Oh *et al*. [202] achieved an ~80% reduction in the density of spectral splittings from two-level fluctuators in the tunnel barrier. Transmons avoid the problem largely by using junction of very small area, nevertheless, TLS defects located at the material interfaces can be a dominant dissipation source for transmon, especially for 2D geometries. Applying (2.94), the relaxation rate of a transmon due to dielectric loss is given by

$$\frac{1}{T_{1,\tan\delta}} = \frac{\omega_{ge}}{Q_{\tan\delta}} = \omega_{ge}(P_{AS}\tan\delta_{AS} + P_{SC}\tan\delta_{SC} + P_{CA}\tan\delta_{CA})\,. \tag{3.77}$$

Here P_k is the participation ratio, defined as the fraction of EM energy stored in the volume of region k with intrinsic quality factor Q_k and loss tangent $tan\ \delta_k$. AS, SC, CA denote the air-to-substrate, substrate-to-conductor, and conductor-to-air interfaces, respectively. A detailed analysis of the expected interface loss in my transmon design can be found in Section 6.2.2.

Silicon is a relatively common choice for the substrate of superconducting chips due to its low cost and ready availability. The loss tangent at millikelvin temperatures is typically on the order of 10^{-7} [65]. However, native oxides on the surface of silicon give rise to a high $\tan\delta$ on the order of 10^{-3} [203]. To reduce this loss mechanism (casted in P_{SC}), the native silicon oxide can be removed using hydrofluoric acid immediately prior to the deposition of superconducting film. An alternative way to reduce P_{AS}, and P_{SC} is to switch the substrate material to sapphire (Al_2O_3), which typically has $\tan\delta < 10^{-7}$ [46] and does not form a lossy native oxide. However, lattice mismatch at the substrate-to-conductor interface [65][204][205], contamination and native oxide on the surface of exposed conductors can still cause loss. For example, the participation ratio for the substrate-to-conductor interface for transmons is P_{SC}~10^{-4} to 10^{-3} [203].

For a transmon in a 3D superconducting cavity, studies have found that features of small size and complicated design tend to correspond to lower T_1 [203][206], possibly because these features concentrate electric field near the material interfaces, which enhances the sensitivity to atomic scale TLSs.

3.8.3 Tunneling Two Level Systems

Experimental studies of individual TLS defects in superconducting chip via cQED have been carried out by B. Sarabi *et al.* in 2016 [207] (see Figure 3. 9 [207]). In 2019, S. Schlör *et al.* [208] observed correlation between TLS located near a device's conducting edge and slow

fluctuations in the transmon ω_{ge}, T_ϕ and T_1. The effect on T_1 was relatively weaker as compared to the effect on ω_{ge} and T_ϕ.

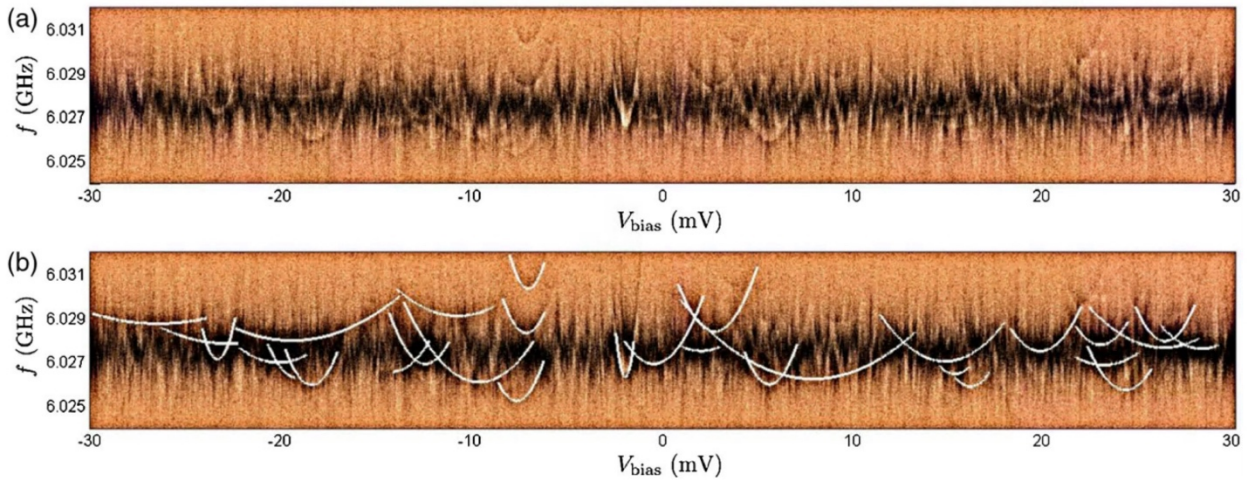

Figure 3. 9 Spectroscopy of individual TLS defects in a superconducting chip via cQED, carried out by B. Sarabi *et al.* in 2016. Figure from ref. [207]. (a) False-color plot of transmission $|S_{21}| = |V_{out}/V_{in}|$ vs frequency f and bias voltage V_{bias}. Data are taken at $T = 25\ mK$ and $\bar{n}_{max} \backsimeq 0.4$. Light copper and black correspond to $|S_{21}| = 0.56$ and $|S_{21}| = 0.40$, respectively. TLSs are observed with minia in energy (the tunneling energy Δ_0) nearly degenerate with the circuit photon energy $\hbar\omega_c$. (b) Fits with energy model to data in (a) are shown which yield the projected moment p_z and tunneling energy Δ_0 of 30 TLSs.

A simple model using the temperature and power dependence of $\tan\delta$ from (2.94) and plugging into (3.77) gives

$$\frac{1}{T_{1,TLS}} = \frac{\omega_{ge}}{Q_{TLS}(P_{rf},T)} \tag{3.78}$$

$$= \omega_{ge}\tanh\left(\frac{\hbar\omega}{2k_BT}\right)\left(\frac{P_{AS}}{\sqrt{1+P_{rf}/P_{s,AS}}}\tan\delta^0_{AS} + \frac{P_{SC}}{\sqrt{1+P_{rf}/P_{s,SC}}}\tan\delta^0_{SC} + \frac{P_{CA}}{\sqrt{1+P_{rf}/P_{s,CA}}}\tan\delta^0_{CA}\right),$$

where P_{rf} is the applied RF power and $P_{s,j}$ is the saturation power in region j.

3.8.4 Quasiparticle Loss

In addition to dielectric loss [61][200][201] and coupling to microwave modes [43], non-equilibrium quasiparticles have recently been found to be a potential source of significant relaxation [209]-[212]. This relatively late recognition of the importance of quasiparticle induced loss in superconducting qubits is somewhat surprising, especially since the presence of non-equilibrium quasiparticles at millikelvin temperatures has been well-known from work on superconducting single electron transistors [95][213]-[217], charge qubits [218]-[221] and microwave kinetic inductance detectors (MKIDs) [222].

Quasiparticles can cause energy dissipation in a transmon if they tunnel through the Josephson junction [209][223][224]. The dissipation is intimately connected to the noise produced by the quasiparticle current. The quasiparticle current noise spectrum can be written as [225]

$$S_I(f_{ge}) = e(I_{L\to R} + I_{R\to L})\,, \tag{3.79}$$

where $f_{ge} = \omega_{ge}/2\pi$ is the qubit $|g\rangle$ to $|e\rangle$ transition frequency, $I_{L\to R}$ is the current flowing through the junction due to quasiparticles moving from the left to the right electrode when there is a voltage hf_{ge}/e across the junction and $I_{R\to L}$ is the corresponding current from quasiparticles moving from the right to the left electrode. This quasiparticle tunneling noise induces spontaneous transitions back and forth between the qubit states $|e\rangle \leftrightarrow |g\rangle$. $S_I(f_{ge})$ is a double-sided quantum noise spectrum [192] with positive frequency corresponding to the transition $|e\rangle \to |g\rangle$ and negative frequency corresponding to the transition $|g\rangle \to |e\rangle$. The rate at which $|e\rangle$ relaxes back to $|g\rangle$ is obtained from Fermi's golden rule, yielding

$$\Gamma_{e\to g} = \left|\langle g|\sin\frac{\hat{\phi}}{2}|e\rangle\right|^2 S_I(f_{ge}) = \frac{E_c}{hf_{ge}e^2} S_I(f_{ge})\,. \tag{3.80}$$

For negative frequencies, the noise produces excitations of the ground state of the transmon at a rate given by

$$\Gamma_{g\to e} = \left|\langle e|\sin\frac{\hat{\phi}}{2}|g\rangle\right|^2 S_I(-|f_{ge}|) = \frac{E_c}{h|f_{ge}|e^2} S_I(-|f_{ge}|)\,. \tag{3.81}$$

Inserting (3.80) and (3.81) into (3.73), the relaxation rate $\Gamma_{1,qp}$ due to quasiparticle tunneling can be written as

$$\Gamma_{1,qp} \equiv \frac{1}{T_{1,qp}} = \frac{E_c}{he^2}\left(\frac{S_I(f_{ge})}{f_{ge}} + \frac{S_I(-|f_{ge}|)}{|f_{ge}|}\right). \tag{3.82}$$

Following derivations from D. Rogovin and D.J. Scalapino in 1974 [225], the quasiparticle tunneling current I_{qp} through a Josephson junction of low-transparency barrier at voltage V_0 between electrodes with the same energy gap Δ can be written as

$$\begin{aligned} I_{qp}(V_0) = \frac{1}{eR_n}\int_{|\Delta(T)|}^{eV_0-|\Delta(T)|} dE\ \frac{E}{\sqrt{E^2-|\Delta(T)|^2}}\frac{(eV_0-E)\theta(eV_0-2|\Delta(T)|)}{\sqrt{(eV_0-E)^2-|\Delta(T)|^2}} \\ \times\big(f(E-eV_0)-f(E)\big) \\ +\frac{2}{eR_n}\int_{|\Delta(T)|}^{\infty} dE\ \frac{E}{\sqrt{E^2-|\Delta(T)|^2}}\frac{(E+eV_0)}{\sqrt{(E+eV_0)^2-|\Delta(T)|^2}} \\ \times\big(f(E)-f(E+eV_0)\big)\,, \end{aligned} \tag{3.83}$$

where R_n is the tunneling resistance when the junction is in the normal state, $\theta(E)$ is the Heaviside step function, and the quasiparticle energy E is measured from the Fermi energy. For the typical operation conditions of a transmon, $|V_0| = hf_{ge}/e \ll 2\Delta(T)$, thus the first term in (3.83) (corresponding to pair breaking due to applied drive) can be dropped, yielding the simpler form

$$I_{qp}\left(\frac{hf_{ge}}{e}\right)=\frac{1}{eR_n}\int_{-\infty}^{\infty}\frac{dE\,|E|}{\sqrt{E^2-\Delta^2}}\frac{\left|E+hf_{ge}\right|}{\sqrt{(E+hf_{ge})^2-\Delta^2}}\Big(f_L(E)-f_R\big(E+hf_{ge}\big)\Big)\,, \qquad (3.84)$$

where the region of integration must exclude $-\Delta< E <\Delta$ and $\left|E+hf_{ge}\right|<\Delta$. $\Delta\equiv\Delta(T\to 0)$ is the low temperature limit for $\Delta(T)$. $f_L(E)$ and $f_R(E)$ are the quasiparticle distributions in the left and right electrodes, respectively. While the focus of my research is on dissipation mechanisms due to non-equilibrium quasiparticles, this section only provides a general theory of quasiparticle dissipation in homogeneous superconducting junctions, and in Chapter 5 I give a detailed analysis of the situation when the tunnel junction has electrodes with different energy gaps.

CHAPTER 4

Theory of Superconducting Coplanar Waveguide Resonators

Studies of superconducting microwave resonators over the last two decades have had great importance for both the astronomical detector community [226] and the quantum information community [195]. For the detector community, being able to manufacture a large array of detectors with a large responsivity to pair-breaking radiation is of utmost importance. For the quantum information community, being able to reliably operate long-lived and highly coherent qubits is the most important consideration. In both these quests, being able to make stable superconducting resonators with quality factors (Q) in excess of one million is important.

4.1. Coplanar Waveguide

First described by Cheng P. Wen in 1969 [227], a coplanar waveguide (CPW) is a planar geometry device that supports broadband transmission of electromagnetic wave on a center conducting strip line coupled to ground plane on either sides, all patterned on the same surface of a dielectric substrate (see Figure 4. 1). For a quasi-TEM (transverse electromagnetic) mode of propagation, the CPW geometry supports an elliptically shaped magnetic field around the center strip and electric field between the gaps on either side of the center strip (see Figure 4. 1). Since

the fields are largely confined to the surface and gaps, radiative dissipation due to undesired parasitic coupling is relatively small. I also note that the characteristics of CPW do not rely on using a specific substrate thickness.

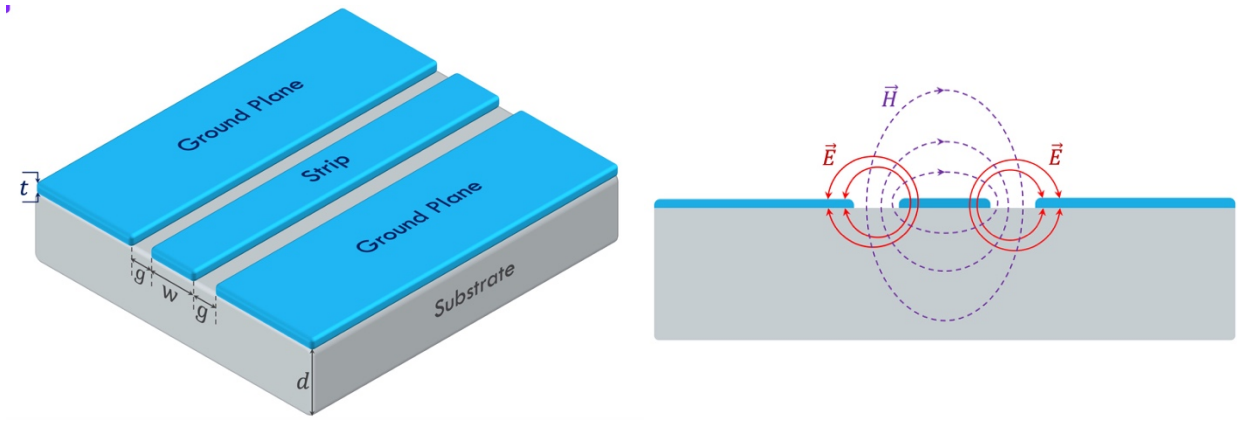

Figure 4. 1 (Left) Illustration of coplanar waveguide (CPW), where a center conducting strip line is coupled to ground planes on either side on the surface of a dielectric substrate. (Right) In the quasi-TEM mode of propagation, the CPW supports an elliptically magnetic field around the center strip and electric fields in the gaps on either side of the center strip.

For a thin superconducting film with thickness t that is much smaller than the London penetration depth λ_{L0} and substrate thickness $d \gg g$, a CPW can be modelled using a distributed capacitance [228]

$$C_{geo} = 2\epsilon_0 \frac{\mathrm{K}\big(k(2t)\big)}{\mathrm{K}\big(k'(2t)\big)} + 2\epsilon_r\epsilon_0 \frac{\mathrm{K}\big(k(0)\big)}{\mathrm{K}\big(k'(0)\big)} \tag{4. 1}$$

and a distributed inductance

$$L_{geo} = \frac{\mu_0}{4} \frac{\mathrm{K}\big(k'(t)\big)}{\mathrm{K}\big(k(t)\big)}, \tag{4. 2}$$

such that the characteristic impedance is $Z_0 = \sqrt{L_{geo}/C_{geo}}$. Here, ϵ_0 and μ_0 are the permittivity and permeability of free space respectively, ϵ_r is the relative permittivity of the substrate, $\mathrm{K}(k)$ is

the complete elliptic integral with modulus k. $k(t) = (w + t/\pi)/(w + 2g - t/\pi)$ and $k'(t) = \sqrt{1 - k^2(t)}$ for a center conductor strip with width w and strip-to-ground gap width g. The values of w and g are typically designed to give $Z_0 = 50\ \Omega$ to allow impedance matching with I/O coaxial cables and minimize the reflection coefficient

$$\Gamma = \frac{Z_L - Z_0}{Z_L + Z_0}. \tag{4. 3}$$

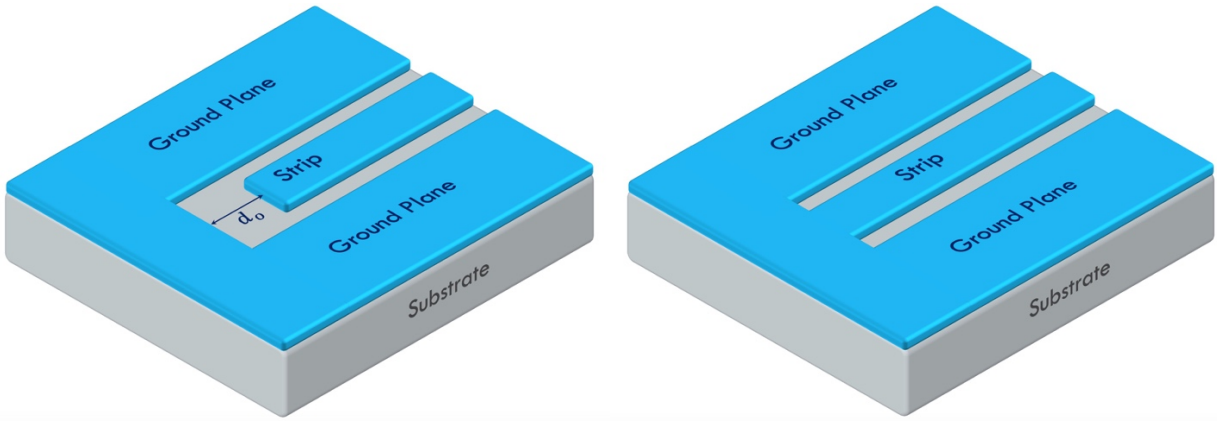

Figure 4. 2 The center strip of CPW can either have an *open-end* (left) or a *short-end* (right) termination. An open end has capacitive storage of electric energy, whereas a shorted end has inductive storage of magnetic energy.

The center strip of the CPW can either have an *open-end* or a *short-end* termination, as illustrated in Figure 4. 2 (a) and (b), respectively. An *open-end* termination has a capacitive storage of electric energy and corresponds to an effective length extension [229]

$$\Delta l_{open} \simeq \frac{\lambda}{2} - d_e\ , \tag{4. 4}$$

where λ is the wavelength of a propagating wave and d_e is the distance from the termination point of center strip to the closest absolute maximum of the electric field standing wave. At the *short-*

end termination is an inductive storage of magnetic energy and corresponds to an effective length extension [229]

$$\Delta l_{short} \simeq \frac{\lambda}{4} - d_e. \tag{4. 5}$$

The *open-end* and *short-end* effective length extensions can be used to calculate the respective normalized reactance of the termination [229]

$$X_{open} = \cot \beta_g \Delta l_{open} \tag{4. 6}$$

$$X_{short} = \tan \beta_g \Delta l_{short} \tag{4. 7}$$

where $\beta_g = 2\pi/\lambda$ is the phase constant from the complex propagation constant $\gamma_g = \alpha_g + i\beta_g$ with the attenuation constant α_g.

4.2. Kinetic Inductance

Due to the inertia of Cooper pairs, there is contribution to the total inductance from the motion of the pairs. The contribution is called the kinetic inductance. Kinetic inductance is included in the imaginary part of the complex conductivity $\sigma(\omega)$ in (2.23), as when $\tau_s \to \infty$, the motion of the Cooper pairs induces a phase lag between $\vec{E}(t)$ and $\vec{J}(t)$ that behaves like an equivalent series inductance. For a uniform current distribution, one finds

$$L_k = -\frac{1}{\omega \operatorname{Im} \sigma(\omega)} \frac{l}{A} = \frac{m_e}{n_s e^2} \frac{l}{A}, \tag{4. 8}$$

where n_s is the density of "superconducting electrons" (twice the density of Cooper pairs), l is length of the wire, and A is cross-sectional area.

For a typical CPW geometry, the current density is not uniform in the superconductor and the kinetic inductance is approximately [230]

$$L_k \simeq g_0 \mu_0 \lambda_{eff} . \tag{4.9}$$

Here, λ_{eff} is the effective penetration depth given by (2.29), and g_0 is a dimensionless geometrical factor given by

$$g_0 = \frac{\int_{\mathcal{C}} H_{||}^2 \, dl}{I^2} \tag{4.10}$$

for current I producing magnetic field $H_{||}$ parallel to the surface contour $\mathcal{C}$ of the superconductor in the cross-sectional plane. For a thin conductor with $t \ll w$, g_0 can be written as [230]

$$g_0 \simeq g_{ctr} + g_{gnd} \tag{4.11}$$

$$g_{ctr} \simeq \frac{1}{2w\mathrm{K}^2(k_0)(1-k_0^2)}\left(\pi + \ln\frac{2\pi w}{t} - k_0 \ln\frac{1+k_0}{1-k_0}\right) \tag{4.12}$$

$$g_{gnd} \simeq \frac{1}{2w\mathrm{K}^2(k_0)(1-k_0^2)}\left(\pi + \ln\frac{2\pi(w+2g)}{t} - \frac{1}{k_0}\ln\frac{1+k_0}{1-k_0}\right), \tag{4.13}$$

where g_{ctr} and g_{gnd} are the contributions from the center strip and ground planes respectively. My devices are in the limit $t \ll \lambda_{eff}$. As described in (2.36), this gives $L_k = g_0 L_{sur}$.

4.3. Resonance

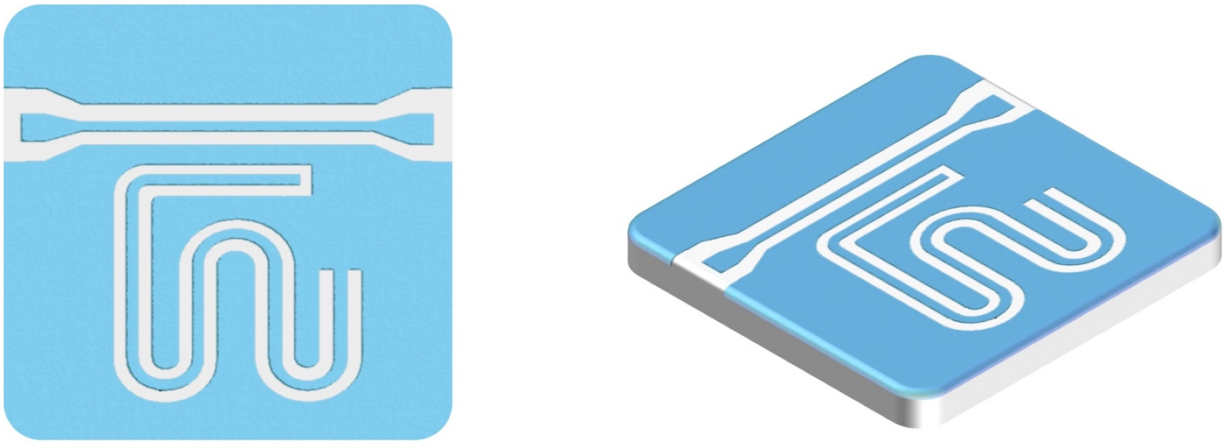

Figure 4. 3 Top view (left) and 3D perspective view (right) showing a quarter-wave resonator made using a combination of an *open-end* and a *short-end* terminations. The bending of the waveguide is to create a compact design. Superconducting film is shown in blue while substrate is shown in gray.

When patterned as a resonator, the length of the waveguide determines the wavelength of the resonant electromagnetic standing waves. *Open-end* and *short-end* terminations correspond to the peak and node of the electric field of the standing wave, respectively. A quarter-wave resonator can be achieved using a combination of an *open-end* and a *short-end* (see Figure 4. 3). In Figure 4. 3, the CPW bends to fit the long line onto a small chip. The resonance frequency for the n^{th} harmonic mode is given by

$$f_{0n} = \frac{v_p}{4l}(2n-1)\,, \tag{4.14}$$

where v_p is the phase velocity of wave, l is the total effective length of the waveguide (including the effective length extension as in (4. 4) and (4. 5)). For a thin conductor, without considering the term L_k,

$$v_p \simeq c\sqrt{\frac{2}{1+\epsilon_r}} = \left(L_{geo}C_{geo}\right)^{-\frac{1}{2}}, \tag{4.15}$$

and the fundamental resonance frequency $f_{01} \equiv f_0$ is

$$f_0 = \frac{1}{4l\sqrt{L_{geo}C_{geo}}}. \tag{4.16}$$

Effects of L_k can be taken into account by replacing L_{geo} with the total inductance $L = L_{geo} + L_k$.

To allow the resonator to be driven and measured, a CPW transmission line is patterned near the resonator (see Figure 4. 3). The strength of coupling to the n^{th} harmonic mode can be quantified by the inverse of the coupling quality factor

$$\frac{1}{Q_c} \simeq \frac{2Z_0 Z_L (2\pi f_{0n} C_c)^2 (2n-1)}{n\pi} \tag{4.17}$$

where the coupling capacitance C_c is determined by the proximity of the resonator to the I/O line.

4.4. Finite Element Simulation of Current Density

To get better insight into the distribution of current in my TiN coplanar waveguide resonator and the participation ratio of energy, I performed finite element simulations of the CPW geometry. The TiN CPW resonator on my chip has a center conducting strip with a width of 10 μm with 5 μm gaps on either side (as illustration in Figure 4. 1). The TiN film is ~50 nm thick, approximately 4 × smaller than the nominal TiN penetration depth of λ_L~200 nm. Since λ_L is comparable to the thickness of the waveguide and much smaller than the waveguide center strip width, the current density in the center strip cannot be well-approximated by a surface density. In the simulation, the current density $\vec{J}$ was obtained by solving the Maxwell–London equations at

the resonance frequency ω_0 of the alternating current. This was done in the finite element simulation by treating the superconductor as a region with a complex permittivity given by [231]

$$\varepsilon_r = \varepsilon_0 - \frac{1}{\omega_0^2 \mu_0 \lambda_{eff}(T)^2} - i\frac{\sigma_1(\omega_0,T)}{\omega_0}, \tag{4.18}$$

where $\sigma_1(\omega, T)$ is the real component of Mattis-Bardeen conductivity and $\lambda_{eff}(T)$ is an effective penetration depth.

Instead of trying to simulate the entire 3D resonator, I simulated a 2D cross-section of my CPW geometry using COMSOL Multiphysics [232]. This sped up the simulation and let me use dense meshing on real-sized dimensions (see Figure 4. 4). A set of representative simulation results for the electric field $\vec{E}$ and magnetic field $\vec{H}$ using $\lambda_{eff} = 200$ nm, $\sigma_1 = 10$ GS m^{-1} are plotted in Figure 4. 5 and Figure 4. 6, respectively. As shown in the plots, both the electric and magnetic fields are highly concentrated near the gaps on either side of the center strip. Hence the field will mainly penetrate into the center strip from the strip edges, adjacent to the gaps. A detailed view of the magnetic field magnitude $|\vec{H}|$ and current density J_z along the CPW (in the direction normal to the cross-sectional view) are shown in Figure 4. 7. From these results, we see that most of the electromagnetic energy stored in the magnetic field or carried by the current density is highly concentrated near the edge of the center superconducting strip.

In the simulations, I fixed σ_1 in (4.18) to 161 MS m^{-1} (~62 pΩ cm), a value ~10^6 times smaller than the normal conductance of the TiN film in my resonators. The normalized current density J_z as a function of distance into the superconductor from the edge is calculated for various values of λ_{eff} (see Figure 4. 8). From the simulation results, higher λ_{eff} generally corresponds to (1) a slower decay of J_z as a function of distance into the superconductor and (2) a

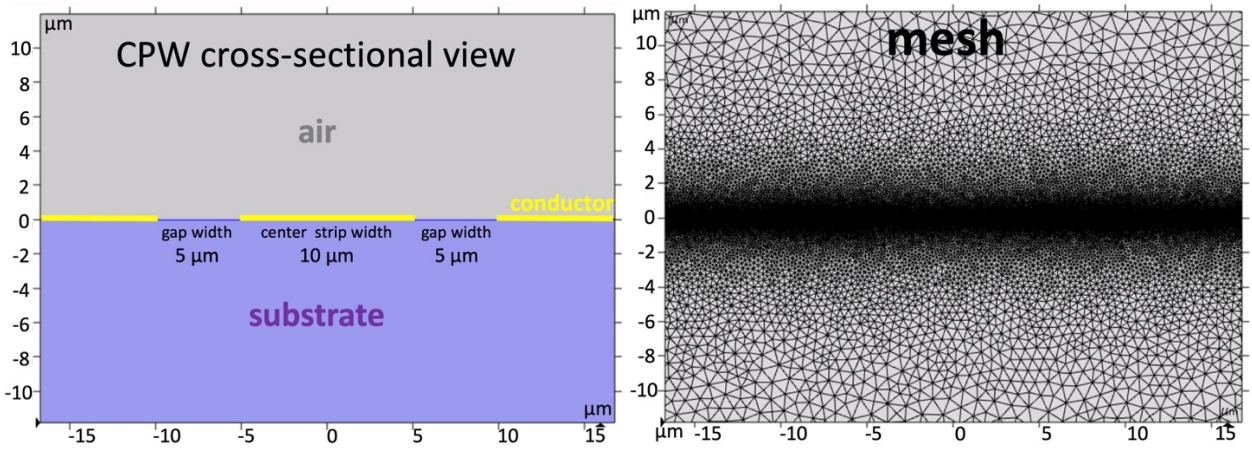

Figure 4. 4 2D finite element simulation of the CPW cross-section performed on COMSOL [232] with real-sized dimensions (left). Dense meshing (right) was used. The center conducting strip has width of 10 µm with 5 µm gaps on either side. The TiN film is ~50 nm thick.

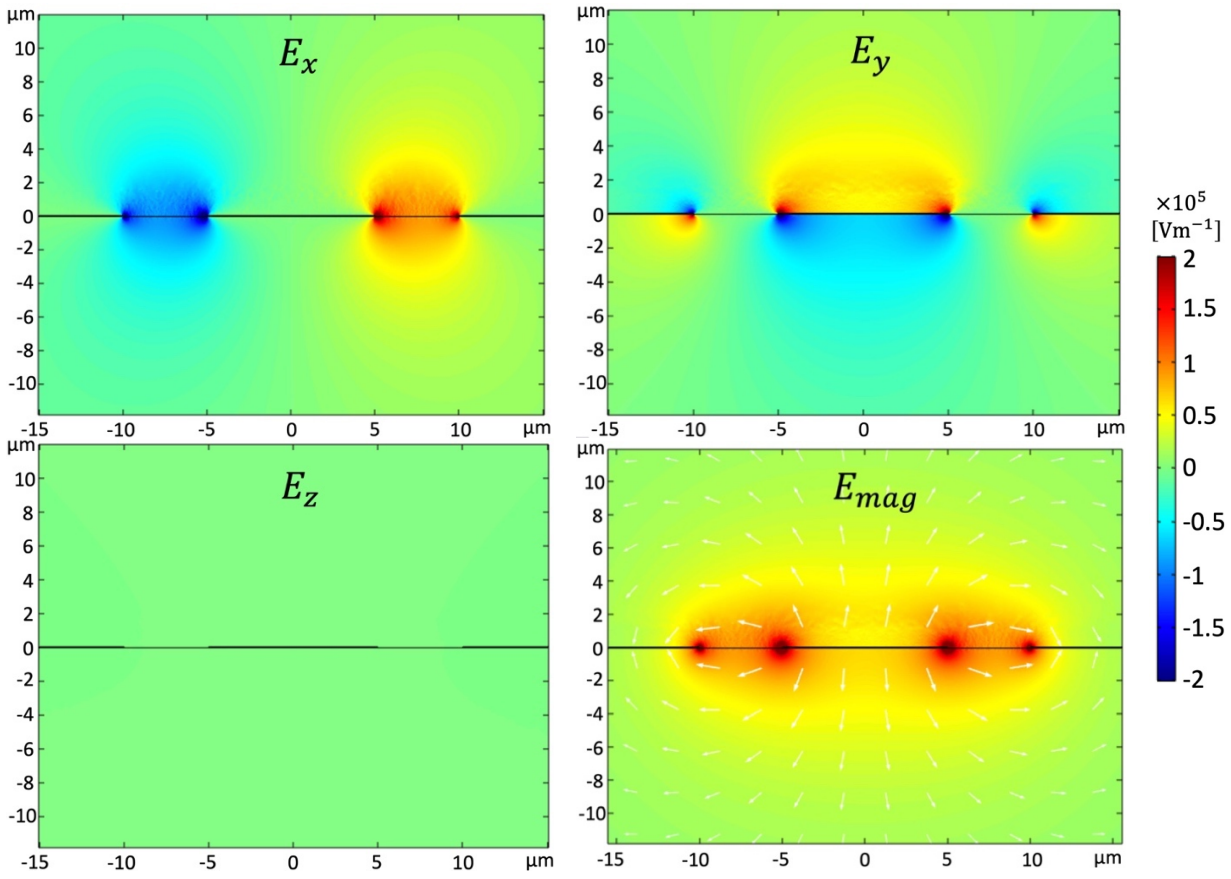

Figure 4. 5 A set of representative simulation results of electric field $\vec{E}$ using $\lambda_{eff} = 200\ nm$, $\sigma_1 = 10\ GS\ m^{-1}$. Electric fields are highly concentrated near the gaps on either side of the center strip.

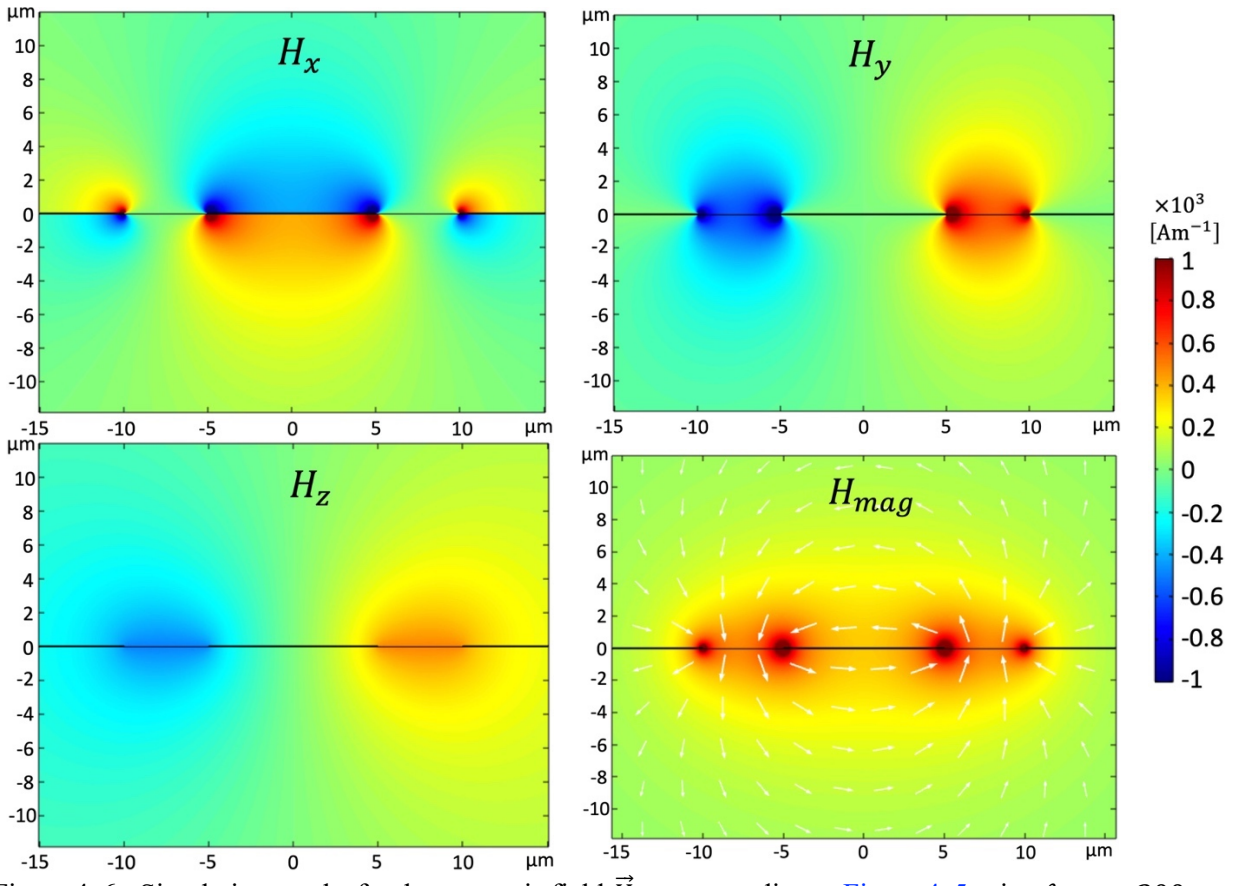

Figure 4. 6 Simulation results for the magnetic field $\vec{H}$ corresponding to Figure 4. 5 using $\lambda_{eff} = 200\ nm$, $\sigma_1 = 10\ GS\ m^{-1}$. The color scale for H_z is magnified 100 times for visualization. Magnetic fields are highly concentrated near the gaps on either side of the center strip.

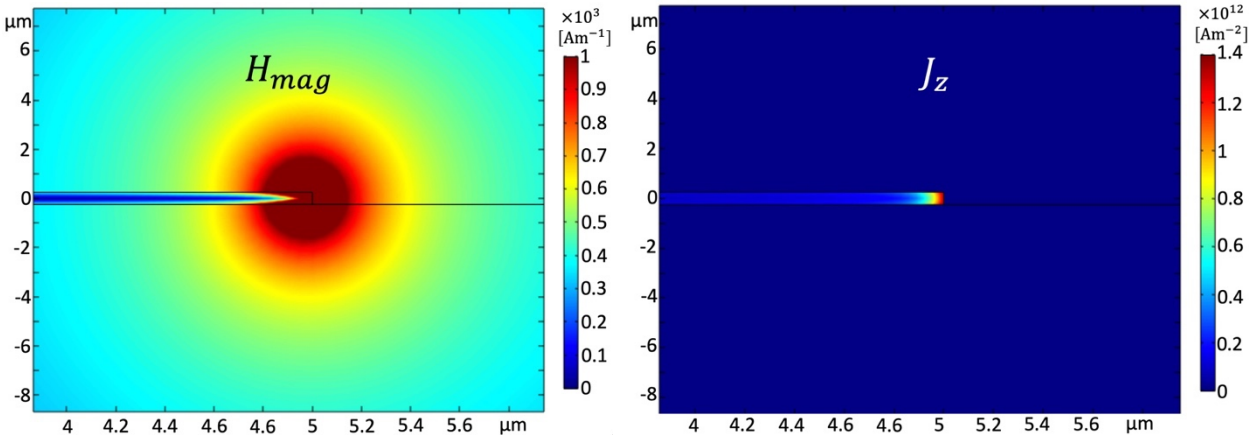

Figure 4. 7 Magnified view near the edge of CPW center conducting strip showing the magnetic field magnitude $|\vec{H}|$ and current density J_z along the CPW (normal to the cross-sectional view, pointing out of the page).

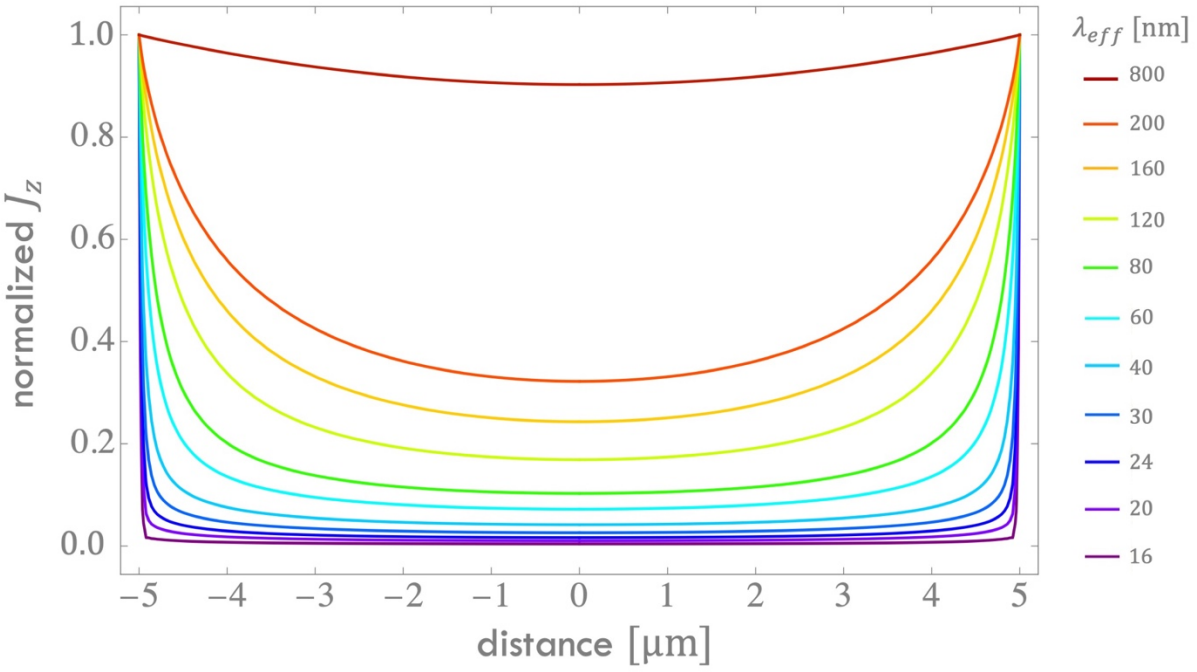

Figure 4. 8 Simulation of J_z as a function of distance into the superconductor from the edge for different values of λ_{eff}, σ_1 in (4.18) was fixed to 161 $MS\ m^{-1}$ (~62 $p\Omega\ cm$).

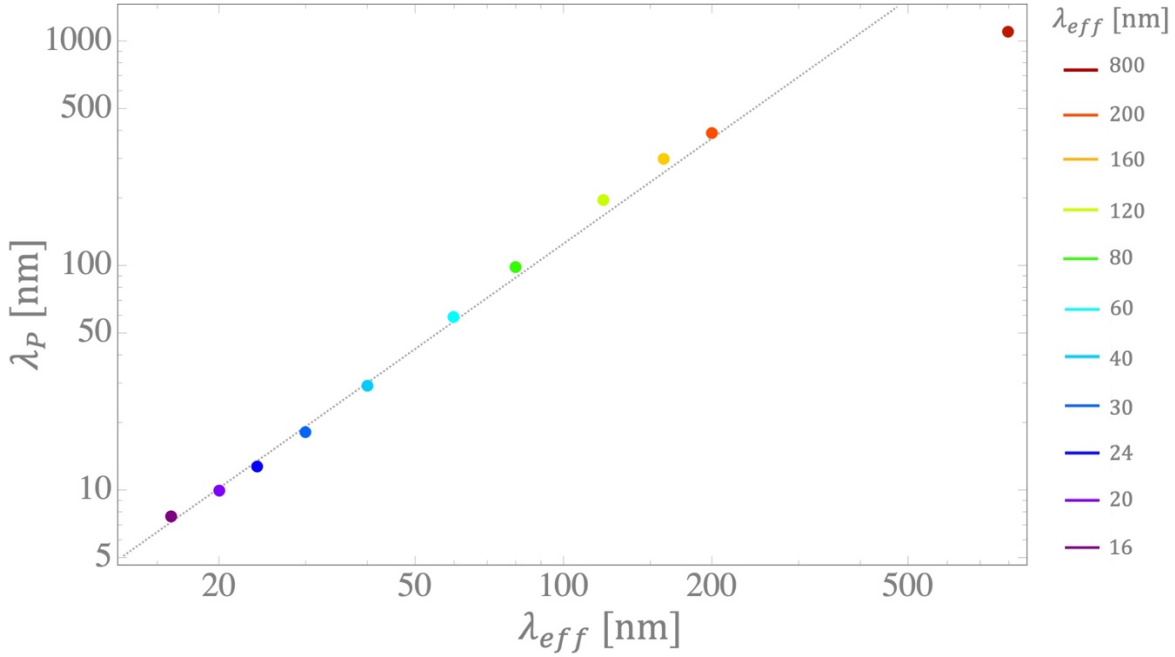

Figure 4. 9 Plot of λ_P calculated from simulations versus λ_{eff} from Figure 4. 8. A linear relation $\lambda_P \propto \lambda_{eff}$ is plotted as visual guide.

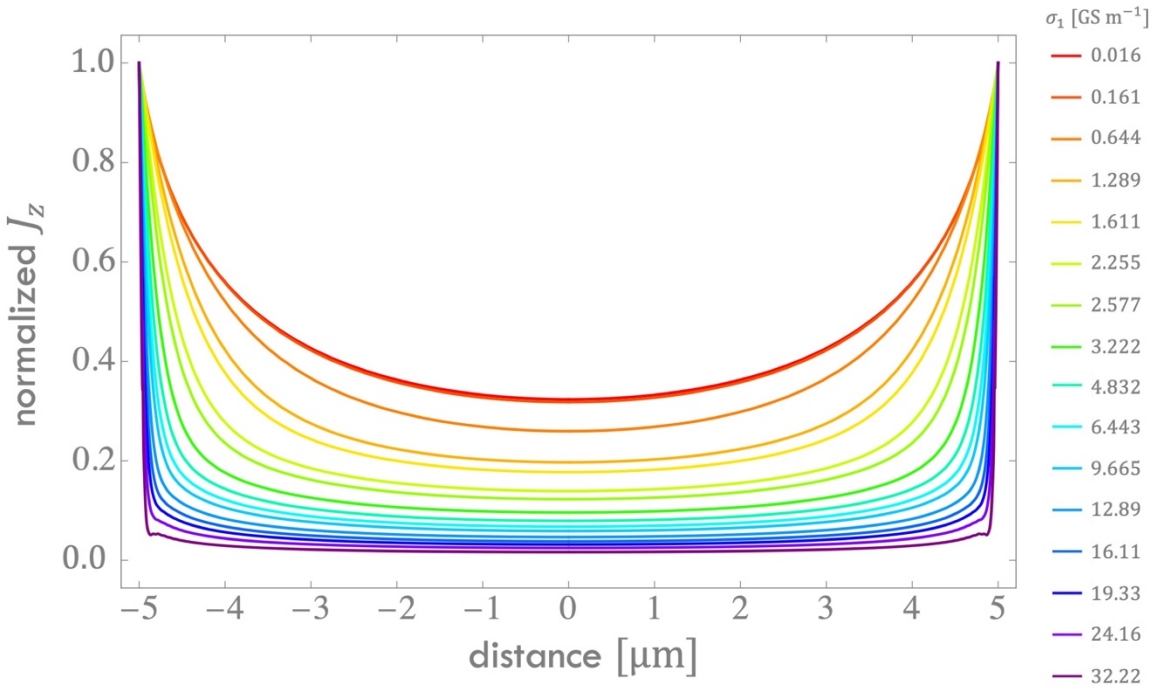

Figure 4. 10 Simulation of J_z as a function of distance into the superconductor from the edge for different values of σ_1. λ_{eff} in (4.18) was fixed at 200 nm.

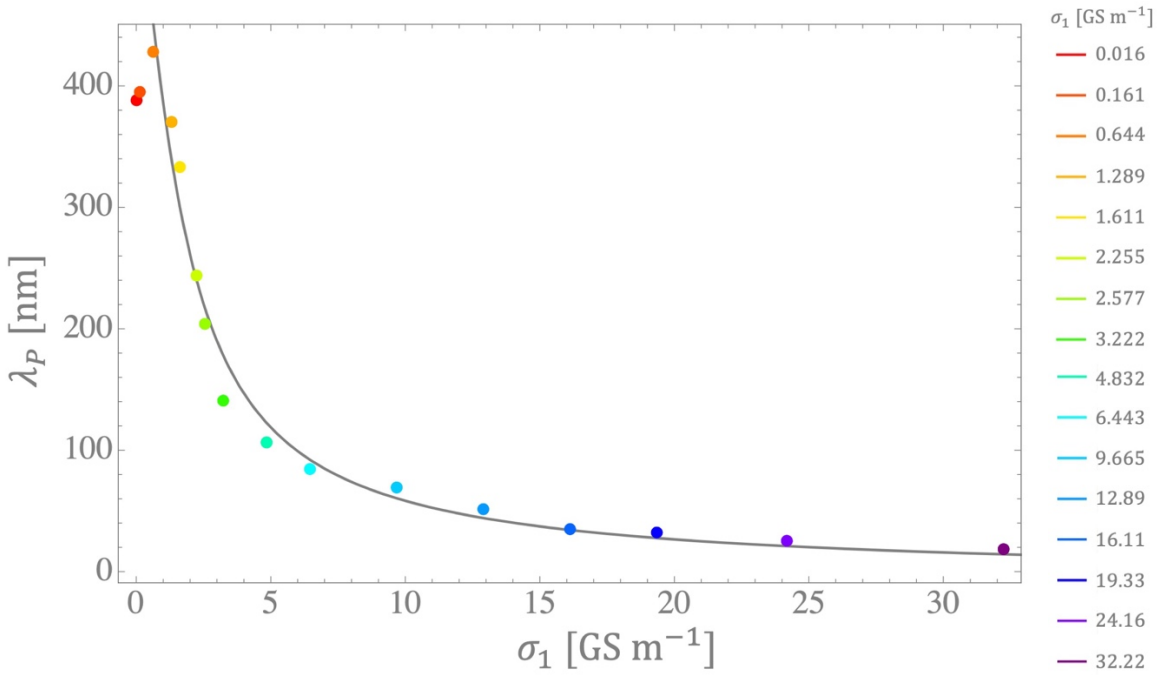

Figure 4. 11 Plot of λ_P calculated from simulations for the various σ_1 values used in Figure 4. 10 yields $\lambda_P \sim (-375\, tan^{-1}(0.58\sigma_1) + 0.58)\ nm$.

larger constant background J_z in the superconductor. I define the penetration depth λ_P as the distance that $\left(J_z - J_{z,min}\right)^2$ decays to e^{-1} of its value, measured at 0 and 5 μm when moving towards the interior of the center superconducting strip. Figure 4. 9 shows a plot of λ_P from the simulation for various λ_{eff}. This yields a linear relation $\lambda_P \propto \lambda_{eff}$ [87]. Fixing $\lambda_{eff} = 200$ nm and varying σ_1 causes a similar effect (see Figure 4. 10). Plotting λ_P from the simulations for the σ_1 in Figure 4. 10 yields $\lambda_P \sim (-375 \tan^{-1}(0.58\sigma_1) + 0.58)$ nm (see Figure 4. 11). The purpose of this simulation was to provide insight into the distribution of current in the CPW center superconducting strip and the participation ratio for inductive energy near the surface of strip.

4.5. Average Photon Number

The energy in a CPW resonator can be quantified by the average photon number injected via RF microwave drive/readout. In this section, I provide a short derivation of the average stored photon number from the resonator Qs. Damping from internal losses of the resonator being driven at the fundamental resonance frequency f_0 can be quantified by the internal quality factor

$$Q_I \equiv \frac{E_{int}}{E_{dis}} = 2\pi f_0 \frac{E_{int}}{P_{loss}}, \tag{4.19}$$

where E_{int} is the mean energy stored in the resonator during a cycle, E_{dis} is the mean energy dissipated during a cycle due to internal losses, and P_{loss} is the average power dissipated during a cycle of oscillation.

When the input drive to the resonator is turned off, E_{int} decays exponentially as a function of time t, given by

$$E_{int}(t) = \frac{1}{R_L}\left(V_{int}(t)\right)^2 = \frac{1}{R_L}\left(V_0 e^{-\frac{t}{\tau_p}}\right)^2 = \frac{{V_0}^2}{R_L}\left(e^{-\frac{t}{\tau_p}}\right)^2 = E_0 e^{-\frac{2t}{\tau_p}}, \tag{4.20}$$

where $V_{int}(t) = V_0 e^{-\frac{t}{\tau}}$ is the voltage corresponding to $E_{int}(t)$ with a total load resistance R_L, $E_0 = \frac{{V_0}^2}{R_L}$ is the initial energy stored, τ_p is the exponential decay time constant of the resonator voltage $V_{int}(t)$ ring-down. The loaded quality factor is defined by

$$Q_L \equiv \frac{f_0}{\Delta f} = 2\pi\tau_p f_0, \tag{4.21}$$

where $\Delta f = 1/2\pi\tau_p$ is the bandwidth of the resonance. Expressing (4.20) in terms of Q_L gives

$$E_{int}(t) = E_0 e^{-\frac{4\pi f_0}{Q_L}t}. \tag{4.22}$$

From this expression, we see that Q_L can be thought as the number of oscillations it takes for the energy to decay by $e^{-4\pi}$.

Q_L takes into account all the energy loss channels, including the loss from coupling to the I/O line, as described by Q_c, and the intrinsic loss from dissipation, as described by Q_I, where

$$\frac{1}{Q_L} = \frac{1}{Q_c} + \frac{1}{Q_I}. \tag{4.23}$$

On resonance and in the steady state, I can also relate Q_L to insertion loss IL using [233]

$$Q_I = \frac{Q_L}{1 - 10^{-IL/20}} = \frac{Q_L}{1 - T_{IL}} \tag{4.24}$$

where $T_{IL} \equiv 10^{-\frac{IL}{20}} = P_c/P_{app}$ is the coupling coefficient, P_{app} is the applied microwave power,

and P_c is the power of energy coupled into the resonator. Comparison between (4.23) and (4.22) gives the coupling coefficient as

$$T_{IL} = \frac{Q_L}{Q_c}. \tag{4.25}$$

The average amount of energy stored in the resonator can then be written as

$$\langle E_{int} \rangle = \tau_p P_c \,. \tag{4.26}$$

The average number of photons $\langle N_p \rangle$ stored in the resonator can be calculated from the average energy stored in the resonator and the energy of a photon at the resonance frequency as

$$\langle N_p \rangle = \frac{\langle E_{int} \rangle}{hf_0} = \frac{P_c \tau_p}{hf_0} = \frac{TP_{app}\,\tau_p}{hf_0} = \frac{P_{app}}{2\pi h {f_0}^2} \frac{{Q_L}^2}{Q_c}. \tag{4.27}$$

I note that this result differs by a factor of two from the expression in ref. [233], because here I have taken both the capacitive and inductive energy into account.

4.6. Dissipation Mechanisms

From Q_c, one can determine the amount of energy that can be coupled into the resonator from the input energy, and vice versa. Q_c also gives the ratio of the stored internal energy that is coupled out of the resonator. Q_I is mostly determined by the properties of the materials and quantifies the energy dissipated internally in the material. Over the past decade, great efforts has been made to identify and study possible dissipation mechanisms [203]-[224]. Reducing internal dissipation has greatly improved performance of superconducting qubits [61][210] and superconducting detectors [213]-[217] [222]. In the rest of this chapter, I briefly review the dominant dissipation mechanisms in superconducting resonators.

4.6.1 Radiation Loss

An energy loss channel that is inherent to the CPW resonator design is radiation from the CPW. The inverse quality factor due to radiation will scale as [234]

$$\frac{1}{Q_{rad}} \propto \left(\frac{w+2g}{l}\right)^2 w^2 . \tag{4.28}$$

Since radiation loss is associated with the geometry of the materials, it is relatively easy to reduce to a negligible value. For my 2D devices in shielded enclosures where $w = 2g \sim 10$ μm and $l \sim 4$mm, radiation loss is practically eliminated.

4.6.2 Dielectric Loss

Another well-known loss mechanism comes from the interaction of the resonator's electric field with nearly resonant TLSs of dipoles or dangling ions in the nearby dielectrics. A distribution of TLSs gives loss tangent $\tan\delta$ as in (2.92). Applying (2.94) to the case of a CPW, the dielectric loss can be written as

$$\frac{1}{Q_{\tan\delta}} = P_{AS}\tan\delta_{AS} + P_{SC}\tan\delta_{SC} + P_{CA}\tan\delta_{CA} , \tag{4.29}$$

where P_k is the participation ratio for region k, which is the fraction of EM energy stored in the volume of region k with intrinsic quality factor Q_k and loss tangent $\tan\delta_k$. AS, SC, CA denote the air-to-substrate, substrate-to-conductor, and conductor-to-air interfaces, respectively.

High resistivity silicon, for example, is a fairly common choice for the substrate of superconducting chips due to its low cost and ready availability. Loss for high resistivity Si has been measured as $\tan\delta < 10^{-7}$ [65]. This is a good but not exceptionally low level of loss. Moreover, native silicon oxide formed on the surface of a silicon substrate has been found to give high $\tan\delta$ on the order of 10^{-3} [203]. By etching a silicon wafer in hydrofluoric acid, the native silicon oxide can be removed before the deposition of superconductor, so this contribution to the loss from the substrate-to-air interface may be greatly reduced. Nevertheless, after patterning the chip, the silicon surface exposed to air will again develop a layer of silicon oxide, contributing significantly to P_{AS} due to loss in the gap/slot region of the CPW where electric field is most concentrated [235]. A trenched design [235] can be incorporated into the fabrication processes to reduce P_{AS}, where the substrate is etched down over the gap/slot region of the CPW (see Figure 4. 12) to reduce the volume of native oxide in the region with concentrated electric field. Experiments have shown a factor of ~ 1.75 improvement in the measured $Q_{\tan\delta}$, achieved via increasing the trench depth [235][236].

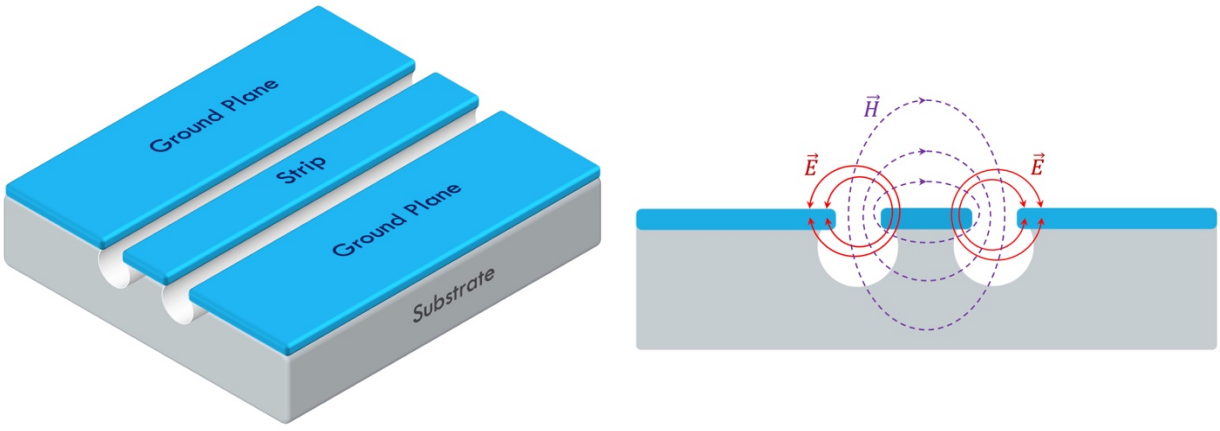

Figure 4. 12 A trenched design can be incorporated into the fabrication processes to reduce P_{AS}, where the substrate is etched down over the gap/slot region of the CPW to reduce the volume of native oxide in the region with concentrated electric field.

An alternative approach to reducing P_{AS} and P_{SC} is to use sapphire (Al_2O_3) for substrate, which has $\tan\delta$ typically of order $< 10^{-8}$ [46] and does not form a native oxide. Nevertheless, oxide layer grew on the surface of the CPW conductor during exposure to air can post a significant amount of loss due to P_{CA} [236]. In 2020, A. Melville et al [236] reported that switching the CPW conductor from aluminum to titanium nitride (TiN) could potentially improve $\tan\delta_{CA}$ at the conductor-to-air interfaces by a factor of 10. My measurements on TiN CPW resonators will be discussed in Chapter 10.

4.6.3 Two Level System Loss

At the microscopic level, the temperature and power dependence of $\tan\delta$ for dielectric interfaces can be modelled using (2.90), yielding

$$\frac{1}{Q_{TLS}(P_{rf},T)} = \tanh\left(\frac{\hbar\omega}{2k_BT}\right)\left[\frac{P_{AS}\tan\delta_{AS}^0}{\sqrt{1+(P_{rf}/P_{s,AS})^{\beta}}} + \frac{P_{SC}\tan\delta_{SC}^0}{\sqrt{1+(P_{rf}/P_{s,SC})^{\beta}}} + \frac{P_{CA}\tan\delta_{CA}^0}{\sqrt{1+(P_{rf}/P_{s,CA})^{\beta}}}\right]. \quad (4.30)$$

Here P_{rf} is the applied RF power and $P_{s,i}$ is the saturation power of region i. $\beta = 1$ for the standard distribution of TLSs. Wang *et al.* argued that the electric field distribution of the CWP geometry gives $\beta \sim 0.8$ [237]. The corresponding frequency shift is proportional to the TLS contribution to the real dielectric constant, as described by (2.91), and is given by

$$\frac{\delta f_0}{f_0} = \frac{C_P}{\pi}\left[Re\,\psi\left(\frac{1}{2}+\frac{hf_0}{2\pi ik_BT}\right) - \log\frac{hf_0}{k_BT}\right]\left(P_{AS}\tan\delta_{AS}^0 + P_{SC}\tan\delta_{SC}^0 + P_{CA}\tan\delta_{CA}^0\right), \quad (4.31)$$

where C_P is a power dependent constant, related to the distribution of tunneling states, that would need to be determined empirically [238].

4.6.4 Quasiparticle Loss

The presence of non-equilibrium quasiparticles at low temperatures $T \ll T_c$ is a surprising but well-known possible dissipation mechanism for superconducting devices. For this case, the interaction of the stored oscillating current with quasiparticles results in loss (Q_I^{-1}) as well as fractional frequency shifts which depend on the quasiparticle density [106]. The effects of quasiparticles in the CPW resonator can be incorporated into the complex conductivity (see (2.23)). From (4. 9) for a conductor with thickness $t \ll \lambda_{eff}$, one finds

$$L_k = g\frac{\sigma_2 t}{\omega}|Z_s|^2 . \tag{4.32}$$

It will be useful to consider the ratio of kinetic inductance to the total inductance:

$$\alpha_k \equiv \frac{L_k}{L_{geo} + L_k}. \tag{4.33}$$

For empirical convenience, I will also consider an effective fraction

$$\alpha_{\Delta k} \equiv \frac{\Delta L_k}{L_{geo} + L_k^0 + \Delta L_k}, \tag{4.34}$$

where ΔL_k is the change in kinetic inductance from a reference value L_k^0.

At temperatures well below T_c, $n_{qp} \ll n_s$, and this gives ΔL_k small relative to $\left(L_{geo} + L_k^0\right)$. The effect of ΔL_k on the resonance can be linearized by performing a Taylor series expansion:

$$\begin{aligned} f_0 &= \frac{1}{4l}\left(\left(L_{geo} + L_k^0 + \Delta L_k\right)C_{geo}\right)^{-0.5} \\ &\simeq \frac{1}{4l}\left(\left(L_{geo} + L_k^0\right)C_{geo}\right)^{-0.5}\left(1 - \frac{\Delta L_k}{2\left(L_{geo}+L_k^0\right)}\right). \end{aligned} \tag{4.35}$$

For a small shift in L_k due to quasiparticles, it is convenient to define the fractional frequency shift as

$$\frac{\delta f_0}{f_0} \coloneqq \frac{f_0(T)-f_0(T_{ref})}{f_0(T_{ref})} \simeq -\frac{\alpha}{2}\frac{L_k(T)-L_k(T_{ref})}{L_k(T_{ref})} \simeq -\frac{\alpha}{2}\frac{\delta\sigma_2(T)}{\sigma_2(T_{ref})}. \tag{4.36}$$

Similarly, the loss due to quasiparticles can be written as

$$\frac{1}{Q_{qp}} = \alpha\frac{R_s(T)}{X_s(T)} \simeq \alpha\frac{R_s(T)}{\omega L_k(T)} \simeq \alpha\frac{\sigma_1(T)}{\sigma_2(T)}. \tag{4.37}$$

While the exact distribution function for the non-equilibrium quasiparticles is not known [112], I use a simple Parker model [107] (see Section 2.1.2.2) for the quasiparticle distribution $f^*(E) = \left(e^{E/k_BT^*}+1\right)^{-1}$, where T^* is an effective temperature. Using Mattis-Bardeen theory [106][110] for the complex conductivities (see （2.34） and （2.35）), the loss and fractional frequency shift from （4.36） and （4.37） can be written as

$$\frac{1}{Q_{qp}} \simeq \alpha\frac{4}{\pi}e^{-\Delta/k_BT^*}\sinh(\xi)K_0(\xi) \tag{4.38}$$

$$\simeq \alpha\frac{\sigma_n}{\sigma_2(T_{ref})}\frac{2\Delta}{\hbar\omega}\frac{n_{qp}}{N_0\sqrt{2\pi k_BT^*\Delta}}\sin(\xi)K_0(\xi), \tag{4.39}$$

$$\frac{\delta f_0}{f_0} \simeq \frac{\alpha}{2}\left[1-\frac{\sigma_n}{\sigma_2(T_{ref})}\frac{\pi\Delta}{\hbar\omega}+\frac{\sigma_n}{\sigma_2(T_{ref})}\frac{2\pi\Delta}{\hbar\omega}\,e^{-\frac{\Delta}{k_BT^*}}e^{-\xi}I_0(\xi)\right] \tag{4.40}$$

$$\simeq \frac{\alpha}{2}\left[1-\frac{\sigma_n}{\sigma_2(T_{ref})}\frac{\pi\Delta}{\hbar\omega}+\frac{\sigma_n}{\sigma_2(T_{ref})}\frac{\pi\Delta}{\hbar\omega}\frac{n_{qp}}{N_0\sqrt{2\pi k_BT^*\Delta}}e^{-\xi}I_0(\xi)\right], \tag{4.41}$$

where $\xi = \frac{\hbar\omega}{2k_BT^*}$ and $n_{qp} \simeq 2N_0\sqrt{2\pi k_BT^*\Delta}\,e^{-\Delta/k_BT^*}$. The effective temperature T^* of the non-equilibrium quasiparticles alters the temperature dependence in the terms of $\sinh(\xi)K_0(\xi)/\sqrt{T^*}$ and $e^{-\xi}I_0(\xi)/\sqrt{T^*}$. If we have a model for how T^* depends on T, then we could see if this gives

a flat temperature dependence in Q_{qp}^{-1} and $\delta f_0/\delta f_0$ at low temperatures. This distribution function will be used to mode my data in Chapter 10.

4.6.5 Vortex Motion Loss

As discussed in Section 2.2, flow of Abrikosov vortices [111] in a superconducting thin film causes a complex vortex resistivity ρ_{vm}. The real and imaginary components of ρ_{vm} may contribute to loss (Q_I^{-1}) and fractional frequency shift in a coplanar resonator, respectively. Adopting the Coffey-Clem model [122][123] of vortex motion resistivity given by (2.72) yields

$$\frac{1}{Q_{vm}} = P_{vm}\, n_v \,\mathrm{Re}\,\rho_{vm,CC} = P_{vm}\,(B - B_m)\frac{\Phi_0}{\eta}\left(\epsilon_c + \frac{\omega^2}{\omega_0^2}\right)/\left(1 + \frac{\omega^2}{\omega_0^2}\right), \tag{4.42}$$

$$\frac{\delta f_0}{f_0} = P_{vm}\, n_v \,\mathrm{Im}\,\rho_{vm,CC} = P_{vm}\,(B - B_m)\frac{\Phi_0}{\eta}(1 - \epsilon_c)/\left(\frac{\omega}{\omega_0} + \frac{\omega_0}{\omega}\right), \tag{4.43}$$

where P_{vm} is a participation ratio related to the distribution of vortices in the inductive section of the CPW, and n_v is the effective vortex density. Since CPW resonators are typically measured in shielded enclosures and have small strip widths, the ρ_{vm} contribution to Q_I^{-1} is typically small compared to loss from TLS and non-equilibrium quasiparticles [239]. Nevertheless, it could cause non-negligible loss and resonance frequency shift should $P_{vm}\, n_v$ be sufficiently large. In fact, the motion of one vortex in a high-Q resonator can be detected [127].

CHAPTER 5

Impact of Spatial Variations in Superconducting Gap for Low Loss Devices

After reviewing the various dissipation mechanisms in thin-film superconducting devices of transmon and coplanar waveguide resonator, we finally come to the focus of my research – an examination of dissipation phenomenon induced by non-equilibrium quasiparticle redistribution due to superconducting energy gap inhomogeneity. In my aluminum 3D transmon and PAMBE titanium nitride coplanar waveguide resonator, I observed a decrease in dissipation as the temperature was increased. As I discuss in this chapter, this peculiar temperature dependence of energy loss can be explained by the behavior of non-equilibrium quasiparticles that are moving in structures that have variations in the superconducting energy gap Δ. This chapter provides a detailed theoretical discussion of the phenomenon.

5.1. Quasiparticle Transfer Between Regions with Different Gaps

To model the loss due to quasiparticles that are moving in a sample that has spatial variations in the superconducting energy gap, consider the simple situation where there are two regions with energy gaps Δ_1 and Δ_2, respectively. I assume that the regions are in direct contact, such that quasiparticles are free to flow between them. The net rate of change of the quasiparticle

density in each region can then be written as

$$\frac{dn_{qp,1}}{dt} = G_{p1} + G_{g1} - G_{tr1}n_{qp,1} - G_r\Omega_1 n_{qp,1}^2 - G_{1\to2}An_{qp,1} + G_{2\to1}An_{qp,2} \quad (5.1)$$

$$\frac{dn_{qp,2}}{dt} = G_{p2} + G_{g2} - G_{tr2}n_{qp,2} - G_r\Omega_2 n_{qp,2}^2 - G_{2\to1}An_{qp,2} + G_{1\to2}An_{qp,1}\,, \quad (5.2)$$

where $n_{qp,j}$ refers to the quasiparticle density in the region denoted by the subscript j, G_{pj} is the rate at which the density of non-equilibrium quasiparticles are being generated in region j, G_{gj} is the rate at which the density of quasiparticles are being generated thermally in region j, G_{trj} is the rate at which the density of quasiparticles are being trapped by vortices in region j, G_r is the temperature-dependent rate at which density of quasiparticles are being recombined in region j of volume Ω_j, $G_{i\to j}$ is the rate at which the density of quasiparticles are being transferred from region i to region j per unit area of contact, and A is the contact area between the two regions. In steady state,

$$\frac{dn_{qp,1}}{dt} = \frac{dn_{qp,2}}{dt} = 0 \quad (5.3)$$

and the quasiparticle density $n_{qp,1}$ can be solved in terms of $n_{qp,2}$. However, to obtain explicit expressions for the densities, the presence of superconducting energy gap inhomogeneity in the device geometry has to be taken into consideration. In subsequent sections, I examine the effect of gap inhomogeneity in aluminum transmons and titanium nitride coplanar waveguide resonators. The resulting model gives the temperature dependence of non-equilibrium quasiparticle induced transmon T_1 and resonator Q_I.

5.2. Gap Variation in Transmon Electrodes

In practice, the complicated response of non-equilibrium quasiparticles to applied microwave power [93][99][223][240] can produce loss that mimics some of the non-linear behavior seen in two-level systems, making it challenging to identify the underlying mechanism causing relaxation in a device. Observations on the temperature dependence of my transmon relaxation time T_1 showed a striking and unexpected increase in T_1 as the temperature T was increased from about 30 mK to 100 mK ($\sim T_c/10$). This behavior is not unique; it was also observed in transmons from our collaborator's group. In the rest of this section, I explain how this dependence can arise from the behavior of non-equilibrium quasiparticles when the junction electrodes have slightly different superconducting gaps [95][218]-[220].

5.2.1. Modeling Quasiparticle Density

To develop a realistic model of the quasiparticle tunneling currents $I_{L\to R}$ and $I_{R\to L}$ in (3.79) for calculating transmon T_1, we need to consider the physical layout of the transmon. My transmons were made using double-angle evaporation [241] of two thin-film aluminum layers that create a Josephson junction, as illustrated by the simplified structure in Figure 5. 1. Al layer 1 was deposited on the sapphire substrate and the exposed Al surface oxidized to form a thin AlOx tunnel barrier. Al layer 2 was then deposited on top of layer 1 through an e-beam resist-bridge stencil that created a small overlap junction between the two layers (shown in red in Figure 5. 1). The two Al layers have different thicknesses, and the growth conditions may also be somewhat different, which can lead to the layers having somewhat different superconducting gaps [242]-[247]. For example, the layer 2 Al may be deposited under higher oxygen pressure compared to layer 1, since

this layer is deposited shortly after oxygen is pumped from the chamber. The effect of oxygen on the energy gap will be further discussed in the Section 9.4. In Figure 5. 1, the left electrode of the junction is formed from layer 1, with superconducting gap Δ_1, and connects to the left pad of the transmon, which is formed from both layers 1 and 2 with volumes Ω_{1L} and Ω_{2L}, respectively. Similarly, the right electrode of the junction is formed from layer 2, with superconducting gap Δ_2, and connects to the right pad of the transmon, which is formed from both layers 1 and 2 with volumes Ω_{1R} and Ω_{2R}, respectively. In our devices the left and right transmon pads have the same surface area, but the second layer is about twice as thick as the first layer to ensure good coverage, thus $\Omega_{1L} \cong \Omega_{1R} \cong \Omega_{2R}/2 \cong \Omega_{2L}/2$. Aside from Δ_1 and Δ_2, the ratio of the two volumes plays an important role in the temperature dependence of the relaxation as well.

To evaluate (3.82) and obtain $T_{1,qp}$ as a function of temperature T, we need to determine how the quasiparticle densities n_{1L} and n_{2R} vary with temperature. A significant complication is that there can be quasiparticles generated by non-equilibrium pair-breaking processes, as well as thermally generated quasiparticles. It is not known whether the non-equilibrium pair-breaking is caused by high-energy phonons, infrared photons, optical photons or other mechanisms [61][133][140]. For simplicity, I assume that a steady, temperature-independent source is generating non-equilibrium quasiparticles in layer 1 (which is in direct contact with the substrate) in both the left and right transmon pads. I also assume that the quasiparticles have thermalized to the temperature T of the substrate and that the two layers in each pad are in good diffusive contact. A simplified cross-sectional illustration for the configuration of regions in contact near the junction and the corresponding energy level diagram is shown in Figure 5. 2.

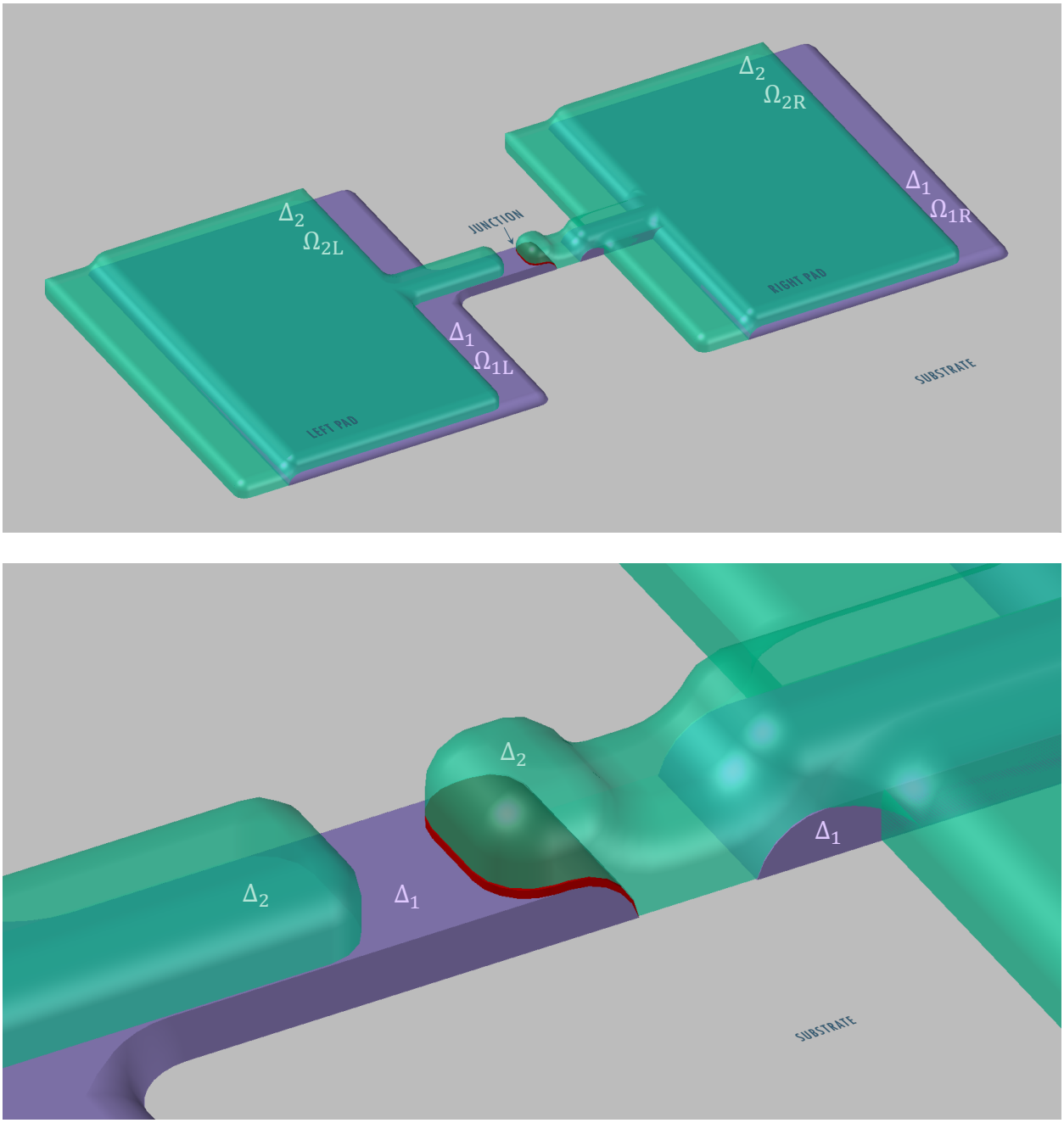

Figure 5. 1 Simplified illustration of the physical layout of my transmons. The devices are made using double-angle evaporation of two thin-film aluminium layers that create a Josephson junction. Al layer 1 (purple) is deposited on a sapphire substrate (gray) and the surface oxidized to form a thin tunnel barrier. Al layer 2 (green) is deposited on top of layer 1 (purple) through an e-beam resist-bridge stencil that creates a small overlap junction between the two layers (red).

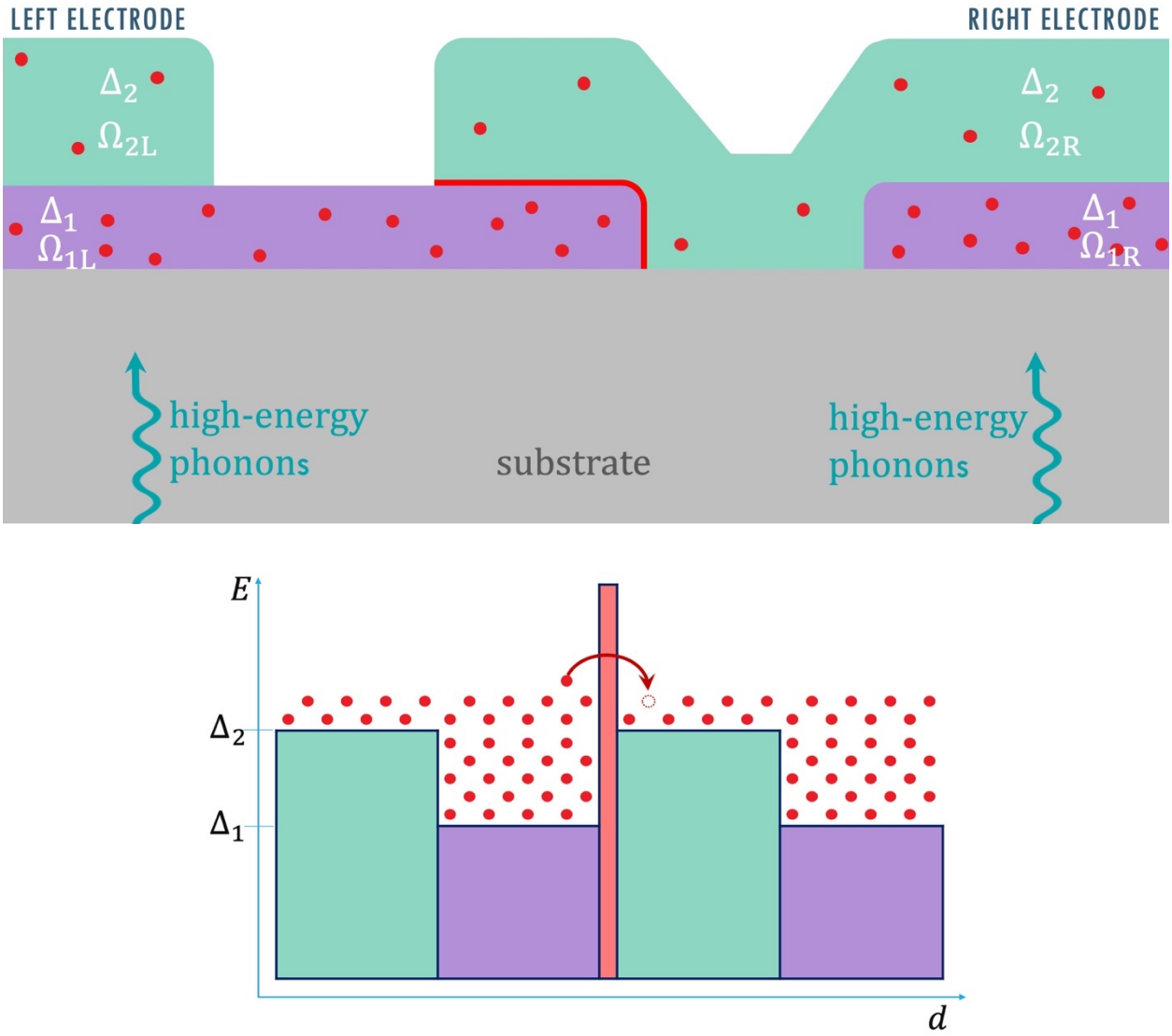

Figure 5. 2 (Upper) Simplified cross-sectional illustration for the configuration of regions in contact near the junction, and (lower) the corresponding energy level diagram. A steady, temperature-independent source is assumed to be generating non-equilibrium quasiparticles in layer 1 (purple), which is in direct contact with the substrate, in both the left and right transmon pads. I assume that the quasiparticles have thermalized to the temperature T of the substrate and that the two layers in each pad are in good diffusive contact.

Consider the case where quasiparticle trapping is present and quasiparticle recombination can be ignored. For simplicity, I will assume that the quasiparticle traps [222] are due to trapped magnetic flux vortices which thread both Al layers. This non-trivial assumption may explain some

of the behavior we observe, including run-to-run variations in T_1 and fluctuations in T_1 during the same cool-down. Since the number of vortices trapped in the transmon's left pad may be different than the number trapped in the right pad, and both may vary from one cool-down to the next, this assumption naturally allows for different quasiparticle trapping rates in the left and right pads, as well as variations in the trapping rate from one run to the next. In addition it suggests that spontaneous changes in T_1 which we observed may have been caused by flux motion in the pads. To proceed, I now make the following set of assumptions:

(1) The left side of the junction has a low-gap region with gap Δ_1 and small volume Ω_{1L} and a high-gap region with gap Δ_2 and large volume Ω_{2L}.

(2) The right side of the junction has a low-gap region with gap Δ_1 and small volume Ω_{1R} and a high-gap region with gap Δ_2 and large volume Ω_{2R}.

(3) The junction only makes contact between the low gap Δ_1 region on the left side and the high gap Δ_2 region on the right side.

(4) When finding the steady state density, we can ignore the transfer of quasiparticles through the junction.

(5) On each side of the junction, region 1 can freely exchange quasiparticles with region 2.

(6) On each side of the junction, non-equilibrium quasiparticles are only generated in region 1, which is in contact with the substrate.

(7) We ignore quasiparticle recombination and assume that quasiparticles can be trapped by vortices that thread through both layers.

I can now write the net rate at which quasiparticles are generated in each region. For example, in the steady state we can write for the two regions on the left side:

$$\frac{dN_{1L}}{dt} = G_{p1} + G_{g1} - G_{tr1}N_{1L} - G_{L,1\to2}A_L\frac{N_{1L}}{\Omega_{1L}} + G_{L,2\to1}A_L\frac{N_{2L}}{\Omega_{2L}} = 0\,, \tag{5.4}$$

$$\frac{dN_{2L}}{dt} = G_{g2} - G_{tr2}N_{2L} - G_{L,2\to1}A_L\frac{N_{2L}}{\Omega_{2L}} + G_{L,1\to2}A_L\frac{N_{1L}}{\Omega_{1L}} = 0\,, \tag{5.5}$$

where N refers to the number of quasiparticles in the region denoted by the subscript, A_L is the contact area between the two regions on the left, G_{p1} is the rate at which non-equilibrium quasiparticles are being generated in region 1 on the left, G_{gj} is the rate at which quasiparticles are being generated thermally in region j on the left, G_{trj} is the rate at which quasiparticles are being trapped by vortices region j, and $G_{L,i\to j}$ is the rate at which quasiparticles are moving from region i to region j on the left. Solving for the number of quasiparticles in region 1 on the left, I find

$$N_{1L} = \frac{\left(\frac{G_{p1}}{G_{tr1}} + \frac{G_{g1}}{G_{tr1}}\right) + \frac{G_{L,2\to1}}{G_{tr2}}\frac{A_L}{\Omega_{2L}}\left(\frac{G_{p1}}{G_{tr1}} + \frac{G_{g1}}{G_{tr1}} + \frac{G_{g2}}{G_{tr1}}\right)}{1 + \frac{G_{L,2\to1}}{G_{tr2}}\frac{A_L}{\Omega_{2L}} + \frac{G_{L,1\to2}}{G_{tr1}}\frac{A_L}{\Omega_{1L}}}. \tag{5.6}$$

We now proceed to rewrite this expression in terms of the number of thermal quasiparticles and non-equilibrium quasiparticles in each region. To make these identifications notice that in the limit $T \to 0$, all of the quasiparticles will be produced by the non-equilibrium pair breaking process. In this limit the thermal generation terms G_{g1}, G_{g2} and $G_{L1,2}$ go to zero and we get simply

$$N_{1L} = G_{p1}/G_{tr1} \equiv N_{1L,ne}\,, \tag{5.7}$$

where I have introduced the temperature independent parameter $N_{1L,ne}$ that determines the number

of non-equilibrium quasiparticles in the steady state at zero temperature in region 1 on the left. A similar argument allows us to identify the number of thermal quasiparticles in regions 1 and 2 as

$$N_{th,1} \equiv G_{g1}/G_{tr1} \tag{5.8}$$

$$N_{th,2} \equiv G_{g2}/G_{tr2}. \tag{5.9}$$

Next consider the trapping terms. There are different possible types of quasiparticle traps, including normal metal inclusions, normal metal surface layers, normal metal interfaces and trapped flux vortices. These different traps may be expected to have different scaling with the dimensions of the region. Here I assume that the trapping is caused by vortices that penetrate both layers simultaneously. The rate at which quasiparticles will be trapped in layer 1 will scale with the density of quasiparticles, the speed v of the quasiparticles, the number of vortices N_{v1}, and the effective area of a vortex tube

$$A_v = 2\pi r_v h_1 \,, \tag{5.10}$$

where r_v is the effective radius of the vortex (refer to Chapter 2.2) and the length of the vortex is assumed to be equal to the thickness h_1 of the layer 1. Thus the total rate at which quasiparticles are trapped in region 1L is

$$G_{tr1,L}N_{1L} = \frac{N_{1L}}{\Omega_{1L}} v(2\pi r_v h_1)N_{v1}. \tag{5.11}$$

Since we are assuming the same vortices penetrate each layer, we have $N_{v1} = N_{v2}$ and thus can write for the trapping rate in layer 2 that

$$G_{tr2,L}N_{2L} = \frac{N_{2L}}{\Omega_{2L}} v(2\pi r_v h_2)N_{v1}. \tag{5.12}$$

Thus we find the ratio

$$\frac{G_{tr1,L}}{G_{tr2,L}} = \frac{\Omega_{2L}}{\Omega_{1L}} \frac{v(2\pi r_v h_1) N_{v1}}{v(2\pi r_v h_2) N_{v1}} = \frac{\Omega_{2L}}{\Omega_{1L}} \frac{h_1}{h_2} = \frac{A_{2L}}{A_{1L}} = 1\,, \tag{5.13}$$

where $A_{2L} = A_{1L}$ is the planar area of layers 1 and 2. With this result, we can write the general expression for N_{1L} as

$$N_{1L} = \frac{\left(N_{1L,ne} + N_{th,1}\right) + \frac{G_{L,2\to1}}{G_{tr1}} \frac{A_L}{\Omega_{2L}} \left(N_{1L,ne} + N_{th,1} + N_{th,2}\right)}{1 + \frac{G_{L,2\to1}}{G_{tr1}} \frac{A_L}{\Omega_{2L}} + \frac{G_{L,1\to2}}{G_{tr1}} \frac{A_L}{\Omega_{1L}}}. \tag{5.14}$$

Next, I make the plausible, but not necessarily true, assumption that the trapping is relatively slow compared to exchange from region 2 to region 1. In this case

$$G_{L2\to1} \frac{A_L}{\Omega_{1L}} > G_{L2\to1} \frac{A_L}{\Omega_{2L}} \gg G_{tr1,L}. \tag{5.15}$$

In this limit, (5.14) gives

$$N_{1L} \cong \frac{1}{1 + \frac{G_{L,1\to2}}{G_{L,2\to1}} \frac{\Omega_{2L}}{\Omega_{1L}}} \left(N_{1L,ne} + N_{th,1} + N_{th,2}\right). \tag{5.16}$$

In thermal and diffusive equilibrium with no pair breaking, we must have that there is no net particle exchange between the two regions, and thus the transfer rates obey

$$G_{L,1\to2} A_L \frac{N_{1L,th}}{\Omega_{1L}} = G_{L,2\to1} A_L \frac{N_{2L,th}}{\Omega_{2L}}, \tag{5.17}$$

which then gives

$$\frac{G_{L,1\to2}}{G_{L,2\to1}} \frac{\Omega_{2L}}{\Omega_{1L}} = \frac{N_{2L,th}}{N_{1L,th}} \cong \frac{\Omega_{2L}}{\Omega_{1L}} \sqrt{\frac{\Delta_2}{\Delta_1}} e^{-\frac{(\Delta_2 - \Delta_1)}{k_B T}}, \tag{5.18}$$

and thus

$$N_{1L} \cong \frac{\Omega_{1L} \sqrt{\Delta_1} e^{-\Delta_1/k_B T}}{\Omega_{1L} \sqrt{\Delta_1} e^{-\Delta_1/k_B T} + \Omega_{2L} \sqrt{\Delta_2} e^{-\Delta_2/k_B T}} \left(N_{1L,ne} + N_{th,1} + N_{th,2}\right). \tag{5.19}$$

Similar expressions can be obtained for N_{2L}, N_{1R}, and N_{2R}.

To proceed, consider the Fermi distribution functions $f_L(E)$ and $f_R(E)$ (see Section 2.1) for the quasiparticles in the left and right electrodes, respectively. By adopting the effective chemical representation of nonequilibrium quasiparticles in (2.12), the quasiparticle distribution functions can be expressed as

$$f_L(E) \to f(E, \mu_{1L}) \tag{5.20}$$

$$f_R(E) \to f(E, \mu_{2R}), \tag{5.21}$$

where μ_{1L} and μ_{2R} are the chemical potential for the $E > 0$ quasiparticles in region 1 on the left and region 2 on the right, respectively. The density of quasiparticles n_{1L} and n_{2R} in volumes Ω_{1L} and Ω_{2R}, respectively, are then given by

$$n_{1L} = 4N_0 \int_{\Delta_1}^{\infty} \frac{E}{\sqrt{E^2 - \Delta_1^2}} f(E, \mu_{1L})\, dE = 4N_0 \Delta_1 \sum_{n=1}^{\infty} (-1)^{n+1} e^{n\mu_{1L}/k_B T} K_1\left(\frac{n\Delta_1}{k_B T}\right) \tag{5.22}$$

$$n_{2R} = 4N_0 \int_{\Delta_2}^{\infty} \frac{E}{\sqrt{E^2 - \Delta_2^2}} f(E, \mu_{2R})\, dE = 4N_0 \Delta_2 \sum_{n=1}^{\infty} (-1)^{n+1} e^{n\mu_{2R}/k_B T} K_1\left(\frac{n\Delta_2}{k_B T}\right), \tag{5.23}$$

where K_1 is the *modified* Bessel function of the second kind of order 1. By setting $\mu = 0$, one can find a relationship between the thermal densities $n_{1L,th}$ and $n_{2R,th}$ in the two regions as

$$\frac{n_{2R,th}}{n_{1L,th}} \cong \sqrt{\frac{\Delta_2}{\Delta_1}} e^{-\frac{(\Delta_2 - \Delta_1)}{k_B T}}. \tag{5.24}$$

With rearrangement of (5.19), I arrive at

$$n_{1L} \cong n_{1L,th} + \left(\frac{\Omega_{1L}\sqrt{\Delta_1} e^{-\Delta_1/k_B T}}{\Omega_{1L}\sqrt{\Delta_1} e^{-\Delta_1/k_B T} + \Omega_{2L}\sqrt{\Delta_2} e^{-\Delta_2/k_B T}}\right) n_{1L,ne}. \tag{5.25}$$

Here $n_{1L,ne}$ quantifies the density of non-equilibrium quasiparticles being generated in region 1L and is equal to the rate at which an external source is generating non-equilibrium quasiparticles divided by the quasiparticle trapping rate in region 1L. Similar analysis of the density of quasiparticles in region 2R yields

$$n_{2R} \cong n_{th,2} + \left(\frac{\Omega_{2R}\sqrt{\Delta_2}e^{-\Delta_2/k_BT}}{\Omega_{1R}\sqrt{\Delta_1}e^{-\Delta_1/k_BT} + \Omega_{2R}\sqrt{\Delta_2}e^{-\Delta_2/k_BT}} \right) \left(\frac{\Omega_{1R}}{\Omega_{2R}} \right) n_{1R,ne}\,, \tag{5.26}$$

where I have again assumed that non-equilibrium quasiparticles are only produced in layer 1, and this accounts for the differences in form between (5.25) and (5.26).

Finally, I note that the above steady state approach can be extended to an arbitrary number N of regions with different volumes and gaps. If I again assume that non-equilibrium quasiparticles are only produced in layer 1, one finds in general that the density of quasiparticles in region 1 is

$$n_{1L} \cong n_{th,1} + \left(\frac{\Omega_{1L}\sqrt{\Delta_1}e^{-\Delta_1/k_BT}}{\sum_{n=1}^{N} \Omega_{nL}\sqrt{\Delta_n}e^{-\Delta_n/k_BT}} \right) n_{1L,ne} \tag{5.27}$$

and for region j not equal to 1, one obtains

$$n_{jL} \cong n_{th,j} + \left(\frac{\Omega_{jL}\sqrt{\Delta_j}e^{-\Delta_j/k_BT}}{\sum_{n=1}^{N} \Omega_{nL}\sqrt{\Delta_n}e^{-\Delta_n/k_BT}} \right) \left(\frac{\Omega_{1L}}{\Omega_{jL}} \right) n_{1L,ne}. \tag{5.28}$$

Now that we have derived the expression of quasiparticle densities in the electrodes on either side of the Josephson tunneling junction, the subsequent section will incorporate this ingredient into the quasiparticle tunneling currents $I_{L\to R}$ and $I_{R\to L}$ in (3.79), thus calculating the transmon T_1.

5.2.2. Calculating Relaxation Time T_1

For my transmon, hf_{ge}~17 μeV and Δ~200 μeV. Therefore, I am interested in the case where $hf_{ge} \ll \Delta_1$ and $hf_{ge} \ll \Delta_2$. One of my assumptions is that non-equilibrium quasiparticles have been created in the junction electrodes due to an external source that causes pair-breaking [248]. In the semiconductor model of a superconductor [87], this produces an equal number of quasiparticles with energy $E > 0$ and $E < 0$, where we take the zero of energy at the Fermi level. I also assumed that the quasiparticles in each pad have thermalized to the temperature T of the substrate and that the two layers in each pad are in good diffusive contact. These assumptions imply that in each region the quasiparticles have a Fermi-Dirac distribution $f(E,\mu)$ for $E > 0$, while for hole-like excitations with $E < 0$, $f(-|E|,-\mu) = 1 - f(E,\mu)$. In this case quasiparticles with $E > 0$ and $E < 0$ will contribute equally to the current noise, and (3.84) becomes

$$I_{qp}\left(\frac{hf_{ge}}{e}\right) = \frac{1}{eR_n}\int_{-\infty}^{\infty} \frac{dE\,|E|}{\sqrt{E^2-\Delta_1^2}} \frac{\left|E+hf_{ge}\right|}{\sqrt{(E+hf_{ge})^2-\Delta_2^2}} \left(f_L(E) - f_R\left(E+hf_{ge}\right)\right), \tag{5.29}$$

where the region of integration must exclude $-\Delta_1 < E < \Delta_1$ and $-\Delta_2 < E + hf_{ge} < \Delta_2$. Incorporating these regions of exclusion into the limits for integration yields

$$\begin{aligned} I_{qp}(f_{ge}) = \frac{1}{eR_n}\Bigg[& \int_{\Delta_1}^{\infty} dE \frac{E}{\sqrt{E^2-\Delta_1^2}} \frac{E+hf_{ge}}{\sqrt{(E+hf_{ge})^2-\Delta_2^2}} \left(f_L(E) - f_R\left(E+hf_{ge}\right)\right) \\ & + \int_{\Delta_2}^{\infty} dE \frac{E+hf_{ge}}{\sqrt{(E+hf_{ge})^2-\Delta_1^2}} \frac{E}{\sqrt{E^2-\Delta_2^2}} \left(f_R(E) - f_L\left(E+hf_{ge}\right)\right)\Bigg]. \end{aligned} \tag{5.30}$$

By adopting the effective chemical representation of nonequilibrium quasiparticles, the contribution to I_{qp} in (5.30) from the current flow in the direction $L \rightarrow R$ can be written as

$$I_{L\rightarrow R} = \frac{2}{eR_n}\int_0^\infty \frac{|E|\theta(E-\Delta_1)}{\sqrt{E^2-\Delta_1^2}} \frac{\left|E+hf_{ge}\right|\theta\left(E+hf_{ge}-\Delta_2\right)}{\sqrt{\left(E+hf_{ge}\right)^2-\Delta_2^2}} \times f(E,\mu_{1L})\left(1-f\left(E+hf_{ge},\mu_{2R}\right)\right)dE\,. \tag{5.31}$$

As discussed in Chapter 6, my devices operated in the limit $|\Delta_2-\Delta_1| < hf_{ge}$, $\Delta_1-\mu_{1L} \gg k_BT$ and $\Delta_2-\mu_{2R} \gg k_BT$. Expressing the quasiparticle distribution function $f(E,\mu)$ in terms of the quasiparticle densities n_{1L} and n_{2R} (see preceding section), (5.31) is well approximated by

$$I_{L\rightarrow R} \cong \frac{\alpha(\Delta_1,\Delta_2)}{eR_n}\frac{n_{1L}}{2N_0}\left\{1-\frac{e^{-(\Delta_1+hf_{ge}-\Delta_2)/k_BT}}{\sqrt{\pi k_BT\Delta_2}}\beta_1\frac{n_{2R}}{8N_0}\right\}, \tag{5.32}$$

where the functions $\alpha(x,y)$ and β_1 are defined as

$$\alpha(x,y) \equiv \frac{x+hf_{ge}+x_ok_BT}{\sqrt{\left(x+hf_{ge}+x_ok_BT\right)^2-y^2}}, \tag{5.33}$$

$$\beta_1 \equiv \frac{\sqrt{2\Delta_2+x_ok_BT}}{(\Delta_2+x_ok_BT)}\frac{(2\Delta_1+x_ok_BT)^{3/2}}{(\Delta_1+x_ok_BT)}\frac{\sqrt{\Delta_2}}{\sqrt{4\Delta_1+x_ok_BT}} \approx 2\,. \tag{5.34}$$

Here, the quantity x_ok_BT can be interpreted as the effective thermal energy of the quasiparticles that contribute to the noise current. Evaluating (5.32) for different values of x_o and comparing to the numerical integration of (5.31), one find that $x_o = 0.3$ yields a good approximation within 5% accuracy for typical parameters. A similar expression for $I_{R\rightarrow L}$ can be obtained by exchanging

the subscript pairs $1 \leftrightarrow 2$ and $1L \leftrightarrow 2R$ in (5.32) to (5.34).

For typical parameters, the second term in the parentheses in (5.32) is very small compared to unity, thus (3.79) reduces to

$$S_I(f_{ge}) \cong \frac{1}{R_n N_0}\left(\frac{\alpha(\Delta_1,\Delta_2)}{2} n_{1L} + \frac{\alpha(\Delta_2,\Delta_1)}{2} n_{2R}\right). \tag{5.35}$$

Substituting this into (3.80) gives

$$\Gamma_{e\to g} \cong \frac{1}{\tau_o n_e}\left\{\frac{\alpha(\Delta_1,\Delta_2)}{2} n_{1L} + \frac{\alpha(\Delta_2,\Delta_1)}{2} n_{2R}\right\}, \tag{5.36}$$

where n_e is the density of electrons in aluminum and τ_o is a characteristic time constant related to the material and qubit frequency given by

$$\tau_o \equiv 3R_n C\left(\frac{hf_{ge}}{2\varepsilon_F}\right). \tag{5.37}$$

A similar analysis of the excitation rate corresponding to the negative frequencies gives

$$\Gamma_{g\to e} \cong \frac{e^{-h|f_{ge}|/k_BT}}{\tau_o n_e}\left\{\frac{\gamma(\Delta_1,\Delta_2)}{2} n_{1L} e^{-(\Delta_2-\Delta_1)/k_BT} + \frac{\gamma(\Delta_2,\Delta_1)}{2} n_{2R} e^{-(\Delta_1-\Delta_2)/k_BT}\right\}, \tag{5.38}$$

where the function $\gamma(x,y)$ is defined by

$$\gamma(x,y) \equiv \frac{(y+h|f_{01}|+x_o k_B T)}{\sqrt{(y+h|f_{01}|+x_o k_B T)^2 - x^2}} \frac{(y+x_o k_B T)}{\sqrt{2y+x_o k_B T}} \frac{\sqrt{2x+x_o k_B T}}{(x+x_o k_B T)}. \tag{5.39}$$

From (3.79), (5.36) and (5.38) I then obtain for the relaxation time

$$T_{1,qp} \cong 2\tau_o n_e \Big[n_{1L}\big(\alpha(\Delta_1,\Delta_2) + \gamma(\Delta_1,\Delta_2) e^{-h|f_{ge}|/k_BT} e^{-(\Delta_2-\Delta_1)/k_BT}\big) + n_{2R}\big(\alpha(\Delta_2,\Delta_1) + \gamma(\Delta_2,\Delta_1) e^{-h|f_{ge}|/k_BT} e^{-(\Delta_1-\Delta_2)/k_BT}\big)\Big]^{-1}. \tag{5.40}$$

This expression will be adopted in Chapter 9 to model the temperature dependence of my transmon T_1. I note that if $\Delta_1 = \Delta_2 = \Delta$, the expression in (5.40) simplifies to

$$T_{1,qp} \cong \frac{\sqrt{\big(\Delta + h|f_{ge}| + x_o k_B T\big)^2 - \Delta^2}}{\big(1 + e^{-h|f_{ge}|/k_BT}\big)\big(\Delta + h|f_{ge}| + x_o k_B T\big)} \frac{2\tau_o n_e}{(n_{1L} + n_{2R})} \tag{5.41}$$

and the relaxation time scales inversely with the average quasiparticle density in the two electrodes.

As another example, in the limit $k_BT \ll \Delta_2 - \Delta_1 < hf_{ge}$, the non-equilibrium quasiparticles will accumulate in layer 1. Since $\Delta_1 < \Delta_2$ and this will tend to give $n_{2R} \ll n_{1L}$, (5.40) reduces to

$$T_{1,qp} \approx 2\tau_o \left(\frac{n_e}{\alpha(\Delta_1,\Delta_2) n_{1L}}\right). \tag{5.42}$$

Thus, in this limit, we expect the relaxation time at sufficiently low temperatures to scale inversely with the quasiparticle density in the junction's low-gap electrode.

I should emphasize that (5.40) is only valid for $\Delta_2 - \Delta_1 < hf_{ge}$. In contrast, $T_{1,qp}$ versus T shows distinctly different behavior for $\Delta_2 - \Delta_1 > h|f_{ge}|$. In this limit of large difference in the energy gaps, analysis gives

$$\Gamma_{1\to 0} \approx \frac{1}{\tau_0 n_e}\left[\frac{\zeta\alpha_3}{2} e^{-(\Delta_2-\Delta_1-h|f_{ge}|)/k_BT} n_{1L} + \frac{\alpha_2}{2} n_{2R}\right] \tag{5.43}$$

$$\Gamma_{0\to1} \approx \frac{1}{\tau_0 n_e}\left[\frac{\zeta\alpha_2}{2}e^{-(\Delta_2-\Delta_1+h|f_{ge}|)/k_BT}n_{1L} + \frac{\alpha_3}{2}n_{2R}\right] \tag{5.44}$$

$$T_{1,qp} \approx \frac{2n_e\tau_0}{\zeta\left(\alpha_2 e^{h|f_{ge}|/k_BT} + \alpha_3 e^{-h|f_{ge}|/k_BT}\right)e^{-(\Delta_2-\Delta_1)/k_BT}n_{1L} + (\alpha_2+\alpha_3)n_{2R}}, \tag{5.45}$$

where terms that are of second order in the quasiparticle densities have been dropped, and the functions α_2, α_3, and ζ are defined as

$$\alpha_2 \equiv \frac{\Delta_2 + hf_{ge} + \chi_o k_B T}{\sqrt{\left(\Delta_2 + hf_{ge} + \chi_o k_B T\right)^2 - \Delta_1^2}} \tag{5.46}$$

$$\alpha_3 \equiv \frac{\Delta_2 - h|f_{ge}| + \chi_o k_B T}{\sqrt{\left(\Delta_2 - h|f_{ge}| + \chi_o k_B T\right)^2 - \Delta_1^2}} \tag{5.47}$$

$$\zeta \equiv \frac{\Delta_2 + \chi_o k_B T}{\sqrt{2\Delta_2 + \chi_o k_B T}}\frac{\sqrt{2\Delta_1 + \chi_o k_B T}}{\Delta_1 + \chi_o k_B T} \approx \sqrt{\frac{\Delta_2}{\Delta_1}}. \tag{5.48}$$

In the low temperature limit $|\Delta_2 - \Delta_1| > hf_{ge} \gg k_B T$, (5.45) simplifies to

$$T_{1,qp} \approx \frac{2n_e\tau_0}{\zeta\alpha_2 e^{-(\Delta_2-\Delta_1-h|f_{ge}|)/k_BT}n_{1L} + (\alpha_2+\alpha_3)n_{2R}}. \tag{5.49}$$

For $\Delta_2 - \Delta_1 \gg k_B T$ we expect all of the quasiparticles to condense into layer 1, since its gap is smaller than the gap of layer 2 and n_{2R} scales with a Boltzmann factor as $e^{-\frac{\Delta_2-\Delta_1}{k_BT}}$. Thus, the first term in the denominator of (5.49) will tend to dominate the second, giving the low temperature limit of $T_{1,qp}$ as

$$T_{1,qp} \approx \frac{2n_e\tau_0}{\zeta\alpha_2 n_{1L}} e^{(\Delta_2-\Delta_1-h|f_{ge}|)/k_BT}. \quad (5.50)$$

We note that when the gap difference is large, this result implies that the relaxation time of a transmon due to quasiparticles will increase exponentially as the temperature decreases below $(\Delta_2 - \Delta_1 - h|f_{ge}|)/k_B$, providing a distinct signature.

Substituting (5.25) and (5.26) for the quasiparticle densities n_{1L} and n_{2R} into (5.40) gives the temperature dependence of the transmon relaxation time in the limit $hf_{ge} \ll |\Delta_{2R} - \Delta_{1L}|$. Unfortunately, the resulting expression is unwieldy and not very transparent. In contrast, the main cause for the anomalous temperature dependence of the relaxation time can be found by examining (5.25) and (5.26) for the case $\Delta_{1L} < \Delta_{2R}$. At sufficiently low temperatures, the density of thermal quasiparticles $n_{th,1} \approx n_{th,2} \approx 0$ and the first term in (5.25) and (5.26) can be ignored. For $k_BT \ll \Delta_{2R} - \Delta_{1L}$, one finds that $n_{1L} = n_{ne,1L}$ and $n_{2R} \approx 0$. Thus all of the quasiparticles in the left pad will tend to accumulate in region 1L, which is connected to the junction and will cause loss. On the other hand, all of the quasiparticles in the right pad will collect in region 1R, which is not in direct contact with the junction and will not cause loss. In this case, the average density of quasiparticles at the junction interface is $\frac{n_{ne,1L}}{2}$. In contrast, for $k_BT > \Delta_{2R} - \Delta_{1L}$ (but $k_BT \ll \Delta_{1L} < \Delta_{2R}$ so that quasiparticles are not generated thermally) the non-equilibrium quasiparticles will tend to uniformly disperse in both layers, producing equal densities in both layers of a pad. For a volume ratio $\frac{\Omega_{2R}}{\Omega_{1R}} = \frac{\Omega_{2L}}{\Omega_{1L}} = 2$, this reduces the density of quasiparticles in region 1L to $\frac{n_{ne,1L}\Omega_{1L}}{(\Omega_{1L}+\Omega_{2L})} \cong \frac{n_{ne,1L}}{3}$ while increasing the density of quasiparticles in region 2R to $\frac{n_{ne,1R}}{3}$. The average density of quasiparticles at the junction is then $\frac{(n_{ne,1L}+n_{ne,1R})}{6}$. This quasiparticle density will be

smaller than the low temperature value of $\frac{n_{ne,1L}}{2}$, provided $n_{ne,1L} < 2n_{ne,1R}$, and will lead to a proportionally smaller loss rate. Thus we expect $T_{1,qp}$ may increase with increasing temperature T near $T \cong \frac{(\Delta_{2R}-\Delta_{1L})}{k_B}$.

Figure 5. 3 shows an illustration of the temperature dependence of $T_{1,qp}$ for the case $\Delta_{1L} < \Delta_{2R}$ in different limits, along with the cases $\Delta_{1L} = \Delta_{2R}$ and $\Delta_{1L} > \Delta_{2R}$ for comparison. As seen from the plot, by exchanging the value of the energy gaps $\Delta_{1L} \leftrightarrow \Delta_{2R}$, the predicted low temperature $T_{1,qp}$ for the case $\Delta_{1L} > \Delta_{2R}$ is boosted by a factor of 5 compared to the case $\Delta_{1L} < \Delta_{2R}$. I note that this prediction may have been confirmed in a transmon made with gap engineered aluminum [62].

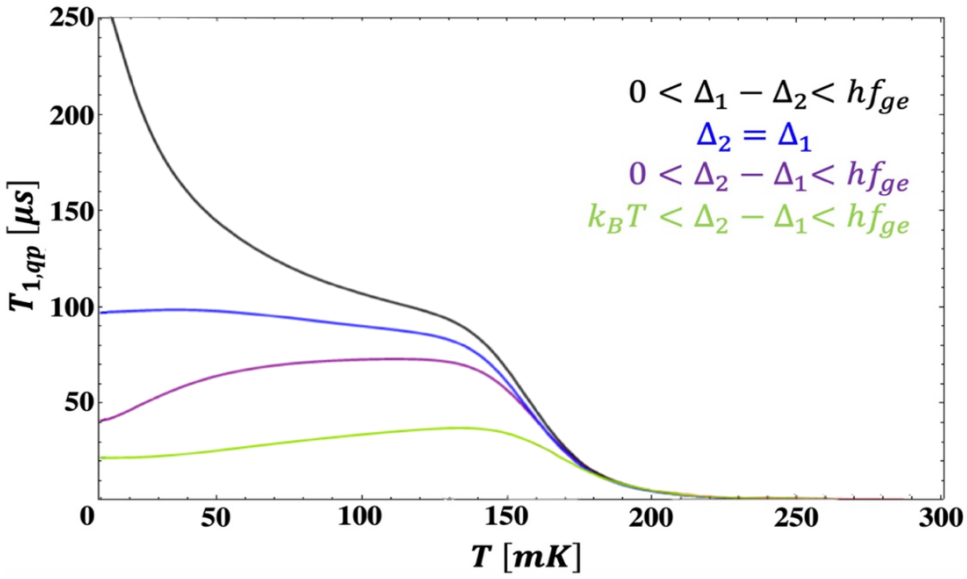

Figure 5. 3 Illustration of the temperature dependence of $T_{1,qp}$ for the case $\Delta_{1L} < \Delta_{2R}$ when $0 < \Delta_{2R} - \Delta_{1L} < hf_{ge}$ (purple), $k_B T < \Delta_{2R} - \Delta_{1L} < hf_{ge}$ (green), $hf_{ge} \ll \Delta_{2R} - \Delta_{1L}$ (pink), along with the cases $\Delta_{1L} = \Delta_{2R}$ (blue) and $\Delta_{1L} > \Delta_{2R}$ (black) for comparison.

5.3. Spatial Gap Inhomogeneity in Coplanar Waveguide Resonator

In Section 10.4, I discuss my observations of loss in a TiN thin film resonator deposited by plasma-assisted molecular beam epitaxy (PAMBE) [65]. As the temperature is increased from 30 mK to 600 mK, the Q_I of the resonator increased by a factor of 2. The resulting plot of Q_I versus T looks qualitative similar to my plots of T_1 versus T for the transmon. This suggested that a common mechanism may be at work. While further discussions on the experimental aspects will be discussed in later chapters, here I focus on modelling the phenomena as resulting from the behavior of non-equilibrium quasiparticles.

5.3.1. Modeling Quasiparticle Density

To model the loss and change in resonant frequency of a CPW resonator, I assume the TiN superconductor has two superconducting regions of volumes Ω_1 and Ω_2, and corresponding superconducting energy gaps Δ_1 and Δ_2. At a low enough temperature, quasiparticles accumulate in the lower gap Δ_1 region, increasing the quasiparticle density in that region and resulting in more loss per energy stored in that region of the device. As the temperature is increased, the non-equilibrium quasiparticles begin to have enough thermal energy to diffuse into the higher gap Δ_2 region, leading to a decrease in the quasiparticle density in region 1. The difference $\Delta_2 - \Delta_1$ in the two gaps sets the behavior at the lower temperature.

Consider the geometry of a CPW resonator (see Figure 5. 4), a possible situation that could produce the temperature behavior observed in my CPW resonator would be to have a lower energy gap Δ_1 at the surface of the CPW center conducting strip (see Figure 5. 5) and a higher gap Δ_2 in the interior. At the lowest temperature, quasiparticles accumulate in the low-gap surface, which is

where current flows, and this causes loss. Increasing the temperature allows non-equilibrium quasiparticles to diffuse into the higher gap Δ_2 interior of the strip, where there is less current, thus reducing the loss. The corresponding energy diagram is shown in Figure 5. 6, which can be translated into an effective temperature (see Figure 5. 7) using Parker's model (see Section 2.1.2.2). The superconducting current density is concentrated near the surface that takes up a large participation ratio of stored energy (see Section 4.4). Therefore, the microwave loss will be reduced if non-equilibrium quasiparticles diffuse into the higher gap region when temperature increases (see Figure 5. 8). The simulation of current distribution in the CPW geometry is discussed in Chapter 4.4. Here I restrict the attention to theoretical modelling for the loss.

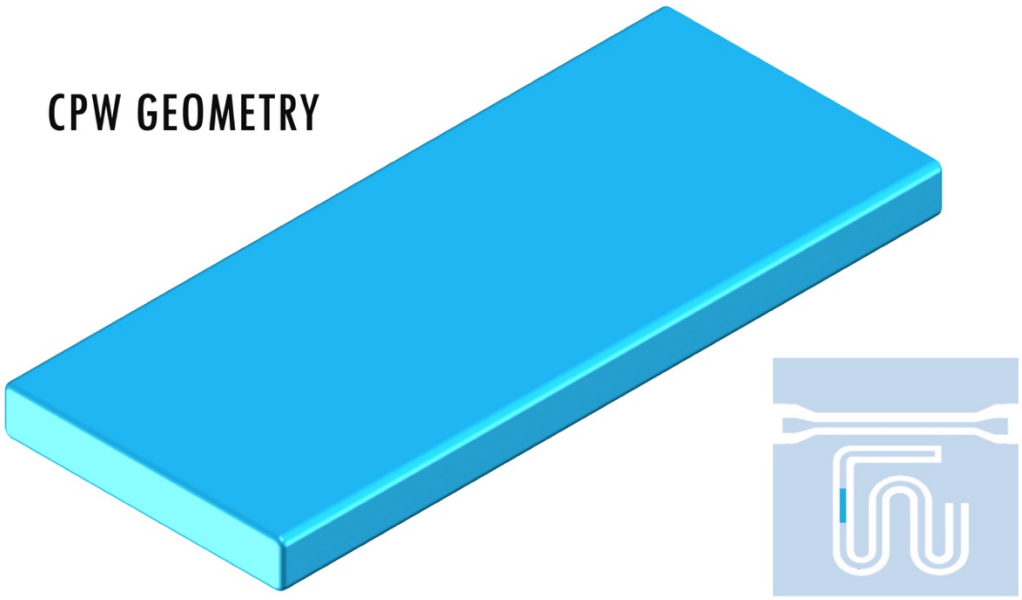

Figure 5. 4 Illustration of a section of the CPW resonator. A possible structure that could produce the temperature behavior observed in my CPW resonator corresponds to a lower energy gap Δ_1 region (blue) at the surface of the center conducting strip, and higher energy gap Δ_2 region (cyan) at the interior of strip.

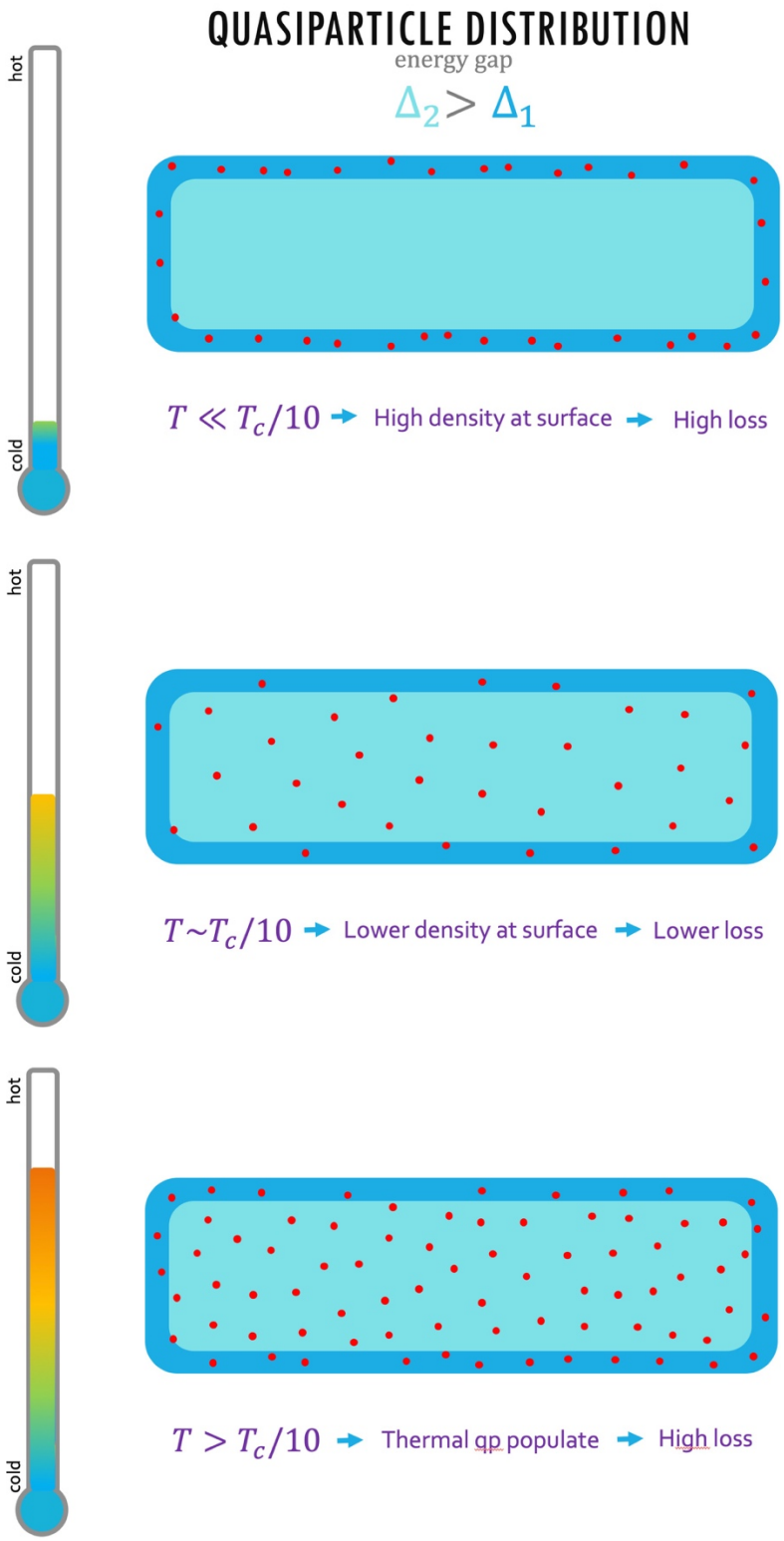

Figure 5. 5 Cross-sectional view of the CPW center stripe for $T \ll T_c/10$, $T \sim T_c/10$, and $T > T_c/10$. As the temperature rises, non-equilibrium quasiparticles diffuse into the higher gap Δ_2 region located at the interior of the strip.

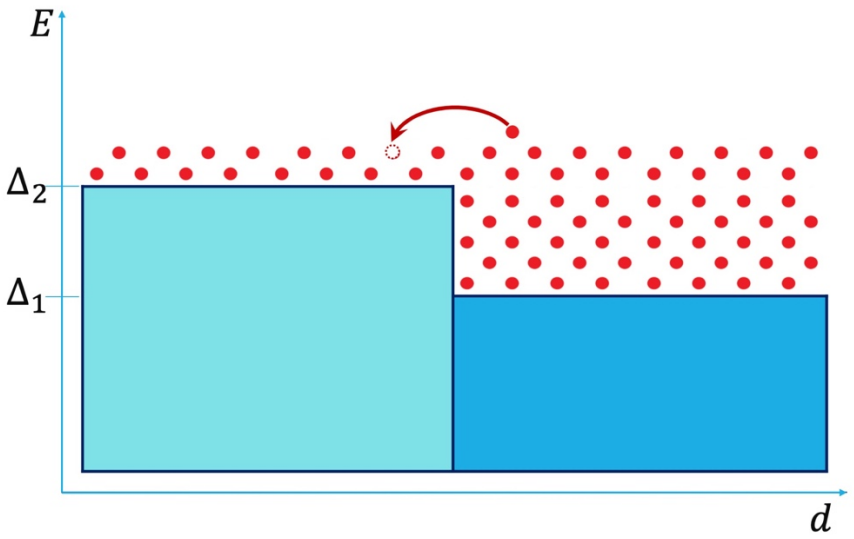

Figure 5. 6 Energy diagram corresponding to the non-equilibrium quasiparticle redistribution illustrated in Figure 5. 5. d is the distance from interior of the film, with higher gap Δ_2 region shown in cyan and lower gap Δ_1 region shown in blue. Quasiparticles are illustrated as red dots.

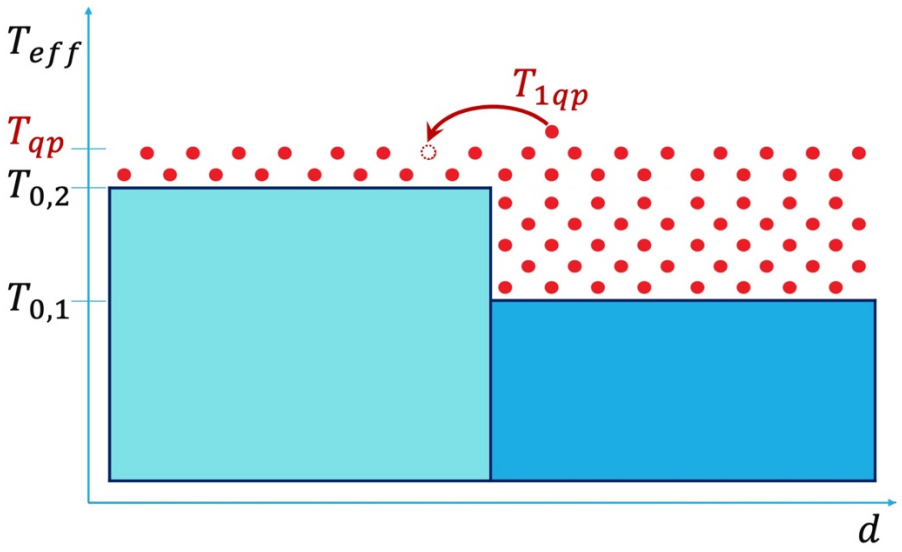

Figure 5. 7 A representation of the effective temperature T_{eff} from the Parker model, translated from the energy diagram shown in Figure 5. 6. The non-equilibrium quasiparticle densities are represented by an effective temperature T_{qp} and transfer of quasiparticles between the regions are represented as transfer of temperature quanta T_{1qp}.

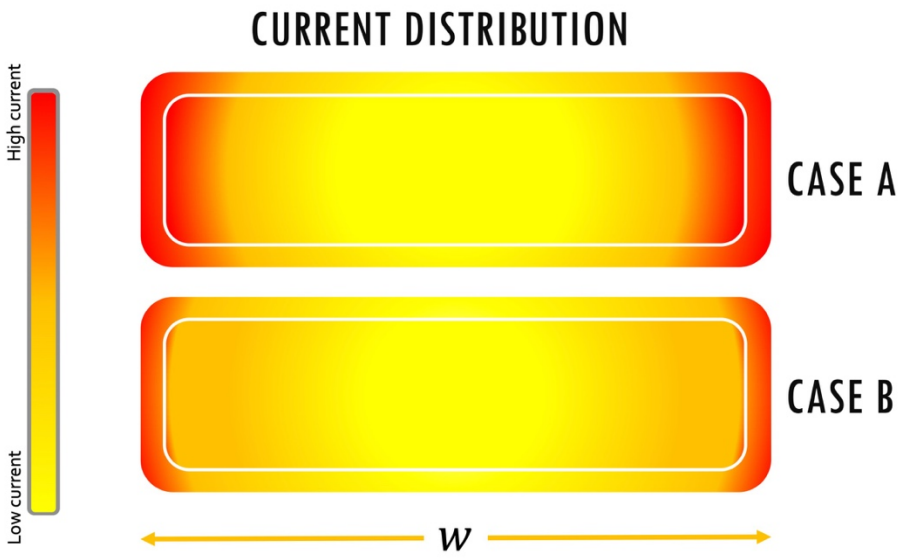

Figure 5. 8 Cross-sectional illustration of possible distributions of superconducting current density in a CPW. In case A, the superconducting current density is concentrated near the edges of the strip. The lower gap region near the surface has a large participation ratio. In case B, current is more concentrated and energy stored in interior is negligible.

To describe the temperature dependent distribution of quasiparticle densities $n_{qp,1}$ and $n_{qp,2}$ in the two regions with different superconducting energy gap, we need to solve （5. 1） and （5. 2）. Since the trapping dominated case is solved in the previous section in （5.25） and （5.26）, here I will show the derivation of the recombination dominated case. I start by assuming a constant (temperature independent) creation rate of non-equilibrium quasiparticles ($G_p A_i$ for region i) and a thermal quasiparticle generation rate ($G_{gi}\Omega_i$ for region i). These creation rates are balanced with the temperature-dependent quasiparticle recombination rates ($G_r \Omega_i n_{qp,i}$ for region i) and diffusion rate between the two regions ($G_{i\to j} n_{qp,i}$ for quasiparticles moving from region i to region j), where $n_{qp,i}$ is the density of quasiparticles in region i. Considering the net rate of change in the quasiparticle densities, I can write

$$\frac{dn_{qp,1}}{dt} = G_p A_1 + G_{g1}\Omega_1 - G_r\Omega_1 {n_{qp,1}}^2 - G_{1\to2} n_{qp,1} + G_{2\to1} n_{qp,2} = 0 \tag{5.51}$$

$$\frac{dn_{qp,2}}{dt} = G_p A_2 + G_{g2}\Omega_2 - G_r\Omega_2 {n_{qp,2}}^2 - G_{2\to1} n_{qp,2} + G_{1\to2} n_{qp,1} = 0 \tag{5.52}$$

$$\Longrightarrow \frac{dn_{qp,1}}{dt} + \frac{dn_{qp,2}}{dt} = G_p A_1 + G_{g1}\Omega_1 - G_r\Omega_1 {n_{qp,1}}^2 + G_p A_2 + G_{g2}\Omega_2 - G_r\Omega_2 {n_{qp,2}}^2 = 0. \tag{5.53}$$

Introducing an effective temperature T^* from Parker model (refer to Chapter 2.1.4.1) to describe the exchange of quasiparticles between the two regions gives

$$n_{qp} = 4N_0 \int_0^\infty \frac{d\epsilon}{1+e^{(E)/k_B T^*}} \approx 2N_0\sqrt{2\pi k_B T^* \Delta}\, e^{-\Delta/k_B T^*}. \tag{5.54}$$

Thus, the quasiparticle densities in the two regions can be expressed as

$$n_{qp,1} \approx 2N_0\sqrt{2\pi k_B T_1^* \Delta_1} e^{-\Delta_1/k_B T_1^*} \tag{5.55}$$

$$n_{qp,2} \approx 2N_0\sqrt{2\pi k_B T_2^* \Delta_2} e^{-\frac{\Delta_2}{k_B T_2^*}} = \sqrt{\frac{T_2^*\Delta_2}{T_1^*\Delta_1}}\, e^{\frac{\left(\frac{\Delta_1}{T_1^*}-\frac{\Delta_2}{T_2^*}\right)}{k_B}} n_{qp,1}\,, \tag{5.56}$$

where T_i^* is the effective temperatures for region i due to the presence of non-equilibrium quasiparticles. For two regions in diffusive contact, the condition for balanced energy transfer can be written as

$$\left(\frac{1}{2} ln\, T_1^* - \frac{\Delta_1}{k_B T_1^*} + \frac{\Delta_1}{k_B T}\right) = \left(\frac{1}{2} ln\, T_2^* - \frac{\Delta_2}{k_B T_2^*} + \frac{\Delta_2}{k_B T}\right). \tag{5.57}$$

This condition is equivalent to describe the quasiparticle transfer between the regions by assigning a common effective chemical potential μ to the quasiparticle distribution functions (see Section 5.2.1). Here, an effective temperature representation of the quasiparticles is adopted for

convenience in the simplification of the quasiparticle distribution function discussed in Chapter 2.1.4.1. In practice, I used condition (5.57) to eliminate T_1^* and T_2^* in (5.55) and (5.56).

I now consider the rate at which the number of quasiparticles change in region 1. In the steady state, (5.51) and (5.52) gives $dn_{qp,1}/dt = dn_{qp,1}/dt = 0$, thus for $\Delta_1 < \Delta_2$,

$$G_p A_1 + G_p A_2 + G_{g1}\Omega_1 + G_{g2}\Omega_2 - G_r\Omega_1 {n_{qp,1}}^2 - G_r\Omega_2 \frac{\Delta_2}{\Delta_1} e^{2(\Delta_1-\Delta_2)/k_B T} {n_{qp,1}}^2 = 0 \tag{5.58}$$

$$\Rightarrow n_{qp,1} = \sqrt{\frac{\frac{G_p A_1}{G_r \Omega_1} + \frac{G_p A_2}{G_r \Omega_1} + \frac{G_{g1}\Omega_1}{G_r \Omega_1} + \frac{G_{g2}\Omega_2}{G_r \Omega_1}}{1 + \frac{\Omega_2 \Delta_2}{\Omega_1 \Delta_1} e^{2(\Delta_1-\Delta_2)/k_B T}}} . \tag{5.59}$$

Consider the limit $T \to 0\ K$ where the thermal contributions become negligible ($G_{g1} = G_{g2} = 0$), (5.55) reduces to the non-equilibrium quasiparticle density $n_{neqp,1}$, thus

$$n_{qp,1}(T \to 0) = \sqrt{\frac{G_p}{G_r}\frac{A_1}{\Omega_1} + \frac{G_p}{G_r}\frac{A_2}{\Omega_1}} = n_{neqp,1} . \tag{5.60}$$

Next, consider the thermal equilibrium limit where the non-equilibrium quasiparticle production rate is zero ($G_p = 0$), we have

$$\frac{G_{1\to2}}{G_r} - \frac{G_{2\to1}}{G_r}\sqrt{\frac{\Delta_2}{\Delta_1}} e^{(\Delta_1-\Delta_2)/k_B T} = 0 . \tag{5.61}$$

$$\Rightarrow n_{qp,1} = \sqrt{\frac{G_{g1}}{G_r}} \sqrt{\frac{1 + \frac{G_{g2}\Omega_2}{G_{g1}\Omega_1}}{1 + \frac{\Omega_2 \Delta_2}{\Omega_1 \Delta_1} e^{2(\Delta_1-\Delta_2)/k_B T}}} = n_{th,1} . \tag{5.62}$$

Substituting the two limits in (5.60) and (5.62) into (5.59) yields the total quasiparticle density

$$n_{qp,1}(T) = \sqrt{\frac{n_{neqp,1}^2}{1+\frac{\Omega_2\Delta_2}{\Omega_1\Delta_1}e^{2(\Delta_1-\Delta_2)/k_BT}} + n_{th,1}^2}\,. \tag{5.63}$$

The same arguments goes for region 2, except $n_{neqp,2} = \sqrt{\frac{G_p}{G_r}\frac{A_2}{\Omega_2} + \frac{G_p}{G_r}\frac{A_1}{\Omega_2}}$ and $n_{qp,2}(T \to 0) \to 0$ as quasiparticles condense into region 1, which has a smaller gap. Similar derivation yields

$$n_{qp,2}(T) = \sqrt{\frac{n_{neqp,2}^2}{1+\frac{\Omega_1\Delta_1}{\Omega_2\Delta_2}e^{2(\Delta_2-\Delta_1)/k_BT}} + n_{th,2}^2}\,. \tag{5.64}$$

5.3.2. Calculating Resonator Q_I and f_0

The quasiparticle densities affect the energy dissipation and kinetic inductance of superconducting thin films, causing temperature dependent resonator Q_I and f_0. With the densities $n_{qp,1}(T)$ and $n_{qp,2}(T)$ derived in the preceding sections of this chapter, either for the trapping or recombination limited case, (4.39) and (4.41) can be written as

$$\frac{1}{Q_I} = \frac{2\alpha}{\pi N_0\sqrt{2\pi k_B}}\left(\frac{sinh(\xi_1)K_0(\xi_1)}{\sqrt{T_1^*}}\frac{1}{\sqrt{\Delta_1}}P_1 n_{qp,1} + \frac{sinh(\xi_2)K_0(\xi_2)}{\sqrt{T_2^*}}\frac{1}{\sqrt{\Delta_2}}P_2 n_{qp,2}\right), \tag{5.65}$$

$$\frac{\delta f_0}{f_0} \propto \frac{\alpha}{2}\left[1 - \frac{\sigma_n}{\sigma_2(T_{ref})}\frac{\pi\Delta}{\hbar\omega} + \frac{\sigma_n}{\sigma_2(T_{ref})}\frac{\pi\Delta}{\hbar\omega}\frac{1}{N_0\sqrt{2\pi k_B}}\left(\frac{e^{-\xi_1}I_0(\xi_1)}{\sqrt{T_1^*}}\frac{1}{\sqrt{\Delta_1}}P_1 n_{qp,1} + \frac{e^{-\xi_2}I_0(\xi_2)}{\sqrt{T_2^*}}\frac{1}{\sqrt{\Delta_2}}P_2 n_{qp,2}\right)\right]. \tag{5.66}$$

Here P_1 and P_2 are the fractions of inductive energy stored in regions 1 and 2, respectively, which in general can be different than $\Omega_1/(\Omega_1+\Omega_2)$ and $\Omega_2/(\Omega_1+\Omega_2)$. To significantly change the contribution to the loss in this model, the volume for region 2 must be large compared to region 1. Based on my TiN resonator data, the majority of the inductive energy is stored in region 1 of

smaller superconducting gap and volume. This means that $P_2 n_{qp,2} \sim 0$, so that the loss in region 2 can be neglected. Physically, this is qualitatively consistent with the edges and surfaces of the TiN resonator (where the RF currents are concentrated [110][231]) having a lower superconducting gap than the interior. See Section 4.4 for simulations of the RF current density in the CPW geometry.

Figure 5. 9 shows plots of Q_I, $\delta f_0/f_0$ and T^* versus T for the case $\Delta_1 < \Delta_2$, $\Delta_1 = \Delta_2$, and $\Delta_1 > \Delta_2$. As seen from these plot, by exchanging $\Delta_1 \leftrightarrow \Delta_2$, Q_I at low temperatures changes by a factor of > 5, and we see a similar trend as that shown for the transmon T_1.

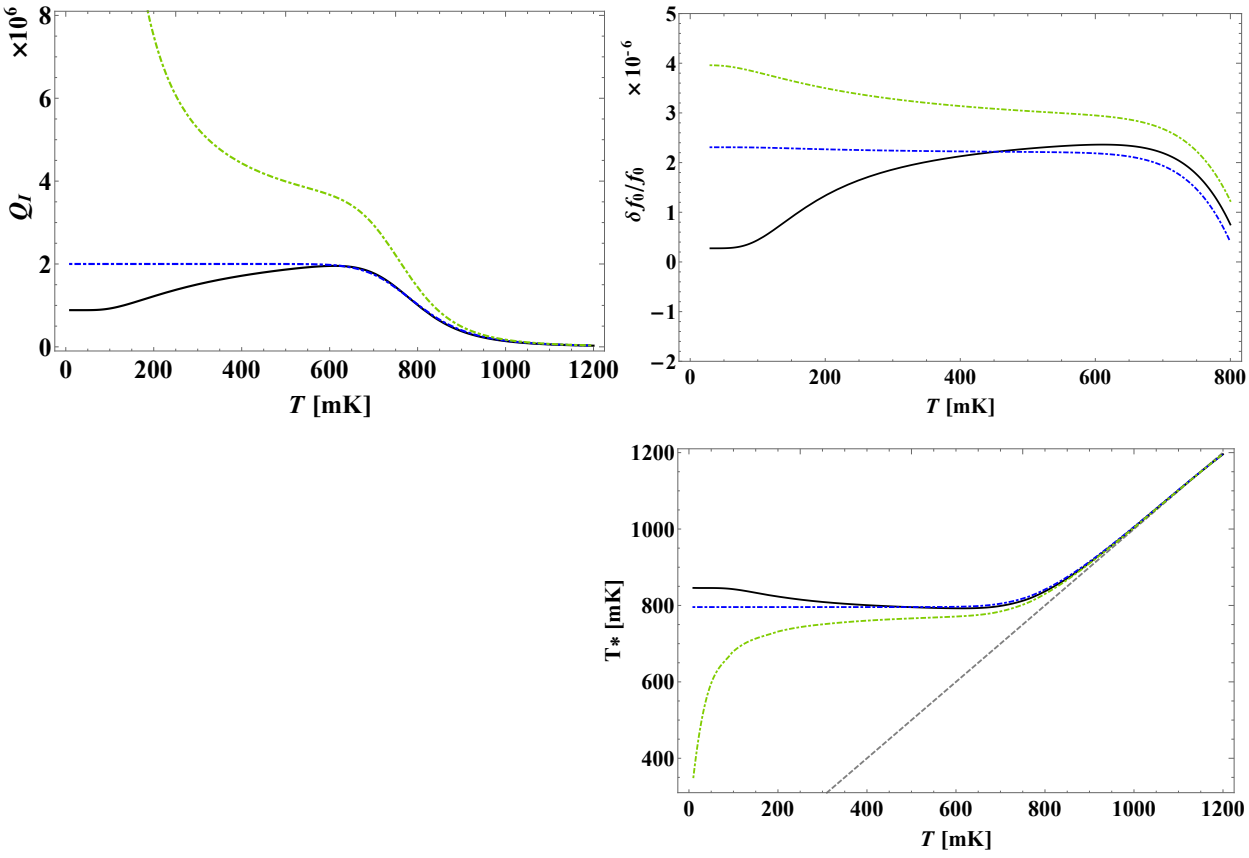

Figure 5. 9 Plot of the temperature dependence of Q_I and $\delta f_0/f_0$. In both plots, black corresponds to $\Delta_1 < \Delta_2$ with $\Delta_1 = 917.5$ μeV, $\Delta_2 = 897.6$ μeV, $\Omega_1/\Omega_2 = 0.1002$, $n_{neqp,1} = 160$ μm^{-3}, and $\alpha = 0.7009$. Blue corresponds to $\Delta_1 = \Delta_2$ with $\Delta_1 = \Delta_2 = 897.6$ μeV. Green corresponds to $\Delta_1 > \Delta_2$ with $\Delta_1 = 897.6$ μeV, $\Delta_2 = 917.5$ μeV.

CHAPTER 6

Building a Transmon

My transmon qubit had a 3-dimensional (3D) configuration [46]. This means the transmon was fabricated on a dielectric chip that was then inserted into a 3D microwave cavity made of superconducting aluminum, as in H. Paik's original design. This is in contrast to a 2D design where the transmon is coupled to an on-chip CPW or lumped-element resonator. The 3D design greatly reduces decoherence from resonator surface dielectric loss, thus potentially achieving a long lifetime, limited by other decoherence mechanisms such as non-equilibrium quasiparticles.

6.1. Design

6.1.1. Transmon Design

The design for my transmon is illustrated in Figure 6. 1, in which two metal pads act as shunting capacitor for the Josephson junction, and at the same time function as a dipole antenna to couple to the fundamental mode of the cavity. As studies have found that reduction of stray capacitance near the material interfaces (refer to Chapter 3.8.2) of complex structures correlates to prolonged qubit coherence time [132][206], my transmon design adopted a simple geometry with pad dimensions of $700\ \mu m \times 375\ \mu m \times 80\ nm$ [249][250], which gave $E_c/h \simeq 222$ MHz. The

transmon frequency was $|\omega_r - \omega_{ge}|/2\pi \sim 4$ GHz detuned from the cavity resonance, designed for a reduced effective coupling strength such that the Purcell contribution (refer to Chapter 3.8.1) to the relaxation time was small. A byproduct of the large detuning frequency is the considerably reduced dispersive shift χ. For ease of measurement with commercial instruments, the cavity resonance was set at ~8 GHz. To be in the transmon regime, I aimed for $E_J/E_c \to 40$, which implies a qubit frequency $f_{ge} \sim 4$ GHz, corresponding to a normal tunneling resistance $R_n \sim 17$ kΩ.

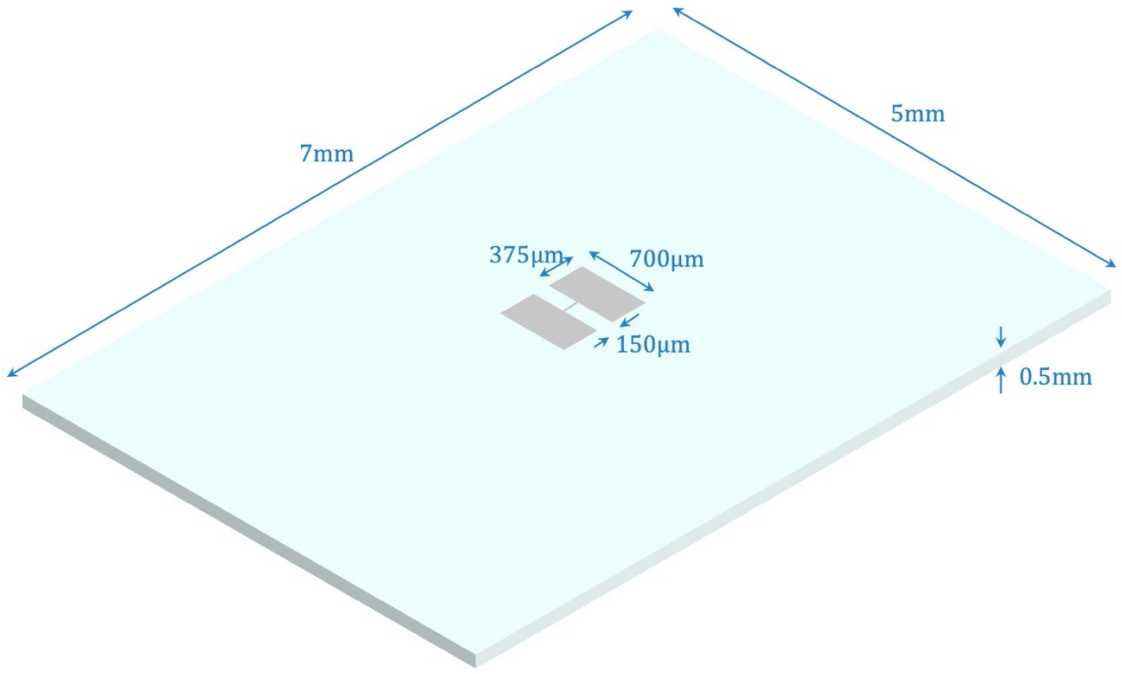

Figure 6. 1 Illustration of my transmon and chip dimensions. Figure not drawn to scale.

The transmon chip had a sapphire substrate with dimensions 7 mm × 5 mm × 0.5 mm, which was mounted in a 3D resonance cavity. About 90% of the electric field energy is stored in the substrate. Thus, the dielectric loss tangent of the substrate is critical. We adopted aluminum for the material of our transmon due to the ease of deposition and the ability to grow aluminum

oxide tunnel junction barriers. The commercially available high purity aluminum 99.999% pellets that we used produced high quality superconducting thin films. Alternative choices for the superconducting material including titanium nitride [48], niobium [251] and tantalum [252] were not used because of the difficulty in preparing suitable junctions.

6.1.2. Cavity Design

The design of the cavity that held the transmon was based on cavities developed by Dr. Sergey Novikov [250]. The geometry and dimensions of the cavity are illustrated in Figure 6. 2. The cavity supports a TE101 fundamental resonance mode with electric field parallel to the transmon dipole at frequency ~ 8 GHz [190]. Setting the cavity resonance higher than the qubit transition frequency reduces the Purcell effect from higher modes, thus enhancing the qubit coherence time. Aluminum was used for the cavity due to its low energy dissipation in the superconducting state. Two non-magnetic SubMiniature version A (SMA) feedthrough connectors were bolted to openings in the cavity for input drive and output readout [253]. The cavity coupling strengths to the respective ports were tuned by adjusting the length of the SMA center conducting pin that pokes into the cavity.

6.2. Microwave Simulations

The layout of the transmon chip and cavity were drawn using computer-aided design (CAD) software AutoCAD [254] and imported into finite element simulation software Ansys HFSS [255] or COMSOL Multiphysics [232] for microwave simulations. Material attributes were imported

from the material libraries with loss tangent of the substrate set to $\tan\delta \sim 10^{-7}$ - 10^{-8}. The superconducting regions for both the 3D cavity and transmon pads were set to be perfect conductors. Surface meshing sizes were typically restricted with maximum meshing length $<$ 5 to 10% of the wavelength propagating in the object (see Figure 6. 3).

Figure 6. 2 CAD drawing of (a) cavity top, with slits to hold the transmon chip, and (b) cavity bottom.

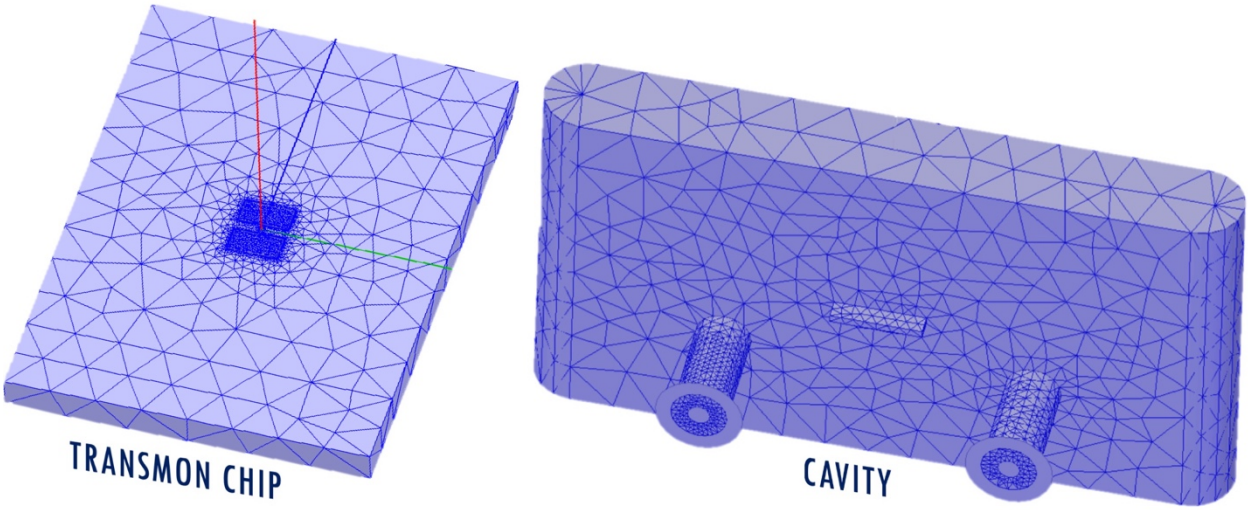

Figure 6. 3 Surface meshing for the transmon chip (left) and cavity interior (right), with maximum meshing length restricted to < 5 to 10% of the wavelength propagating in the object.

6.2.1. Extracting Qubit Parameters Via *Black Box Quantization*

An initial set of qubit parameter estimations were obtained using finite element simulations. Due to its speed at locating resonance frequencies, Ansys HFSS [255] is a good choice for finding the resonance frequencies and coupling for cavities and qubits. For simulation efficiency, the transmon was modeled as a 2D *perfect conducting surface* with zero thickness. The Josephson junction was modeled as a *lumped port* normalized to > 10 GΩ impedance to minimize resistive dissipation. The SMA connectors were modeled as coaxial *waveports* normalized to $50\,\Omega$ impedance to account for I/O coupling losses. The simulation was performed using the HFSS *driven modal* method with a frequency scan around the cavity and qubit resonances.

Black box quantization (BBQ) [256][257] is a semi-classical method for estimating the energy level structure of a coupled transmon-cavity system, in which the electromagnetic environment seen by the Josephson junction is treated as a black box with admittance $Y_{JJ}(\omega)$ connected in series with the junction. For my transmon design, the electromagnetic environment

seen by the Josephson junction was simulated and the self-admittance $Y_{JJ}(\omega)$ measured at the *lumped port* was extracted. I then used Mathematica [258] to interpolate between the simulated frequencies to obtain a smooth function. The total admittance of the Josephson junction was analytically written as

$$Y_J(\omega) = Y_{JJ}(\omega) + \frac{1}{i\omega L_{J0}} + i\omega C_J \,, \tag{6.1}$$

where C_J~80 fF and L_{J0}~$\Phi_0 h/2eE_J$ were obtained from estimations for the junction capacitance and Josephson energy. The cavity resonance ω_r corresponds to the pole in $Y_J(\omega)$, and the qubit frequency ω_{ge} is given by the frequency where $Y_J(\omega)$ crosses through zero. An example of the function $Y_J(\omega)$ is plotted in Figure 6. 4, with $\omega_r/2\pi = 7.7$ GHz and $\omega_{ge}/2\pi = 3.9$ GHz.

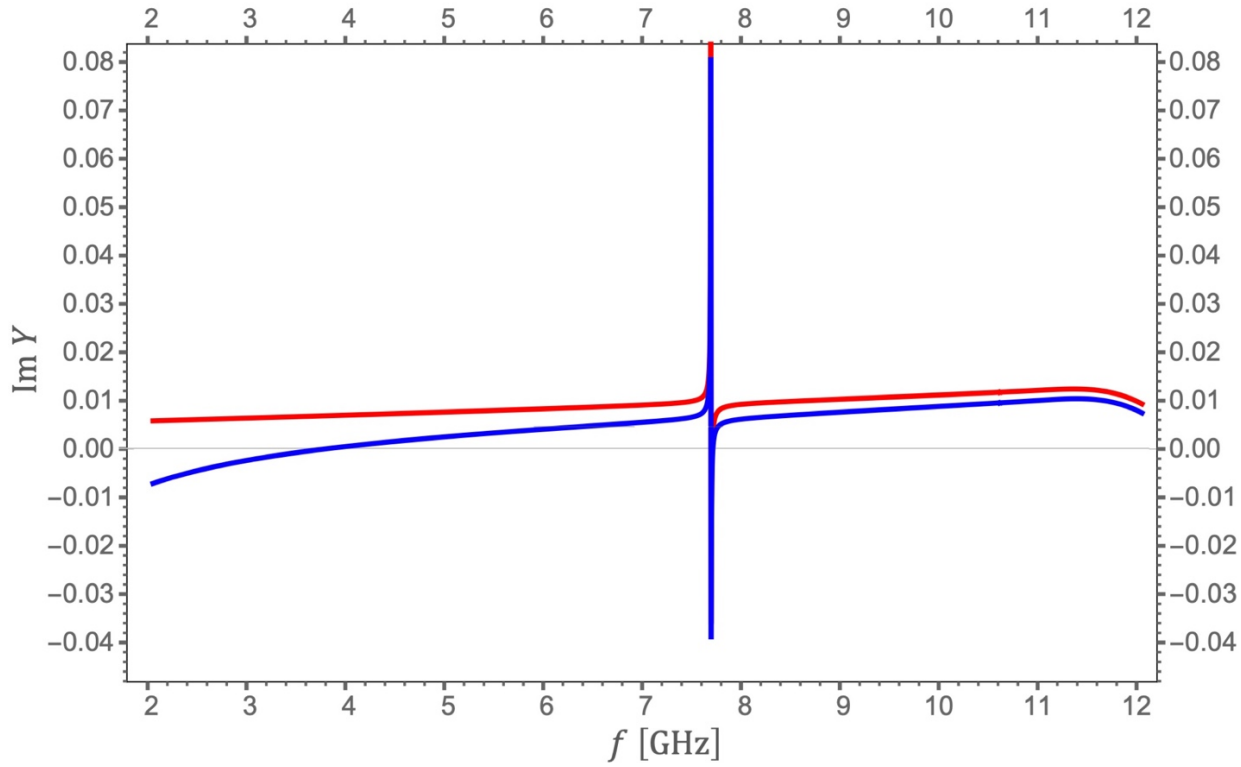

Figure 6. 4 Plot showing the imaginary part of junction admittance $Y_{JJ}(f)$ (red) and total admittance $Y_J(f)$ (blue) versus f. The pole at 7.7 GHz is the cavity resonance and $\mathrm{Im}Y_{JJ} = 0$ at 3.9 GHz corresponds to qubit frequency.

6.2.2. Extracting Dielectric Dissipation and Participation Ratio

To get a sense of expected transmon T_1 due to dielectric dissipation in various regions and interfaces in (3.77), I performed finite element simulations using COMSOL Multiphysics [232]. I found COMSOL is a better tool for simulating energy dissipation compared to HFSS due to issues regarding impedance matching. From my simulation results in particular, the *lumped port* (for simulation of Josephson junction) in COMSOL can be modeled as a port impedance connected in parallel to a voltage source for measurement (as illustrated in Figure 6. 5), thus setting a sufficiently large port resistance renders parasitic resistive loss negligible. In contrast, *lumped port* in HFSS is defined by a port impedance connected in parallel to a current source for measurement, thus setting the port resistance matching the environment impedance merely minimizes the parasitic resistive loss, which is also impractical to achieve.

Figure 6. 5 *Lumped port* in COMSOL is defined by a port impedance connected in parallel to a voltage source, while *lumped port* in HFSS is defined by a port impedance connected in parallel to a current source.

For simulation of small features, a thin layer of oxide (4 to 20 nm) was drawn at the material interfaces (see Figure 6. 6). The COMSOL stationary solver tolerance was balanced between the solving time and the convergence of the solution (see Table 6. 1). The Flexible Generalized Minimal Residual method (FGMRES) solver was used to help convergence and decrease the

simulation time, and the maximum number of iterative was set to a large number (*e.g.* 2×10^6).

To determine the contribution to T_1 from different material interfaces, the simulation was performed for different combinations of oxide layer thickness at the interfaces and $\tan\delta_i$. The transmon T_1 was calculated from the real and imaginary part of the junction admittance that was extracted from the COMSOL simulation by using [250]

$$T_1 = \frac{1}{2\mathrm{Re}\,Y_J(\omega)} \frac{\mathrm{dIm}\,Y_J(\omega)}{\mathrm{d}\omega}\Big|_{\omega=\omega_{ge}}. \tag{6.2}$$

The dielectric quality factor $Q_T \equiv \omega_{ge} T_1$ obtained from the simulation results of T_1 was found to be linearly proportional to the material thickness divided by the corresponding dielectric loss tangent $\tan\delta_i$ (see Figure 6. 7). This is expected qualitatively from the dielectric interface participation ratio (see Section 3.8.2), in the case, written as

$$\frac{1}{Q_T} \equiv \frac{1}{\omega_{ge} T_1} = P_{AS} \tan\delta_{AS} + P_{SC} \tan\delta_{SC} + P_{CA} \tan\delta_{CA}\,, \tag{6.3}$$

where P_i and $\tan\delta_i$ are the energy participation ratio and dielectric loss tangent for the corresponding interfaces of air-substrate (AS), substrate-conductor (SC) and conductor-air (CA), respectively. My simulations yielded $P_{AS} \simeq 2P_{SC} \simeq 40P_{CA}$, in qualitative agreement with the electromagnetic energy concentration in the corresponding regions. My transmon was made of aluminum on a sapphire substrate. I found that a 4 nm layer of Al_2O_3 with $\tan\delta_{CA} = 10^{-3}$ yielded $T_1 = 5$ ms. This suggest that the oxide on the conductor-to-air interface is unlikely to be the limiting loss for my transmon T_1. In contrast, the simulation of a transmon on a silicon substrate with 4 nm layer of oxide on the substrate surface yielded $T_1 = 69$ μs, whereas removing the oxide from between the transmon and substrate (SC interface) improved the relaxation time to $T_1 = 145$ μs.

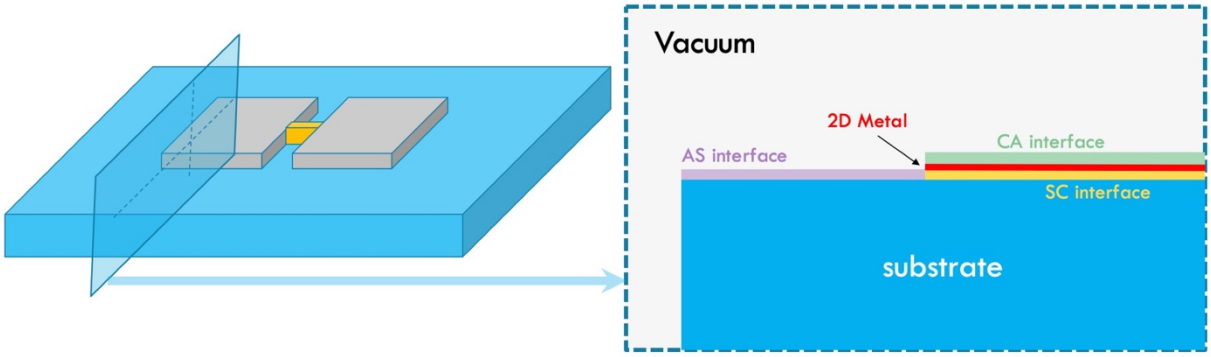

Figure 6. 6 A thin layer of oxide was drawn at the material interfaces of air-substrate AS (purple), substrate-conductor SC (yellow) and conductor-air CA (green). Blue is the substrate and red is the 2D metal layer.

Table 6. 1 Oxide thickness versus stationary solver tolerance.

Oxide [nm]	tolerance
none	10^{-3}
5	10^{-4}
10	10^{-5}

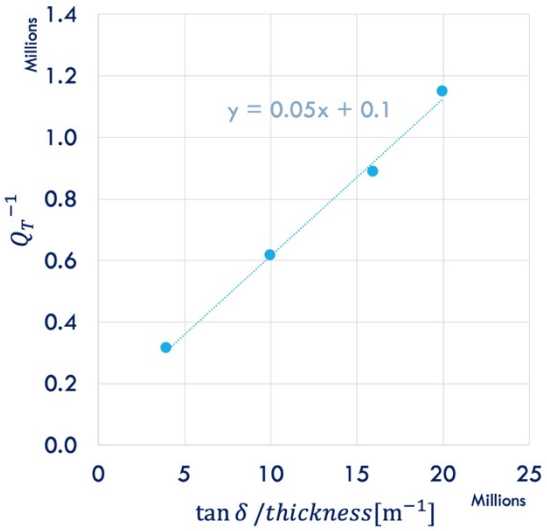

Figure 6. 7 Inverse of dielectric quality factor $Q_T \equiv \omega_{ge} T_1$ obtained from simulation results was found to be linearly proportional to loss tangent $tan\,\delta_i$ (10^{-7} to 10^{-3}) divided by the dielectric thickness (4, 10, 16, 20 nm). Similar trend applies to the all the interfaces and simulation yields $P_{AS} \simeq 2P_{SC} \simeq 40P_{CA}$.

6.3. Fabrication

In order to obtain transmons that have long relaxation times, good fabrication practices are necessary. Dust, native oxide between the superconductor and substrate, contaminants, impurities and lattice mismatching in material may lead to short coherence times. To reduce contamination, *in situ* fabrication is preferred. For my devices discussed in the dissertation, all of the fabrication was performed at the Laboratory for Physical Sciences (LPS). In this section, I start with an overview of the fabrication techniques and proceed by giving detailed recipes for all fabrication steps and procedures.

6.3.1. Transmon Fabrication

One of the key challenges in making a good transmon is to create high-quality Josephson junctions. Some problems can be avoided by using *in situ* fabrication procedure utilizing native metal oxide as the tunnel barrier. This is one reason that aluminum is a natural choice for making transmons, with which small Josephson junctions can be conveniently made with the Niemeyer-Dolan suspended bridge technique [241]. The Dolan bridge in my structure is composed of a narrow strip of ZEP resist suspended on MMA resist, as illustrated in Figure 6. 8. This structure can be obtained by choosing a top layer resist that is less sensitive to electron beam (e-beam) exposure compared to the bottom layer. After writing the pattern via e-beam lithography, development of resist stack leaves a desired undercut in the bottom layer (see Figure 6. 9). The suspended top layer acts as a stencil mask, supported by the thicker undercut bottom layer. Two aluminum layers were then deposited at positive and negative angles ($\pm 12.5°$) of incidence to create an overlapped region under the bridge (see Figure 6. 10). In between the depositions, an

oxide layer was grown by bleeding pure oxygen into the deposition vacuum chamber at ~25 mTorr for 25 mins, creating a Josephson tunneling junction at the overlapped region under the bridge.

Figure 6. 11 shows a scanning electron microscope (SEM) image of one of my Josephson junctions. The area of the junction is about 100 nm × 108 nm. Such small junctions are very sensitive to electrostatic discharge (ESD) and ESD protections need to be taken to great lengths during handling or direct-contact probe measurements of the junctions. An SEM photograph of an ESD damaged junction is shown in Figure 6. 12. Since the offset of pattern from tuning the deposition angle is only ~100 nm, the larger features of the transmon are unaltered (as shown in the photomicrograph in Figure 6. 13).

For the transmons discussed in this dissertation, the bi-layer photoresist preparation for electron beam lithography was done by Dr. Sergey Novikov [250] in our group, while I completed the other fabrication steps. The sequential procedures and detailed recipes for the fabrication are covered in the subsequent sections.

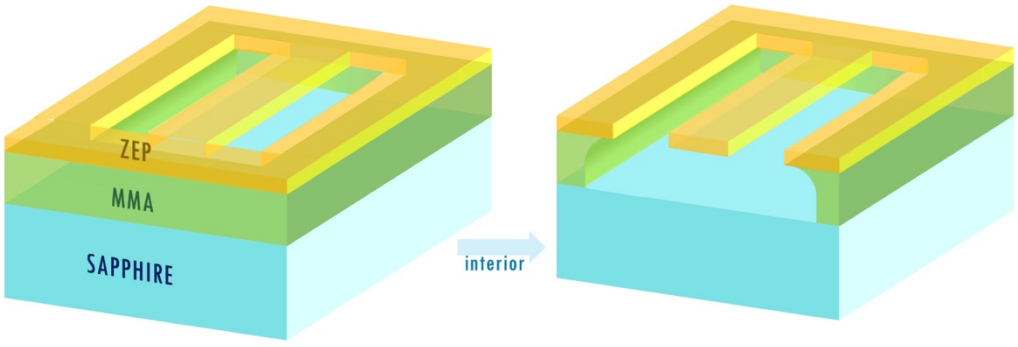

Figure 6. 8 Illustration of the Niemeyer-Dolan bridge composed of a narrow strip of ZEP e-beam resist (yellow) suspended on an etched layer of MMA (green).

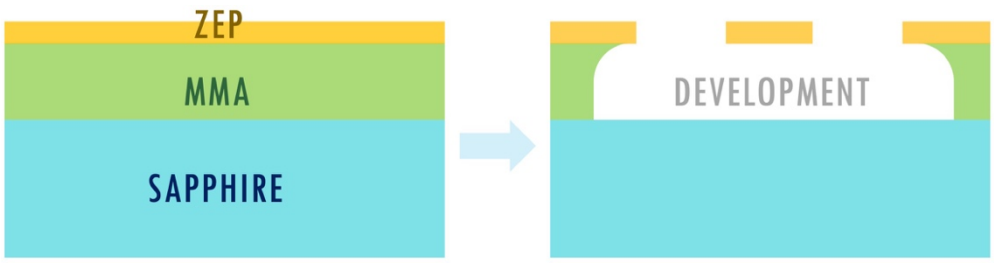

Figure 6. 9 Cross-sectional view of photoresist development. The top layer of ZEP (yellow) is less sensitive to e-beam exposure compared to the bottom layer of MMA, such that development of resist stack leaves an undercut in the bottom layer

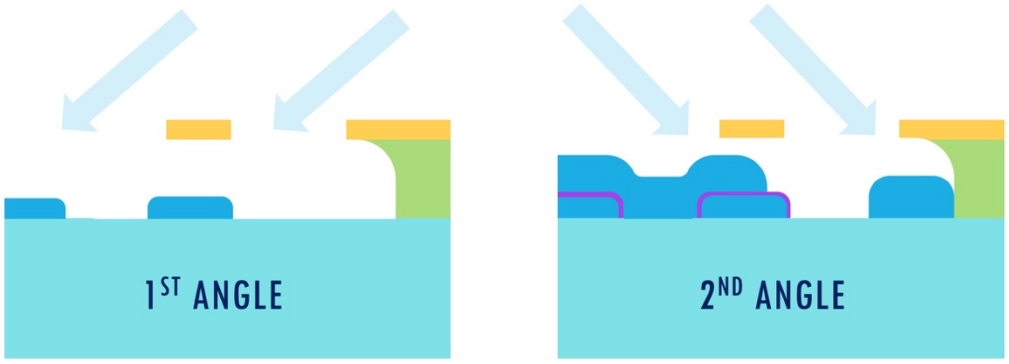

Figure 6. 10 Deposition of two superconducting film layers at positive and negative incidence angles (e. g. $\pm 12.5°$) creates an overlapped region under the bridge. Oxide layer grown in between the two depositions is shown in purple.

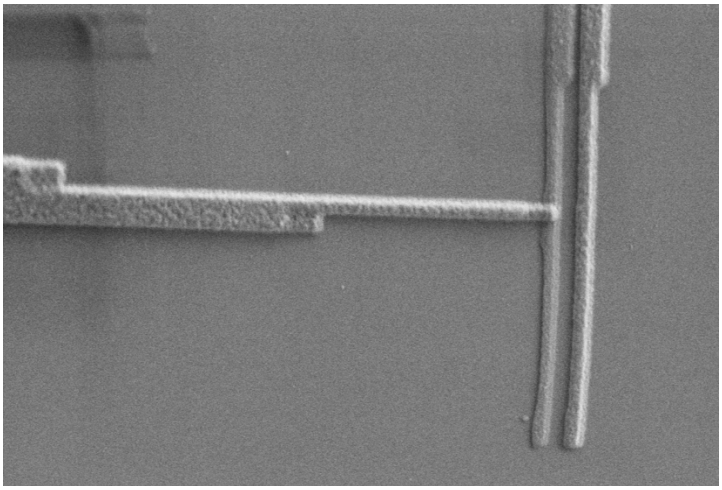

Figure 6. 11 Scanning electron microscope image of double-angle evaporated junction. The lateral dimensions of the junction are about 100 nm × 108 nm.

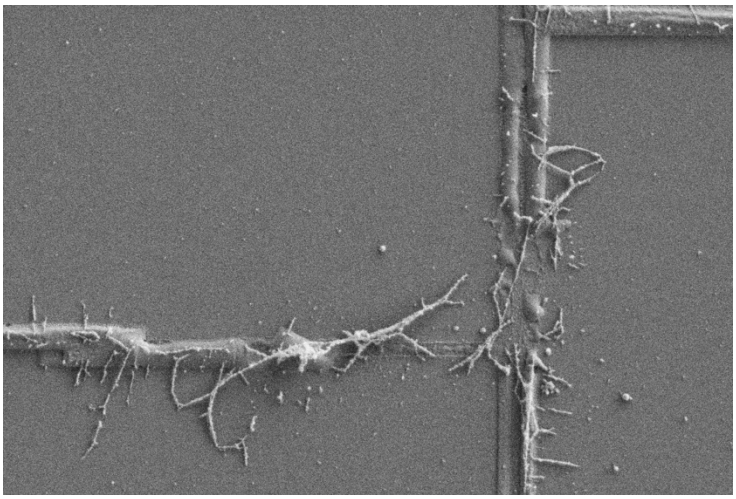

Figure 6. 12 SEM image of an ESD damaged junction.

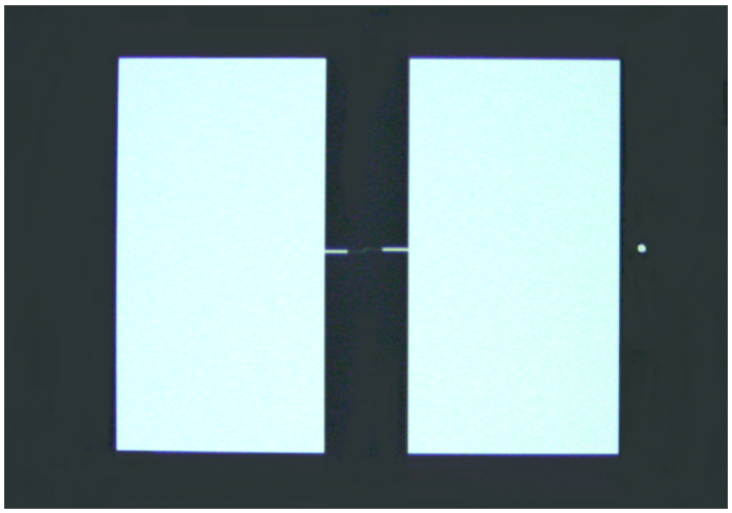

Figure 6. 13 Confocal optical micrograph of Al/AlOx/Al transmon. The dot to the right of the transmon is an SEM focusing spot.

6.3.1.1. Substrate Preparation

The substrate preparation for electron beam lithography was done in the LPS clean room as follows:

1. Obtain a 3” c-plane oriented sapphire wafer with single-side polish from Kyocera. Clean by rinsing with acetone, methanol, and isopropyl alcohol (IPA) in sequence and blow dry with nitrogen.

2. Spin a 900 nm layer of MMA(8.5)MMA EL11 (MicroChem) on the wafer at 1000 rpm for 60 s.

3. Bake for 5 min on a hot plate at 180 °C.
4. Let the wafer cool to room temperature.
5. Spin a 100 nm layer of ZEP 520A DR2.3 (Zeon Chemicals) at 5000 rpm for 60 s.
6. Bake for 5 min on a hot plate at 180°C.
7. Hard-bake the wafer in an oven at 180°C for at least 30 min.
8. Deposite a 10 nm thick anti-charging layer of Al using the thermal evaporator.
9. Spin a 5 µm thick protective layer of FSC-M (blue resist) at 2000 rpm for 60 s.
10. Bake for 5 min at 120 °C.
11. Apply tape to the backside of wafer.
12. Dice the wafer into 5 mm × 7 mm chips using a 2 inch hubbed resin-bonded diamond blade CX-010-325-080-H (Dicing Blade Technology) at 22,000 rpm spin-rate and 0.75mm/s feed-rate using the Disco DAD321 dicing saw.
13. Before e-beam writing, remove the FSC-M protective layer by rinsing in acetone for 40 s, followed by successive rinsing in methanol and isopropanol for 30 s each, then blow dry with nitrogen.

6.3.1.2. Electron-Beam Lithography

The electron beam writing was performed using a JEOL 6500F Scanning Electron Microscope (SEM). I partitioned the transmon pattern into three regions (see Figure 6. 14) and then wrote them in the order of increasing feature size:

1. Write the yellow region with 175 μCcm^{-2} dosage (~30 pA beam current) at magnification of 500×.
2. Write the cyan region with 100 μCcm^{-2} dosage at magnification of 500×.
3. Write the blue region with 100 μCcm^{-2} dosage (~2.5 nA beam current) at magnification of 70×.

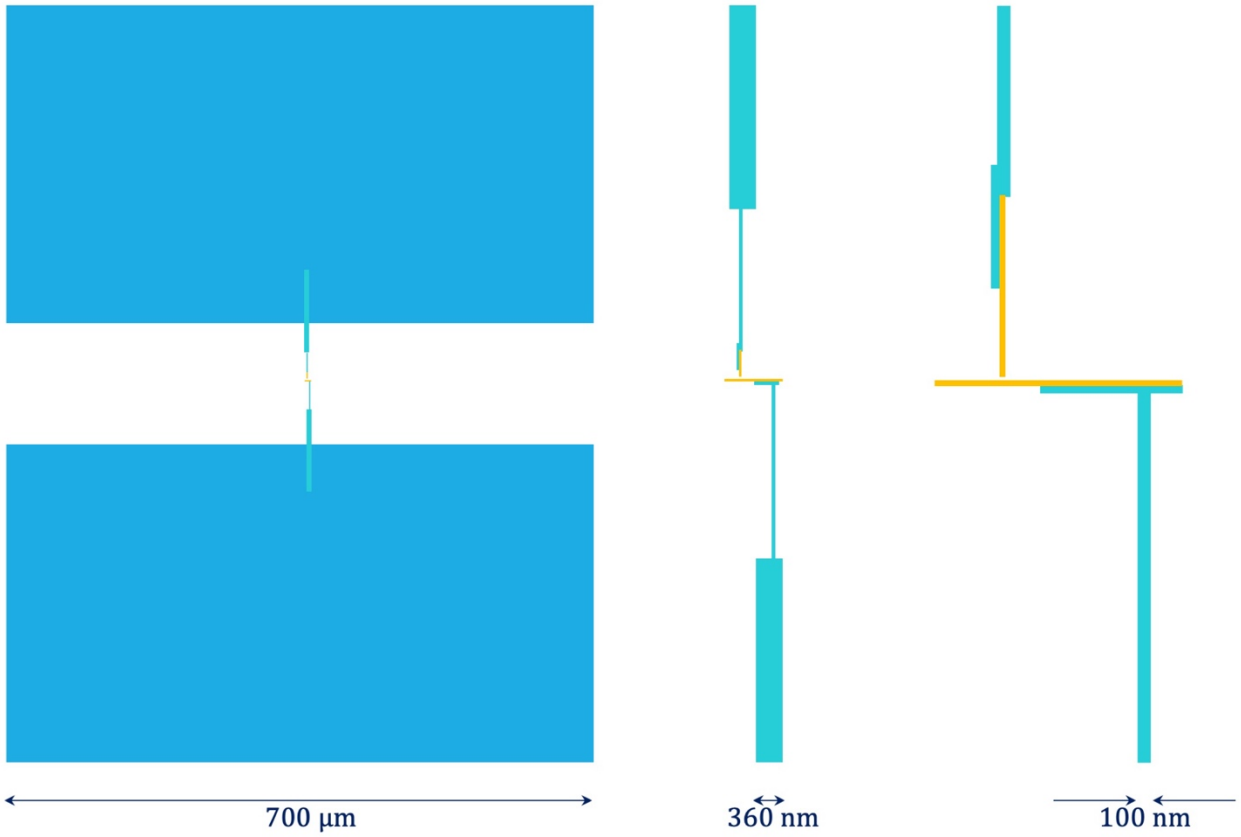

Figure 6. 14 The transmon pattern was partitioned into three regions and wrote in in order of increasing feature size: {yellow} → {cyan} → {blue}.

6.3.1.3. Development of e-Beam Pattern

1. Dip the chip in OPD4262 Positive Photoresist Developer to strip the Al anti-charging layer.
2. Rinse the chip in deionized (DI) water for 1 min, followed by 3 sec in isopropyl alcohol (IPA), and blow dry with nitrogen.
3. Dip the chip in amyl acetate for 2 min to develop ZEP 520A DR2.3. No apparent change will be observed with the naked eye.
4. Rinse the chip in IPA for 1 min and blow dry with nitrogen.
5. Dip the chip in 5:1 solution of IPA:DI for 4 min 20 sec to develop MMA(8.5)MMA EL11.
6. Rinse the chip in DI for 1 min and blow dry with nitrogen gun.

6.3.1.4. Double Angle Thermal Evaporation of Aluminum

1. Mount chip on sample holder and place in thermal evaporator. Vacuum pump the chamber with a Varian turbomolecular pump overnight to reach pressure $< 10^{-6}$ Torr with heating tape turned on to degas the chamber wall.

2. Turn off the heating tape and allow the chamber pressure to reach $< 10^{-7}$ Torr.

3. Using a tungsten boat filament loaded with 99.999% Al pellets, deposit the bottom layer of Al at an angle of $+12.5°$ to the normal at ~ 5Å/sec rate to get a thickness of 30 nm.

4. Oxidize the bottom Al surface at appropriate O_2 pressure and time to achieve the desired tunnel junction resistance (see Figure 6. 15). Vacuum pump the chamber immediately after desired oxidation time.

5. Deposit the top layer of Al at an angle of $-12.5°$ to the normal at ~ 5Å/sec rate to get a thickness of 50 nm, such that the overlapping region of the two layers forms a junction.

6. Passivate the top layer of Al by oxidizing the chip at ~ 247 mTorr O_2 pressure for ~ 30 min.

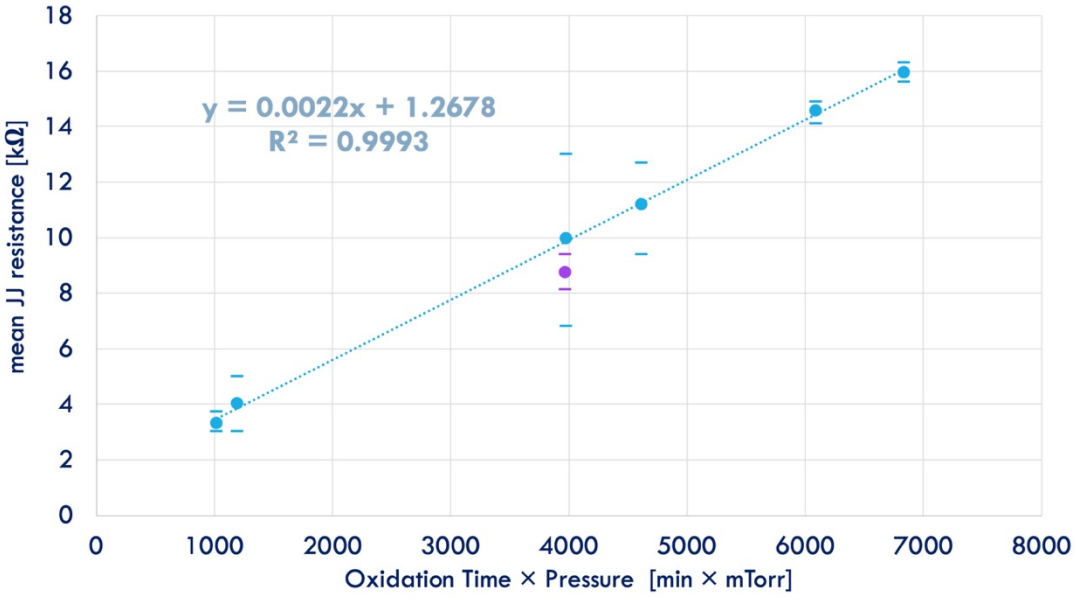

Figure 6. 15 Plot of the measured mean junction normal resistance R_n verses oxygen exposure time τ and pressure P_{oz}.

6.3.1.5. Excess Aluminum Lift-off

1. Half-fill a beaker with acetone and place the chip in it, facing down at 45° in a basket.
2. Since acetone evaporates quickly, cover the beaker with a concave glass lid.
3. Leave the setup for > 8 hrs until all residue has peeled off. If some fragments of aluminum are still attached to the chip, grab the chip face-down with tweezers and shake gently until the fragments come off. Do not take the chip out of the acetone before all residue comes off.
4. Remove the chip from the acetone with tweezers and immediately dip in a beaker filled with isopropyl alcohol (IPA). Shake the chip gently in IPA.
5. Remove the chip from the IPA and rinse with a stream of IPA from a squeeze-bottle.
6. Blow dry with nitrogen.

6.3.2. Cavity Fabrication

Starting from CAD drawings, the 3D cavity was machine milled out of AA 6063 aluminum alloy by the LPS machine shop. To ensure a high internal quality factor Q_I, the surface was carefully cleaned and polished using the procedures described in the following section.

6.3.2.1. Surface Polishing

1. Inspect the tapped holes and remove any residual debris with dental pick and tweezers.
2. Degrease parts using acetone, methanol and isopropyl alcohol (IPA) in an ultrasonic cleaner for 20 minutes in each bath.
3. Using a hot plate with spinner, heat Al etchant to approximately 50 ℃. Use extra PPE (gloves and googles) when working with the aluminum etchant.
4. Etch part for one hour. Once the piece is in the bath, rotate it with large tweezers rapidly a few times to remove any air trapped in the screw-holes.

5. Change to a second bath at 50 ℃ and etch for another hour. Rotate the piece rapidly a few times.
6. Rinse piece well using water and the spray nozzle for more than one minute. Ensure the screw-holes are thoroughly rinsed.
7. Place in baths of acetone, methanol and IPA. Rotate the piece rapidly a few times.
8. Rinse piece well using water and the spray nozzle for greater than one minute.
9. Dry immediately with nitrogen.
10. Place on 150 ℃ hot plate to evaporate any residual chemicals.

6.3.3. Device Packaging

Two non-magnetic SubMiniature version A (SMA) feedthrough connectors were bolted to the openings in the aluminum cavity to allow input drive and output readout lines to be attached. The cavity I/O coupling strengths Q_{in} and Q_{out} to the respective ports were tuned by adjusting the length of the SMA center conducting pin that pokes into the cavity [249]. A test transmon chip or bare sapphire chip can be installed in the cavity to accurately mimic the cavity dielectric environment while tuning the input and output coupling Qs. To obtain Q_{in} and Q_{out}, the in-phase and quadrature components of the transmission coefficient S_{21} were measured using the VNA setup (see Chapter 7.2) and fitted to the real and imaginary parts of the expression [249]

$$S_{21}(\omega) = \frac{2Q_I\omega\omega_r\sqrt{Q_{in}Q_{out}}}{(Q_{in}Q_{out} + Q_IQ_{in} + Q_IQ_{out})\omega\omega_r + iQ_IQ_{in}Q_{out}(\omega^2 - \omega_r^2)}, \quad (6.4)$$

where $\omega_r/2\pi$ is the cavity resonance frequency and Q_I is the internal quality factor.

After the tuning Q_{in} to ~9000 and Q_{out} to ~90000, the transmon chip was slid into the slots on the cavity and secured in place by stuffing the gap with indium. A photograph of the chip

mounted in cavity is shown in Figure 6. 16. The cavity was then sealed by bolting the lid to the cavity body uniformly after placing indium between the two parts.

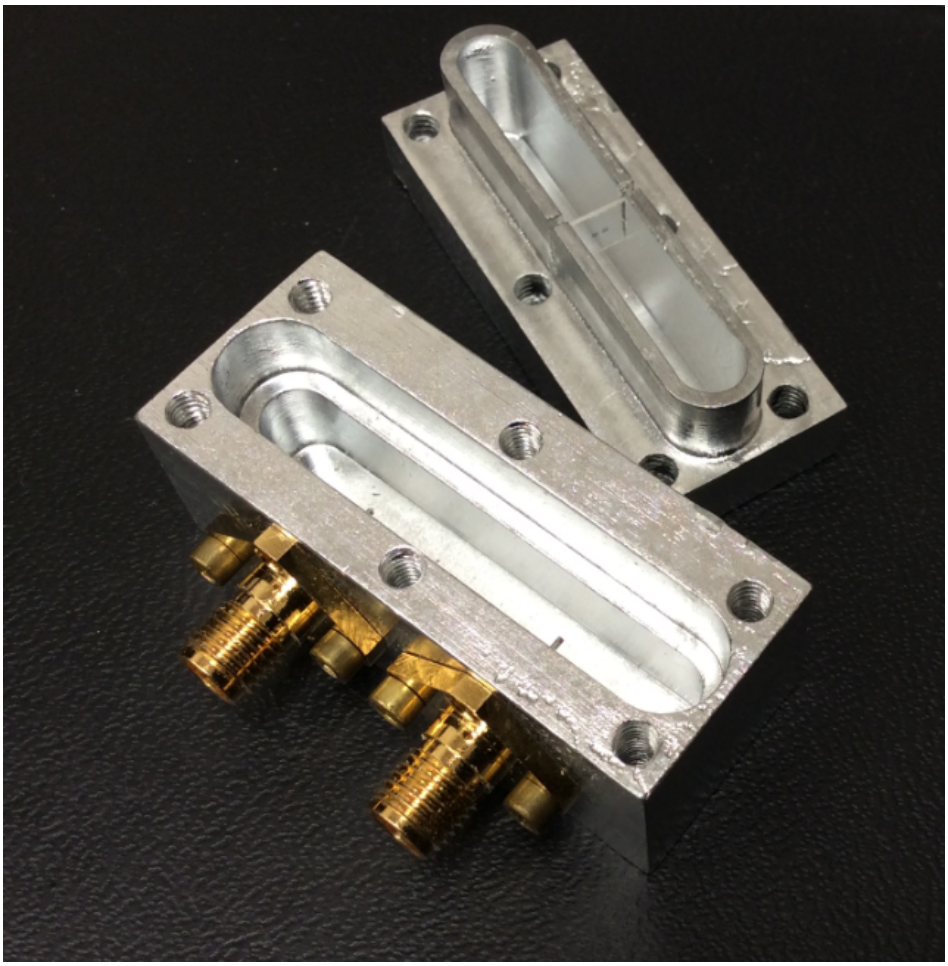

Figure 6. 16 Photograph of transmon chip mounted in the slots of the Al cavity. Note the SMA connectors bolted to the side of the cavity.

CHAPTER 7

Experimental Setup for Control and Measurement

To diminish thermal excitation of the qubit from the cryogenic environment, superconducting qubits are typically designed to operate in the regime

$$k_B T \ll \hbar\omega_q \ll 2\Delta\,. \qquad (7.1)$$

For $\omega_q/2\pi$~4 GHz, one finds a corresponding effective temperature of $T = \hbar\omega_q/k_B$~200 mK. Therefore, to reduce thermal fluctuations in the quantum system, the device needs to be cooled well below this temperature. To meet this criterion, I typically cooled my devices in a dilution refrigerator to temperatures of about 20 mK.

7.1. The Dilution Refrigerator Setup

The majority of my measurements were conducted in a Leiden CF-450 cryogen-free dilution refrigerator [259], which has a nominal cooling power of 450 μW at 120 mK. The refrigerator was situated in an RF-tight shielded room built from grounded copper walls. Electrical cables and vacuum lines required for refrigerator operations and experiments were fed through the shielded room walls. The gas handling system, compressor, and pumps were located in an adjacent

room with walls lined with rubber-sheeting for reduction of acoustic noise. Microwave lines were fed through another wall to the driving and measurement instruments.

The Leiden refrigerator has five cooling stages [250] operating at successively reduced temperatures: the outer-vacuum chamber at 300 K, the first pulse tube stage at 50 K, the second pulse tube stage at 3K, the *still* at 700 mK, the *cold plate* at 75 mK, and the mixing chamber at 20 mK. A photograph of the refrigerator stages can be found in Figure 7. 1. The first two stages are cooled by a Cryomech pulse tube cooler. The Leiden refrigerator has an aluminum outer vacuum can (OVC) that bolts to the 300 K stage plate and an inner vacuum can (IVC) that bolts to the 3K plate. Aluminum shielding cans wrapped in Aluminized Mylars layers were bolted to the pulse tube stages (50 K and 3 K), while gold-plated copper radiation shielding cans were bolted to the *still plate* (700 mK) and *cold plate* (75 mK). In addition to these standard shields on the CF-450, two Amumetal cryo-perm [260] magnetic shielding cans were bolted to the *mixing chamber* (MXC) plate, enclosing the device under test (DUT) thermally anchored to the *mixing chamber* stage. The standard operating procedures for cooldown and warmup can be found in Appendix B in [250].

To deliver microwaves to and from the device, semirigid microwave cables were used. At higher temperature stages, the signal cables are made of cupronickel, a material with large resistivity and therefore small thermal conductivity, to limit the heat conduction between stages. Niobium cables were installed between the cold plate (75 mK) and mixing chamber (20 mK). The input microwave signal was progressively attenuated with attenuators strategically placed at different temperature stages (see Figure 7. 2) to achieve a good noise temperature, producing more than 70 dB of total attenuation. It is worth mentioning that the 30 dB and 20 dB cryogenic attenuators at the cold plate and mixing chamber stages were custom-made by Dr. Jen-Hao Yeh from our group [188][189], designed for premier cooling-power and low noise temperature at

Figure 7. 1 Photograph of the CF-450 Dilution refrigerator taken by Dr. Shavindra Premaratne from our group [249]. The thermal shields and cryo-perm shields have been removed.

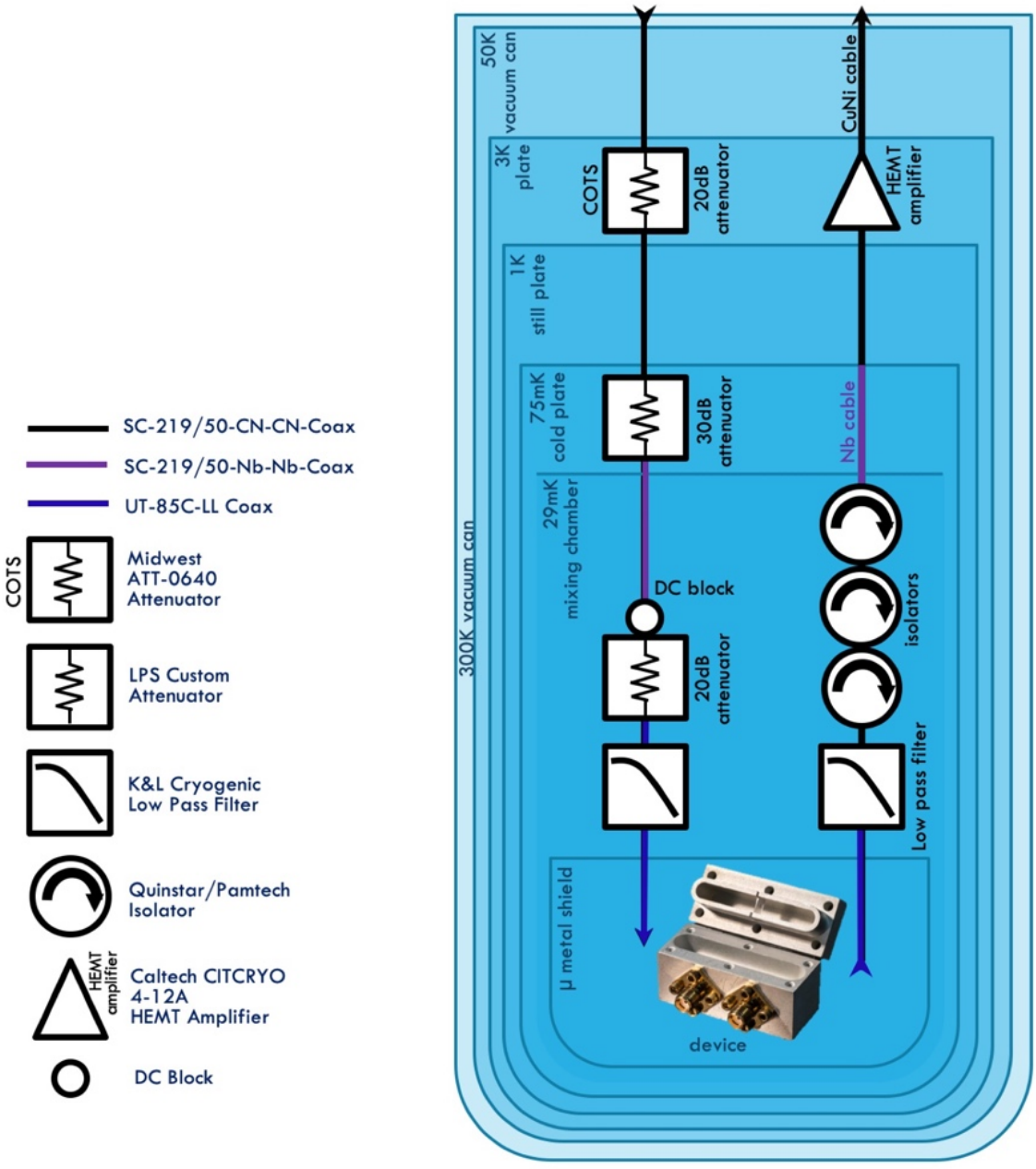

Figure 7. 2 Electrical layout of the dilution refrigerator measurement setup. Input microwaves are sent via cupronickel cables and attenuators placed at the temperature stages, producing ~ 70 dB of total attenuation. Niobium cables were installed between the cold plate (75 mK) and mixing chamber (20 mK) stages. The transmitted output signal from the cavity was fed through a series of microwave isolators on the mixing chamber before being amplified at 3 K by a low-noise HEMT [261]. Low-pass filters with a cut-off frequency of 12 GHz were mounted on the mixing chamber on the input and output lines.

cryogenic temperatures. This filtering allowed us to reduce thermal photons entering the cavity through the input transmission line and achieve a longer dephasing time T_ϕ [188][189]. The transmitted output signal from the cavity was fed through a series of microwave isolators on the mixing chamber before being amplified at 3 K by a low-noise HEMT [261]. Low-pass filters with a cut-off frequency of 12 GHz were also mounted on the mixing chamber on the input and output lines to reduce excitations of higher modes of the cavity. In my experiments, I raised the temperature of my devices by sending a fixed current to a 100 Ω heating resistor installed on the mixing chamber. The mixing chamber temperature as a function of the applied current is shown in Figure 7. 3.

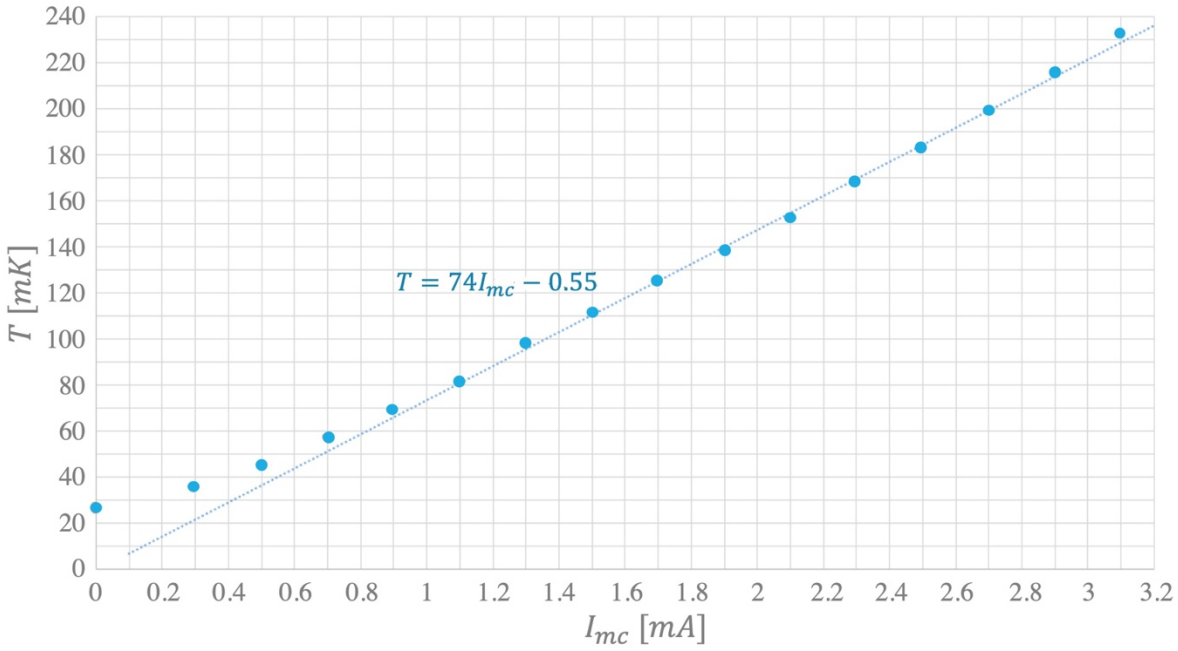

Figure 7. 3 Measured temperature of mixing chamber as a function of the heating current supplied to the heater coil on the mixing chamber.

7.2. Vector Network Analyzer

The preliminary characterizations of my transmon were done using an Agilent E5071C vector network analyzer (VNA) locked to a rubidium atomic clock. I used it to obtain the complex scattering parameters (S-parameters) [262] of both my transmon and TiN resonators. By sweeping the VNA driving frequency at low powers, the bare cavity/resonator resonance frequency could be located. By repeating the frequency sweeps at gradually incremented RF power, the bare cavity frequency ω_r and dressed cavity frequency $\widetilde{\omega}_r$ could be found (see Chapter 8.2), confirming the functionality of the qubit and providing an estimate for the dispersive shift $\chi_{ge} = \omega_r - \widetilde{\omega}_r^{|g\rangle}$.

7.3. Pulsed Qubit Control/Readout

Pulsed qubit control is required to initialize qubit states, implement microwave quantum logic gates, and perform coherence measurements. Here I provide an overview of the methodology and then discuss each specific setup in the subsequent subsections.

In my setup, two Agilent 33250A arbitrary waveform generators (AWGs) functioned as programmable digital switches to turn on/off the qubit (control) and cavity (readout) operation signals independently. The sequence and timing of the qubit operations were coordinated by triggering signals that were distributed to the instruments. Figure 7. 4 shows an example of a timing schematic for the triggering sequence. The resulting microwave signal pulse trains were routed through a Weinschel programmable attenuator and merged using two 6 dB MAC attenuators. The combined microwave drive signal was then filtered through a DC block and fed through the wall of the shielded room to enter the input line at the top of the dilution refrigerator.

Figure 7. 4 Timing diagram illustrating the coordination of the control and readout signal sequence. The cavity and qubit 33250A triggers have an offset time delay t_{delay} to account for the duration of the cavity readout pulse.

7.3.1. Synthesized Microwave Signal Generators

Spectroscopic measurements and simple qubit operations, involving sequential qubit rotations in the Bloch sphere or cavity probe tones, were implemented with Agilent E8257D/E8267D synthesized signal generators (SSGs). The SSGs were capable of outputting highly coherent continuous analog tones at a set frequency between 300 kHz and 20 GHz. It should be noted that the time between the trigger reception and pulse output was a minimum of 70 ns for the SSGs. When timing pulses from different SSGs with respect to each other, this delay had to be properly accounted for.

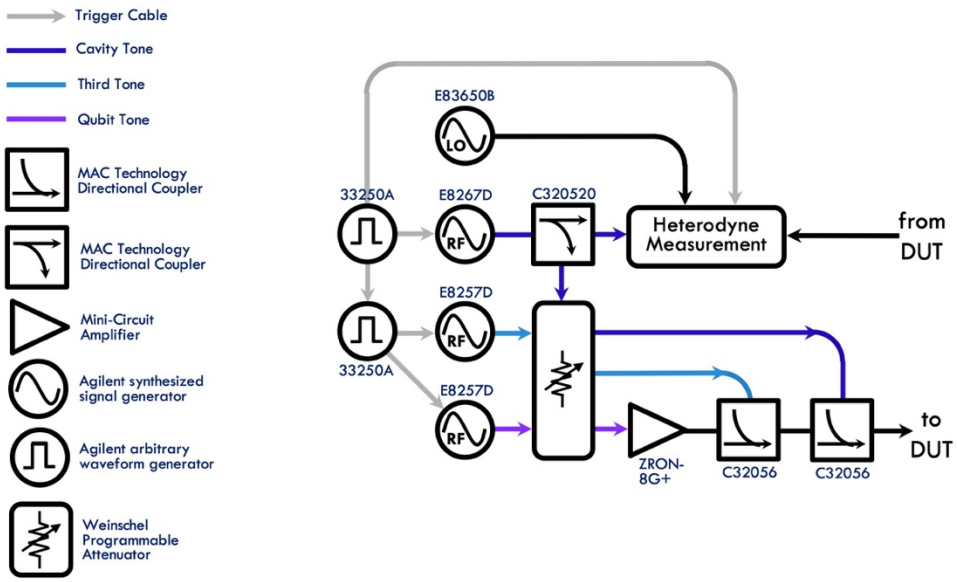

Figure 7. 5 Configuration of the trigger chain and connection of signal lines.

The Agilent 33250A cavity AWG was programmed to provide an initial trigger to both the cavity SSG E8267D and qubit AWG Agilent 33250A, which was then in turn used to trigger the qubit SSG E8257D. The cascade of triggering chain goes as follows: cavity SSG ← cavity AWG → qubit AWG → qubit SSG. Depending on the operation, a third SSG E8257D, either set in continuous or triggered mode, could be used to apply a third tone. A schematic illustrating the configuration of the trigger chain and connection of signal lines is shown in Figure 7. 5.

7.3.2. Arbitrary Waveform Generators

To generate complex qubit gates, an arbitrary waveform generator Tektronix AWG70002A was used to generate microwave pulse sequences. The instrument outputs discrete-time signals programmed to arbitrary pulse shape with up to a 320 ms pulse length (limited by the 16 GB memory) at a sampling rate of 25 GSa/s. A detailed discussion of the system can be found in the dissertation by Dr. Shavindra Premaratne [249].

7.4. Heterodyne Pulsed Measurement

Invented by Reginald A. Fessenden, heterodyne [263] refers to signal frequency created by mixing two closely spaced frequencies, thus shifting the resulting signal to a desired frequency range. The technique does not require extensive calibration for accurate I/Q measurements [250], and is insensitive to harmonic distortion and DC offsets. In my system, it was adopted to mix down the output microwave signal from the cavity tone at ω_{RF} with a local oscillator (LO) signal at ω_{LO}~ω_{RF} to yield an intermediate frequency (IF) at $\omega_{IF} = \omega_{LO} - \omega_{RF}$~1 MHz to 10 MHz suitable for pulsed digital detection, while the component at $\omega_{IF} = \omega_{LO} + \omega_{RF}$ was filtered out. An Agilent Acqiris 1082A digitizer board was used to measure the IF tone. The digitizer board has the capability of onboard averaging to increase efficiency and I routinely used this feature with ~ 6000 averages for ω_{IF}~10 MHz when performing measurements. The in-phase and quadrature (I/Q) components of the RF signal were extracted from the measured amplitude and phase of the IF signal via I/Q demodulation algorithms performed in LabVIEW. A schematic of the heterodyne circuitry is shown in Figure 7. 6, and the circuitry of the full system is traced out in Figure 7. 7.

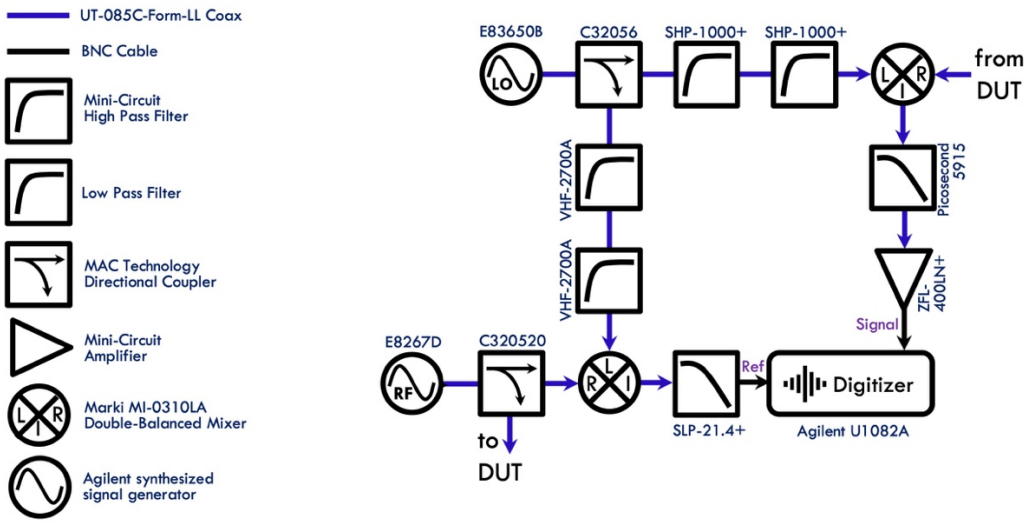

Figure 7. 6 Components and layout of the heterodyne circuitry.

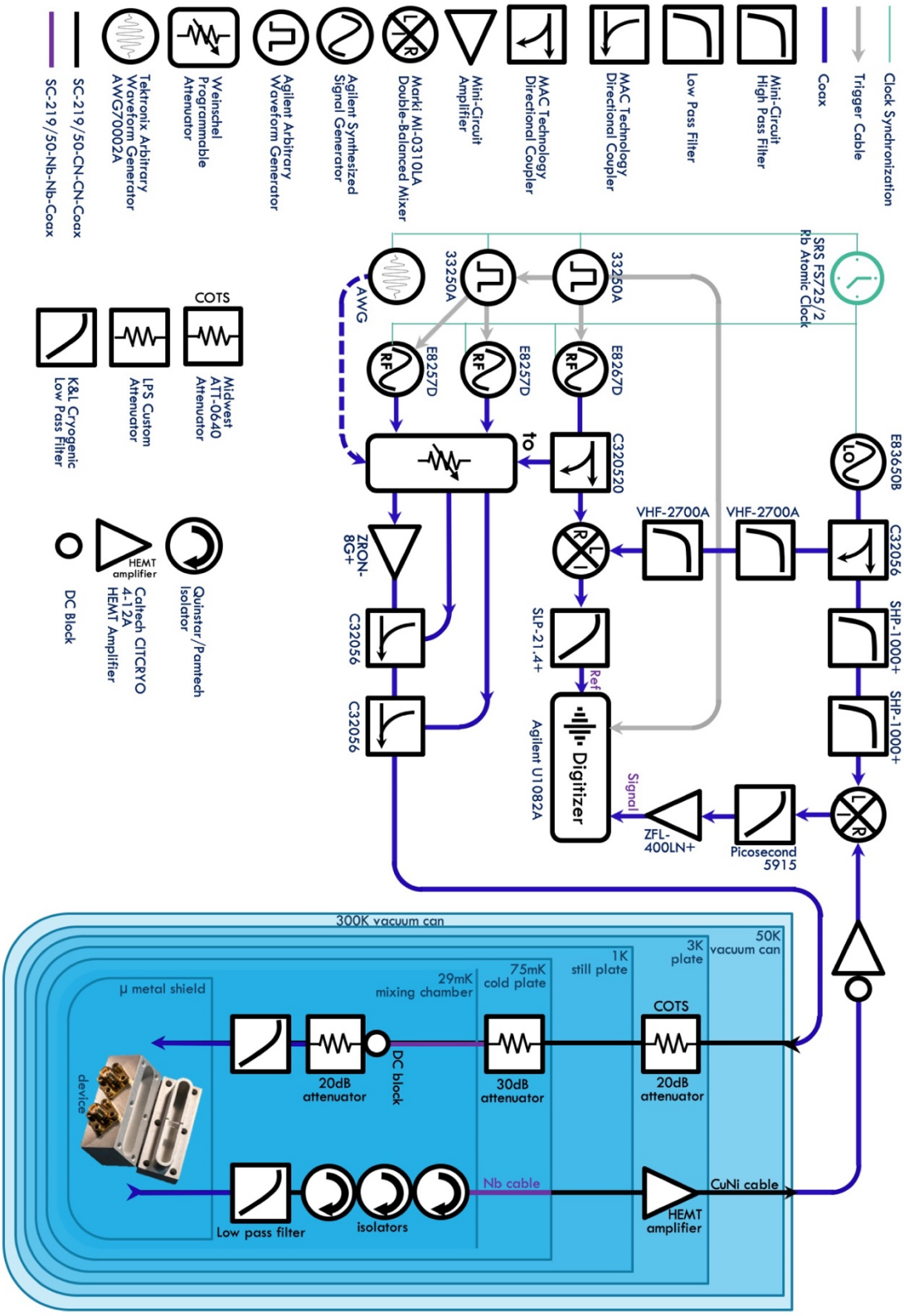

Figure 7. 7 Schematic tracing out the circuitry of the full system.

7.5. Optical Fiber Installation for Resonator Measurement

My experiments on the TiN resonators were performed in the same dilution refrigerator as that I used for the transmon measurements (refer to Section 7.1). To inject non-equilibrium quasiparticles into the resonators, I illuminated the device with IR light via an SMF-28 optical fiber [264]. Light from a 1550 nm IR laser [265] was sent through a few optical attenuators [266] at room temperature and then a fiber coupler. One of the resulting beams was used for power monitoring and the other was coupled to the fiber and used to illuminate the device. I ran the fiber through a vacuum Swagelok feedthrough [267] to reach the refrigerator vacuum space. The fiber was coiled up around a caged mandrel made of copper with a diameter of 20 mm mounted on the 3 K stage to reduce long wavelength blackbody radiation from being transmitted down the optical fiber to the device. There was no detectable heating on the refrigerator from installation of the optical fiber and injecting optical power in a connected fiber into and out of the refrigerator. At the mixing chamber, the fiber was cleaved and glued to a hole in the lid of the resonator package, nominally centered over one of the resonators. The cleaved fiber was placed approximately 1.6 mm over the resonator and based on the numerical aperture of the fiber, a Gaussian beam diameter of 250 μm was estimated at the chip. Figure 7. 8 shows a schematic of the setup and Figure 7. 9 shows a photograph of the fiber connection.

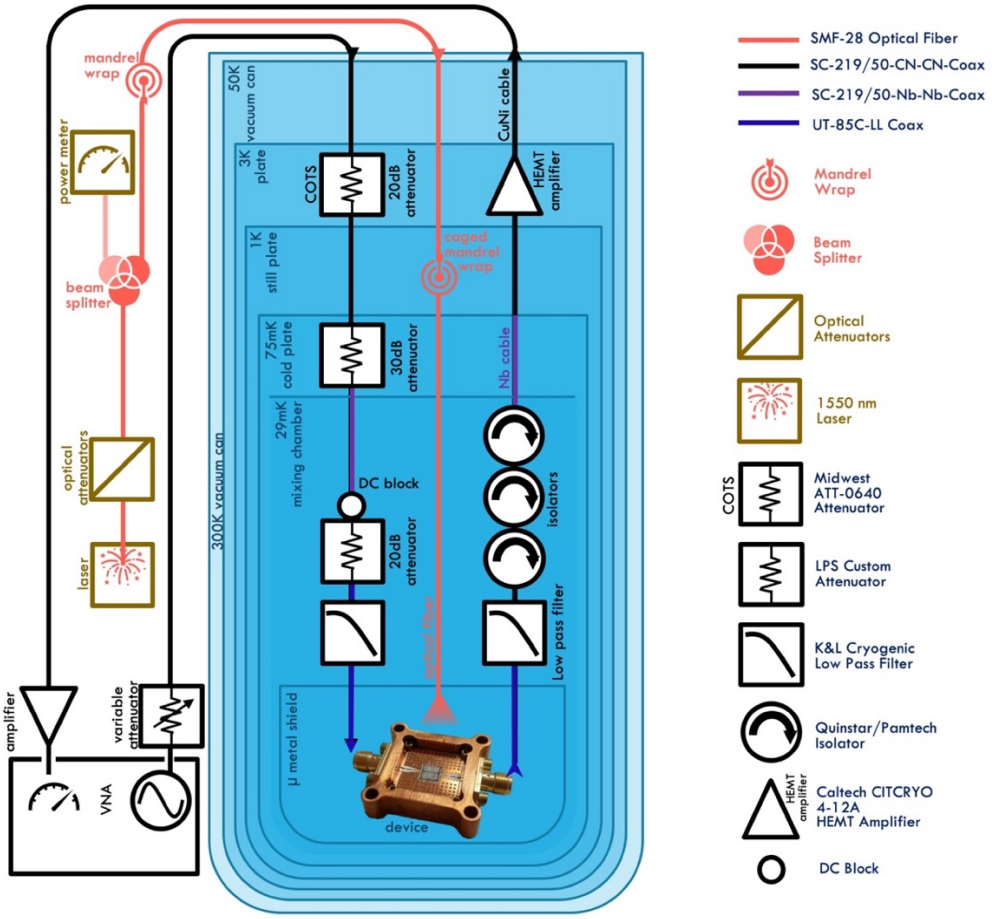

Figure 7. 8 Optical measurement setup has an additional SMF-28 optical fiber installed to illuminate the TiN resonators with IR light.

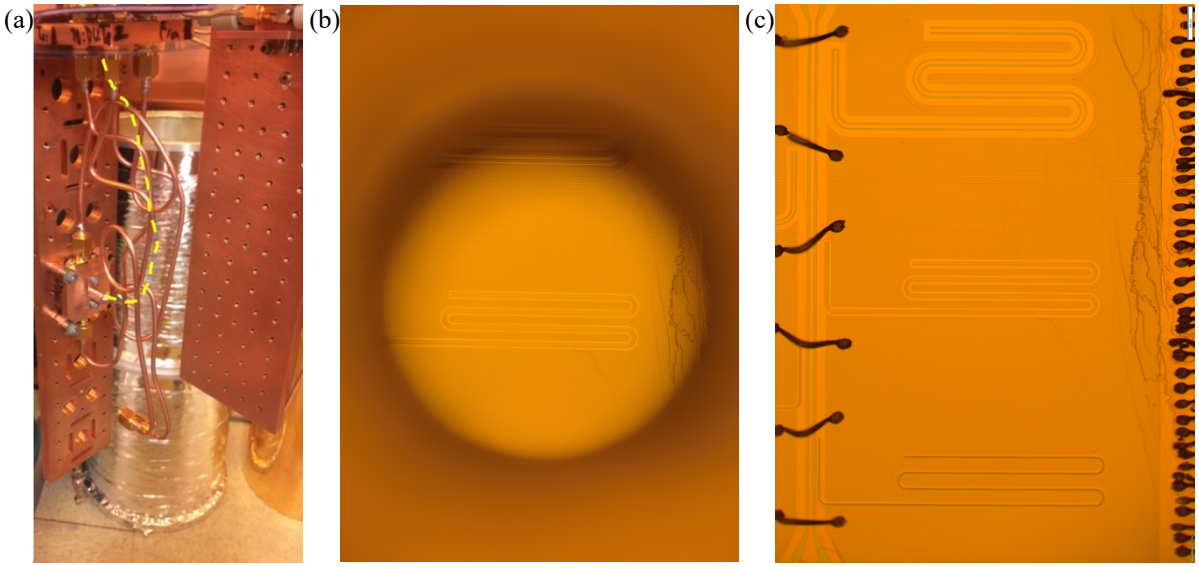

Figure 7. 9 Photograph of (a) fiber connection at the sample stage, where path of the fiber is traced by yellow dashed line to aid visualization, (b) looking at chip inside packaging box via fiber mounting hole, and (c) resonator chip.

CHAPTER 8

Resonator and Transmon Characterization

CPW resonators are a major component used in superconducting quantum circuits to read out 2D transmon/Xmon qubits [158]. They are also used in microwave kinetic inductance detectors (MKID) [230] and other detector applications. In my studies on quasiparticle phenomena, measurements of TiN resonators provided me information on the superconducting energy gap, kinetic inductance, and microwave dissipation.

Characterization of a transmon qubit is essential before one can perform qubit manipulation or gate operations. Characterization is required for each cooldown of the device, because device parameters such as the qubit transition frequency $\omega_{ge}/2\pi$ and coherence time T_1 tend to shift slightly between each cooldown. Parameters such as the junction critical current I_c also tend to drift when the device is stored at room temperature for long periods of time, possibly due to growth or restructuring of the oxide tunnel barrier. I also found that I need to wait approximately one week after the initial cooldown before the qubit T_1 stabilizes; probably due to cooling of refrigerator components that were not well thermalized.

In this chapter, I discuss the measurements and analysis I performed to characterize both the TiNx resonators and 3D transmon qubits for extracting key device parameters. I begin by discussing steady state spectroscopic measurements of the resonators, since this is relatively

simpler than the qubit characterization. The rest of the chapter discusses the different measurements I conducted on the qubits and the parameters extracted (see Table 8. 1).

Table 8. 1 Table of measurement techniques and their extracted qubit parameters.

section	Measurement	Parameters Obtained
7.1	cavity spectroscopy	$\omega_r, \widetilde{\omega}_r, \chi, \chi_{ge}, \kappa, Q_{in}, Q_{out}, Q_I$
7.3	transmon spectroscopy	$\omega_{ge}, \omega_{gf}, E_c, E_J$
7.4	Rabi oscillations	$\mathcal{R}_x^{\pi}, T_{\mathrm{Rabi}}$
7.5	relaxation time measurements	T_1
7.6	Ramsey oscillations	precise ω_{ge}, T_2^*
7.7	spin-echo measurements	T_2, echo

8.1. Resonator Spectroscopy

For characterization of CPW resonators, I used a VNA to measure the transmission $S_{21}(f)$ as a function of frequency (see Figure 7. 8 for the setup schematic). From analysis of these measurements, I extracted the resonance frequency f_0, coupling quality factor Q_c, loaded quality factor Q_L, and internal quality factor Q_I, as well as fluctuations in f_0. These measurements were performed at different RF powers and refrigerator temperatures to investigate energy dissipation mechanisms.

8.1.1. Diameter Correction Method for Parameter Abstraction

An expression for the complex transmission $S_{21}(f)$ of a CPW resonator coupled to a waveguide can be derived using an analogous RLC circuit model of a resonator capacitively

coupled to a matched transmission line [249]. This analysis yields

$$S_{21}(f) = 1 - \frac{Q_L/Q_c}{1 + i\frac{Q_L}{f f_0}(f^2 - f_0^2)} e^{i\phi}, \tag{8. 1}$$

where f_0 is the resonance frequency, Q_L is the loaded quality factor, Q_c is the coupling quality factor and ϕ is the coupling phase. (8. 1) is similar to that for transmission through a cavity (see Section 6.3.3), except that the input and output Qs for the cavity are set to a common coupling Q_c. For an ideal system, the internal quality factor Q_I can be calculated from the extracted values of Q_L and Q_c using (4.23).

In reality, asymmetries in the measured $S_{21}(f)$ arise from non-ideal aspects of the setup such as a mismatched transmission line, series inductance, or mutual inductance. I account for these non-idealities using the Diameter Correction Method (DCM) developed by Khalil *et al.* [268], which introduces a complex coupling quality factor $Q_c \rightarrow \hat{Q}_c$, such that

$$S_{21}(f) = 1 - \frac{Q_L/|\hat{Q}_c|\cos\phi}{1+i\frac{Q_L}{f f_0}(f^2-f_0^2)} e^{i\phi}, \tag{8. 2}$$

where $|\hat{Q}_c|$ and ϕ are the magnitude and phase of coupling quality factor $\hat{Q}_c$. Simultaneous fitting of both the in-phase and quadrature components of $S_{21}(f)$ using (8. 2) yields the resonator parameters $f_0, Q_L, \hat{Q}_c$ and $Q_I = \left(1/Q_L - 1/|\hat{Q}_c|\right)^{-1}$. Figure 8. 1 shows an example of the DCM resonance fitting to my data. Small discrepancies between the data and fitting occured near f_0, due to fluctuations in f_0, as I discuss in the next section.

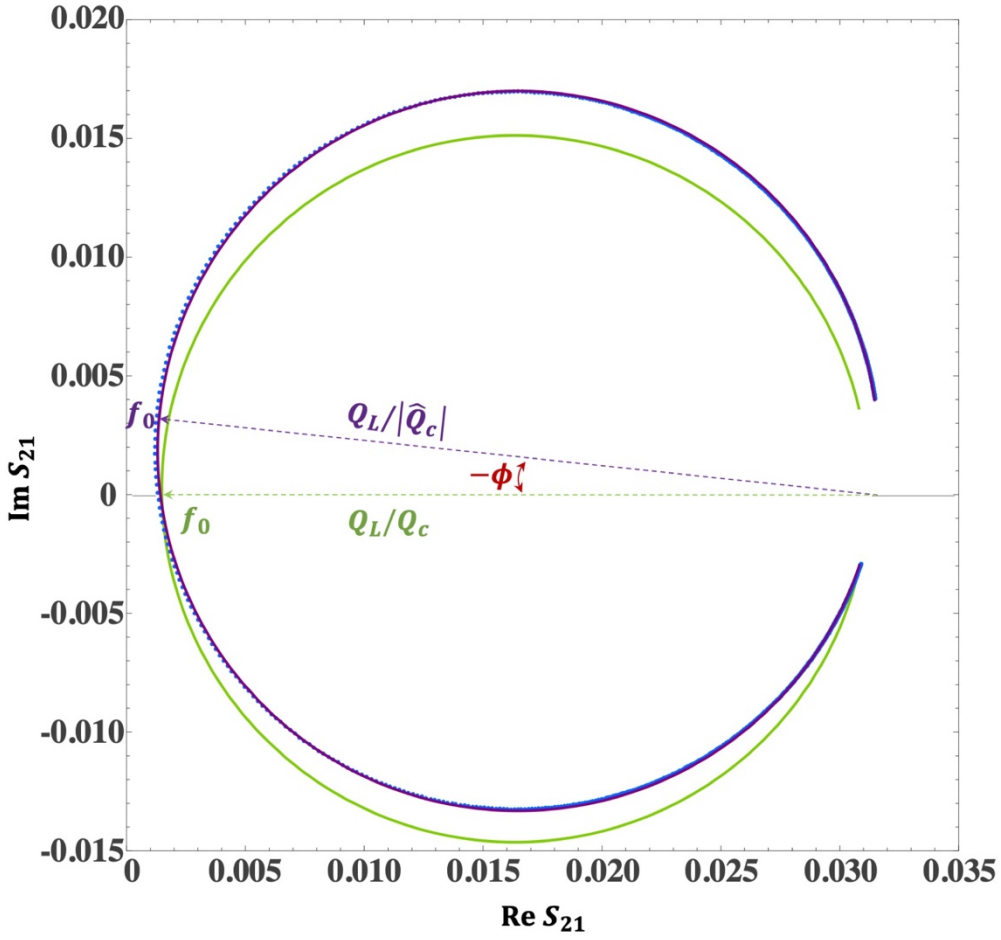

Figure 8. 1 Fitting S_{21} resonance data using the DCM technique. Data is shown as blue dots, fitting function is solid purple curve, and the DCM corrected S_{21} function is shown as solid green curve. The purple and green dashed lines correspond to the diameter of the solid purple and green circles.

8.1.2. Noise Extraction from Repeated Scans and Error Propagation

While fitting my resonator data, I implemented a new procedure to estimate the uncertainties associated with my S_{21} data. This new procedure not only yielded a better fit to my data, but also allowed me to obtain information about phase noise in the resonator. To find the uncertainty in S_{21}, I repeated each $S_{21}(f)$ scan about 600 times to extract the mean $\bar{S}_{21}(f)$ and standard deviation $\sigma_{S21}(f)$ as a function of frequency f. The $\bar{S}_{21}(f)$ and $\sigma_{S21}(f)$ associated with

the representative data set (blue) from Figure 8. 1 are plotted in Figure 8. 2 and Figure 8. 3 respectively. I note that $\bar{S}_{21}(f)$ shows the expected resonance behavior, while the corresponding $\sigma_{S21}(f)$ shows a strong dependence on f. To account for the fluctuations in $S_{21}(f)$, the resonance fittings (purple) using (8. 2) are weighted by the inverse of $\sigma_{S21}(f)$ at each frequency.

The behavior of $\sigma_{S21}(f)$ can be modeled as a constant background fluctuation σ_{bkgnd} associated with the amplifier noise and a resonance frequency fluctuation σ_f. Propagation of errors then gives

$$\frac{\sigma_{S21}}{\sqrt{IF}} = \sqrt{\left(\frac{\sigma_{bkgnd}}{\sqrt{IF}}\right)^2 + \left(s_{21}'(f)\frac{\sigma_f}{\sqrt{IF}}\right)^2}\,, \tag{8. 3}$$

where IF is the bandwidth of the VNA measurement. Fitting (8. 3) to my data yields good agreement (see Figure 8. 3). Whereas σ_{bkgnd} turns out to be independent of refrigerator temperature, σ_f shows more interesting temperature behaviors. Further analysis and explanation of the frequency fluctuations will be given in Section 10.4.

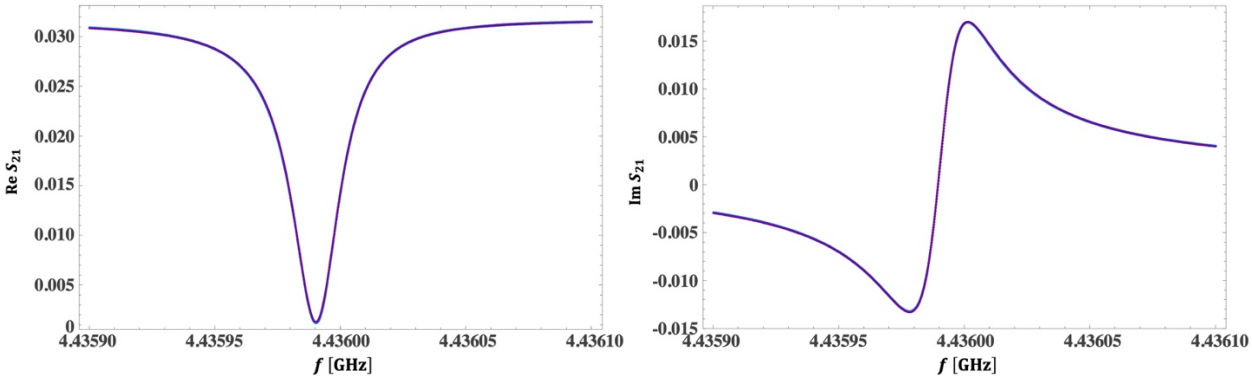

Figure 8. 2 Plot of real and imaginary components of $\bar{S}_{21}(f)$ data obtained from the 600 repetitions of $S_{21}(f)$ scan, where data is shown as blue dots and fitting to (8. 2) shown as purple curve.

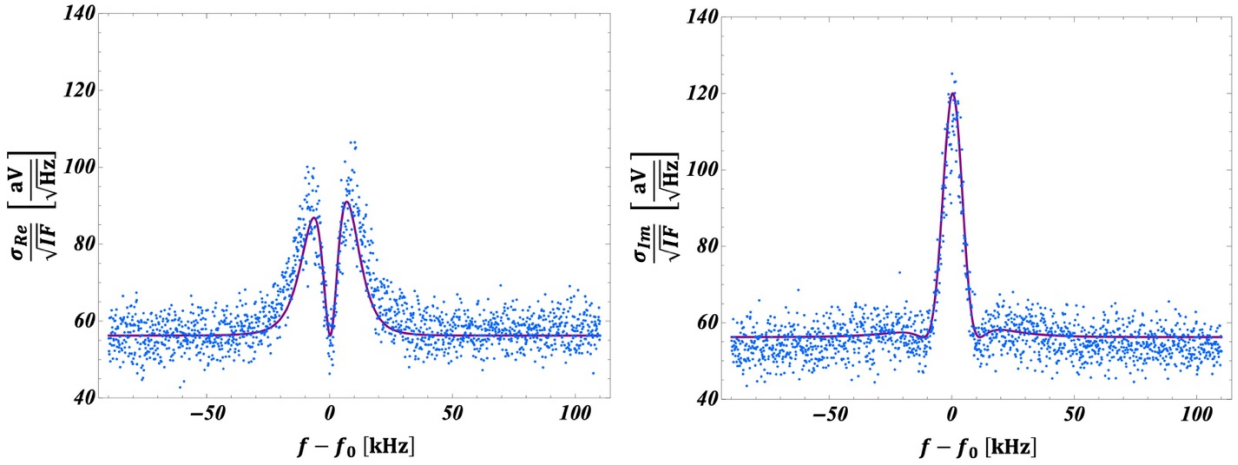

Figure 8. 3 Plot of $\sigma_{S21}(f)$ associated with data in Figure 8. 2. Dots are data and curve is fit to (8. 3).

8.2. Cavity Spectroscopy

Cavity spectroscopy yields the cavity input/output quality factors Q_{in}, Q_{out} (see Section 6.3.3), the dressed cavity frequency $\tilde{\omega}_r/2\pi$, bare cavity $\omega_r/2\pi$, and the dispersive shift χ_{ge}. Measurements of the transmission coefficient $S_{21}(f)$ through the cavity were performed using the VNA (see Section 7.2). The bare and dressed cavity frequencies were extracted by performing frequency sweeps as a function of the applied power; the cavity resonance shifts from the dressed frequency $\tilde{\omega}_r/2\pi$ at low power to the bare frequency $\omega_r/2\pi$ at high power with a sharp transition. Figure 8. 4 shows a plot of the measured $S_{21}(f)$ as the applied power $P_{appl.}$ is increased from -30 dBm to $+10$ dBm. Low applied powers corresponds to the dispersive regime with $\tilde{\omega}_r/2\pi \sim 7.9545$ GHz, while at high applied powers $\omega_r/2\pi \sim 7.952$ GHz, yielding $\chi_{ge}/2\pi = (\tilde{\omega}_r - \omega_r)/2\pi \sim 2.5$ MHz. This frequency shift and transition confirms that the qubit is functional and the value found from χ_{ge} provides a rough idea of the qubit transition frequency $\omega_{ge}/2\pi \sim 4$ GHz.

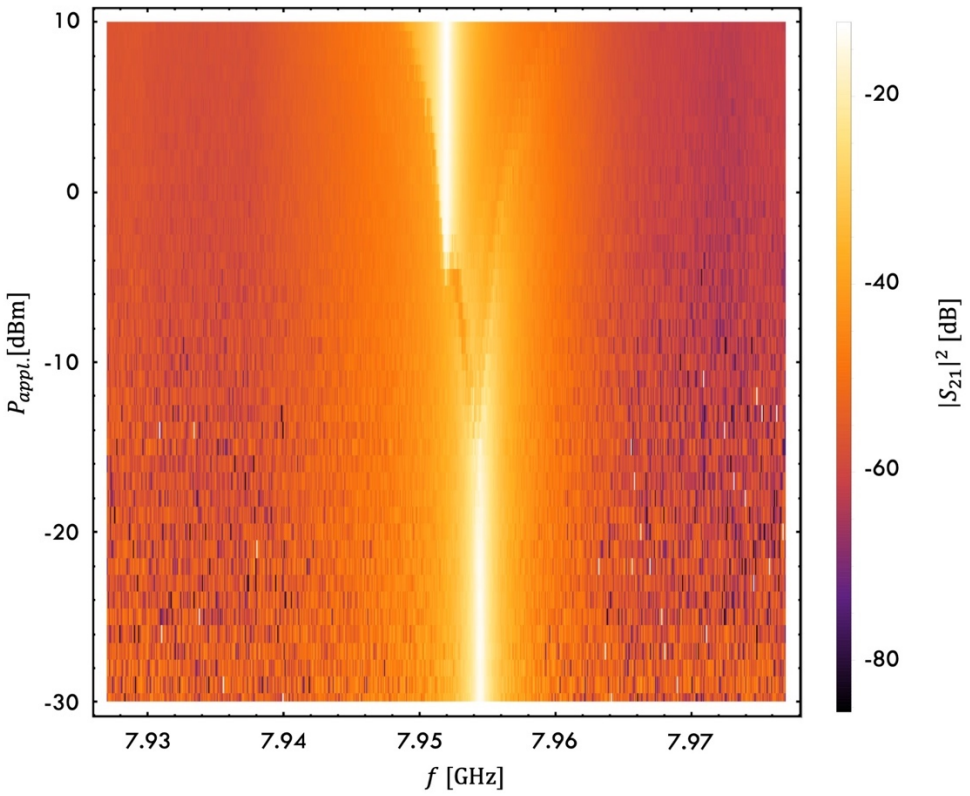

Figure 8. 4 Cavity spectroscopy measured using VNA. $\tilde{\omega}_r/2\pi\sim7.9545\ GHz$ and $\omega_r\sim/2\pi7.952\ GHz$ gives $\chi_{ge}/2\pi\sim2.5\ MHz$.

More accurate values for the qubit parameters $\omega_r, \tilde{\omega}_r, \chi, \chi_{ge}$ and χ_{ef} were extracted by performing pulsed spectroscopy using the heterodyne setup discussed in Section 7.4. In this scheme, heterodyne measurements of the transmission coefficient S_{21} are performed before and after applying a bit-flip gate $\mathcal{R}_x^\pi$ (see Section 8.5) to the qubit. Since bit-flip operation is required, this step was revisited after calibration of the $\mathcal{R}_x^\pi$ gate (see Section 8.5). The pulse sequence is illustrated in Figure 8. 5, where a cavity reference pulse is first applied to obtain the background transmission S_{21}, followed by an idle time for cavity ring down, before the qubit tone is applied and immediately followed by a cavity pulse to track changes in S_{21}. A change in S_{21} relative to the reference pulse occurs when the qubit tone hits the qubit transition frequency and induces an excitation. Details on the transmon readout techniques are provided in the subsequent sections.

Figure 8. 5 Heterodyne pulse sequence for transmon readout. Cavity reference pulse is applied to obtain the background transmission S_{21}, followed by an idle time. A qubit tone is then applied and immediately followed by a cavity readout pulse to track changes in S_{21}.

By performing pulsed frequency sweeps near the cavity resonance at gradually raised readout power with the $\mathcal{R}_x^{\pi}$ gate applied via the pulsing sequence in Figure 8. 5, a refined version of Figure 8. 4 can be obtained, from which the dressed frequency $\tilde{\omega}_r$ at transmon $|g\rangle$ and $|e\rangle$ states can be distinguished. Figure 8. 6 shows an example where the dressed cavity resonance shifts from $\tilde{\omega}_r^{|g\rangle}/2\pi$~7.9545 GHz in the $|g\rangle$ state to $\tilde{\omega}_r^{|e\rangle}/2\pi$~7.9538 GHz in the $|e\rangle$ state at low readout powers (see Chapter 3.5.1). At high readout power, the transmission S_{21} shows an increase around 0 dBm near the bare frequency ω_r for the transmon $|g\rangle \rightarrow |e\rangle$ state transit. This 2D color map provides reference for setting power bias to the transmon readout, as discussed in the next section.

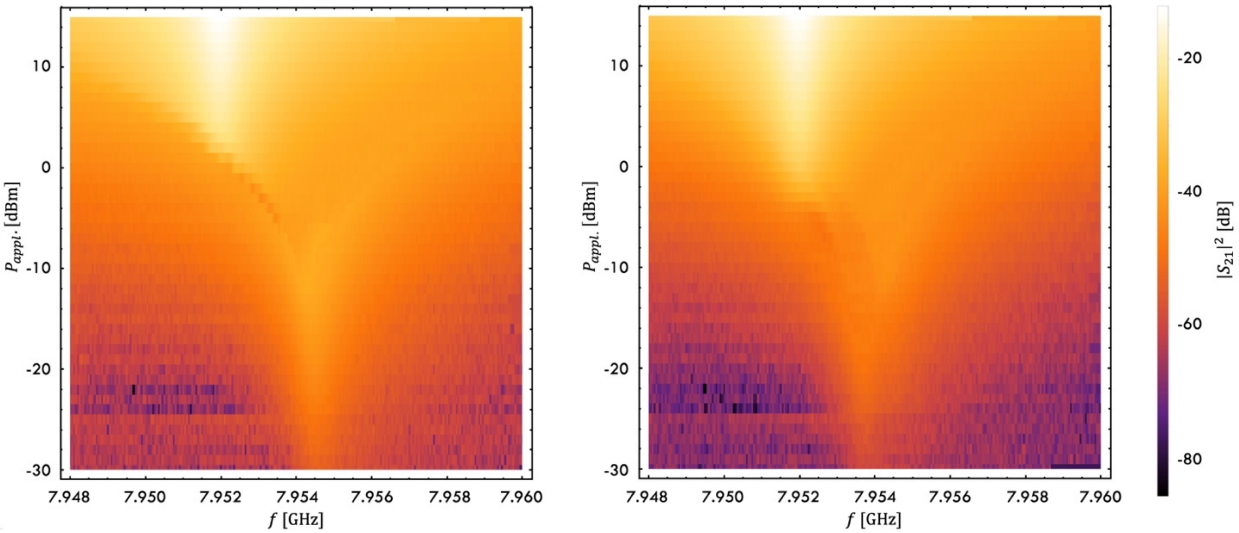

Figure 8. 6 Pulsed cavity spectroscopy performed using heterodyne measurement in qubit ground state (right) and after exciting the qubit (left). $\tilde{\omega}_r^{|e\rangle}/2\pi$~7.9538 GHz and $\tilde{\omega}_r^{|g\rangle}/2\pi$~7.9545 GHz.

A line cut at $P_{cav} = -20$ dBm through the plots in Figure 8. 6 give the profiles of the cavity resonance (see Figure 3. 7). Fitting the resonance to a Lorentzian distribution [269] yields $\omega_r/2\pi \simeq 7.95197$ GHz, $\tilde{\omega}_r^{|e\rangle}/2\pi \simeq 7.95384$ and $\tilde{\omega}_r^{|g\rangle}/2\pi \simeq 7.95459$ GHz (see Figure 8. 7). The dispersive shift can be calculated accordingly as $\chi/2\pi \simeq (\tilde{\omega}_r^{|e\rangle} - \tilde{\omega}_r^{|g\rangle})/2\pi \simeq -0.375$ MHz. The cavity decay rate $\kappa/2\pi \sim 0.8386$ MHz can be obtained from the width at half maximum of the Lorentzian distribution.

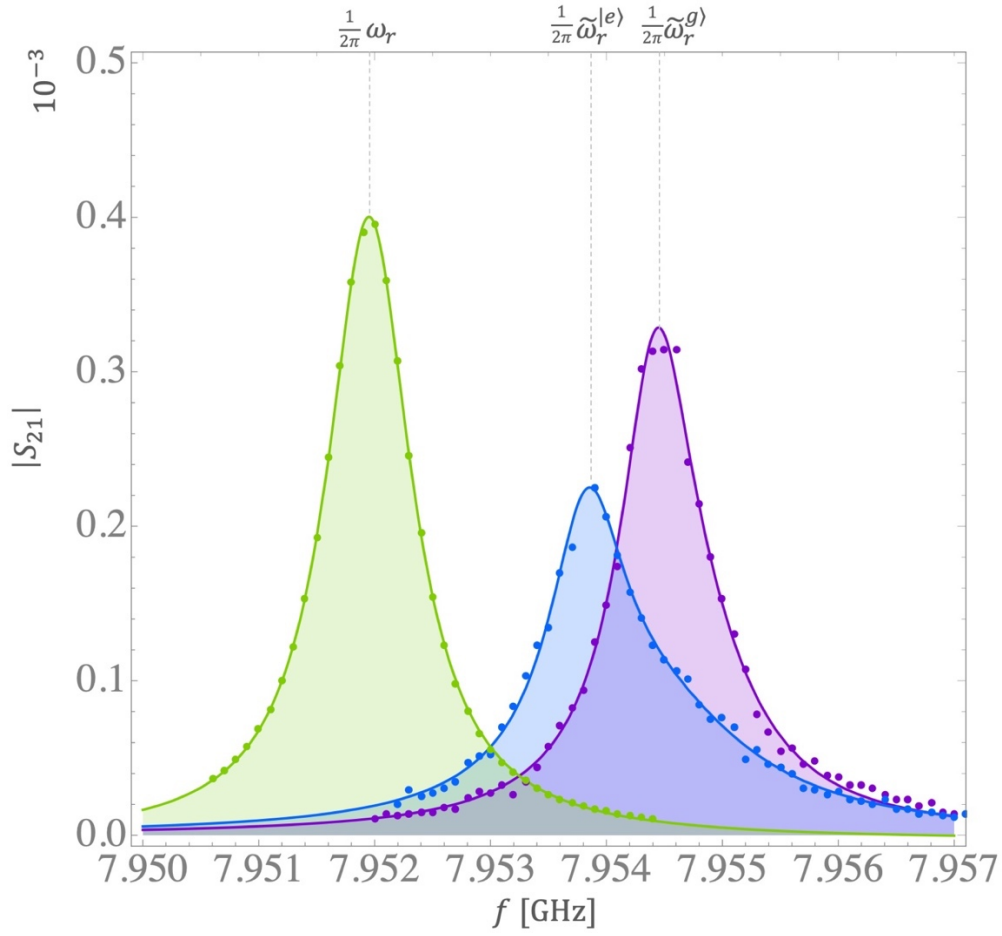

Figure 8. 7 S_{21} versus frequency f at $P_{cav} = 10$ dBm (green) and $P_{cav} = -20$ dBm (blue and purple) corresponding to horizontal line cuts from the plots in Figure 8. 6. Curves correspond to fit with $\omega_r/2\pi \simeq 7.95197$ GHz (green), $\tilde{\omega}_r^{|e\rangle}/2\pi \simeq 7.95384$ (blue) and $\tilde{\omega}_r^{|g\rangle}/2\pi \simeq 7.95459$ GHz (purple).

8.3. Transmon Readout

As discussed in the preceding section, a 3D false-color plot of S_{21} versus frequency and applied readout power gives a clear picture of the boundary between the low-power dispersive readout corresponding to $\tilde{\omega}_r$ and the non-linear high-power readout corresponding to ω_r. Either readout method can be used to get a fairly accurate measure of the qubit transition frequency ω_{ge}. To do this, I fixed the cavity tone readout power to a desired bias point, corresponding to a clearly defined frequency $\tilde{\omega}_r$ or ω_r in Figure 8. 4, and swept the frequency of the qubit tone using the pulsing sequence illustrated in Figure 8. 5. A change in the measured cavity readout S_{21} relative to the reference pulse occurs when the qubit tone hits the qubit transition frequency and induces an excitation. In the subsequent two subsections, I discuss details of the dispersive and high-power readout techniques.

8.3.1. Dispersive Readout

Proposed by Blais *et al.* [270] and demonstrated by Wallraff *et al.* [271] in 2004, the dispersive readout can be used as a quantum non-demolition weak measurement [272][273] implemented by low-power biasing the readout tone at the $|g\rangle$ state dressed cavity frequency $\tilde{\omega}_r^{|g\rangle} = \tilde{\omega}_r - \chi$, at which the transmission drops when a qubit transition $|g\rangle \rightarrow |e\rangle$ occurs. The drawback of this low-power scheme is the inherent low signal-to-noise ratio. Signal readout using a quantum-limited amplifier [274] or a substantial amount of averaging over repeated measurements is required.

8.3.2. Non-linear High-power Readout

The non-linear high-power readout was first demonstrated by Reed *et al.* [275] in 2010. It implements a projective strong measurement by high power biasing the readout tone at the bare cavity frequency ω_r. By carefully choosing the power, the state of the transmon can be mapped to the S_{21} transmission. For example, the best bias point in Figure 8. 6 is near $f = 7.952$ GHz and $P = 0$ dBm, where S_{21} for the $|e\rangle$ state is much larger than that for the $|g\rangle$ state. Fixing the frequency of the readout tone at ω_r and sweeping the applied readout power yields S-curves for the $|g\rangle$ and $|e\rangle$ states, as shown in Figure 8. 8. In this plot, each data point was obtained from the demodulated in-phase voltage of the heterodyne pulsed measurement averaged over 4000 repetitions. The cavity reference pulse in Figure 8. 5 yields the purple curve in Figure 8. 8, while the cavity readout pulse applied immediately after the qubit $|g\rangle \rightarrow |e\rangle$ drive yields the blue S-curve. Replacing the qubit $|g\rangle \rightarrow |e\rangle$ drive with the $|g\rangle \rightarrow |f\rangle$ drive of higher excitation state yields the green S-curve in Figure 8. 8. The difference between the excited state (blue or green) and reference (purple) S-curve corresponds to the distinguishability of the ground and excited state populations. A high distinguishability and a low ground state population stable relative to small fluctuations in readout power are desired when selecting a bias point. In the case of Figure 8. 8, a decent bias occurs at $P_{cav}\sim 0$ dBm for distinguishing between $|g\rangle$ and $|e\rangle$. However, this is not a good choice for distinguishing $|f\rangle$ from $|e\rangle$. If one needs to distinguish $|f\rangle$ from $|e\rangle$, then a power of $P_{cav}\sim -3$ dBm should be used.

This readout scheme can also be used to extract the probability of being in $|g\rangle$ or $|e\rangle$ when the system is in a superposition state, for which repeated averaging would place the output in the colored regions of Figure 8. 8. To extract a value for the populations, I used the following formulas:

$$\frac{P_{|e\rangle}}{P_{|g\rangle}+P_{|e\rangle}} = \frac{\frac{\Delta V}{V}\Big|_{\text{read}} - \frac{\Delta V}{V}\Big|_{\text{ref}}}{\frac{\Delta V}{V}\Big|_{|g\rangle\to|e\rangle} - \frac{\Delta V}{V}\Big|_{\text{ref}}}, \tag{8.4}$$

$$\frac{P_{|f\rangle}}{P_{|g\rangle}+P_{|f\rangle}} = \frac{\frac{\Delta V}{V}\Big|_{\text{read}} - \frac{\Delta V}{V}\Big|_{\text{ref}}}{\frac{\Delta V}{V}\Big|_{|g\rangle\to|f\rangle} - \frac{\Delta V}{V}\Big|_{\text{ref}}}, \tag{8.5}$$

where $\frac{\Delta V}{V}\Big|_{\text{ref}}$ and $\frac{\Delta V}{V}\Big|_{\text{read}}$ are the amplitudes of the heterodyne measurement results for the reference and signal readout cavity pulse, respectively; $\frac{\Delta V}{V}\Big|_{|g\rangle\to|j\rangle}$ is the relative amplitude of the heterodyne measurement immediately after the application of a pulse or pulses that drives the system from $|g\rangle$ to the state $|j\rangle$.

Compared to dispersive readout, the non-linear high-power readout can provide a high signal-to-noise ratio, thus reducing the number of repetitions required to obtain precise values for the qubit population. Therefore, this readout scheme was adopted for most of my measurements.

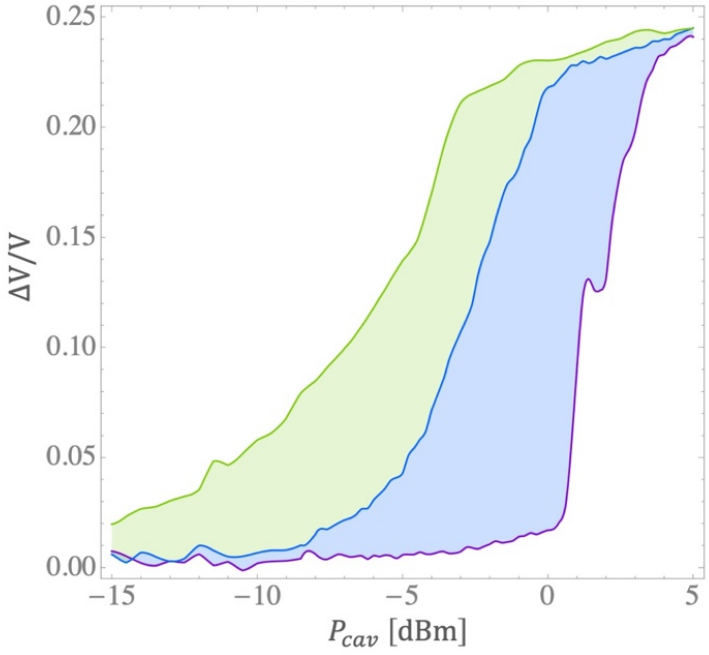

Figure 8. 8 S-curves for mapping the heterodyne amplitude $\Delta V/V$ to the transmon state $|g\rangle$ (purple), $|e\rangle$ (blue) and $|f\rangle$ (green). Decent biasing locates at $P_{cav}{\sim}0\ dBm$ for $|g\rangle, |e\rangle$ detections and $P_{cav}{\sim}-3\ dBm$ for $|g\rangle, |e\rangle, |f\rangle$ detections.

8.4. Transmon Spectroscopy

Transmon spectroscopy yields a preliminary estimation of the qubit transition frequencies ω_{ge} and ω_{gf}. To perform qubit spectroscopy, a qubit tone of long pulse duration and moderate RF power was applied, followed by a pulsed heterodyne measurement of the cavity using the pulse sequence shown in Figure 8. 5. Figure 8. 9 shows a spectroscopic plot of the excess population using a high-power readout. In the plot, the $|g\rangle \leftrightarrow |e\rangle$ transition occurs at $\omega_{ge}/2\pi$~4.049 GHz and a two-photon transition from $|g\rangle$ to $|f\rangle$ occurs at $\omega_{gf}/4\pi$~3.938 GHz. The charging energy can be calculated accordingly as $E_c/h \simeq 2\left(\omega_{ge}/2\pi - \omega_{gf}/4\pi\right) \simeq 222$ MHz.

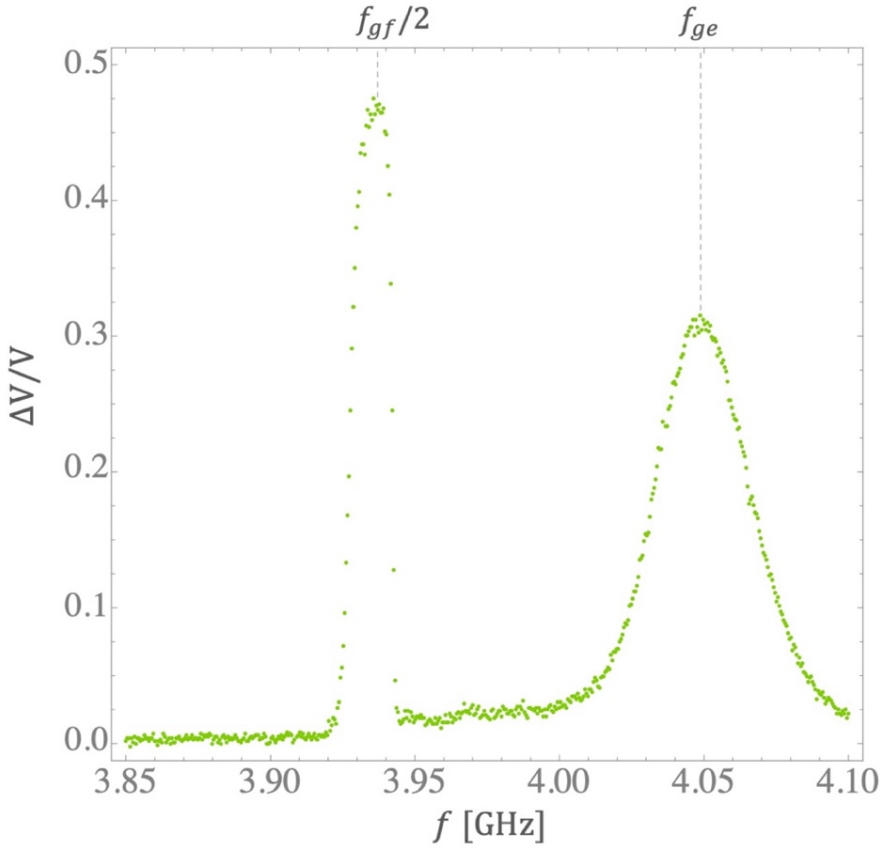

Figure 8. 9 Transmon spectroscopy using the heterodyne pulse measurement techniques, yielding preliminary estimation of qubit transition of $\omega_{ge}/2\pi$~4.049 GHz and $\omega_{gf}/4\pi$~3.938 GHz.

8.5. Rabi Oscillations

Named after Isidor Isaac Rabi, a Rabi oscillation [171] refers to the cyclic behavior between states $|g\rangle \leftrightarrow |e\rangle$ of a two-level quantum system that is driven near its resonance frequency (see Section 3.5.2). For a transmon being driven at the transition frequency ω_{ge}, the sinusoidal Rabi oscillation of the qubit states $|g\rangle \leftrightarrow |e\rangle$ corresponds to a steady rotation of the Bloch vector (see Section 3.6.1) around the $\hat{\imath}$-axis of the Block sphere. To measure Rabi oscillations, I used the pulse sequence illustrated in Figure 8. 10, in which the pulse duration t_{Rabi} of the qubit tone at ω_{ge} is varied to change the angle of Block vector rotation. Figure 8. 11 shows a representative plot of the data obtained.

Figure 8. 10 Pulse sequence for measurement of Rabi oscillations, where the pulse duration t_{Rabi} is varied.

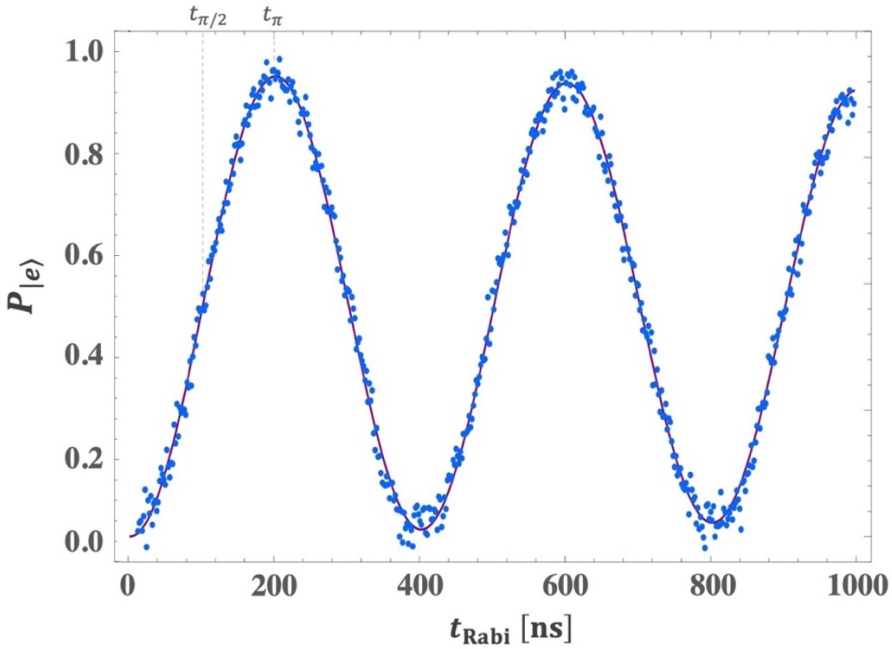

Figure 8. 11 Measured Rabi oscillations (blue dots) and fit (purple curve). A bit-flip or inversion of the population occurs at t_{π}, whereas half-inversion occurs at $t_{\pi/2}$.

If a qubit is initialized in the $|g\rangle$ state, and then undergoes a Bloch rotation around the $\hat{\imath}$-axis until it reaches $\theta = \pi$, the qubit population will be 100% transfered to the $|e\rangle$ state (ignoring relaxation). Such an operation is called a π-pulse snd can be represented by the Pauli-X gate operator [276]

$$\mathcal{R}_x^{\pi} \equiv \sigma_x = |g\rangle\langle e| + |e\rangle\langle g| = \begin{bmatrix} 0 & 1 \\ 1 & 0 \end{bmatrix}. \tag{8. 6}$$

The duration t_π of the $\mathcal{R}_x^{\pi}$ gate is determined by the Rabi oscillation frequency and qubit tone power. Figure 8. 12 shows the extracted the Rabi frequency Ω_R as a function of applied qubit drive voltage V_{in}. For measurements of qubit lifetime, I wanted a π-pulse with a duration that was much shorter than the relaxation time T_1, but did not require too large of an applied power because this could heat passive circuitry in the refrigerator. For this reason, I used a π-pulse with a duration of $\sim$150 ns. After calibrating the π-pulse, the $\mathcal{R}_x^{\pi}$ gate was implemented in the cavity spectroscopy and transmon readout discussed in the previous sections of this chapter.

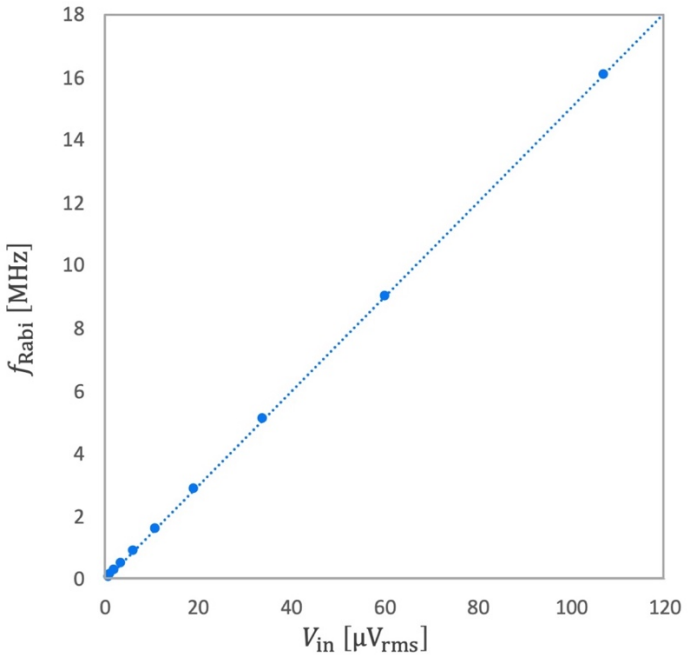

Figure 8. 12 Measured Rabi frequency $f_{Rabi} = \Omega_R/2\pi$ versus applied qubit drive voltage V_{in} at the device.

Due to decoherence, the amplitude of Rabi oscillations decays in time t_{Rabi} with a time constant T_{Rabi}. Figure 8. 13 shows a measurement of Rabi oscillations over a duration of 200 μs. The waveform can be fit to an exponentially decaying sine wave using

$$P_{|e\rangle} = Ae^{-\frac{t}{T_{\mathrm{Rabi}}}}(\sin \Omega_{\mathrm{R}} t_{\mathrm{Rabi}} + C), \tag{8. 7}$$

yielding the Rabi decay time constant $T_{\mathrm{Rabi}} = 50.3$ μs. The constants A~0.5 and C~0.5 here are the oscillation amplitude and steady-state population, respectively. For uniform frequency-independent dissipation and dephasing, the Rabi decay time constant is related to the relaxation time T_1 and dephasing time T_ϕ by

$$\frac{1}{T_{\mathrm{Rabi}}} = \frac{3}{4T_1} + \frac{1}{2T_\phi}. \tag{8. 8}$$

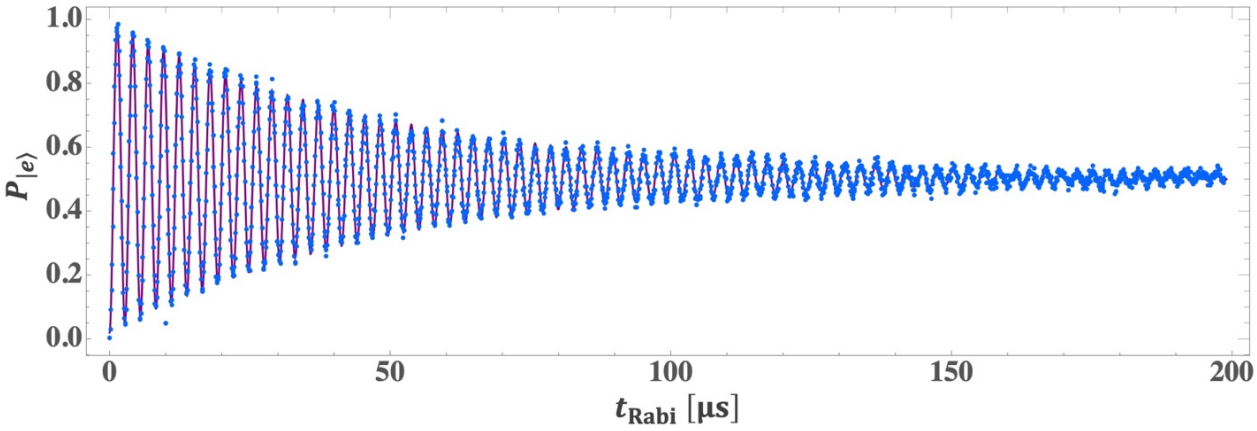

Figure 8. 13 Rabi oscillation decay measurements. Fitting yields an exponential decay with time constant $T_{\mathrm{Rabi}} = 50.3$ μs.

8.6. Relaxation Time Measurements

The relaxation time T_1 is defined as the mean time that it takes for an un-driven qubit to decay from its excited state to the steady-state occupancy due to dissipation of energy. T_1 can be measured by applying an $\mathcal{R}_x^\pi$ gate and inserting a delay t_{lapse} before performing a cavity readout measurement (see Figure 8. 14). I typically used 6000 repetitions of the measurement to obtain the mean decay plot. At short times, $P_{|e\rangle} \sim 1$ while for times $t_{\text{lapse}} \gg T_1$ the state will have relaxed and $P_{|e\rangle} \sim 0$. By sweeping the duration of t_{lapse}, decay plots as shown in Figure 8. 15 were obtained. Note that the time between the cavity readout pulses should be sufficiently longer than T_1 for the qubit to reach steady-state occupancy before each operation. The measured population decay can then be fit to the function

$$P_{|e\rangle} = Ae^{-t_{\text{lapse}}/T_1} + C\,, \tag{8. 9}$$

where $A \sim 1$ is the initial $|e\rangle$ state occupancy, and $C \sim 0$ is the steady-state occupancy or the residue thermal $|e\rangle$ state occupancy. Fitting to the data in Figure 8. 15 yielded $T_1 = 25.2\ \mu\text{s}$.

Figure 8. 14 Pulse sequence for measurement of relaxation time T_1, where the duration of t_{lapse} is varied.

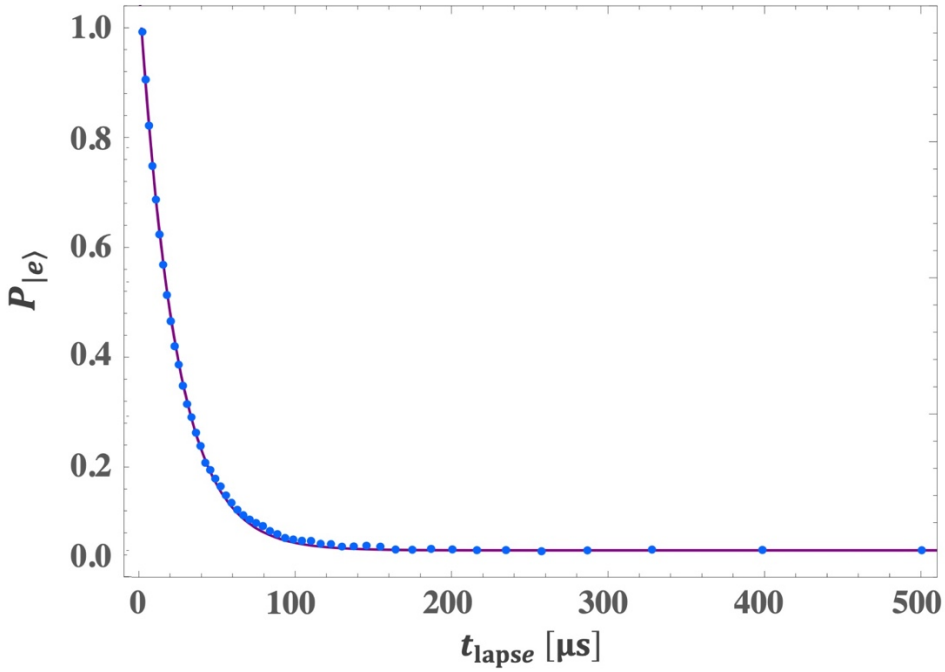

Figure 8. 15 Relaxation time T_1 measurements of $|e\rangle$ state decay (dots). Fitting to (8. 9) yielded $T_1 = 25.2$ μs (solid curve).

8.7. Ramsey Oscillations

Developed by Norman Ramsey, a student of Isidor Rabi, Ramsey interferometry [277] is a technique to determine transition frequencies with high precision and accuracy. It is employed in atomic clocks and in the S.I. definition of the second. Ramsey interferometry is implemented in qubit characterization by sending one $\mathcal{R}_{\mathrm{x}}^{\pi/2}$ gate of duration $t_\pi/2$ creating the state $(|g\rangle + |e\rangle)/\sqrt{2}$, allowing the system to precess for an idle time t_{Ramsey}, and then sending a second $\mathcal{R}_{\mathrm{x}}^{\pi/2}$ gate (see Figure 8. 16). Neglecting decoherence, if the two $\pi/2$ pulses are resonant with the qubit, then this pulse sequence will put the system in the $|e\rangle$ state, whereas if the $\pi/2$ pulses are slightly detuned by Δ_d from the qubit resonance ω_{ge}, the phase of the superposition state accumulated during t_{Ramsey} results in a drop in the final $|e\rangle$ state population measured, thus $P_{|e\rangle}$ will oscillate with

t_{Ramsey} at frequency $f_{\mathrm{Ramsey}} \propto \Delta_d$. Figure 8. 17 shows a Ramsey measurement with an oscillation frequency of f_{Ramsey}~182 kHz. Figure 8. 18 shows a plot of the extracted f_{Ramsey} for different drive frequencies $\omega_d = \omega_{ge} \pm \Delta_d$. Fitting the data to the functional form

$$\mathrm{sign}[\Delta_d]\, f_{\mathrm{Ramsey}} = A\omega_d + C \tag{8.10}$$

and comparing with the relation $f_{\mathrm{Ramsey}} \propto \Delta_d$ yields a precise determination of the qubit frequency ω_{ge} at $f_{\mathrm{Ramsey}} = 0$. Here, $\mathrm{sign}[\Delta_d]$ is the sign of detune Δ_d, A and C are constants. For the data shown, $\omega_{ge}/2\pi = 4.0560144$ GHz. This precise qubit frequency obtained from the Ramsey measurements was implemented in the cavity and transmon spectroscopies discussed in prior sections of this chapter to improve the accuracy of qubit characterizations.

Due to energy relaxation and dephasing, the measured amplitude of Ramsey oscillations decays in time. Figure 8. 19 shows a measurement of the Ramsey oscillation over a duration of 80 μs. The sinusoidal oscillation pattern shows an exponentially decay envelope that can be fit to the function

$$P_{|e\rangle} = e^{-t/\mathrm{T}_2^*}(1 - \sin 2\pi f_{\mathrm{Ramsey}} t_{\mathrm{Ramsey}})\,, \tag{8.11}$$

yielding the Ramsey decay time constant $\mathrm{T}_2^* = 27.6$ μs. In general, the Ramsey decay is related to the T_1 relaxation and T_ϕ dephasing by

$$\frac{1}{\mathrm{T}_2^*} = \frac{1}{2T_1} + \frac{1}{T_\phi} + \frac{1}{T^\dagger}\,, \tag{8.12}$$

where $T^\dagger$ is the time constant for inhomogeneous broadening [278] to be discussed in the succeeding section.

Figure 8. 16 Pulse sequence for Ramsey interferometry measurements, where the duration t_{Ramsey} is varied.

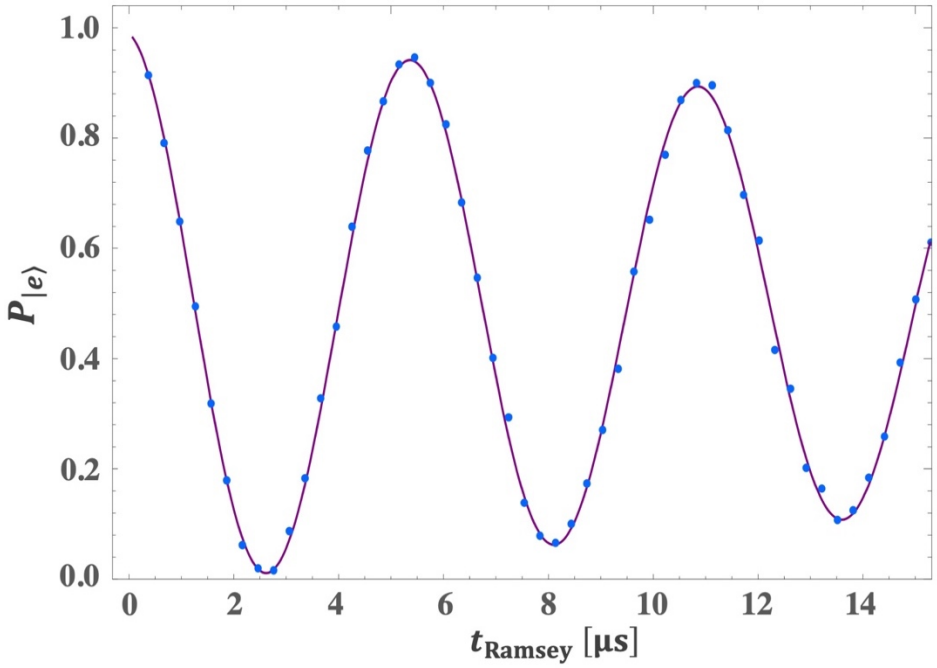

Figure 8. 17 Measurements of the excited state population $P_{|e\rangle}$ versus Ramsey delay time t_{Ramsey} (blue) using the pulse sequence in Figure 8. 16. Fitting to （8.11） (purple) yielded f_{Ramsey}~182 kHz.

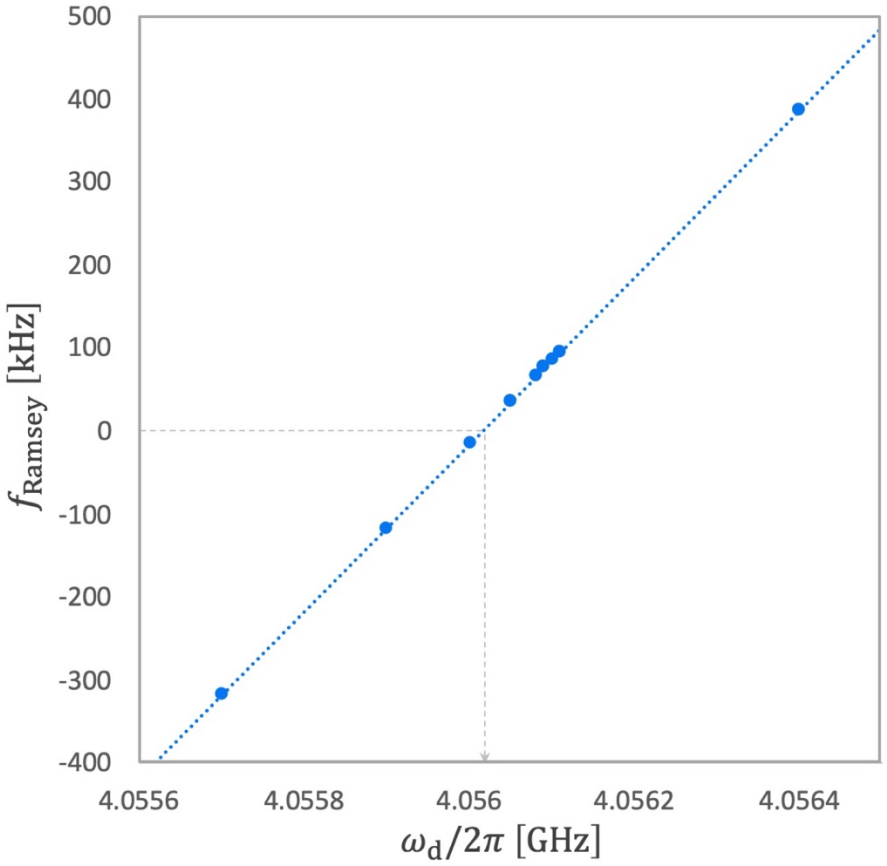

Figure 8. 18 Plot of $\mathrm{sign}[\Delta_d] f_{\mathrm{Ramsey}}$ versus drive frequency $\omega_d/2\pi$, where $\mathrm{sign}[\Delta_d]$ is the sign of detuning Δ_d. The point where $f_{\mathrm{Ramsey}} = 0$ corresponds to the best estimate for the qubit transition frequency $\omega_{ge}/2\pi = 4.0560144$ GHz.

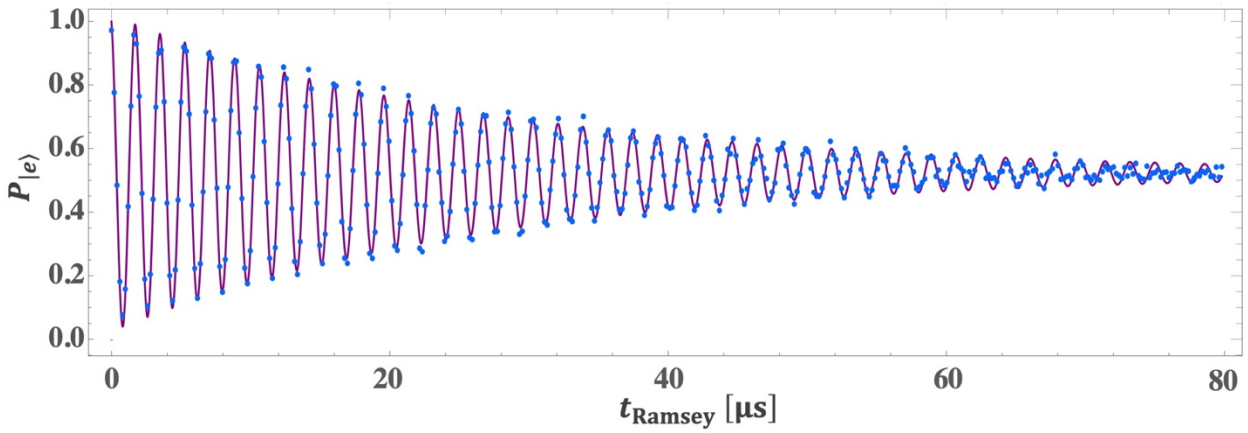

Figure 8. 19 Measurement of Ramsey oscillations over a duration of 80 μs. Fitting yields $T_2^* = 27.6$ μs.

8.8. Spin-Echo Measurements

The spin echo, also referred to as Hahn echo, was invented by Erwin Hahn to reduce effects of inhomogeneous broadening due to inhomogeneity induced frequency variations in spin ensembles. Hahn was using nuclear magnetic resonance (NMR) to study ensembles of spins and realized that magnetic field inhomogeneity was causing significant spectral broadening [279]. His spin echo technique can be implemented in my qubit characterization by introducing a 180° rotation around the $\hat{j}$-axis of the Bloch sphere (see Section 3.6.1) using a Pauli-Y gate $\mathcal{R}_{\mathrm{y}}^{\pi}$ midway in between the two $\mathcal{R}_{\mathrm{x}}^{\pi/2}$ gates in the Ramsey pulsing sequence, as illustrated in Figure 8. 20. The 180° rotation in the orthogonal axis induces a time-reversed evolution in the precession of the qubit state. This causes refocusing of the states that have slightly different transition frequencies. The signal generated by the refocusing of spins resembles an echo, thus the name "spin echo".

When the inhomogeneity is independent of time within the timescale of the free evolution, the ensemble constituents will refocus right before the application of the second $\mathcal{R}_{\mathrm{x}}^{\pi/2}$ gate, hence removing the effects of inhomogeneous broadening. Therefore, with the spin echo scheme, (8.12) reduces to

$$\frac{1}{T_2} = \frac{1}{2T_1} + \frac{1}{T_\phi} \tag{8.13}$$

if the sources of dephasing and relaxation are frequency independent. The coherence time T_2 can be measured by sweeping the duration of t_{echo} in the applied pulse sequence, yielding a plot as in Figure 8. 21. The decay of $P_{|e\rangle}$ can then be fit to

$$P_{|e\rangle} = Ae^{-t_{echo}/T_2} + C\,, \tag{8.14}$$

where $A{\sim}1$ is the initial $|e\rangle$ state occupancy, and $C{\sim}1/2$ is the expected steady-state occupancy. The fit to the data in Figure 8. 21 corresponds to $T_2 = 44.8$ µs. By measuring both T_1 and T_2 time constants, the dephasing time constant T_ϕ could be calculated.

Figure 8. 20 Pulse sequence for the spin echo measurement of coherence time T_2, where the duration of t_{echo} is varied.

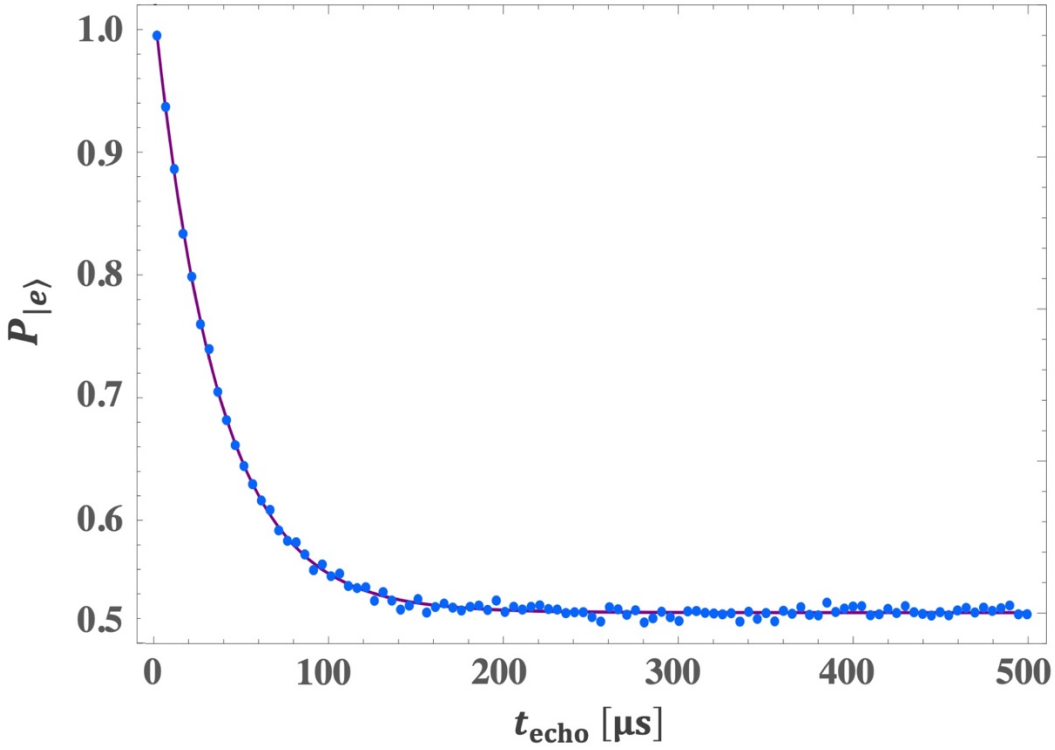

Figure 8. 21 Spin echo measurement (dots) yielding $T_2 = 44.8$ µs (solid curve).

8.9. Cavity Photon Number

Using $T_1 = 25.2\ \mu s$ and $T_2 = 44.8\ \mu s$, the dephasing time constant $T_\phi \geq 403.2\ \mu s$ could be calculated using (8.13). For cavity photon induced dephasing (see Section 3.7.1), T_ϕ can be converted to corresponding mean cavity photon number $\bar{n}_{th} = 1.002 \times 10^{-3}$ using (3.72). Typically, $\bar{n}_{th}$ rises with the applied readout power due to heating of the attenuators in the input transmission line. Figure 8. 22 shows the average cavity photon number detected as a function of an applied heating tone for some of my cooldowns.

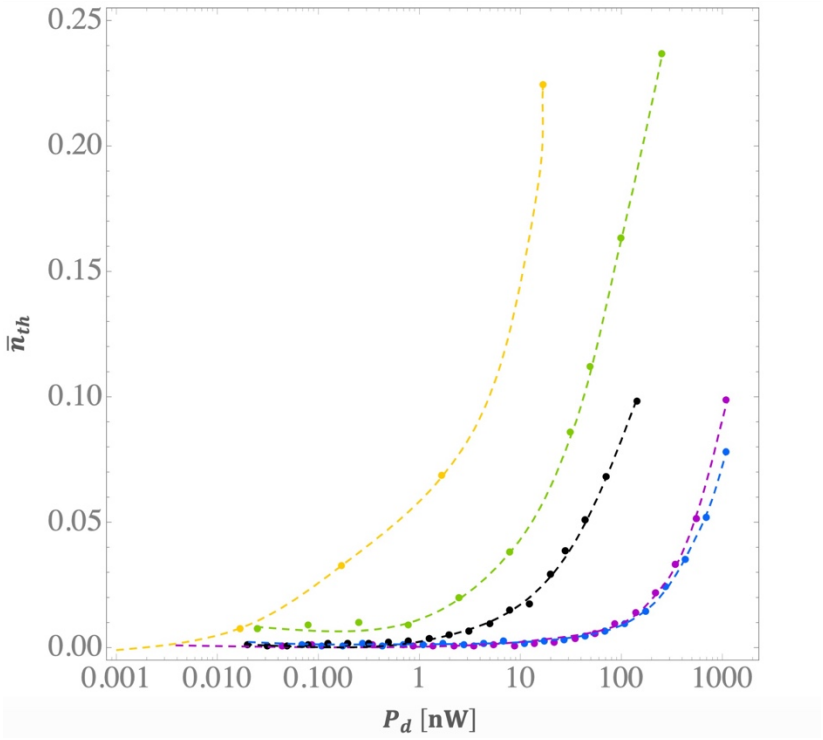

Figure 8. 22 Average cavity photon number $\bar{n}_{th}$ as a function of applied power P_d dissipated in the 20dB attenuators connected before the transmon in cooldowns with different thermal attenuation of the input drive signal at the cold plate and mixing chamber (see Section 7.1) using our 1st generation (black) and 2nd generation (purple and blue) homemade attenuators, commercial attenuator (green), and 0th generation homemade attenuators (yellow), corresponding to the dates Sep (yellow), May (green), Apr (blue), Feb (purple), Jan (black) in Table 8. 2. Dashed lines are visual guides.

8.10. An Overview of the Qubit Characterization

Whereas the subsections in this chapter were given in the same sequence I typically used for transmon characterization, revisiting between the various characterization steps is generally required for obtaining accurate qubit parameters. For my measurements, I followed a cyclic characterization sequence as illustrated in Figure 8. 23, until the qubit parameters converge to an acceptable accuracy and precision. A summary of my cavity and qubit parameters can be found in Table 8. 2. The results of relaxation time measurements, as the key focus of my studies, are discussed in the next chapter.

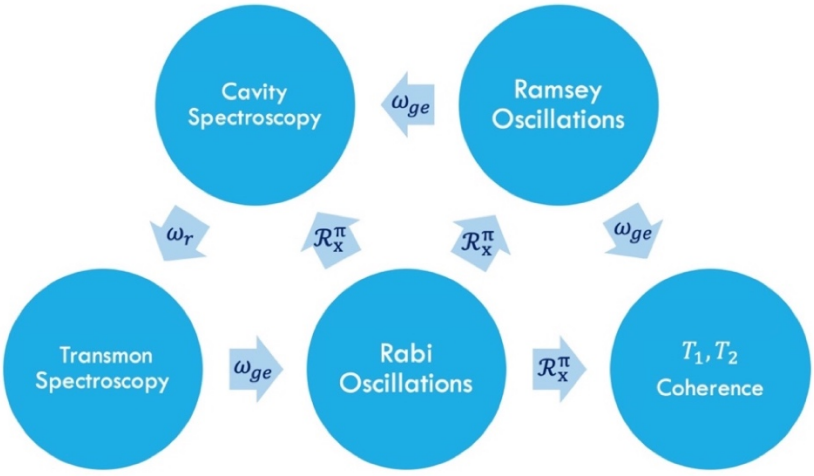

Figure 8. 23 Cyclic qubit characterization sequence to obtain accurate qubit parameters.

Table 8. 2 Summary of qubit parameters measured in consecutive cooldowns from Jan 2017 to Sep 2017.

date	Sep	May	Apr	Feb	Jan
Q_L	10800	10600	9400	11000	9000
Q_{in}, Q_{out}	9000,87000	9000,87000	9000,87000	9000,87000	9000,87000
f_c [GHz]	7.95158	7.95240	7.95197	7.95200	7.95235
f_q [GHz]	3.70713	3.71869	3.90964	4.00995	4.05601
$\kappa/2\pi$ [MHz]	0.7300	0.8944	0.8386	0.7338	0.9070
$\chi/2\pi$ [MHz]	-0.32	-0.39	-0.375	-0.378	-0.425

CHAPTER 9

Redistribution of Non-equilibrium Quasiparticles in Transmon

In my experiments on the transmon characterized in the preceding chapter, I observed a peculiar temperature dependence of transmon relaxation. The phenomenon was not unique and had been seen repeatedly in our experiments as well as by our collaborators [62]. I explained this observed phenomenon with non-equilibrium quasiparticles redistribution due to superconducting energy gap inhomogeneity. The derivation of our theoretical model can be found in Chapter 5. In the current chapter, I present my experimental results and discuss some of the implications for reducing loss due to quasiparticles.

9.1. Curious Temperature Dependence of the T_1 Relaxation Time

In my measurements on the temperature dependence of the relaxation time T_1, I found a striking and unexpected increase in T_1 as the temperature T was increased from about 30 mK to 100 mK (one-tenth of the aluminum T_c). Figure 9. 1 shows a typical plot of the $|e\rangle$ state population decay measured using the pulse sequence in Figure 8. 14 for temperatures ranging from $T = 27$ mK to 232 mK. These relaxation data are fitted with the simple exponential decay in (8. 9). The resulting decay rates depend non-monotonically on temperature, with the extracted T_1 peaks

about 100 mK (see Figure 9. 2). In particular, as the temperature of the qubit was increased from a base temperature of 10 mK, the lifetime increased from $T_1 = 18$ µs up to a maximum $T_1 = 32$ µs at a temperature of 90 mK. Above 150 mK, T_1 rapidly decreased as expected due to the thermal generation of quasiparticles. We note that these measured values for T_1 are far below the estimated Purcell limit of 1.7 ms and also much shorter than expected from dielectric loss (see Section 6.2.2). The highest measured T_1 for this device was 400 µs at ω_{ge}~3 GHz, obtained in one of Dr. Manucharyan's refrigerators.

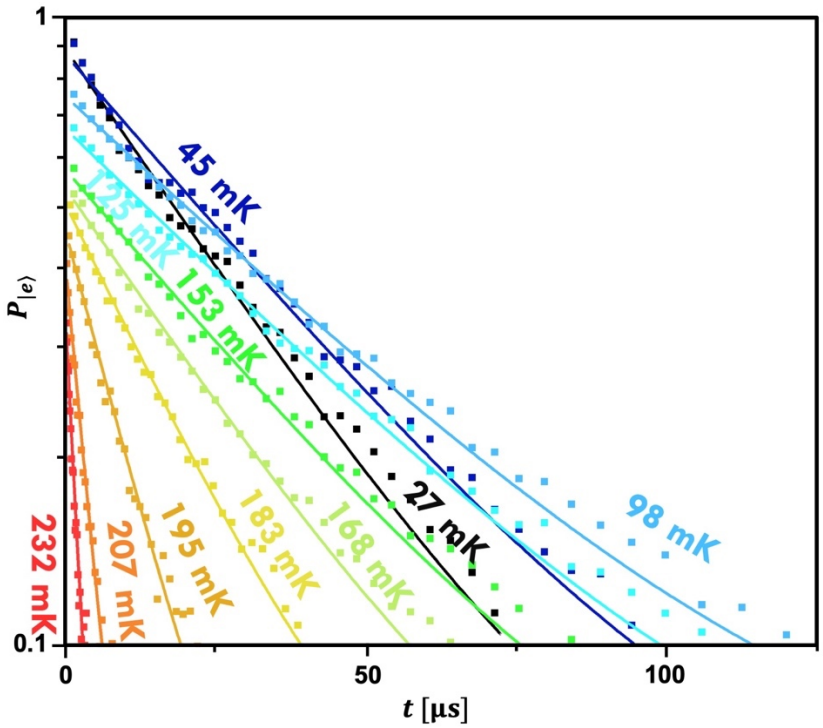

Figure 9. 1 Plot of $|e\rangle$ state population decay at various temperatures for Sep cooldown in Table 8. 2. Dots are data and solid lines are fits to a single exponential decay.

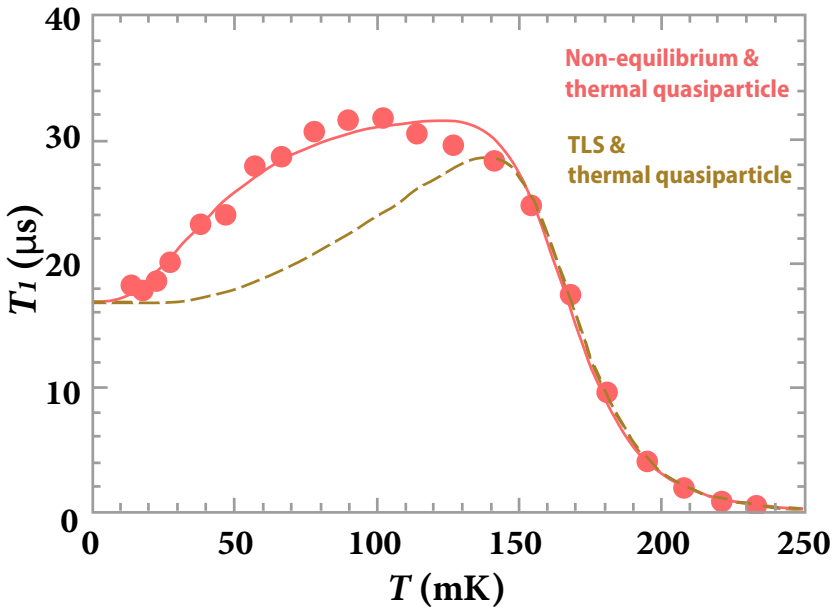

Figure 9. 2 Extracted T_1 (red dots) versus temperature T peaks about 100 mK, with fitting (refer to Table 9. 1) to our model in (5.40) is plotted as solid line (red). Dashed line is a model based on a simple TLS limited case calculated from (4.30).

To explain the initial rise in T_1 from 30 mK to 100 mK, the model in Chapter 5.2.2 was developed. In the model, we assume that the two stacked Al layers have slightly different superconducting energy gaps. At ~30 mK, non-equilibrium quasiparticles accumulate in the thinner 30 nm aluminum layer 1 since it has a slightly lower energy gap. This gives a high quasiparticle density at the Josephson junction, thus inducing a high quasiparticle tunneling rate and short T_1. As the temperature increases, non-equilibrium quasiparticles gain enough thermal energy to diffuse into the higher gap region of the thicker 50 nm aluminum layer. The diffusion reduces the overall quasiparticle density in contact with the Josephson junction, resulting in a lower quasiparticle tunneling rate and a larger T_1. This physical picture is captured in (5.40), which I used to fit the data in Figure 9. 2, yielding $\Delta_1 = 191$ μeV, $\Delta_2 = 196$ μeV, $n_{1\mathrm{L,ne}} = 19.9$ μm^{-3}, $n_{1\mathrm{R,ne}} = 3.3$ μm^{-3}. The resulting energy gaps fall within the typical range for thin-film aluminum and the gap difference $\Delta_2 - \Delta_1 \sim 5$ μeV could be a result of small differences in the film growth conditions. The smaller gap Δ_1 is mainly determined by the temperature of the sharp downturn in

T_1 at higher temperatures, while the gap difference $\Delta_2 - \Delta_1$ is determined by the temperature where T_1 starts to rise at low temperatures.

While conducting experiments with different attenuators (see Section 8.9) on the input transmission line, similar phenomenon was observed repeatedly. For comparison, Figure 9. 3 shows T_1 vs. T from four different cooldowns of the same transmon. Three of the curves show a prominent increase in T_1 as the temperature is increased from 20 mK to 100 mK, while the one with the largest T_1 (black) shows no such increase. For example, during the Feb cooldown (purple), I found that T_1 increased from about 40 μs at 20 mK to about 80 μs at 100 mK. The device was subsequently warmed to room temperature and cooled about 1 week later. During the Apr cooldown (blue), the same device showed an overall reduced T_1 with a similar temperature behavior, where T_1 increasing from about 30 μs at 20 mK to about 50 μs at 100 mK. In contrast, for the May cool-down (black), T_1 had a nearly temperature-independent value of 90 μs between 20 mK and 100 mK. Again, cycling the transmon to room temperature and measuring T_1 for a fourth time (red) in Sep, I saw behavior similar to that seen on the first and second cool-down, but with overall reduced T_1.

I note that the transmon sometimes showed spontaneous changes in T_1 and, for the second cooldown in particular, switching between two relaxation time constants was observed. The data shown in Figure 9. 3 for the Apr cooldown (blue) is the longer of the two-time constants, which was the more frequent. Similar behavior in other superconducting qubits has been attributed to fluctuations in the number of quasiparticles contributing to the loss [216]. When the number fluctuation is slow compared to the relaxation time, non-exponential decay or a distribution of decay time constants is expected [210], while if the fluctuation is fast relative to the decay time constants, a single exponential decay should be observed.

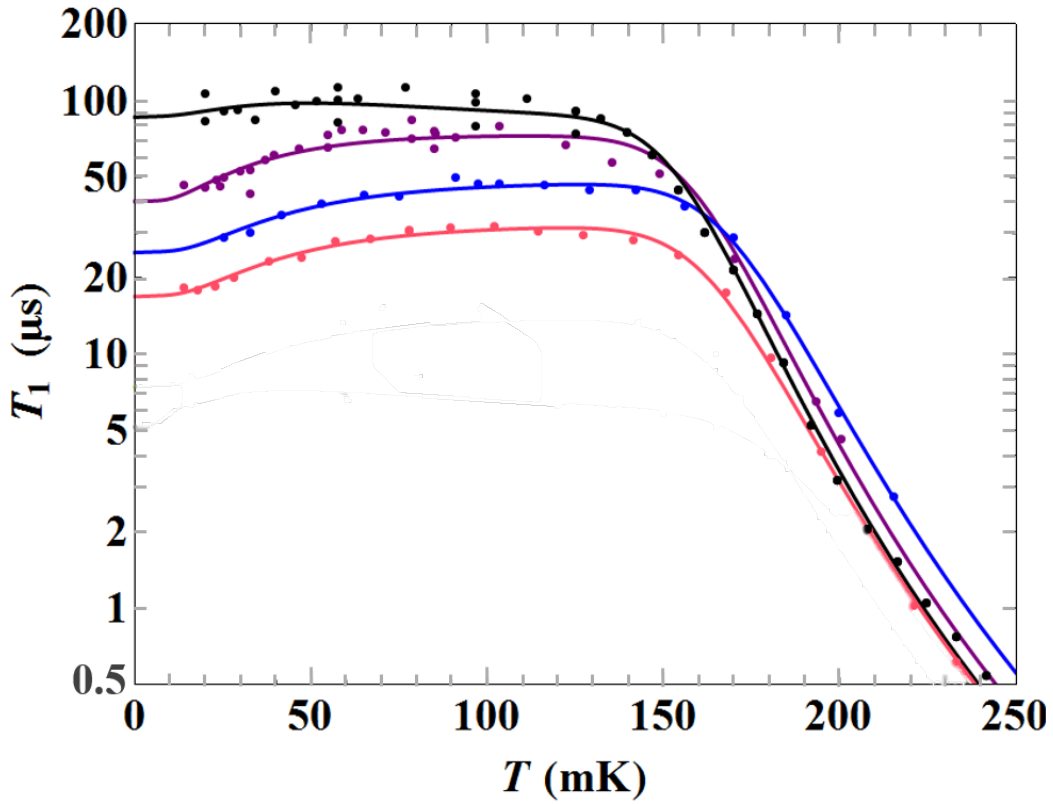

Figure 9. 3 Semi-log plot of relaxation time T_1 versus temperature T for four successive cooldowns in Feb (purple), Apr (blue), May (black), and Sep (red) 2017. Apr cooldown displayed an exponential decay with two time constants - blue points show behavior of the longer of these two time constants. Points are measured values and solid curves are model fits with parameters listed in Table 9. 1.

The solid curves in Figure 9. 3 are fits of (5.40) to the T_1 vs T data, with (5.25) and (5.26) used to model the quasiparticle densities. For each data set, all of the parameters in the model (see Table 9. 1) were determined by independent means and set to be constant, except for Δ_1, $\Delta_2 - \Delta_1$, $n_{1\mathrm{L,ne}}$, and $n_{1\mathrm{R,ne}}$. In determining these four fit parameters, we note that the sharp downturn in T_1 at higher temperatures is mainly determined by the smaller gap. On the other hand, if a plot has a section at low temperature where T_1 increases as the temperature increases, the layer with the smaller volume (layer 1) has the smaller gap and the onset occurs at a temperature that is determined by $\Delta_2 - \Delta_1$. For the data sets that did not show this increase, the two layers have nearly

equal gaps or a serendipitous set of energy gaps and quasiparticle densities. Finally, the parameter $n_{1\mathrm{L,ne}}$ sets the value of T_1 at the lowest temperatures and $n_{1\mathrm{R,ne}}$ affects to some extent how strong the rise is in T_1.

Table 9. 1 Table of device parameters and fit parameters for four consecutive cooldowns in year 2017. I assumed the Fermi energy and density of electrons in Al were $\varepsilon_F = 11.63\,eV$ and $n_e = 1.81x10^{11}\ (\mu m)^{-3}$, respectively [280].

cooldown	Feb	Apr	May	Sep
f_q [GHz]	4.00995	3.90964	3.71869	3.70712
E_c [MHz]	222	222	222	222
E_J [GHz]	10.084	9.612	8.744	8.692
E_J/E_c	45	43	39	39
τ_0 [fs]	2.86	3.04	2.98	2.98
Δ_1 [μeV]	197	204	192	191
Δ_2 [μeV]	201	209	196	196
$\Delta_2 - \Delta_1$ [μeV]	4	5	4	5
$n_{1\mathrm{L,ne}}$ [μm^{-3}]	8.8	13.6	4.0	19.9
$n_{1\mathrm{R,ne}}$ [μm^{-3}]	2.2	2.4	6.2	3.3

I note that the model captures the overall behavior of the T_1 vs T data shown in Figure 9. 3, including when there is a prominent rise in T_1 as T increased. However, a small but noticeable disagreement tends to occur in the 120 mK to 160 mK range. This knee region is where loss from thermally generated quasiparticles begins to contribute significantly, and the model tends to produce T_1 values that are slightly too long. An example of this small discrepancy is more easily seen in the linear plot in Figure 9. 2. Although the reason for this discrepancy is unclear, we can rule out a simplification we made in our model. As discussed in the previous section, our model

includes quasiparticle trapping but not quasiparticle-quasiparticle recombination. Including a recombination term in the model tends to not only reduce the number of quasiparticles but causes a distinct sharpening of the knee in the T_1 vs T curve and leads to an even larger discrepancy with the data.

From Table 9. 1, we can see that the main reason according to the model that T_1 varied from run-to-run was due to differences in the density of non-equilibrium quasiparticles. For example, in the Feb cooldown of the transmon, I found $n_{\mathrm{1L,ne}} = 8.8\ \mu\mathrm{m}^{-3}$ and $n_{\mathrm{1R,ne}} = 2.2\ \mu\mathrm{m}^{-3}$, while for the Apr and May measurements the densities ranged from 2.4 $\mu\mathrm{m}^{-3}$to 14 $\mu\mathrm{m}^{-3}$ for these parameters. In the Sep run of the transmon, cooled down in a different Leiden refrigerator, I found the smallest maximum $T_1(T)$ and densities of $n_{\mathrm{1L,ne}} = 19.9\ \mu\mathrm{m}^{-3}$ and $n_{\mathrm{1R,ne}}$ =3.3 $\mu\mathrm{m}^{-3}$. This behavior suggests that the quasiparticle trapping rate was relatively small in the left pad during the Feb, Apr and Sep cooldowns of the transmon. A plausible explanation is that there are different numbers of vortices trapped in each pad, and these numbers change from one run to the next [223]. Shielding from infrared radiation may also play a key role in the generation rate and fluctuation of non-equilibrium quasiparticle density. It was found, by the group at the University of Maryland led by Professor Wellstood and Professor Lobb, that painting the interior of refrigerator radiation can with photon absorbing material consisting of silicon carbide and black epoxy [62] substantially reduced non-equilibrium quasiparticle densities and improved their transmon T_1 in general.

Examination of Figure 9. 3 reveals that the four T_1 versus T curves for the transmon also showed somewhat different temperature dependence above 150 mK, where T_1 decreases rapidly due to thermal quasiparticles. There are a few possible explanations for this behavior: (1) run-to-run ±10 mK variations in the calibration of the thermometer, (2) actual ±10 μeV variations in the superconducting gap Δ_1 (the smaller of the two gaps) after cycling the devices to room temperature,

or (3) some other variation in the tunneling that is not properly accounted for in the model. The best fit values were $\Delta_1 = 197$, 204, 192, and 191 μeV and $\Delta_2 = 201$, 209, 196, and 196 μeV. Although these values are 5-25% higher than expected for pure bulk Al, they are reasonable for thin-film Al. In particular, the superconducting gap in Al depends on the size of the grains in the film, with smaller grains producing a larger gap [246][281]. My results are consistent with the thinner first layer tending to have a slightly higher gap than the thicker second layer. Typically, one should expect a thinner Al layer to have smaller grains and a larger gap. However, the second Al layer is grown on top of oxide that covers the first layer, and this may be altering the growth conditions slightly so that the second layer has a finer grain structure and a slightly higher gap. It is important to note that while variations in the fit values for Δ_1 could be due to run-to-run variations in the thermometry, this cannot explain a non-zero difference in the gaps for this model; the two layers must have slightly different gaps to produce a T_1 that increases with T. From Table 9. 1, we see that $\Delta_2 - \Delta_1$ ranged from 4-6 μeV for the four different cool-downs of the transmon. Although this range may seem quite small, it represents a significant run-to-run variation in the temperature where T_1 rises and suggests that slight changes may have occurred in the morphology of the Al films when the device was cycled to room temperature. This presence of morphological change is also evident in the small variations in the transmon E_J (refer to Table 9. 1).

9.2. Correlation in T_1 Fluctuations

During the acquisition of the T_1 data, the measurements were repeated to retain statistics such as the standard deviation σ_{T_1}. Figure 9. 4 shows the mean and standard deviation of T_1 from the September run. For this data, each T_1 mean was calculated by fitting to ~30 decay curves,

where each point in a single decay curve measurement consists of ~6000 DAC on-board averages. The standard deviation σ_{T_1} of T_1 and the small refrigerator temperature fluctuation σ_T are plotted as the horizonal and vertical error bars, respectively. Plotting σ_{T_1} as a function of T_1 reveals a $\sigma_{T_1} \propto T_1^{0.8}$ power dependence (see Figure 9. 5). To explain this correlation, consider a system with N_c energy dissipation channels and N_{qp} quasiparticles, such that the relaxation time is given by

$$T_1 = A\left(N_c N_{qp}\right)^{-1}, \tag{9. 1}$$

where A is a scaling constant. If N_c undergoes slow Poisson fluctuations with standard deviation $\sigma_{N_c} = \sqrt{N_c}$, the standard deviation of the relaxation time can be calculated as

$$\sigma_{T_1} = \left|\frac{\partial T_1}{\partial N_c}\right| \sigma_{N_c} = A N_c^{-1.5} N_{qp}^{-1} = \sqrt{\frac{N_{qp}}{A}} T_1^{1.5}. \tag{9. 2}$$

If instead I take N_c to be a constant and assume σ_{T_1} purely due to fluctuations in N_{qp}, one finds

$$\sigma_{T_1} = \left|\frac{\partial T_1}{\partial N_{qp}}\right| \sigma_{N_{qp}} = A N_c^{-1} N_{qp}^{-2} \sigma_{N_{qp}}. \tag{9. 3}$$

The relation in （9. 3） gives the power dependence $\sigma_{T_1} \propto T_1^{1.5}$ for trapping or recombination dominated fluctuation with $\sigma_{N_{qp}} \propto \sqrt{N_{qp}}$ (refer to section 2.1.6.2), similar to the case of a low-transparency tunneling barrier that was assumed in my model quasiparticle redistribution. This result generally agrees with data from our collaborators [282], but differs from my data.

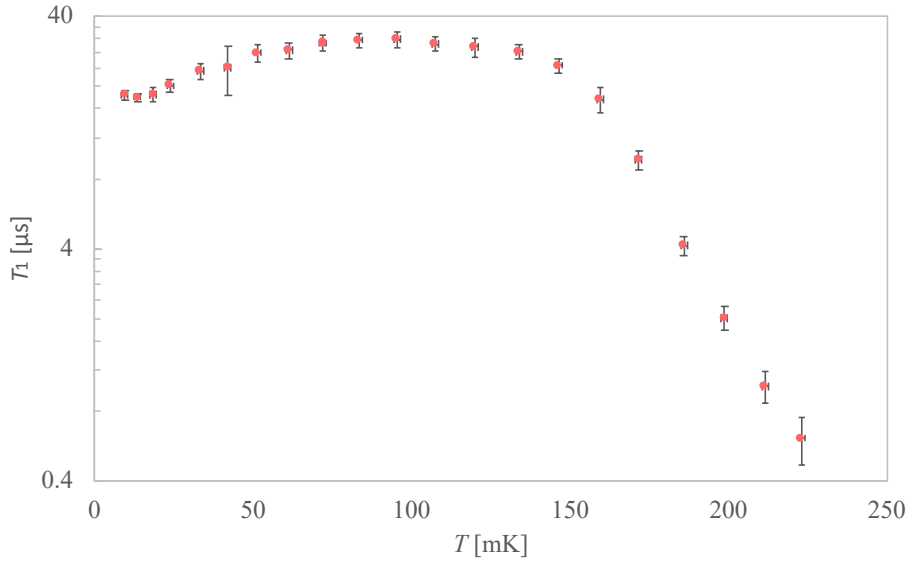

Figure 9. 4 Measured T_1 versus T and corresponding error bars (σ_{T_1} & σ_T) for the Sep cooldown.

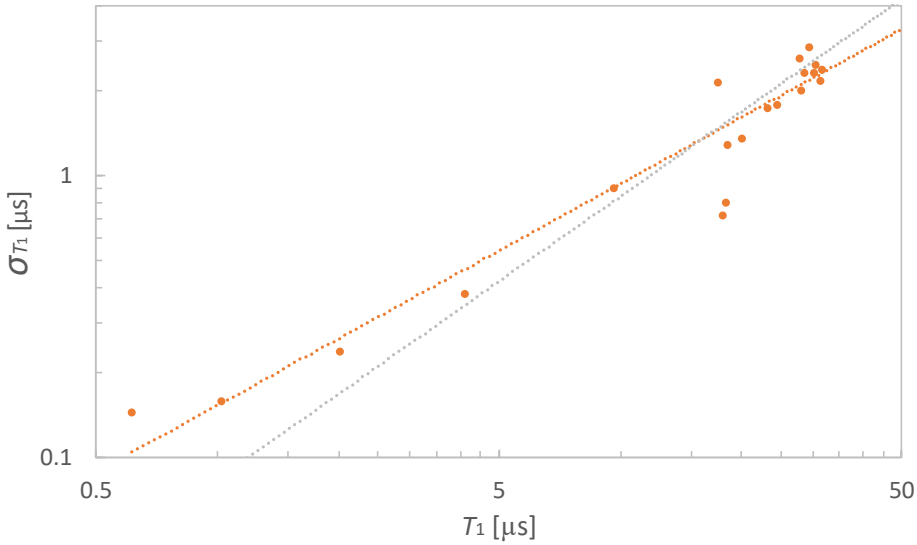

Figure 9. 5 Plot of σ_{T_1} as a function of T_1 mean (dots), fitting to simple power law yields $\sigma_{T_1} \propto T_1^{0.8}$ (pink). $\sigma_{T_1} \propto T_1$ (gray) fit is plotted as comparison.

9.3. Suppressing Non-equilibrium Quasiparticles via Microwave Pumping

To obtain further evidence for the presence of non-equilibrium quasiparticles, I implemented a quasiparticle reduction technique which had previously demonstrated by S. Gustavsson *et al.* [210]. In the technique, a series of $\mathcal{R}_x^\pi$ Pauli-X pumping gates (see Section 8.5)

are implemented before performing qubit operation gates. The idea behind the quasiparticle pumping technique is to temporarily change the energy and spatial distribution of the quasiparticles as to reduce tunneling events through the Josephson junction. The actual qubit operation gates must be performed immediately after the $\mathcal{R}_x^\pi$ pumping gates, before the distribution of non-equilibrium quasiparticles could relax back to its undriven steady state.

By implementing the pulse sequence shown in Figure 9. 6 with 50 $\mathcal{R}_x^\pi$ pumping gates during the Feb cooldown, I measured improvements in the mean T_1 and a reduction in σ_{T_1} (see Figure 9. 7). A few drawbacks of this technique should be noted: (1) prolonged total duration of qubit gates, (2) limited improvements in T_1 as quasiparticles tend to relax back to the original distribution within time scale of microseconds, (3) non-exponential decay in T_1 measurements due to the previous point hinders T_1 extraction from fitting, and (4) fidelity of the initial quantum states could be reduced by errors in the pumping sequence. Therefore, while this technique provides further evidence for the presence of non-equilibrium quasiparticles, the improvements are modest and better solutions are needed.

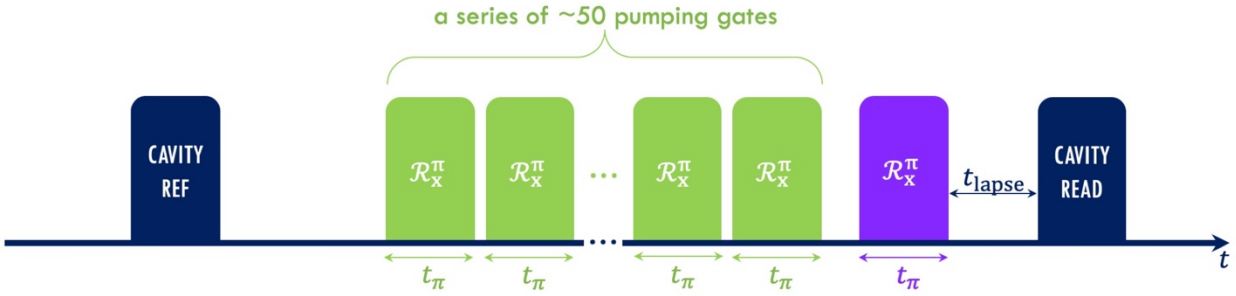

Figure 9. 6 Pulse sequence for measurement of relaxation time T_1 with up to 50 quasiparticle pumping gates (green) implemented before qubit operation gate (purple).

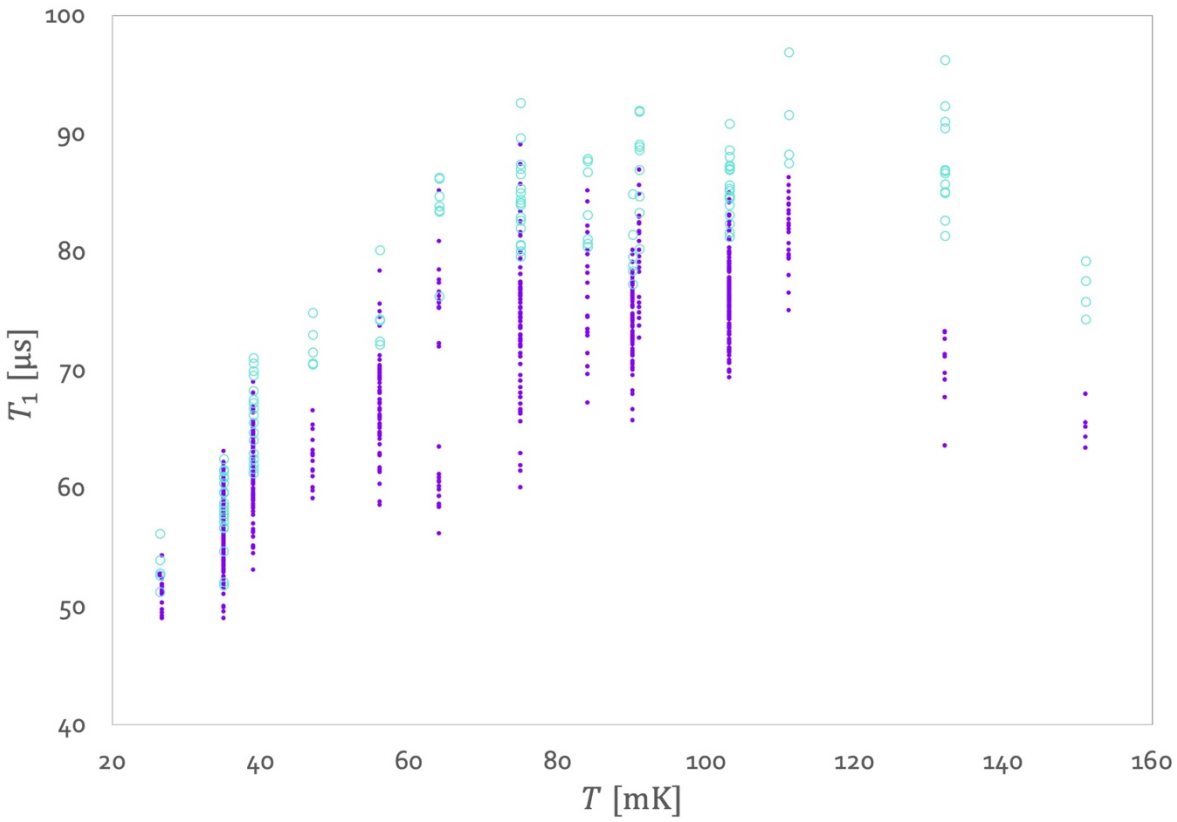

Figure 9. 7 Repeated measurements of T_1 (purple) from Feb cooldown. By implementing the pulse sequence in Figure 9. 6 for quasiparticle pumping, improvements in both T_1 mean and σ_{T_1} were observed (cyan).

9.4. An Integrated Design for Cold Quasiparticle Trap

If T_1 reduction at low temperatures (~ 30 mK) originates from the growth condition of the aluminum film, one way to improve T_1 is to invert the growth conditions, and therefore the gaps, of the two film layers. This would cause non-equilibrium quasiparticles to accumulate in a thick low-gap second layer, thus reducing the total non-equilibrium quasiparticle density seen by the Josephson junction. Figure 9. 8 shows the resulting prediction for the temperature behavior of T_1 with different configuration of energy gaps for the two aluminum layers. From the plot, a 4-fold increase in T_1 at low temperatures (~30 mK) is expected from interchanging the energy gaps of the two layers.

The gap in aluminum can be varied by growing films in the presence of low-pressure O_2. Figure 9. 9 shows measured film T_c versus chamber oxygen pressure during aluminum film evaporation in the LPS thermal evaporator. In a gap engineered Al/AlOx/Al transmon, our collaborators have measured T_1 up to 300 µs [62].

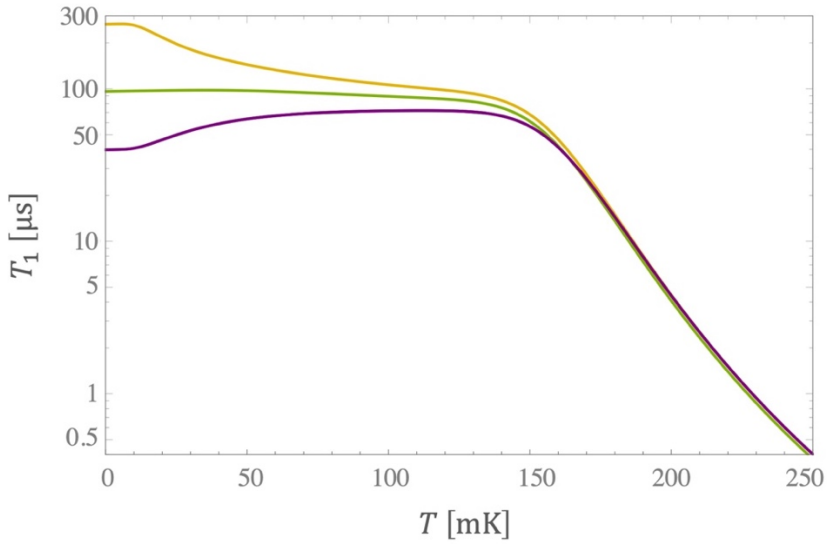

Figure 9. 8 Model prediction of T_1 versus T for transmons with different gaps in the junction electrodes, plotted using fitting parameters obtained from the Feb cooldown (refer to Table 9. 1) (purple), with interchanged gaps $\Delta_1 \leftrightarrow \Delta_2$ (yellow), and with same gaps $\Delta_1 = \Delta_2$ (green).

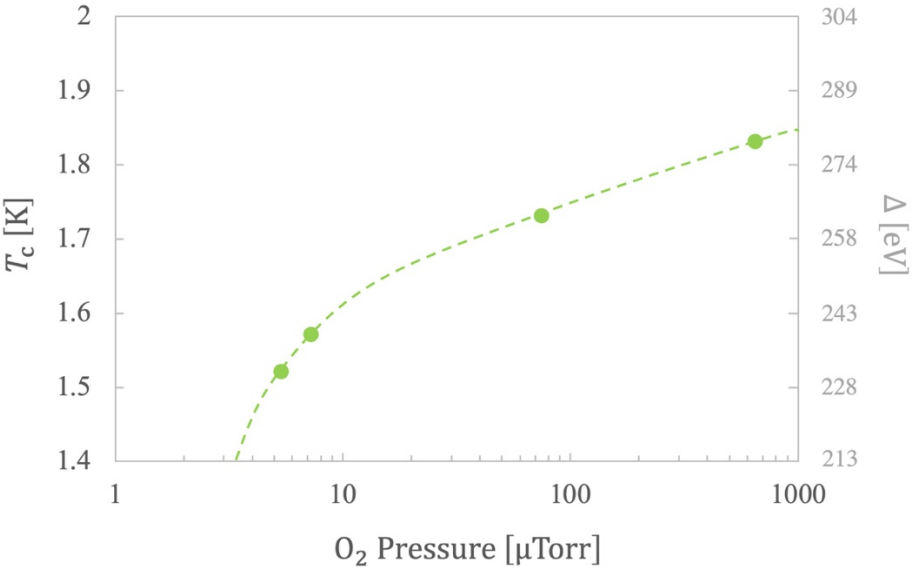

Figure 9. 9 Correlation between our chamber oxygen pressure during aluminum film evaporation and film T_c. Unpublished data taken by Anton Mobley at LPS.

More elaborated quasiparticle trapping designs can in principle be achieved using multilayer structures (see Figure 9. 10), in which non-equilibrium quasiparticles accumulate in layers that are not in direct contact with the Josephson junction, thus reducing quasiparticle tunneling through the junction. This scheme for improving T_1 by gap engineering is not exclusive to transmons. Similar phenomenon likely exists in other superconducting devices. In the next chapter, I present evidence for similar effects in TiN resonators, where we anticipate improvements in resonator Q_I via some variant of our cold quasiparticle trap design.

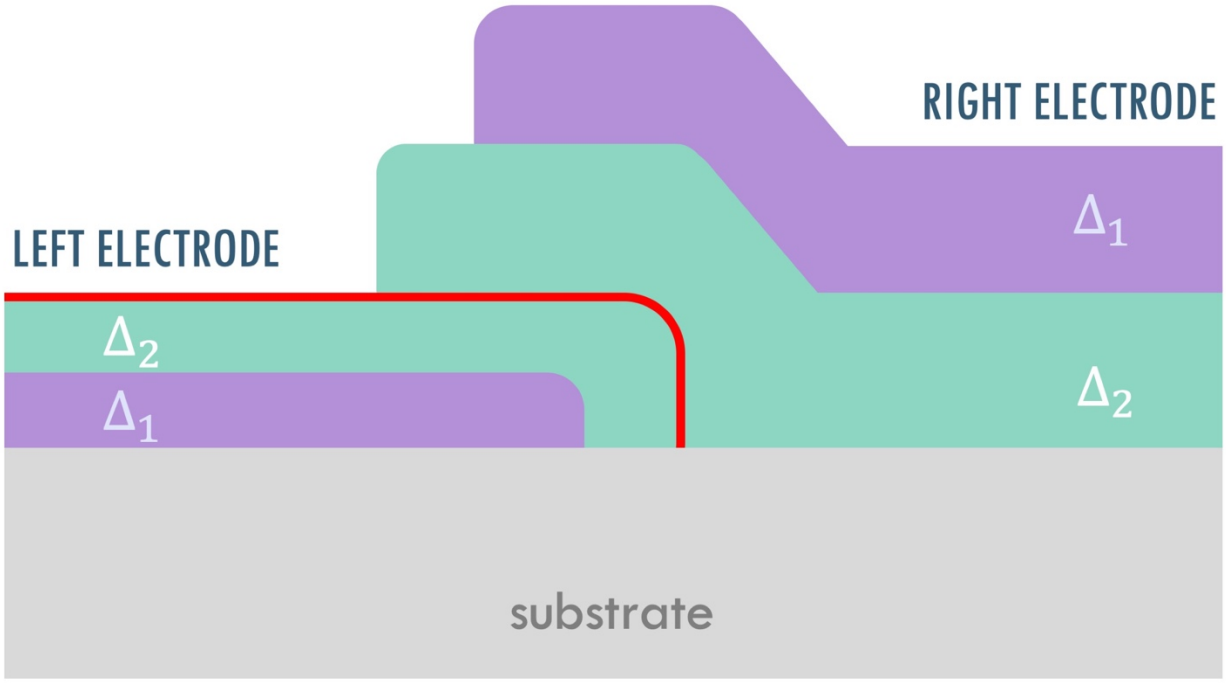

Figure 9. 10 Refinement on the quasiparticle trapping design can be achieved via multilayer structures with $\Delta_1 < \Delta_2$, in which non-equilibrium quasiparticles are condensed into layers that are not in direct contact with the Josephson junction (red), thus reducing quasiparticle tunneling rate through the junction.

9.5. Auxiliary Information

9.5.1. Excess $|e\rangle$ state qubit population

Excess $|e\rangle$ state qubit population refers to unintended excitations due to thermal background, stray radiation, microwave photons in the I/O transmission line, *etc*. At a sufficiently high temperature, non-equilibrium and thermal quasiparticles could gain enough energy to induce excess population in $|e\rangle$. Quasiparticle induced excited state populations can be predicted by the qubit $|i\rangle \rightarrow |j\rangle$ state transition rates $\Gamma_{i\rightarrow j}$ calculated from the quasiparticle tunneling current noise spectrum $S_I(f_{ij})$ given by （3.79） to （3.81）. In the steady state, excess excited population can be written as

$$P_{|e\rangle} = \left[1 + \frac{\Gamma_{1\rightarrow 0}}{\Gamma_{0\rightarrow 1}} + \frac{\Gamma_{1\rightarrow 2}}{\Gamma_{2\rightarrow 1}} + \frac{\Gamma_{2\rightarrow 3}}{\Gamma_{3\rightarrow 2}} + \cdots\right]^{-1}. \tag{9.4}$$

Using the model in （5.40） with the parameters in Table 9. 1, $P_{|e\rangle}$ can be predicted as a function of refrigerator temperature T. This prediction can be compared to the directly measured excess population extracted using （8. 4） and （8. 5） after application of a $\mathcal{R}_x^{\pi}$ gate. Figure 9. 11 shows that the predicted results generally agree with measurement for $70\ \text{mK} < T < 200\ \text{mK}$, but the measurement shows a higher excess population at temperatures below $70\ \text{mK}$. For my experiments, a likely source of excess qubit excitation is stray radiations from higher temperature stages in the refrigerator, cosmic background, radioactive elements and *etc*. Moreover, these stray radiations could also be responsible for the non-equilibrium quasiparticles in my transmon.

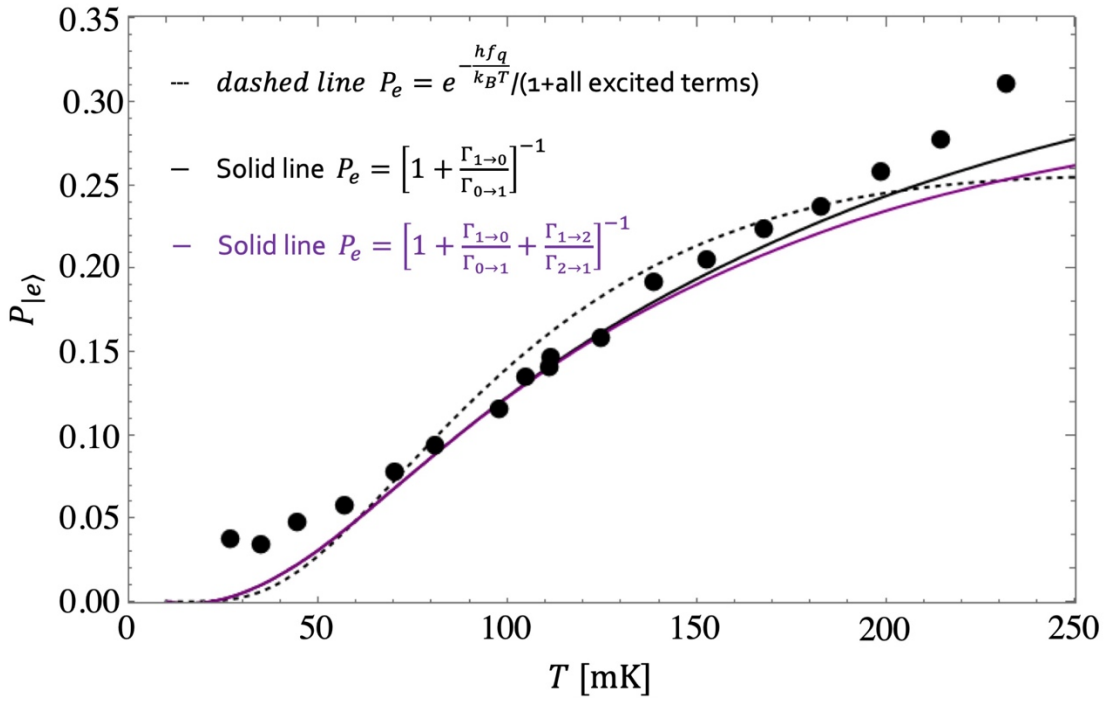

Figure 9. 11 Plot of excess excited state population $P_{|e\rangle}$ versus refrigerator temperature T. Solid dots are measured excess population, while curves are predictions from my theoretical model using (9. 4).

9.5.2. T_1 Drift after Initial Cooldown

As mentioned in Chapter 8 for device characterization, I typically perform measurements at least 1 week after the initial refrigerator cooldown to allow the qubit parameters to stabilize. Figure 9. 12 shows the drift of T_1 in the first week of the cooldown. Here I plot the transmon T_1 for my April cooldown measured in the first week after the initial cooling, in which T_1 increased steadily from 25 μs on the 1^{st} day after the initial cooling to over 40 μs by the 9^{th} day. The reason for this gradual drift is unknown. Possible causes include radiation from refrigerator components that cooled very slowly, lattice rearrangement taking place at the Josephson junction, and contamination being condensed onto the transmon surface.

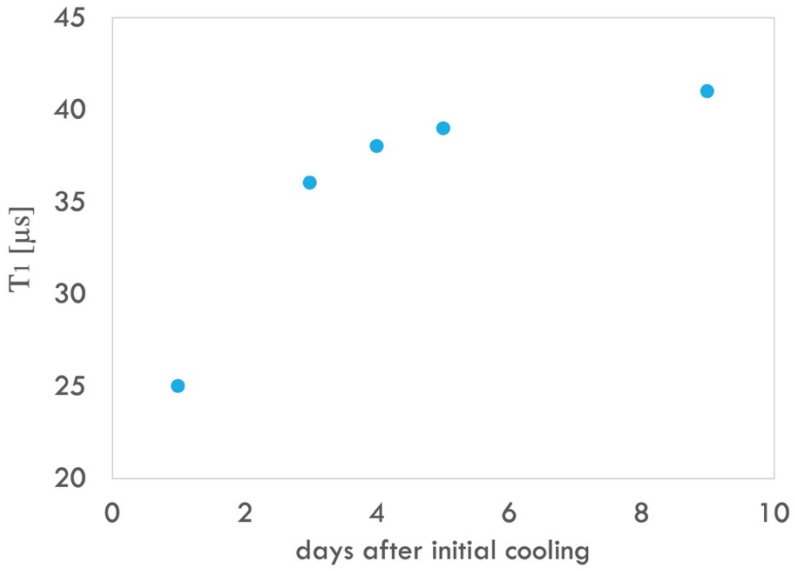

Figure 9. 12 Plot of measured T_1 versus days passed after initial cooling the refrigerator. During the period, T_1 increased steadily from 25 μs on the 1^{st} day to over 40 μs by the 9^{th} day.

9.5.3. Extracting Effective Chemical Potential

As discussed in Section 2.1.2.1, non-equilibrium quasiparticles can be accounted for using a non-zero chemical potential μ^* in the quasiparticle distribution function, as in (2.12). By comparing the quasiparticle tunneling current $I_{L\to R}$ in (5.31) with the parameters obtained from fitting my T_1 data to the model using (5.40), the chemical potentials μ_1 and μ_2 can be solved for the two regions (see Figure 9. 13). These chemical potentials merely account for the non-equilibrium quasiparticle densities and do not introduce any new physics, *i.e.* they are strictly for bookkeeping the density of quasiparticles. As expected, μ_1 and μ_2 go to zero when thermal quasiparticles start to populate at about $\frac{1}{10}T_c \sim 120$ mK.

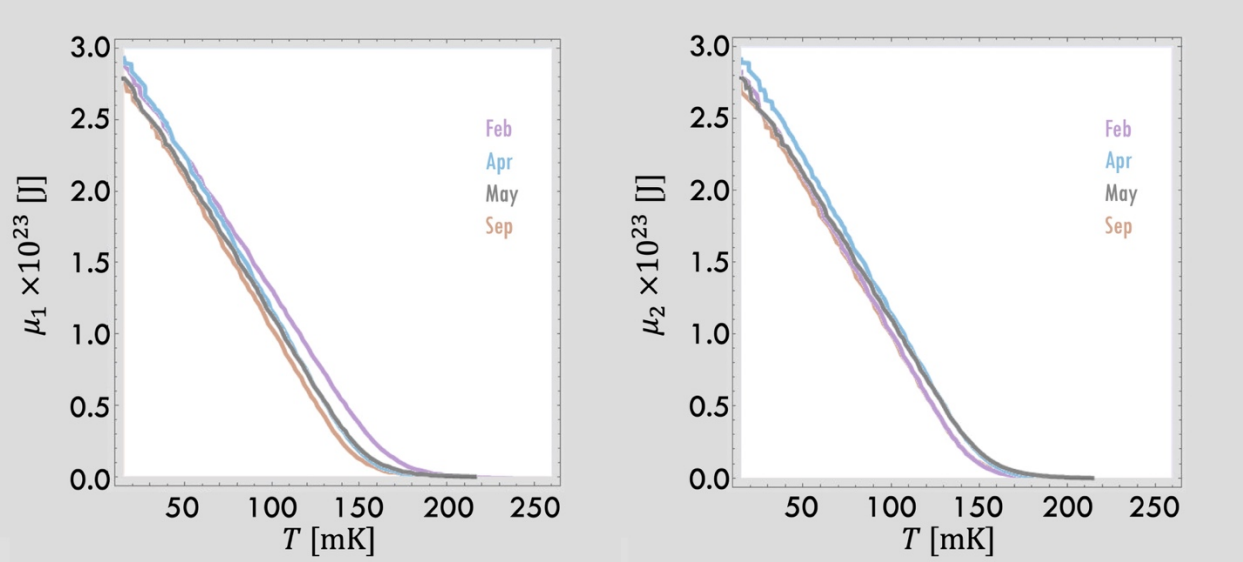

Figure 9. 13 Effective chemical potentials μ_1 and μ_2 solved for the two regions of energy gaps Δ_1 and Δ_2, respectively, for my Feb (purple), Apr (blue), May (gray) and Sep (pink) cooldown data.

CHAPTER 10

Loss in Titanium Nitride Coplanar Resonator

10.1. An overview of Titanium Nitride

Titanium nitride (TiN) is a hard ceramic material widely used as a protective coating on metal tools. Single crystal TiN becomes superconducting at temperatures below ~ 6 K. Depending on growth conditions, a significant amount of morphology change had been observed and its critical temperature T_c can vary significantly [65]. By introducing disorder into TiN thin films, a transition from conductor to insulator can also be observed, which has been used to create a "superinsulator" with resistance rising by factor of 10^5 near zero temperature [283]. Apart from these curious properties, thin film TiN has two attractive attributes: (1) very small dissipation at microwave frequencies, and (2) high kinetic inductance. These qualities make TiN potentially useful for astronomical detectors [284] and superconducting qubits [48].

Microwave resonators fabricated from TiN could attain quality factors on the order of or exceeding one million [65]. In a study by J.B. Chang *et al.*, TiN was used in the shunting capacitor of a transmon and the device showed noticeable improvements in the qubit lifetime [48]. More recently, an extensive set of TiN resonator measurements have been conducted to extract the magnitude and participation of losses associated with various interfaces, with the assumption that the Q_I is limited by dielectric loss [285].

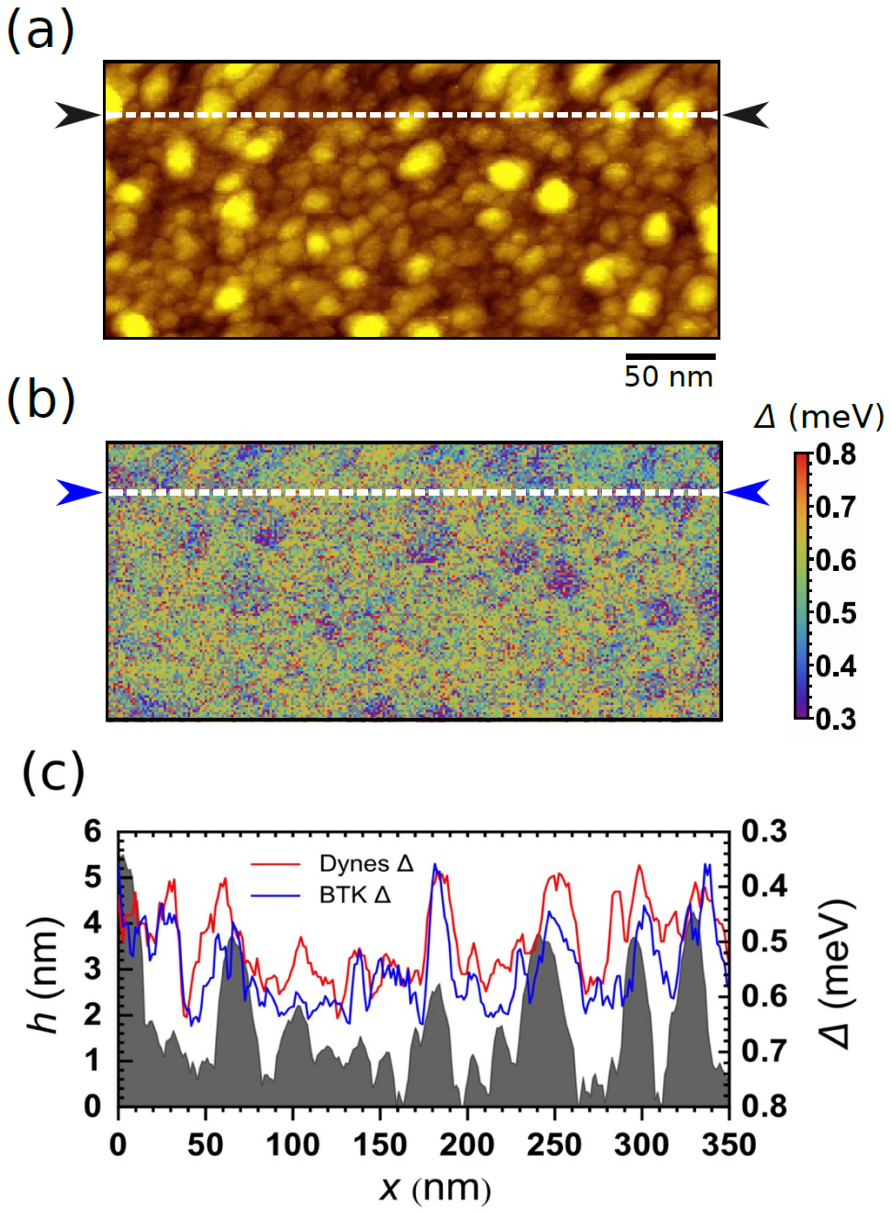

Figure 10. 1 Original figure from ref. [288]. STM scan done by Dr. Wan-Ting Liao on thin film TiN grown by KDO research group both at LPS [67]. (a) Topography of 50 nm thick TiN film taken at 100 pA and 4 mV bias showing rough surface. (b) Corresponding maps of the gap Δ. (c) Line section through (a) and (b) showing anti-correlation between the gap and topography (gray). Note reversed scale for Δ, i.e. large gaps correspond to small h. Red curve shows Δ vs. x from fits to the Dynes model. All data taken at T = 0.5 K using a vanadium tip.

There are still a number of basic questions about thin film TiN. For example, when TiN was used as the shunting capacitor for a transmon, the resonant frequency was found to increase with temperature in a way not explained by two-level system loss [48]. Bueno *et al.* also found that the responsivity to pair-breaking radiation anomalously increased with increased radiation power [286]. To explain this behavior, they speculated that either the superconducting gap varied spatially, trapping non-equilibrium quasiparticles in the low-gap region, or the film consisted of random arrays of superconducting islands connected by weak-link Josephson junctions. Moreover, Hsieh *et al.*, using a low-temperature STM, measured large variations in the superconducting gap for their TiN films [287]. Figure 10. 1 shows an STM scan done by Dr. Wan-Ting Liao [288] on a thin film TiN grown by KDO research group at LPS [67], where the film surface clearly shows a distribution of superconducting gaps. These recent studies motivate further investigations on the energy gap inhomogeneities in thin film TiN.

10.2. PAMBE Growth of TiNx Film

The high-quality TiN film in my studies was deposited via plasma-assisted molecular beam epitaxy (PAMBE) by Dr. Christopher J. K. Richardson *et al.* at LPS [65]. For this deposition technique, titanium was placed in a conventional high-temperature effusion cell and an RF-plasma source was used to crack the nitrogen molecules, providing a nitrogen-rich environment for growth of TiN. The film was grown in the (111) crystallographic orientation (see Figure 10. 2) on a float zone-refined high-resistivity silicon (111) wafer with sheet resistance $> 5000\ \Omega$ cm.

The silicon (111) wafer was prepared by rinsing sequentially in trichloroethylene, acetone, methanol, and isopropyl alcohol. The native oxide was then removed using 5% hydrofluoric acid

etchant, followed by development of step edges with 40% ammonium fluoride etchant. After rapidly loading into the ultrahigh vacuum chamber, the wafer was heated to 150 °C for desorption of surface water, then to 800 °C for 15 mins to remove any organic residue, and finally maintained at 750 °C for film growth.

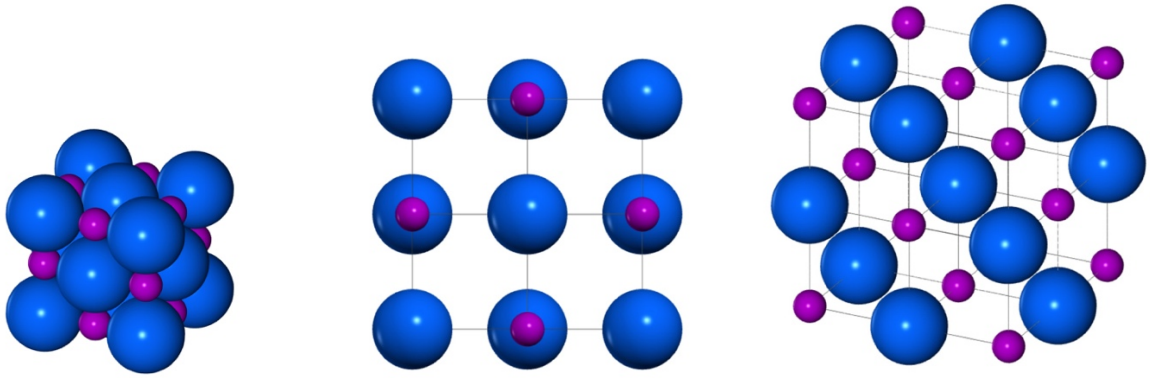

Figure 10. 2 (Left) Illustration of the TiN crystal lattice. (Middle) TiN (111) crystallographic orientation. (Right) TiN (100) crystallographic orientation.

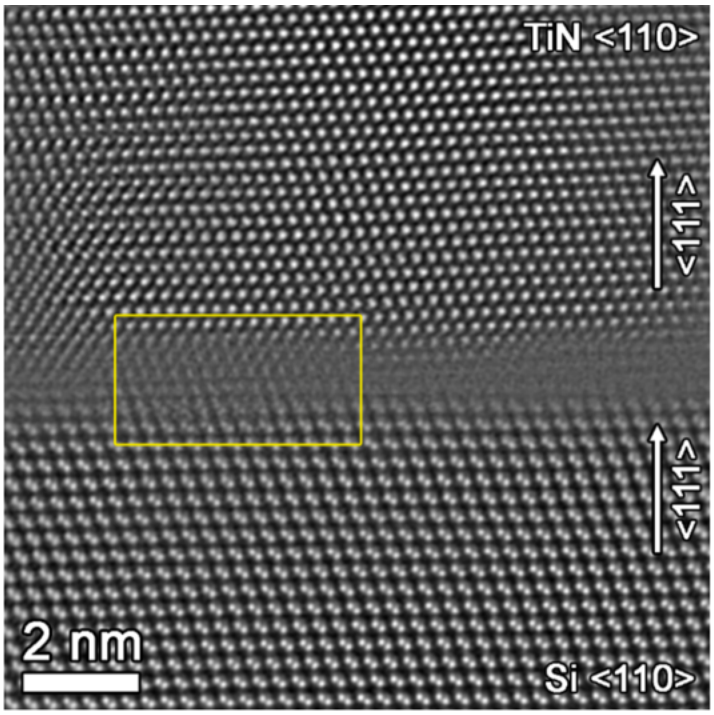

Figure 10. 3 Figure from Ref. [65]. Scanning transmission electron microscopy of the TiN/Si interfacial region.

Film growth was initiated by nearly simultaneous introduction of Ti and N fluxes, with N_2 flow at 2.0 sccm and 5-nines pure titanium held at 1800 °C. The film was grown at $0.061\ \text{Å}/s$ at 3.5×10^{-6} Torr. The 50 nm thick TiN (111) film had a low-temperature normal resistivity of 20 μΩcm with a critical temperature of $T_c = 5.40$ K. Detailed film characterizations are performed [65]. Figure 10. 3 [65] shows an STEM scan of the TiN(111)-Si(111) interface of this film.

10.3. Patterning of the Chip

Coplanar waveguide resonators were patterned onto the TiN chip via projection optical lithography [65] and subsequently dry etched using a reactive ion etch (RIE) system with a gas mixture of 12.5 sccm BCl3, 2.5 sccm Cl2, and 4 sccm He at 3.5 mT pressure with 500 W applied rf power. The resulting etch depth was about 174 nm, including a trench depth (see Section 4.6.2) of 114 nm into the Si. The sample was then dipped in phosphoric acid for softening of photoresist residue and stripped in 80 °C Microposit remover 1165. The chip fabrication was completed with sequential rinses in de-ionized water, acetone, methanol, and isopropanol.

Figure 10. 4 shows a photomicrograph of the fabricated resonator. Each chip contained five quarter-wave coplanar resonators of different fundamental resonant frequencies, ranging from approximately 3.31 GHz to 5.10 GHz. The ground plane surrounding the resonators had 5 μm × 5 μm square perforations to trap vortices from stray magnetic fields. A single 5 mm x 5 mm resonator chip was diced from the wafer and packaged in a copper box attached with non-magnetic SMA connectors. The fabrication was done by Ashish Alexander from the MBE group at LPS and details can be found in refs. [65][205].

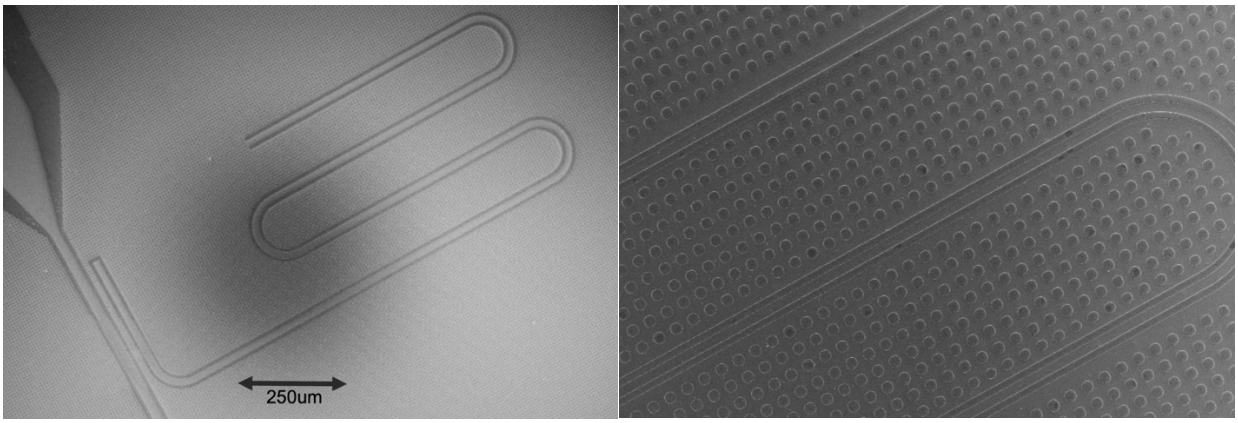

Figure 10. 4 (Left) Photomicrograph of TiN resonator. (Right) Ground plane is perforated for flux trapping.

10.4. Curious Temperature Dependence in Q_I and f_0 shift

In microwave loss studies of a TiN thin film resonator deposited by plasma-assisted molecular beam epitaxy (PAMBE) [65], I measured a curious increase in the resonator Q_I as the temperature of the device was increased from $T \leq 70$ mK to 600 mK. Figure 10. 5 and Figure 10. 6 show the measured Q_I and the fractional frequency shift $\delta f_0/f_0 = f_0(T)/f_0(30\text{ mK}) - 1$ versus T from 30 mK to 1.1 K; this data was acquired with approximately 200 microwave photons stored on resonance. Below $T \leq 70$ mK, both f_0 and Q_I were found to be temperature independent with $Q_I = 850{,}000$. As the temperature of the device was increased above 70 mK, f_0 increased by 2 parts per million at 400 mK and Q_I reached a maximum value of $Q_I = 2 \times 10^6$ at 600 mK. The changes in the fractional frequency at low temperature suggest changes in either the capacitive element or the kinetic inductance of the resonator. Above 600 mK, f_0 and Q_I rapidly decreased as expected due to thermal quasiparticles populating the superconductor.

To explain the temperature dependence below 600 mK, several models were considered (see Figure 10. 5 and Figure 10. 6). The two-level system (TLS) model of dielectric loss (purple dashed curves) given by （4.30） and （4.31） gives a poor fit to the data and the fractional

frequency shift in particular has an opposite trend to the low temperature data. Similarly, the effect of non-equilibrium quasiparticles in a homogeneous superconductor, as given by （4.39） and （4.41）, predicts a flat dependence for the loss and fractional frequency shift below $T^* = 791$ mK (see blue dashed curves), which doesn't explain the observed low temperature behavior. Finally, my model of non-equilibrium quasiparticle redistribution in a superconductor with two regions with different energy gaps (black solid curves) described by （5.65） to （5.66） successfully captures the low temperature features in the data, yielding the fitting parameters $\Delta_1 = 915.0\ \mu eV$, $\Delta_2 = 884.4\ \mu eV$, $\frac{\Omega_1}{\Omega_2} = 0.3919$, $n_{neqp,1} = 74.64\ \mu m^{-3}$, and $\alpha = 0.5895$.

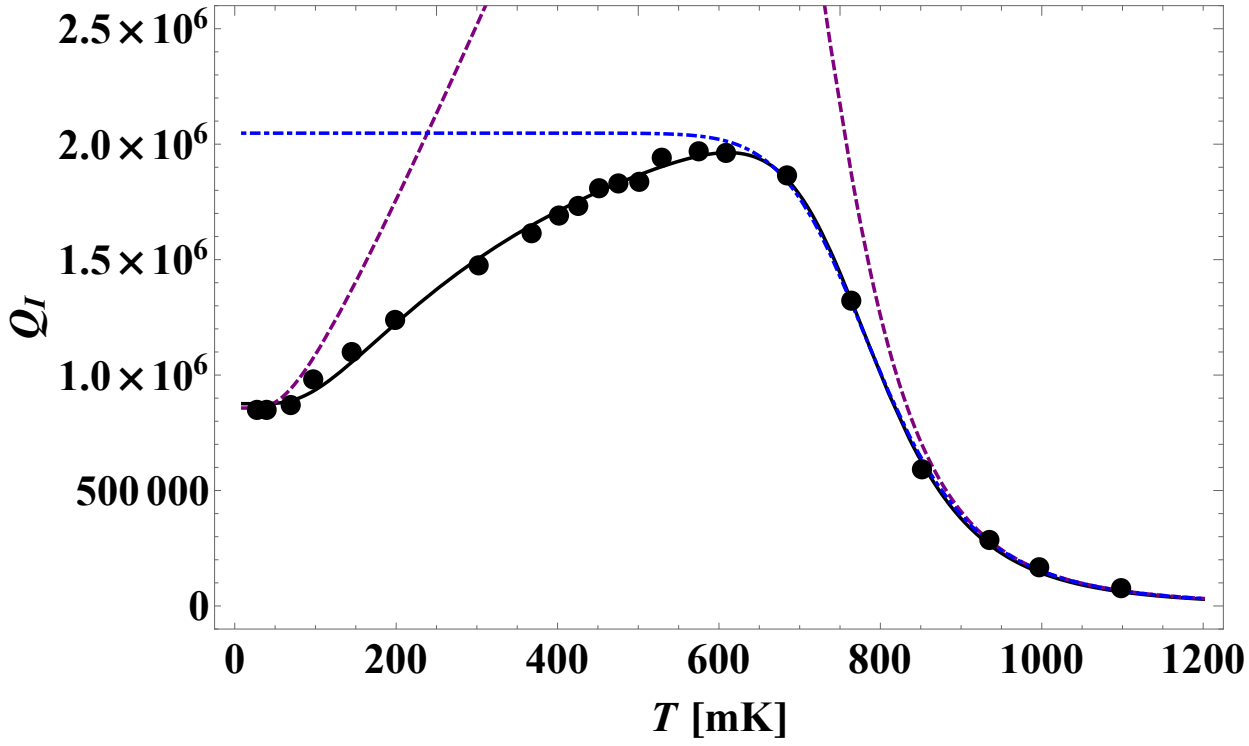

Figure 10. 5 Comparison of measured Q_I (dots) between various loss models of TLS (purple), non-equilibrium quasiparticle in homogeneous (blue), and inhomogeneous (black) superconductors. Black curve is plotted using （5.65） with $\Delta_1 = 915.0\ \mu eV$, $\Delta_2 = 884.4\ \mu eV$, $\frac{\Omega_1}{\Omega_2} = 0.3919$, $n_{neqp,1} = 74.64\ \mu m^{-3}$, and $\alpha = 0.5895$.

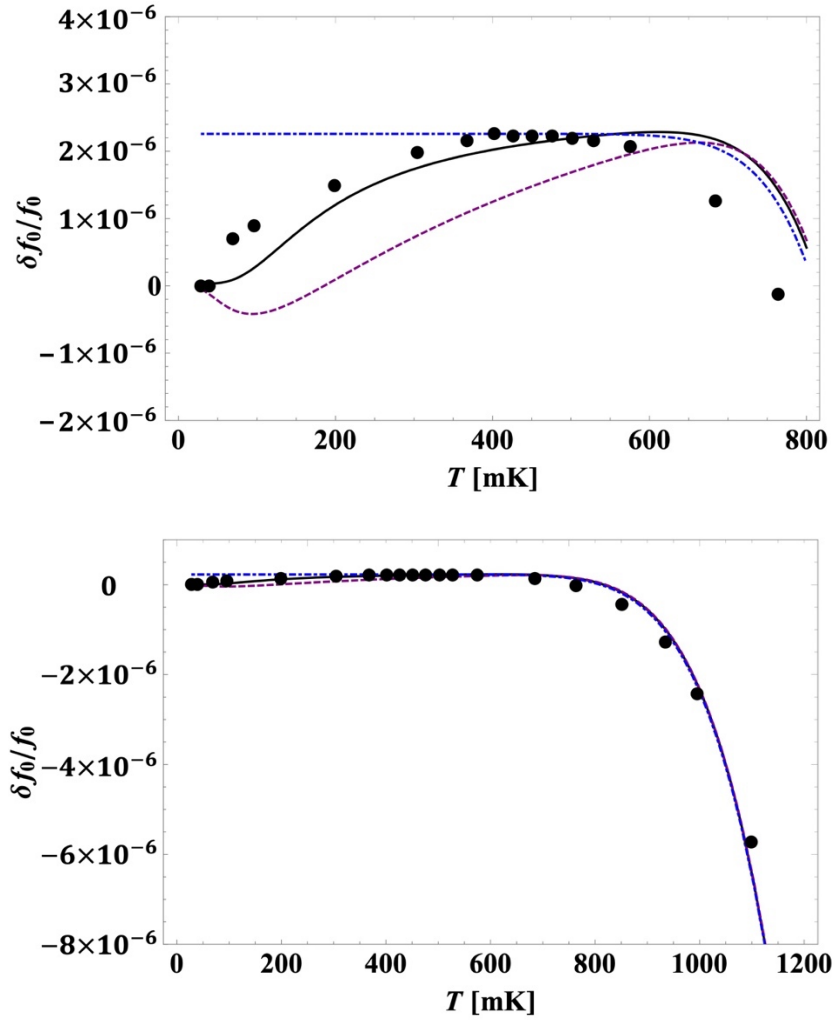

Figure 10. 6 Plot of $\delta f_0/f_0$ for TLS (purple), non-equilibrium quasiparticle in homogeneous (blue), and inhomogeneous (black) superconductors, corresponding to Figure 10. 5. Data shown as black dots. Right plot shows full temperature range.

In my model of non-equilibrium quasiparticles, I assumed that the TiN superconductor had two superconducting regions of volumes Ω_1 and Ω_2, with corresponding superconducting energy gaps Δ_1 and Δ_2. At a low enough temperature, quasiparticles accumulate in the lower gap Δ_1 region, increasing the quasiparticle density in that region resulting in a large distribution temperature T^* and more loss per the energy stored in that region of the device. As the refrigerator temperature is increased, non-equilibrium quasiparticles begin to have enough thermal energy to diffuse into the higher gap Δ_2 region, leading to a decrease in the quasiparticle density in region 1.

Figure 10. 7 shows a plot of the temperature dependence of the quasiparticle density in the lower gap Δ_1 region. This is the region that dominates the loss. The distribution temperature T^*, solved numerically for the data in Figure 10. 5, is plotted in Figure 10. 8. I note that $T^* \gg T$ for $T \lesssim 300$ mK. To fit my data, I find that the volume for region 2 has to be large compared to region 1, with the majority of the inductive energy stored in region 1. This means that the second terms in （5.65） that accounts for loss of region 2 can be neglected. Physically, this is consistent with the edges of the TiN resonator having the lower superconducting gap (see Section 4.4). I note that somewhat weaker temperature behavior for Q_I and $\delta f_0/f_0$ have been reported for Al and Nb thin film resonators by T. Noguchi *et al.* [289], for which they attribute to the interaction of non-equilibrium quasiparticles with the Kondo effect. I also note that many of our Al resonators do not show such a prominent increase in Q with an increase in temperature at the lowest temperatures.

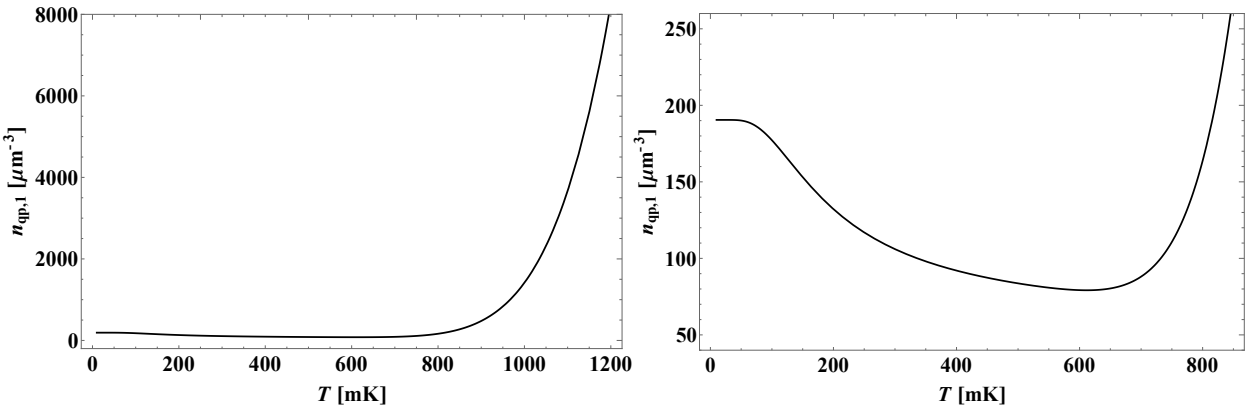

Figure 10. 7 Plot from the model of the quasiparticle density versus temperature in the lower gap Δ_1 region that dominates the loss. As the temperature is increased, non-equilibrium quasiparticles begin to have enough thermal energy to diffuse into the higher gap Δ_2 region, leading to a decrease in the quasiparticle density in region 1. Right plot shows detailed view of low temperature behavior.

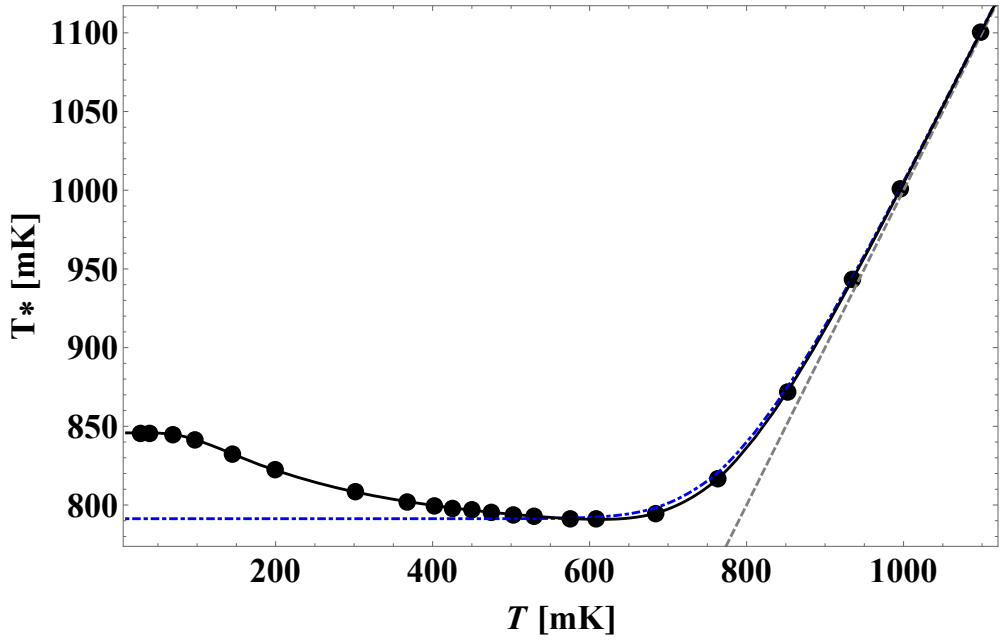

Figure 10. 8 Plot of distribution temperature T^* for region 1 solved numerically (dots) for the data in Figure 10. 5. Curves are solved T^* from model of non-equilibrium quasiparticle in homogeneous (blue), and inhomogeneous (black) superconductors. Above $T\sim900\,mK$, $T^* \simeq T$ as expected (gray dashed line).

To further study these devices, Q_I and $\delta f_0/f_0$ were measured as function of temperature when illuminating the device with $\lambda = 1.55$ mm IR laser light (see Figure 10. 9 to Figure 10. 11). When light is absorbed, two independent effects occur concurrently in my model. First, the phonons in the TiN film and substrate are heated. This heating effect is most apparent for temperatures < 200 mK; note how Q_I increases with illumination in much the same way as it does when the temperature increases. The second effect corresponds to an increase in the density of quasiparticle with increasing laser intensity. While effects from an increase in n_{qp} are most apparent at the largest intensities, a continual monotonic decrease in Q_I is most visible at $T\sim$ 500 to 550 mK, where Q_I reaches a maximum value.

I attempted to incorporate both effects into the two-gap model by replacing the temperature in （5.65） with a power law dependence [186]

$$T_{eff} = (T^{\,n} + {T_0}^n)^{1/n}, \tag{10. 1}$$

where n is a constant and T_0 is the phonon temperature produced by each applied laser intensity. Using (10. 1) and the parameters Δ_1, Δ_2, $\frac{\Omega_1}{\Omega_2}$, $n_{neqp,1}$, and α obtained from fitting with no laser power (see Figure 10. 5), I fit Q_I versus temperature to extract T_0 and $n_{neqp,1}$ at each laser power (see solid curves in Figure 10. 9 to Figure 10. 11). These fits yielding $n = 2.6$. The fitting parameters T_0 and the change in $\delta n_{neqp,1}$ versus laser intensity are plotted in Figure 10. 12 and Figure 10. 13, respectively. The extracted heating can be fit to a power law [186]

$$T_0 = c_T\, I^{v}. \tag{10. 2}$$

The increase in non-equilibrium quasiparticle density as functions of applied laser intensity (I) can be fitted to [186]

$$\delta n_{neqp,1} = c_n\, I\,. \tag{10. 3}$$

Best fits yielded an effective heating coefficient $v = 0.19$, which is similar to a T^5 power law. From fit, $c_T = 79.9\ [\mathrm{mK\ (\mu m^2/fW)^{-v}}]$ and $c_n = 16.9\ [\mathrm{\mu m^2/fW}]$. I note that illuminating the target resonator with IR laser also heats up the neighboring resonators on the same chip, however, the effective heating in resonators separated from the target resonator by a waveguide is significantly less. This may suggest that heat is mainly transferred by flow of quasiparticles instead of phonons.

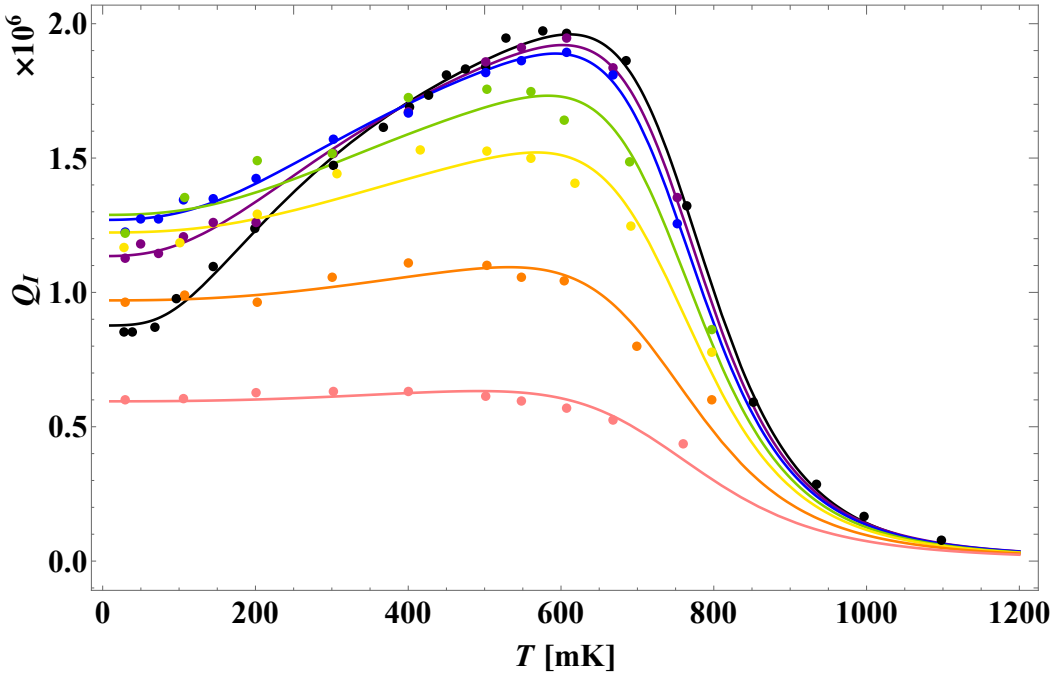

Figure 10. 9 Temperature dependence of Q_I for different applied laser intensities (black: 0 aW μm^{-2}, purple: 47 aW μm^{-2}, blue: 221 aW μm^{-2}, green: 942 aW μm^{-2}, yellow: 2096 aW μm^{-2}, orange: 5000 aW μm^{-2}, pink: 15000 aW μm^{-2}). Fitting to （10. 1） yields $n = 2.578$.

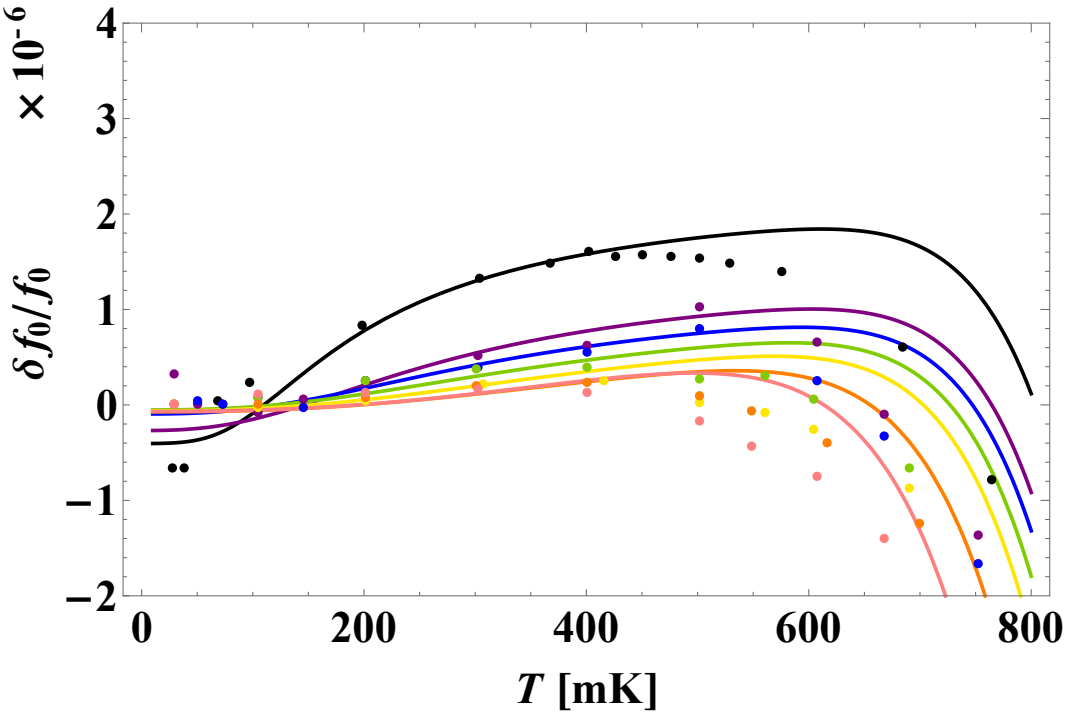

Figure 10. 10 Fractional frequency shift corresponding to Figure 10. 9 for different applied laser intensities (black: 0 aW μm^{-2}, purple: 47 aW μm^{-2}, blue: 221 aW μm^{-2}, green: 942 aW μm^{-2}, yellow: 2096 aW μm^{-2}, orange: 5000 aW μm^{-2}, pink: 15000 aW μm^{-2}).

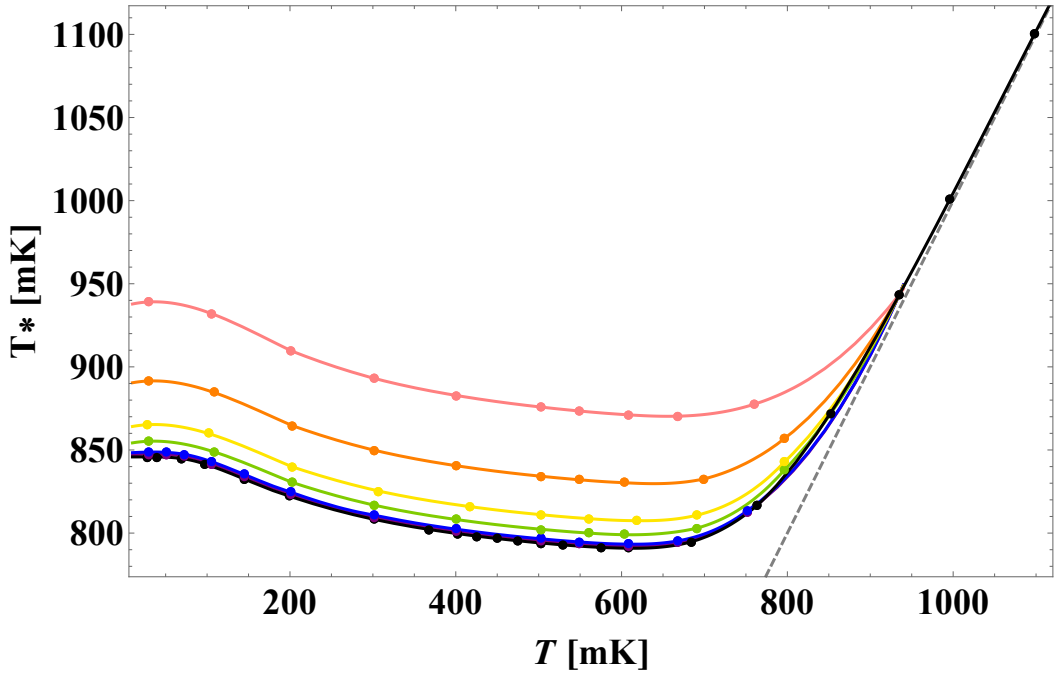

Figure 10. 11 Parker temperature T^* solved for data in Figure 10. 9 for different applied laser intensities (black: 0 aW μm^{-2}, purple: 47 aW μm^{-2}, blue: 221 aW μm^{-2}, green: 942 aW μm^{-2}, yellow: 2096 aW μm^{-2}, orange: 50000 aW μm^{-2}, pink: 15000 aW μm^{-2}).

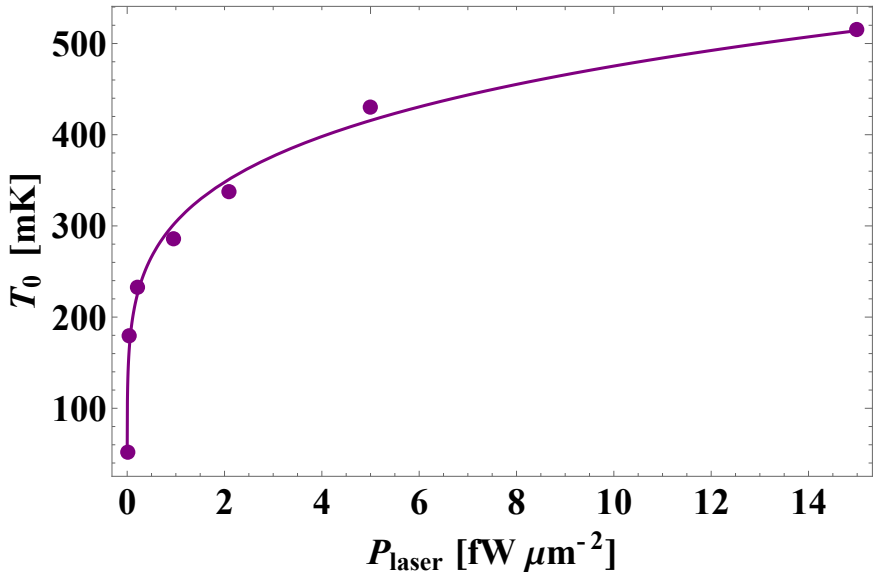

Figure 10. 12 Fit to effective heating model in (10. 2) yields $v = 0.19$ for the power law and $c_T = 80\ [mK\ (\mu m^2/fW)^{-v}]$.

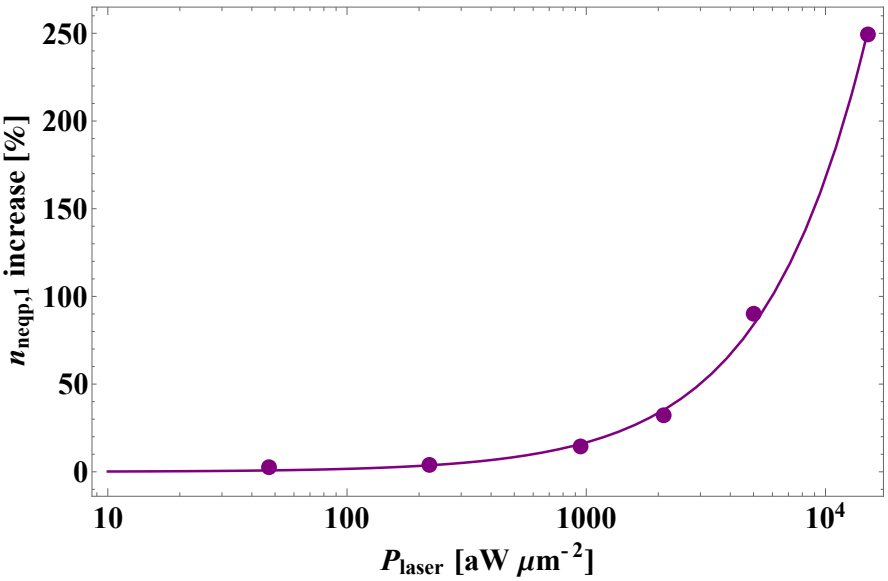

Figure 10. 13 Fit of the percentage increase in quasiparticle density toequation （10. 3） gives $c_n = 16.9\ [\mu m^2/fW]$. The quasiparticle density increases linearly with applied laser power as expected.

10.5. Transient Measurement of Non-equilibrium Quasiparticle Recombination

For the studies discussed in the preceding section, the laser was on continuously at various powers to create steady non-equilibrium quasiparticle generation rates. Figure 10. 14 shows the in-phase and quadrature components of S_{21} data with the laser either on or off. As we can see from this figure, a small change in the depth of the resonance is observed from the in-phase data and a large linear shift in f is observed from the quadrature component. To take transient measurements of quasiparticle population decay, I set the VNA frequency f at a fixed frequency in between the shifted and unshifted resonance frequencies. I then measured the slow thermal relaxation rate from the response of S_{21} over long times after the laser was switched off. This slow timescale was on the order of 10^2 ms, implying that the phonon temperature was relatively stable on the microsecond time scale. Next, I tried to observe the faster quasiparticle population decay by

pulsing the laser on and off with a 50% duty cycle of 5 ms period. The VNA measurements were triggered in tune with the laser pulses.

In pulsed mode laser injection, the S_{21} transmission (see Figure 10. 15) was measured at a fixed frequency f_s near the resonance (see Figure 10. 14). I mapped this change in S_{21} linearly to a shift in f_0, and then to shift in non-equilibrium quasiparticle density n_{neqp}. The decay measurements were then repeated at different temperatures T. The longest decay times occurred at about $T \sim 450$ mK (see Figure 10. 16).

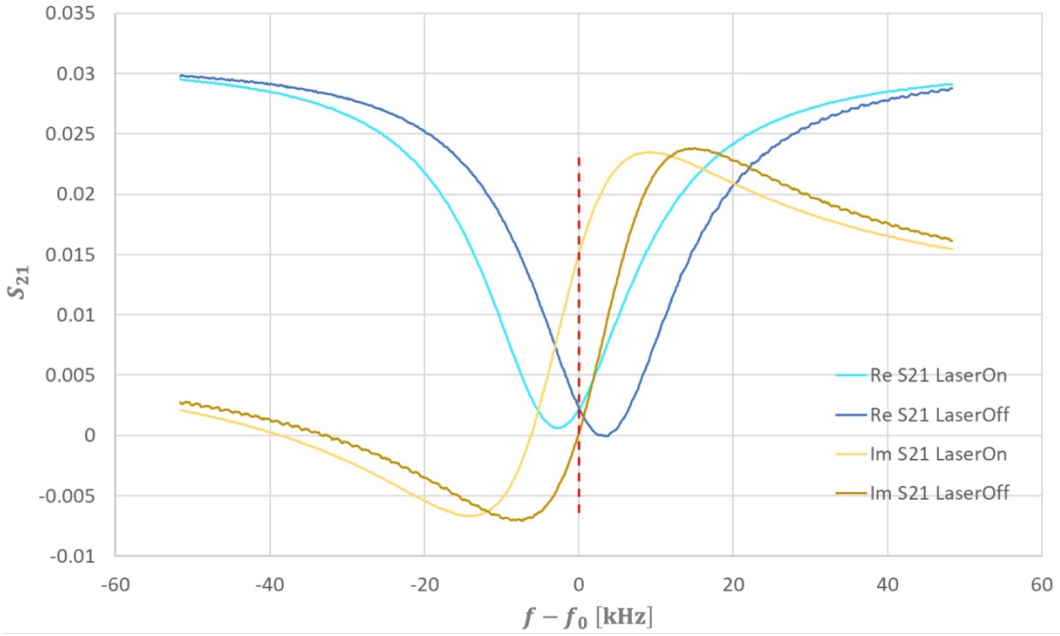

Figure 10. 14 Real and imaginary parts of S_{21} measured when laser is continuously on or off. Red dashed line corresponds to the frequency I used for pulsed laser measurements. After the laser is turned off, Im S_{21}shifts from yellow curve to brown curve, producing a linear drop in Im S_{21} at $f - f_0 = 0$. On the other hand, Re S_{21}shifts from cyan curve to dark blue curve, causing Re S_{21} to decrease and then increase as the resonance dip passes through the point at $f - f_0 = 0$.

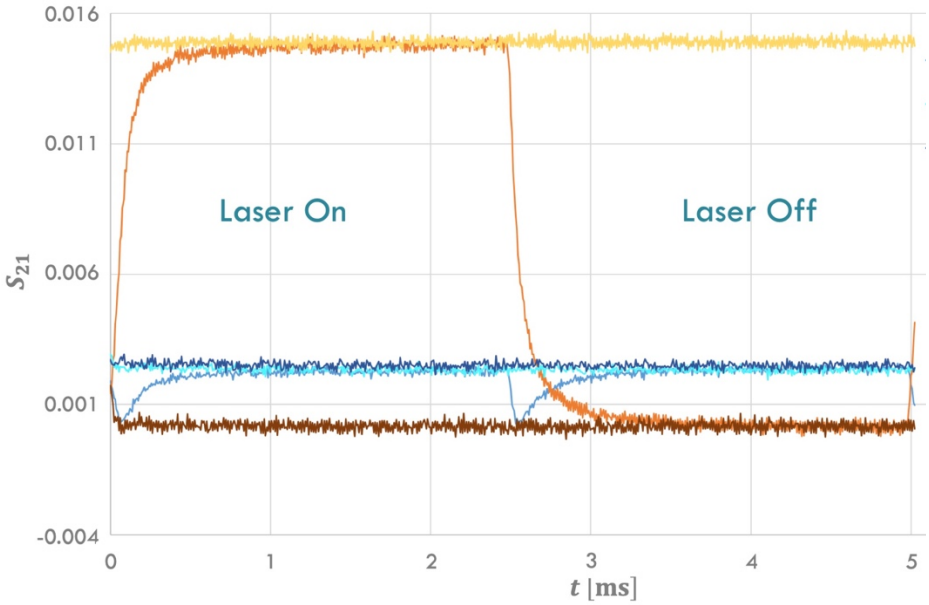

Figure 10. 15 S_{21} transmission measured at a set frequency near the resonance during pulsed laser injection. Laser is turned off at $t{\sim}2.5\ ms$. After laser is turned off, $Im\ S_{21}$ (orange) decays from 0.015 corresponding to the value when laser is continuously on (yellow) to 0 corresponding to the value when laser is continuously off (brown). $Re\ S_{21}$ (light blue) decays from 0.003 corresponding to the value when laser is continuously on (cyan) to 0 and then back to 0.003 corresponding to the value when laser is continuously off (dark blue).

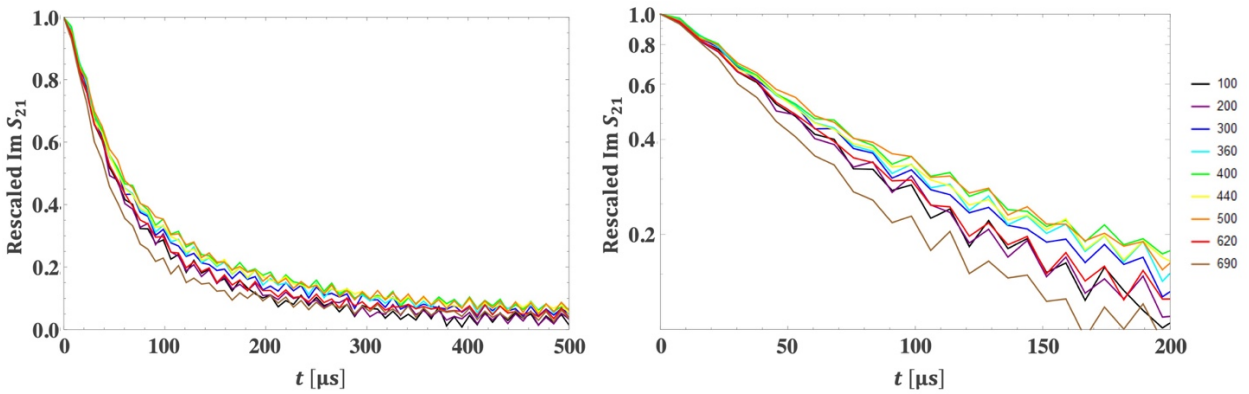

Figure 10. 16 Decay measurement of $Im\ S_{21}$ after laser is switched off for T =100 (black), 200 (purple), 300 (blue), 360 (cyan), 400 (green), 440 (yellow), 500 (orange), 620 (red), 690 (brown) mK.

The extracted decay of the quasiparticle density n_{neqp} after the laser was pulsed off was fit to a decay model consisting of 3 contributions: (1) a recombination term R_r proportional to ${n_{qp}}^2$, (2) a trapping rate Γ_t proprtional to n_{qp}, and (3) a constant equilibrium quasiparticle creation

rate Γ_c due to the thermal bath and the unknown source(s) of nonequilibrium quasiparticles. I can then write

$$\frac{dn_{neqp}}{dt} = -R_r {n_{neqp}}^2 - \Gamma_t n_{neqp} + \Gamma_c. \tag{10. 4}$$

At long times ($t > 800$ μs) after the laser is pulsed off, the creation rate Γ_c balances with the recombination and trapping terms to produce a steady-state quasiparticle density. For trapping limited case where $R_r \to 0$, fitting the data to the solution to (10. 4) yields Γ_t as a function of temperature T. Figure 10. 17 shows an example of a fit curve and data at $T = 101$ mK where $\Gamma_t = 14\ \mathrm{ms}^{-1}$.

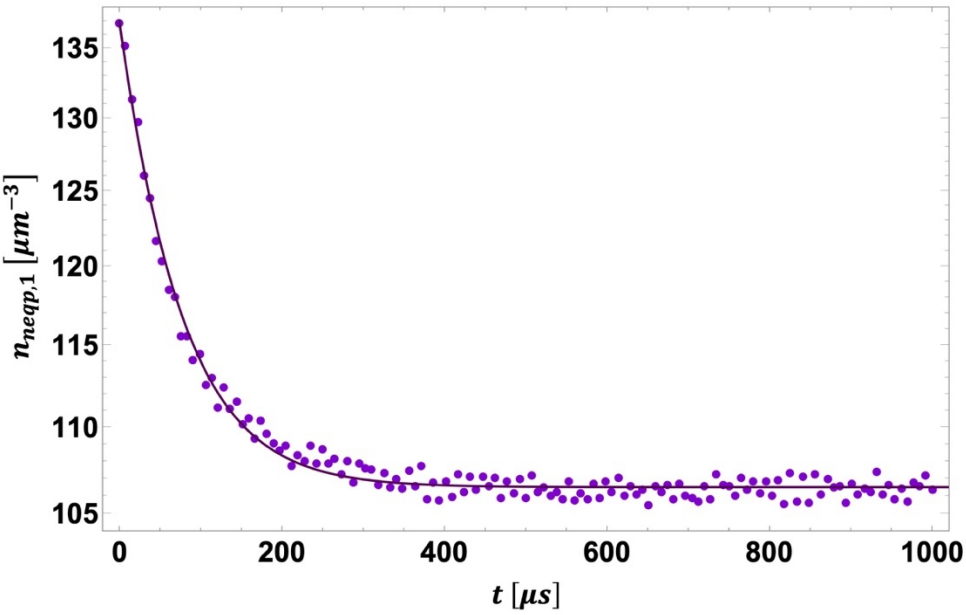

Figure 10. 17 Fit of (10. 4) (solid curve) to data (dots) in for the trapping limited case yielded $\Gamma_t = 14\ ms^{-1}$.

Similar analysis was performed for all the pulsed data shown in Figure 10. 16 and the extracted trapping time $\tau_t = {\Gamma_t}^{-1}$ is plotted Figure 10. 18. Once again, we see a rise at low temperatures with a peak at 450 mK, consistent with the temperature behavior of Q_I (green data

in Figure 10. 9). I believe this consistent behavior is further evidence that non-equilibrium quasiparticles are limiting the Q_I and causing the observed temperature behavior. This is also evident when trapping time τ_r is translated into the trapping rate $\Gamma_t = \tau_t^{-1}$ (see Figure 10. 18). Resulting plot shows that Γ_t is linearly proportional to the non-equilibrium quasiparticle density in the lower-gap-region, in agreement with （5. 2） (see Section 5.1).

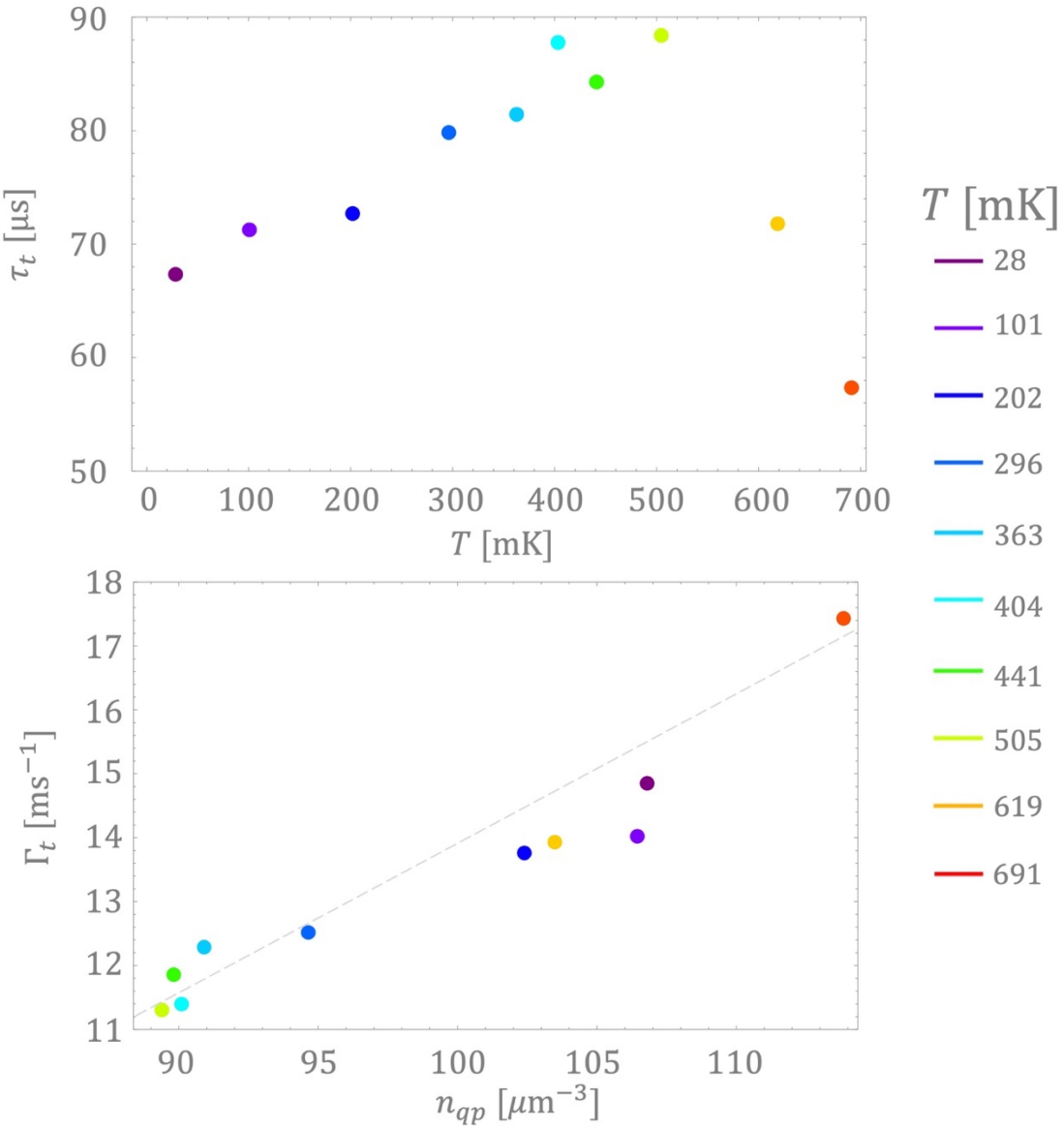

Figure 10. 18 The trapping time τ_t and corresponding rate Γ_t extracted from fitting data in Figure 10. 16 to （10. 4） . Dashed solid line is a linear visual guide.

10.6. Resonance Frequency Noise from Non-equilibrium Quasiparticles

Aside from the change in Q_I, f_0 and the quasiparticle trapping rate, fluctuations in f_0 also showed a strong dependence on the quasiparticle density. By extracting the standard deviation σ_f of f_0 from repeated frequency scans of S_{21} (see Section 8.1.2), fluctuations in the resonance frequency are extracted. Figure 10. 19 shows a plot of σ_f versus n_{qp} for different laser intensities and temperatures, corresponding to the data in Figure 10. 9. In this plot, I used the Q_I fits and my two-gap model to extract the quasiparticle densities. As seen from the plot, the frequency fluctuations measured under different IR radiation intensities (see Figure 10. 19) varied linearly with the quasiparticle density n_{qp}.

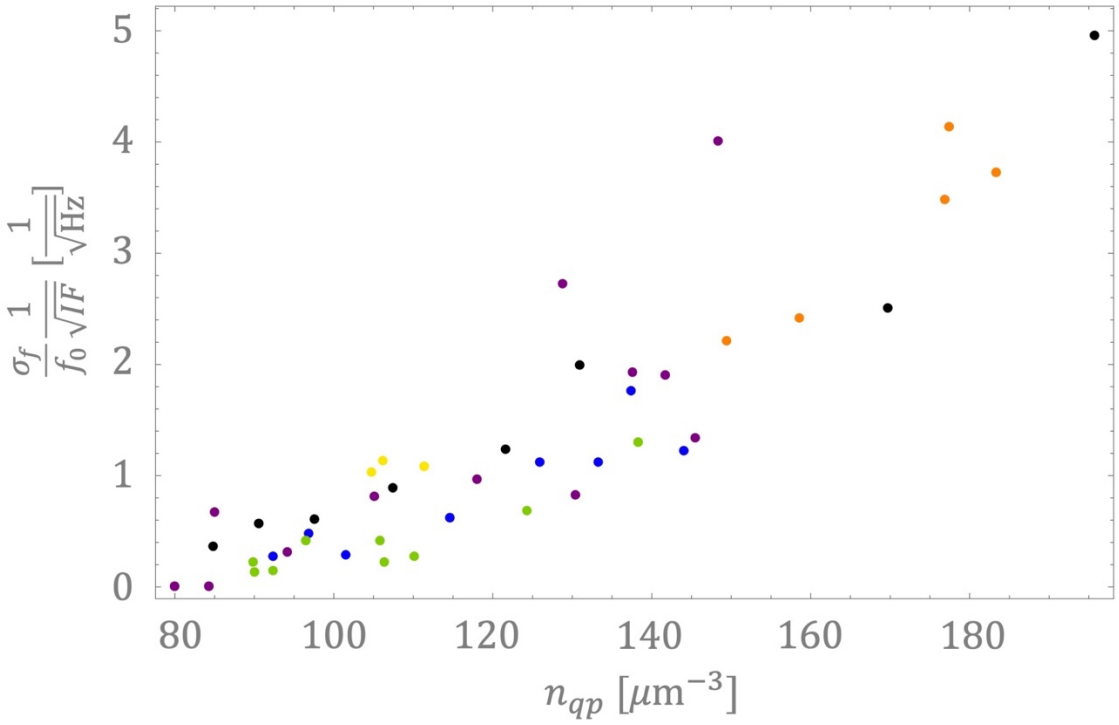

Figure 10. 19 Scaled standard deviation of σ_{f_0} by f_0 and VNA *IF* bandwidth, plotted as a function of quasiparticle densities n_{qp}, measured under different applied laser intensities (black: 0 aW μm^{-2}, purple: 47 aW μm^{-2}, blue: 221 aW μm^{-2}, green: 942 aW μm^{-2}, yellow: 2096 aW μm^{-2}, orange: 5000 aW μm^{-2}).

10.7 An Integrated Design for Cold Quasiparticle Trap

If the resonator Q_I reduction at low temperatures (~ 30 mK) originates from lower gap Δ_1 region at the edge of the CPW center conducting strip, improvements in Q_I could be potentially achieved by inverting the configuration of energy gaps Δ_1 and Δ_2 via gap engineering. The goal would be to condense non-equilibrium quasiparticles into the strip interior, therefore reducing the quasiparticle density in the region of higher superconducting current concentration. A simple design for this is illustrated in Figure 10. 20, in which the surface of the strip is engineered to have a higher gap Δ_2. For TiN, the main challenge is whether the exposed surfaces can be made with a higher gap. Another challenge lies in obtaining a clean interface between the regions of different gaps, without detrimental effects from contaminations, native oxide layer and lattice mismatching. *In situ* deposition of all the required superconducting film layers and avoiding chemical etching might be the path to try. As an example tailored to thermal deposition of superconductor, by using suspended stencil shadow mask, the structure in Figure 10. 21 can be constructed via multilayer depositions at offset angles (see Figure 10. 22). A similar technique has been used to fabricate the gap engineered Al transmons (see Section 9.4). Note that this approach is not applicable to PAMBE TiN,

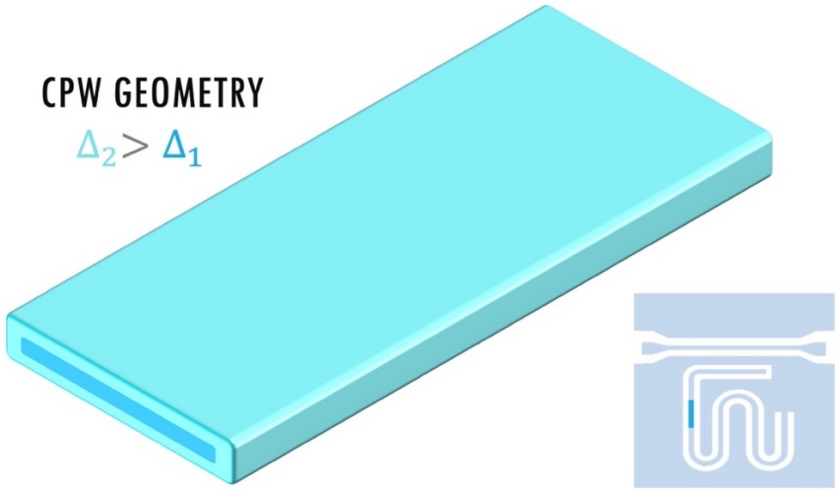

Figure 10. 20 A simple design to trap quasiparticles to the interior (blue) of the CPW center strip of gap Δ_1, in which the surface of the strip (cyan) is engineered to have a higher gap Δ_2.

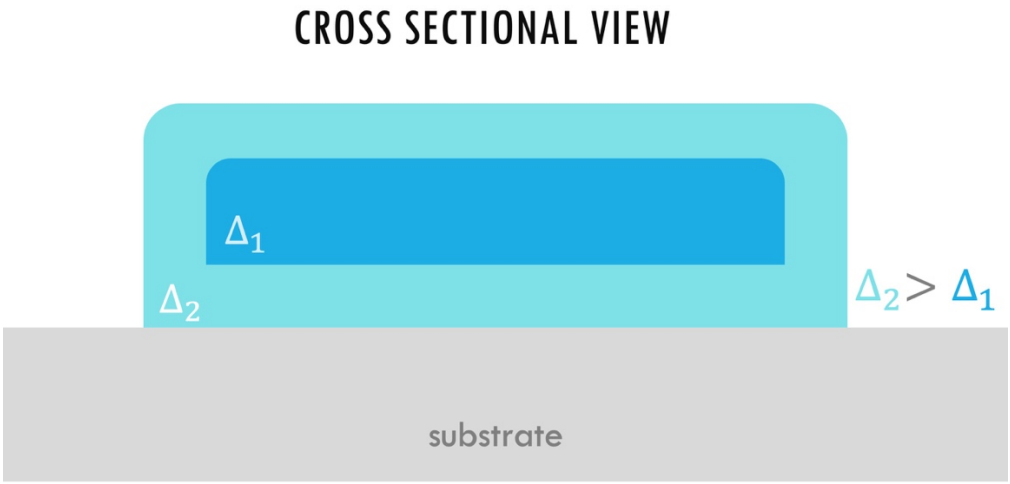

Figure 10. 21 Cross-sectional view of the CPW center strip. As temperature decreases, non-equilibrium quasiparticles condense into the lower gap Δ_1 region (blue) located in the interior of the strip, away from higher gap Δ_2 edge (cyan) where current density is high.

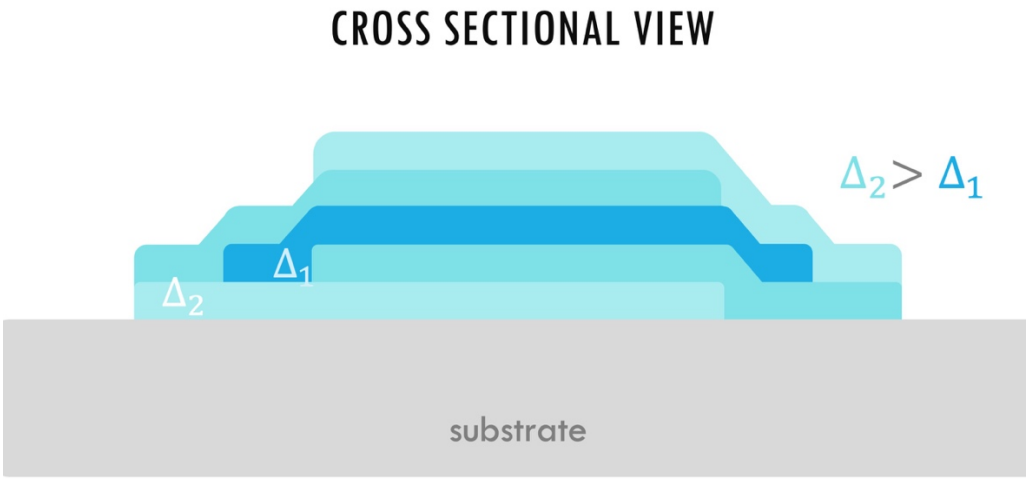

Figure 10. 22 Cross-sectional view of a CPW center stripe, where regions of lower energy gap Δ_1 and higher gap Δ_2 are shown in blue and cyan, respectively. Using suspended stencil shadow mask, each layer of film is deposited *in situ* at different offset angles normal to the substrate (e.g. a $+15°, -15°, 0°, +15°, -15°$ deposition sequence).

CHAPTER 11

Conclusion and Outlook

In summary, I have observed that the relaxation time T_1 of an Al/AlO_x/Al transmon may increase significantly with temperature in the 20 mK to 100 mK range, while increasing the temperature further eventually results in a decrease in the relaxation time due to thermally generated quasiparticles. To explain the full temperature dependence of T_1, I analyzed the quasiparticle current noise spectrum for a junction with electrodes with different superconducting gaps, and modelled the behavior of the quasiparticle density when non-equilibrium quasiparticles are present. Fitting this model to my temperature dependent T_1 data allowed me to extract the superconducting energy gap and density of non-equilibrium quasiparticles in each electrode of the transmon.

I note that my model only shows a prominent increase in T_1 as the temperature increases if the two electrodes have different gaps, the volume of the small-gap region is sufficiently smaller than the volume of the large-gap region, and the gap difference is less than hf_q. In contrast, if $|\Delta_2 - \Delta_1| > hf_q$, the model gives a rapid increase in T_1 as $T \to 0$ for $k_B T$ less than the difference in the gaps. The behavior in this limit is of particular interest for applying gap engineering to increase the lifetime of transmons. Other conditions for seeing this effect are that there must be: (1) a mechanism generating non-equilibrium quasiparticles, (2) a relatively low trapping rate to allow sufficient quasiparticle accumulation in the low gap region at low temperatures, and (3) an

absence of other loss mechanisms producing substantially larger loss.

Finally, I note that a substantial increase or decrease in transmon T_1 as T increases for temperatures such that $k_B T \ll hf_q$ provides a distinct qualitative signature suggesting the presence of quasiparticle induced loss. Devices that show this effect could be used for performing quantitative measurements on non-equilibrium quasiparticles, pin down accurate values for the electrodes' superconducting gaps, the difference in the gaps, and perhaps aid in identifying sources causing the pair-breaking.

I also observed similar temperature dependent behavior in my measurements of TiN CPW resonators. Once again, I modeled this loss behavior by assuming that non-equilibrium quasiparticles redistribute to the edges of the CPW center strip due to the edge having a lower superconducting gap than the interior of the film. Since this is also the region where the superconducting current is concentrated, the redistribution of quasiparticles to a larger density results in higher microwave loss at low temperatures. A variant of our model for non-equilibrium quasiparticle loss in transmons can be applied to the case of the resonator to explain and predict Q_I behaviors. In particular, I used the model to fit the behavior observed in Q_I, f_0 , frequency fluctuations and quasiparticle trapping times. This analysis also provided us with insights into possible problems in the resonator fabrication procedure.

I should emphasize that non-equilibrium quasiparticles and energy gap inhomogeneity is not exclusive to my transmon devices. Similar effects were observed in devices made by our collaborators [62][282]. They found that better isolation from external radiation in their refrigerator significantly improved relaxation times to a maximum $T_1 \gtrsim 300$ μs. Since the source of the residual quasiparticles is unknown and complete isolation has been difficult to attain, improving coherence by gap engineering appears to be a more practical solution. Using the

phenomenon of non-equilibrium quasiparticles redistribution and energy gap engineering, a simple trap design improved transmon T_1 beyond 300 μs [62]. Even better T_1 are anticipated, since the best measured T_1 for my Al/AlO_x/Al transmon was $\sim 400\,\mu s$, obtained in one of Dr. Manucharyan's refrigerators. We hope this goal may be accomplished with the more elaborated quasiparticle trap designs discussed in this dissertation for both the transmon and CPW resonator.

Bibliography

[1] Van Gael, J., 2005. The Role of Interference and Entanglement in Quantum Computing.

[2] Benioff, P., 1980. The computer as a physical system: A microscopic quantum mechanical Hamiltonian model of computers as represented by Turing machines. Journal of statistical physics, 22(5), pp.563-591.

[3] Landauer, R., 1961. Irreversibility and heat generation in the computing process. IBM journal of research and development, 5(3), pp.183-191.

[4] Manin, Y., 1980. Computable and uncomputable. Sovetskoye Radio, Moscow, 128.

[5] Feynman, R.P., 1980. La nature de la physique. Le Seuil.

[6] Deutsch, D., 1985. Quantum theory, the Church–Turing principle and the universal quantum computer. Proceedings of the Royal Society of London. A. Mathematical and Physical Sciences, 400(1818), pp.97-117.

[7] Igeta, K. and Yamamoto, Y., 1988, July. Quantum mechanical computers with single atom and photon fields. In International Quantum Electronics Conference (p. TuI4). Optical Society of America.

[8] Deutsch, D. and Jozsa, R., 1992. Rapid solution of problems by quantum computation. Proceedings of the Royal Society of London. Series A: Mathematical and Physical Sciences, 439(1907), pp.553-558.

[9] Shor, P.W., 1994, November. Algorithms for quantum computation: discrete logarithms and factoring. In Proceedings 35th annual symposium on foundations of computer science (pp. 124-134). Ieee.

[10] Rivest, R.L., Shamir, A. and Adleman, L., 1978. A method for obtaining digital signatures and public-key cryptosystems. Communications of the ACM, 21(2), pp.120-126.

[11] Cirac, J.I. and Zoller, P., 1994. Preparation of macroscopic superpositions in many-atom systems. Physical Review A, 50(4), p.R2799.

[12] Monroe, C., Meekhof, D.M., King, B.E., Itano, W.M. and Wineland, D.J., 1995. Demonstration of a fundamental quantum logic gate. Physical review letters, 75(25), p.4714.

[13] Cory, D.G., Fahmy, A.F. and Havel, T.F., 1997. Ensemble quantum computing by NMR spectroscopy. Proceedings of the National Academy of Sciences, 94(5), pp.1634-1639.

[14] Gershenfeld, N.A. and Chuang, I.L., 1997. Bulk spin-resonance quantum computation. science, 275(5298), pp.350-356.

[15] Kitaev, A.Y., 1997. Quantum computations: algorithms and error correction. Russian Mathematical Surveys, 52(6), p.1191.

[16] Jones, J.A., Mosca, M. and Hansen, R.H., 1998. Implementation of a quantum search algorithm on a quantum computer. Nature, 393(6683), pp.344-346.

[17] Kane, B.E., 1998. A silicon-based nuclear spin quantum computer. nature, 393(6681), pp.133-137.

[18] Nakamura, Y., Pashkin, Y.A. and Tsai, J.S., 1999. Coherent control of macroscopic quantum states in a single-Cooper-pair box. nature, 398(6730), pp.786-788.

[19] Knill, E., Laflamme, R. and Milburn, G.J., 2001. A scheme for efficient quantum computation with linear optics. nature, 409(6816), pp.46-52.

[20] Ristè, D., Bultink, C.C., Lehnert, K.W. and DiCarlo, L., 2012. Feedback control of a solid-state qubit using high-fidelity projective measurement. Physical review letters, 109(24), p.240502.

[21] Pla, J.J., Tan, K.Y., Dehollain, J.P., Lim, W.H., Morton, J.J., Zwanenburg, F.A., Jamieson, D.N., Dzurak, A.S. and Morello, A., 2013. High-fidelity readout and control of a nuclear spin qubit in silicon. Nature, 496(7445), pp.334-338.

[22] Dolde, F., Bergholm, V., Wang, Y., Jakobi, I., Naydenov, B., Pezzagna, S., Meijer, J., Jelezko, F., Neumann, P., Schulte-Herbrüggen, T. and Biamonte, J., 2014. High-fidelity spin entanglement using optimal control. Nature communications, 5(1), pp.1-9.

[23] Barends, R., Kelly, J., Megrant, A., Veitia, A., Sank, D., Jeffrey, E., White, T.C., Mutus, J., Fowler, A.G., Campbell, B. and Chen, Y., 2014. Superconducting quantum circuits at the surface code threshold for fault tolerance. Nature, 508(7497), pp.500-503.

[24] Nichol, J.M., Orona, L.A., Harvey, S.P., Fallahi, S., Gardner, G.C., Manfra, M.J. and Yacoby, A., 2017. High-fidelity entangling gate for double-quantum-dot spin qubits. npj Quantum Information, 3(1), pp.1-5.

[25] Levine, H., Keesling, A., Omran, A., Bernien, H., Schwartz, S., Zibrov, A.S., Endres, M., Greiner, M., Vuletić, V. and Lukin, M.D., 2018. High-fidelity control and entanglement of rydberg-atom qubits. Physical review letters, 121(12), p.123603.

[26] Reed, M.D., DiCarlo, L., Nigg, S.E., Sun, L., Frunzio, L., Girvin, S.M. and Schoelkopf, R.J., 2012. Realization of three-qubit quantum error correction with superconducting circuits. Nature, 482(7385), pp.382-385.

[27] Taminiau, T.H., Cramer, J., van der Sar, T., Dobrovitski, V.V. and Hanson, R., 2014. Universal control and error correction in multi-qubit spin registers in diamond. Nature nanotechnology, 9(3), p.171.

[28] Ofek, N., Petrenko, A., Heeres, R., Reinhold, P., Leghtas, Z., Vlastakis, B., Liu, Y., Frunzio, L., Girvin, S.M., Jiang, L. and Mirrahimi, M., 2016. Extending the lifetime of a quantum bit with error correction in superconducting circuits. Nature, 536(7617), pp.441-445.

[29] Gambetta, J.M., Chow, J.M. and Steffen, M., 2017. Building logical qubits in a superconducting quantum computing system. npj Quantum Information, 3(1), pp.1-7.

[30] Knight, W., 2017. Ibm raises the bar with a 50-qubit quantum computer. Sighted at MIT Review Technology.

[31] Devitt, S.J., 2016. Performing quantum computing experiments in the cloud. Physical Review A, 94(3), p.032329.

[32] DiVincenzo, D.P., 1997. Topics in quantum computers. In Mesoscopic electron transport (pp. 657-677). Springer, Dordrecht.

[33] Schumacher, B., 1995. Quantum coding. Physical Review A, 51(4), p.2738.

[34] Preskill, J., 2012. Quantum computing and the entanglement frontier-Rapporteur talk at the 25th Solvay Conference.

[35] Preskill, J., 2012. Quantum computing and the entanglement frontier. arXiv preprint arXiv:1203.5813.

[36] Harrow, A.W. and Montanaro, A., 2017. Quantum computational supremacy. Nature, 549(7671), pp.203-209.

[37] Bouchiat, V., Vion, D., Joyez, P., Esteve, D. and Devoret, M.H., 1998. Quantum coherence with a single Cooper pair. Physica Scripta, 1998(T76), p.165.

[38] Kjaergaard, M., Schwartz, M.E., Braumüller, J., Krantz, P., Wang, J.I.J., Gustavsson, S. and Oliver, W.D., 2020. Superconducting qubits: Current state of play. Annual Review of Condensed Matter Physics, 11, pp.369-395.

[39] Nakamura, Y., Pashkin, Y.A., Yamamoto, T. and Tsai, J.S., 2002. Charge echo in a Cooper-pair box. Physical review letters, 88(4), p.047901.

[40] Vion, D., Aassime, A., Cottet, A., Joyez, P., Pothier, H., Urbina, C., Esteve, D. and Devoret, M.H., 2002. Manipulating the quantum state of an electrical circuit. Science, 296(5569), pp.886-889.

[41] Chiorescu, I., Nakamura, Y., Harmans, C.M. and Mooij, J.E., 2003. Coherent quantum dynamics of a superconducting flux qubit. Science, 299(5614), pp.1869-1871.

[42] Bertet, P., Chiorescu, I., Burkard, G., Semba, K., Harmans, C.J.P.M., DiVincenzo, D.P. and Mooij, J.E., 2005. Dephasing of a superconducting qubit induced by photon noise. Physical review letters, 95(25), p.257002.

[43] Houck, A.A., Schreier, J.A., Johnson, B.R., Chow, J.M., Koch, J., Gambetta, J.M., Schuster, D.I., Frunzio, L., Devoret, M.H., Girvin, S.M. and Schoelkopf, R.J., 2008. Controlling the spontaneous emission of a superconducting transmon qubit. Physical review letters, 101(8), p.080502.

[44] Manucharyan, V.E., Koch, J., Glazman, L.I. and Devoret, M.H., 2009. Fluxonium: Single cooper-pair circuit free of charge offsets. Science, 326(5949), pp.113-116.

[45] Bylander, J., Gustavsson, S., Yan, F., Yoshihara, F., Harrabi, K., Fitch, G., Cory, D.G., Nakamura, Y., Tsai, J.S. and Oliver, W.D., 2011. Noise spectroscopy through dynamical decoupling with a superconducting flux qubit. Nature Physics, 7(7), pp.565-570.

[46] Paik, H., Schuster, D.I., Bishop, L.S., Kirchmair, G., Catelani, G., Sears, A.P., Johnson, B.R., Reagor, M.J., Frunzio, L., Glazman, L.I. and Girvin, S.M., 2011. Observation of high coherence in Josephson junction qubits measured in a three-dimensional circuit QED architecture. Physical Review Letters, 107(24), p.240501.

[47] Rigetti, C., Gambetta, J.M., Poletto, S., Plourde, B.L.T., Chow, J.M., Córcoles, A.D., Smolin, J.A., Merkel, S.T., Rozen, J.R., Keefe, G.A. and Rothwell, M.B., 2012. Superconducting qubit in a waveguide cavity with a coherence time approaching 0.1 ms. Physical Review B, 86(10), p.100506.

[48] Chang, J.B., Vissers, M.R., Córcoles, A.D., Sandberg, M., Gao, J., Abraham, D.W., Chow, J.M., Gambetta, J.M., Beth Rothwell, M., Keefe, G.A. and Steffen, M., 2013. Improved superconducting qubit coherence using titanium nitride. Applied Physics Letters, 103(1), p.012602.

[49] Pop, I.M., Geerlings, K., Catelani, G., Schoelkopf, R.J., Glazman, L.I. and Devoret, M.H., 2014. Coherent suppression of electromagnetic dissipation due to superconducting quasiparticles. Nature, 508(7496), pp.369-372.

[50] Jin, X.Y., Kamal, A., Sears, A.P., Gudmundsen, T., Hover, D., Miloshi, J., Slattery, R., Yan, F., Yoder, J., Orlando, T.P. and Gustavsson, S., 2015. Thermal and residual excited-state population in a 3D transmon qubit. Physical Review Letters, 114(24), p.240501.

[51] Yan, F., Gustavsson, S., Kamal, A., Birenbaum, J., Sears, A.P., Hover, D., Gudmundsen, T.J., Rosenberg, D., Samach, G., Weber, S. and Yoder, J.L., 2016. The flux qubit revisited to enhance coherence and reproducibility. Nature communications, 7(1), pp.1-9.

[52] Nguyen, L.B., Lin, Y.H., Somoroff, A., Mencia, R., Grabon, N. and Manucharyan, V.E., 2019. High-coherence fluxonium qubit. Physical Review X, 9(4), p.041041.

[53] Larsen, T.W., Petersson, K.D., Kuemmeth, F., Jespersen, T.S., Krogstrup, P., Nygård, J. and Marcus, C.M., 2015. Semiconductor-nanowire-based superconducting qubit. Physical review letters, 115(12), p.127001.

[54] Casparis, L., Larsen, T.W., Olsen, M.S., Kuemmeth, F., Krogstrup, P., Nygård, J., Petersson, K.D. and Marcus, C.M., 2016. Gatemon benchmarking and two-qubit operations. Physical review letters, 116(15), p.150505.

[55] Luthi, F., Stavenga, T., Enzing, O.W., Bruno, A., Dickel, C., Langford, N.K., Rol, M.A., Jespersen, T.S., Nygård, J., Krogstrup, P. and DiCarlo, L., 2018. Evolution of nanowire transmon qubits and their coherence in a magnetic field. Physical review letters, 120(10), p.100502.

[56] Joel, I., Wang, J., Rodan-Legrain, D., Bretheau, L., Campbell, D.L., Kannan, B., Kim, D., Kjaergaard, M., Krantz, P., Samach, G.O. and Yan, F., 2019. Coherent control of a hybrid superconducting circuit made with graphene-based van der Waals heterostructures. Nature nanotechnology, 14(2), pp.120-125.

[57] Wang, H., Hofheinz, M., Ansmann, M., Bialczak, R.C., Lucero, E., Neeley, M., O'connell, A.D., Sank, D., Wenner, J., Cleland, A.N. and Martinis, J.M., 2008. Measurement of the decay of Fock states in a superconducting quantum circuit. Physical Review Letters, 101(24), p.240401.

[58] Wang, C., Gao, Y.Y., Reinhold, P., Heeres, R.W., Ofek, N., Chou, K., Axline, C., Reagor, M., Blumoff, J., Sliwa, K.M. and Frunzio, L., 2016. A Schrödinger cat living in two boxes. Science, 352(6289), pp.1087-1091.

[59] Rosenblum, S., Reinhold, P., Mirrahimi, M., Jiang, L., Frunzio, L. and Schoelkopf, R.J., 2018. Fault-tolerant detection of a quantum error. Science, 361(6399), pp.266-270.

[60] Hu, L., Ma, Y., Cai, W., Mu, X., Xu, Y., Wang, W., Wu, Y., Wang, H., Song, Y.P., Zou, C.L. and Girvin, S.M., 2019. Quantum error correction and universal gate set operation on a binomial bosonic logical qubit. Nature Physics, 15(5), pp.503-508.

[61] Paik, H. and Osborn, K.D., 2010. Reducing quantum-regime dielectric loss of silicon nitride for superconducting quantum circuits. Applied Physics Letters, 96(7), p.072505.

[62] Li, K., Wellstood, F., Lobb, C., Dutta, S., Zhang, R., Keshvari, S. and Poppert, D., 2020. T1 of transmons with electrodes that have different gaps. Bulletin of the American Physical Society, 65.

[63] Jones, N.C., Van Meter, R., Fowler, A.G., McMahon, P.L., Kim, J., Ladd, T.D. and Yamamoto, Y., 2012. Layered architecture for quantum computing. Physical Review X, 2(3), p.031007.

[64] Schreier, J.A., Houck, A.A., Koch, J., Schuster, D.I., Johnson, B.R., Chow, J.M., Gambetta, J.M., Majer, J., Frunzio, L., Devoret, M.H. and Girvin, S.M., 2008. Suppressing charge noise decoherence in superconducting charge qubits. Physical Review B, 77(18), p.180502.

[65] Richardson, C.J.K., Alexander, A., Weddle, C.G., Arey, B. and Olszta, M., 2020. Low-loss superconducting titanium nitride grown using plasma-assisted molecular beam epitaxy. Journal of Applied Physics, 127(23), p.235302.

[66] Sage, J.M., Bolkhovsky, V., Oliver, W.D., Turek, B. and Welander, P.B., 2011. Study of loss in superconducting coplanar waveguide resonators. Journal of Applied Physics, 109(6), p.063915.

[67] Liao, W.T., Kohler, T.P., Osborn, K.D., Butera, R.E., Lobb, C.J., Wellstood, F.C. and Dreyer, M., 2019. Scanning tunneling Andreev microscopy of titanium nitride thin films. Physical Review B, 100(21), p.214505.

[68] Onnes, H.K., 1911. The disappearance of the resistivity of mercury. Comm. Leiden, 122(2).

[69] Onnes, H.K., 1908. The liquefaction of helium. Koninklijke Nederlandse Akademie von Wetenschappen, Proceedings, 11, pp.1908-1909.

[70] Matthias, B.T., Geballe, T.H. and Compton, V.B., 1963. Superconductivity. Reviews of Modern Physics, 35(1), p.1.

[71] Eisenstein, J., 1954. Superconducting elements. Reviews of Modern Physics, 26(3), p.277.

[72] Cochran, J.F. and Mapother, D.E., 1958. Superconducting transition in aluminum. Physical Review, 111(1), p.132.

[73] Oya, G.I. and Saur, E.J., 1979. Preparation of Nb 3 Ge films by chemical transport reaction and their critical properties. Journal of Low Temperature Physics, 34(5-6), pp.569-583.

[74] Domashnev, I.A., Marchenko, V.A. and Troitskii, V.N., 1982. Magnetic properties of titanium nitride in superconducting state. Soviet Physics-Solid State, 24(4), pp.689-690.

[75] Pracht, U.S., Scheffler, M., Dressel, M., Kalok, D.F., Strunk, C. and Baturina, T.I., 2012. Direct observation of the superconducting gap in a thin film of titanium nitride using terahertz spectroscopy. Physical Review B, 86(18), p.184503.

[76] Wu, M.K., Ashburn, J.R., Torng, C., Hor, P.H., Meng, R.L., Gao, L., Huang, Z.J., Wang, Y.Q. and Chu, A., 1987. Superconductivity at 93 K in a new mixed-phase Y-Ba-Cu-O compound system at ambient pressure. Physical review letters, 58(9), p.908.

[77] Bednorz, J.G. and Müller, K.A., 1986. Possible highT c superconductivity in the Ba− La− Cu− O system. Zeitschrift für Physik B Condensed Matter, 64(2), pp.189-193.

[78] Yan, S.L., Cao, H.L., Yang, X.M. and Zhou, X.D., 1991. Preparation of TlCaBaCuO high-T c superconducting thin films on LaAlO3 substrates. Journal of applied physics, 70(1), pp.526-528.

[79] Ekimov, E.A., Sidorov, V.A., Bauer, E.D., Mel'Nik, N.N., Curro, N.J., Thompson, J.D. and Stishov, S.M., 2004. Superconductivity in diamond. nature, 428(6982), pp.542-545.

[80] Ekimov, E.A., Sidorov, V.A., Zoteev, A.V., Lebed, J.B., Thompson, J.D. and Stishov, S.M., 2009. Structure and superconductivity of isotope-enriched boron-doped diamond. Science and technology of advanced materials.

[81] Nagamatsu, J., Nakagawa, N., Muranaka, T., Zenitani, Y. and Akimitsu, J., 2001. Superconductivity at 39 K in magnesium diboride. nature, 410(6824), pp.63-64.

[82] Grafe, H.J., Paar, D., Lang, G., Curro, N.J., Behr, G., Werner, J., Hamann-Borrero, J., Hess, C., Leps, N., Klingeler, R. and Büchner, B., 2008. As 75 NMR Studies of Superconducting LaFeAs O 0.9 F 0.1. Physical review letters, 101(4), p.047003.

[83] Nakai, Y., Ishida, K., Kamihara, Y., Hirano, M. and Hosono, H., 2008. Evolution from Itinerant Antiferromagnet to Unconventional Superconductor with Fluorine Doping in LaFeAs (O1-x F x) Revealed by 75As and 139La Nuclear Magnetic Resonance. Journal of the Physical Society of Japan, 77(7), p.073701.

[84] Moll, P.J., Puzniak, R., Balakirev, F., Rogacki, K., Karpinski, J., Zhigadlo, N.D. and Batlogg, B., 2010. High magnetic-field scales and critical currents in SmFeAs (O, F) crystals. Nature materials, 9(8), pp.628-633.

[85] Martinelli, A., Ferretti, M., Manfrinetti, P., Palenzona, A., Tropeano, M., Cimberle, M.R., Ferdeghini, C., Valle, R., Bernini, C., Putti, M. and Siri, A.S., 2008. Synthesis, crystal structure, microstructure, transport and magnetic properties of SmFeAsO and SmFeAs (O0. 93F0. 07). Superconductor Science and Technology, 21(9), p.095017.

[86] Bardeen, J., Cooper, L.N. and Schrieffer, J.R., 1957. Theory of superconductivity. Physical review, 108(5), p.1175.

[87] Tinkham, M., 2004. Introduction to superconductivity. Courier Corporation.

[88] Gubser, D.U. and Hein, R.A., 1974. Relation between superconducting energy gaps and critical magnetic fields. In Low Temperature Physics-LT 13 (pp. 790-793). Springer, Boston, MA.

[89] Meissner, W. and Ochsenfeld, R., 1933. Ein neuer effekt bei eintritt der supraleitfähigkeit. Naturwissenschaften, 21(44), pp.787-788.

[90] London, F. and London, H., 1935. The electromagnetic equations of the supraconductor. Proceedings of the Royal Society of London. Series A-Mathematical and Physical Sciences, 149(866), pp.71-88.

[91] Mühlschlegel, B., 1959. Die thermodynamischen funktionen des supraleiters. Zeitschrift für Physik, 155(3), pp.313-327.

[92] Khukhareva, I.S., 1963. The superconducting properties of thin aluminum films. Soviet Physics JETP, 16, pp.828-832.

[93] De Visser, P.J., Goldie, D.J., Diener, P., Withington, S., Baselmans, J.J.A. and Klapwijk, T.M., 2014. Evidence of a nonequilibrium distribution of quasiparticles in the microwave response of a superconducting aluminum resonator. Physical review letters, 112(4), p.047004.

[94] Knowles, H.S., Maisi, V.F. and Pekola, J.P., 2012. Probing quasiparticle excitations in a hybrid single electron transistor. Applied Physics Letters, 100(26), p.262601.

[95] Aumentado, J., Keller, M.W., Martinis, J.M. and Devoret, M.H., 2004. Nonequilibrium quasiparticles and 2 e periodicity in single-cooper-pair transistors. Physical review letters, 92(6), p.066802.

[96] Day, P.K., LeDuc, H.G., Mazin, B.A., Vayonakis, A. and Zmuidzinas, J., 2003. A broadband superconducting detector suitable for use in large arrays. Nature, 425(6960), pp.817-821.

[97] De Visser, P.J., Baselmans, J.J.A., Bueno, J., Llombart, N. and Klapwijk, T.M., 2014. Fluctuations in the electron system of a superconductor exposed to a photon flux. Nature communications, 5(1), pp.1-8.

[98] Sun, L., DiCarlo, L., Reed, M.D., Catelani, G., Bishop, L.S., Schuster, D.I., Johnson, B.R., Yang, G.A., Frunzio, L., Glazman, L. and Devoret, M.H., 2012. Measurements of quasiparticle tunneling dynamics in a band-gap-engineered transmon qubit. Physical review letters, 108(23), p.230509.

[99] Ristè, D., Bultink, C.C., Tiggelman, M.J., Schouten, R.N., Lehnert, K.W. and DiCarlo, L., 2013. Millisecond charge-parity fluctuations and induced decoherence in a superconducting transmon qubit. Nature communications, 4(1), pp.1-6.

[100] Pop, I.M., Geerlings, K., Catelani, G., Schoelkopf, R.J., Glazman, L.I. and Devoret, M.H., 2014. Coherent suppression of electromagnetic dissipation due to superconducting quasiparticles. Nature, 508(7496), pp.369-372.

[101] Barends, R., Wenner, J., Lenander, M., Chen, Y., Bialczak, R.C., Kelly, J., Lucero, E., O'Malley, P., Mariantoni, M., Sank, D. and Wang, H., 2011. Minimizing quasiparticle generation from stray infrared light in superconducting quantum circuits. Applied Physics Letters, 99(11), p.113507.

[102] Krinner, S., Storz, S., Kurpiers, P., Magnard, P., Heinsoo, J., Keller, R., Luetolf, J., Eichler, C. and Wallraff, A., 2019. Engineering cryogenic setups for 100-qubit scale superconducting circuit systems. EPJ Quantum Technology, 6(1), p.2.

[103] Christensen, B.G., Wilen, C.D., Opremcak, A., Nelson, J., Schlenker, F., Zimonick, C.H., Faoro, L., Ioffe, L.B., Rosen, Y.J., DuBois, J.L. and Plourde, B.L.T., 2019. Anomalous charge noise in superconducting qubits. Physical Review B, 100(14), p.140503.

[104] Owen, C.S. and Scalapino, D.J., 1972. Superconducting state under the influence of external dynamic pair breaking. Physical Review Letters, 28(24), p.1559.

[105] Kim, Z., Suri, B., Zaretskey, V., Novikov, S., Osborn, K.D., Mizel, A., Wellstood, F.C. and Palmer, B.S., 2011. Decoupling a Cooper-pair box to enhance the lifetime to 0.2 ms. Physical review letters, 106(12), p.120501.

[106] Gao, J., Zmuidzinas, J., Vayonakis, A., Day, P., Mazin, B. and Leduc, H., 2008. Equivalence of the effects on the complex conductivity of superconductor due to temperature change and external pair breaking. Journal of Low Temperature Physics, 151(1-2), pp.557-563.

[107] Parker, W.H., 1975. Modified heating theory of nonequilibrium superconductors. Physical Review B, 12(9), p.3667.

[108] Rothwarf, A. and Taylor, B.N., 1967. Measurement of recombination lifetimes in superconductors. Physical Review Letters, 19(1), p.27.

[109] Gorter, C.J., Casimir, H.B.G., 1933. Physica, 1

[110] Mattis, D.C. and Bardeen, J., 1958. Theory of the anomalous skin effect in normal and superconducting metals. Physical Review, 111(2), p.412.

[111] Abrikosov, A.A., Gor'Kov, L.P. and Khalatnikov, I.M., 1959. A superconductor in a high frequency field. Sov. Phys. JETP, 35, p.182.

[112] Goldie, D.J. and Withington, S., 2012. Non-equilibrium superconductivity in quantum-sensing superconducting resonators. Superconductor Science and Technology, 26(1), p.015004.

[113] Kaplan, S.B., Chi, C.C., Langenberg, D.N., Chang, J.J., Jafarey, S. and Scalapino, D.J., 1976. Quasiparticle and phonon lifetimes in superconductors. Physical Review B, 14(11), p.4854.

[114] Eliashberg, G.M., 1972. Inelastic electron collisions and nonequilibrium stationary states in superconductors. SOV PHYS JETP, 34(3), pp.668-676.

[115] Wilson, C.M. and Prober, D.E., 2004. Quasiparticle number fluctuations in superconductors. Physical Review B, 69(9), p.094524.

[116] Gubner, J.A., 2006. Probability and random processes for electrical and computer engineers. Cambridge University Press.

[117] Ginzburg, V.L. and Landau, L.D., 2009. On the theory of superconductivity. In On Superconductivity and Superfluidity (pp. 113-137). Springer, Berlin, Heidelberg.

[118] Abrikosov, A.A., 1957. The magnetic properties of superconducting alloys. Journal of Physics and Chemistry of Solids, 2(3), pp.199-208.

[119] Buchacek, M., Willa, R., Geshkenbein, V.B. and Blatter, G., 2019. Strong pinning theory of thermal vortex creep in type-II superconductors. Physical Review B, 100(1), p.014501.

[120] Kossowsky, R., Bose, S., Durusoy, Z. and Pan, V. eds., 1999. Physics and materials science of vortex states, flux pinning and dynamics (No. 356). Springer Science & Business Media.

[121] Gittleman, J.I. and Rosenblum, B., 1966. Radio-frequency resistance in the mixed state for subcritical currents. Physical Review Letters, 16(17), p.734.

[122] Clem, J.R. and Coffey, M.W., 1992. Effects of flux flow, flux pinning, and flux creep upon the rf surface impedance of type-II superconductors. Journal of superconductivity, 5(4), pp.313-318.

[123] Coffey, M.W. and Clem, J.R., 1991. Unified theory of effects of vortex pinning and flux creep upon the rf surface impedance of type-II superconductors. Physical review letters, 67(3), p.386.

[124] Brandt, E.H., 1992. Linear ac response of high-Tc superconductors and the irreversibility line. Physica Scripta, 1992(T45), p.63.

[125] Lütke-Entrup, N., Plaçais, B., Mathieu, P. and Simon, Y., 1998. RF-studies of vortex dynamics in isotropic type-II superconductors. Physica B: Condensed Matter, 255(1-4), pp.75-85.

[126] Pautrat, A., Goupil, C., Simon, C., Lütke-Entrup, N., Plaçais, B., Mathieu, P., Simon, Y., Rykov, A. and Tajima, S., 2001. Evidence for vortex surface pinning in YBa 2 Cu 3 O 7− δ from the frequency dependence of the complex penetration depth. Physical Review B, 63(5), p.054503.

[127] Pompeo, N. and Silva, E., 2008. Reliable determination of vortex parameters from measurements of the microwave complex resistivity. Physical Review B, 78(9), p.094503.

[128] Parks, B., Spielman, S., Orenstein, J., Nemeth, D.T., Ludwig, F., Clarke, J., Merchant, P. and Lew, D.J., 1995. Phase-sensitive measurements of vortex dynamics in the terahertz domain. Physical review letters, 74(16), p.3265.

[129] Phillips, W.A., 1972. Tunneling states in amorphous solids. Journal of Low Temperature Physics, 7(3-4), pp.351-360.

[130] Anderson, P.W., Halperin, B.I. and Varma, C.M., 1972. Anomalous low-temperature thermal properties of glasses and spin glasses. Philosophical Magazine, 25(1), pp.1-9

[131] Dial, O., McClure, D.T., Poletto, S., Keefe, G.A., Rothwell, M.B., Gambetta, J.M., Abraham, D.W., Chow, J.M. and Steffen, M., 2016. Bulk and surface loss in superconducting transmon qubits. Superconductor Science and Technology, 29(4), p.044001.

[132] Wang, C., Axline, C., Gao, Y.Y., Brecht, T., Chu, Y., Frunzio, L., Devoret, M.H. and Schoelkopf, R.J., 2015. Surface participation and dielectric loss in superconducting qubits. Applied Physics Letters, 107(16), p.162601.

[133] Martinis, J.M., Cooper, K.B., McDermott, R., Steffen, M., Ansmann, M., Osborn, K.D., Cicak, K., Oh, S., Pappas, D.P., Simmonds, R.W. and Clare, C.Y., 2005. Decoherence in Josephson qubits from dielectric loss. Physical review letters, 95(21), p.210503.

[134] O'Connell, A.D., Ansmann, M., Bialczak, R.C., Hofheinz, M., Katz, N., Lucero, E., McKenney, C., Neeley, M., Wang, H., Weig, E.M. and Cleland, A.N., 2008. Microwave dielectric loss at single photon energies and millikelvin temperatures. Applied Physics Letters, 92(11), p.112903.

[135] Lenander, M., Wang, H., Bialczak, R.C., Lucero, E., Mariantoni, M., Neeley, M., O'Connell, A.D., Sank, D., Weides, M., Wenner, J. and Yamamoto, T., 2011. Measurement of energy decay in superconducting qubits from nonequilibrium quasiparticles. Physical Review B, 84(2), p.024501.

[136] Barends, R., Hortensius, H.L., Zijlstra, T., Baselmans, J.J.A., Yates, S.J.C., Gao, J.R. and Klapwijk, T.M., 2008. Contribution of dielectrics to frequency and noise of NbTiN superconducting resonators. Applied Physics Letters, 92(22), p.223502.

[137] Pekola, J.P., Anghel, D.V., Suppula, T.I., Suoknuuti, J.K., Manninen, A.J. and Manninen, M., 2000. Trapping of quasiparticles of a nonequilibrium superconductor. Applied Physics Letters, 76(19), pp.2782-2784.

[138] Gao, J., Daal, M., Vayonakis, A., Kumar, S., Zmuidzinas, J., Sadoulet, B., Mazin, B.A., Day, P.K. and Leduc, H.G., 2008. Experimental evidence for a surface distribution of two-level systems in superconducting lithographed microwave resonators. Applied Physics Letters, 92(15), p.152505.

[139] Gao, J., Daal, M., Martinis, J.M., Vayonakis, A., Zmuidzinas, J., Sadoulet, B., Mazin, B.A., Day, P.K. and Leduc, H.G., 2008. A semiempirical model for two-level system noise in superconducting microresonators. Applied Physics Letters, 92(21), p.212504.

[140] Pappas, D.P., Vissers, M.R., Wisbey, D.S., Kline, J.S. and Gao, J., 2011. Two level system loss in superconducting microwave resonators. IEEE Transactions on Applied Superconductivity, 21(3), pp.871-874.

[141] Bruno, A., Skacel, S.T., Kaiser, C., Wünsch, S., Siegel, M., Ustinov, A.V. and Lisitskiy, M.P., 2012. Investigation of Dielectric Losses in Hydrogenated Amorphoussilicon (a-Si: H) thin Films Using Superconducting Microwave Resonators. Physics Procedia, 36, pp.245-249.

[142] Bloch, F., Hansen, W.W. and Packard, M.E., 1946. Physical review. Phys Rev, 70, pp.460-473.

[143] Gao, J., 2008. The Physics of Superconducting Microwave Resonators. PhD thesis (California Institute of Technology, 2008).

[144] Ramo, S., Whinnery, J.R. and Van Duzer, T., 1994. Fields and waves in communication electronics. John Wiley & Sons.

[145] Fuchs, J., 1995. Affine Lie algebras and quantum groups: An Introduction, with applications in conformal field theory. Cambridge university press.

[146] Friedrichs, K.O., 1953. Mathematical aspects of the quantum theory of fields. Part V. Fields modified by linear homogeneous forces. Communications on Pure and Applied Mathematics, 6(1), pp.1-72.

[147] Klauder, J.R. and Skagerstam, B.S., 1985. Coherent states: applications in physics and mathematical physics. World scientific.

[148] Joesphson, B.D., 1962. Possible new effects in superconductive tunneling. Phys. Lett, 1(7), p.251.

[149] Josephson, B.D., 1974. The discovery of tunnelling supercurrents. Reviews of Modern Physics, 46(2), p.251.

[150] Andreev, A.F., 1964. The thermal conductivity of the intermediate state in superconductors. Журнал экспериментальной и теоретической физики, 46(5), pp.1823-1828.

[151] Dubos, P., Courtois, H., Pannetier, B., Wilhelm, F.K., Zaikin, A.D. and Schön, G., 2001. Josephson critical current in a long mesoscopic SNS junction. Physical Review B, 63(6), p.064502.

[152] Sauls, J.A., 2018. Andreev bound states and their signatures.

[153] Ota, Y., Nakai, N., Nakamura, H., Machida, M., Inotani, D., Ohashi, Y., Koyama, T. and Matsumoto, H., 2010. Ambegaokar-Baratoff relations for Josephson critical current in heterojunctions with multigap superconductors. Physical Review B, 81(21), p.214511.

[154] Landauer, R., 1957. Spatial variation of currents and fields due to localized scatterers in metallic conduction. IBM Journal of research and development, 1(3), pp.223-231.

[155] Ambegaokar, V. and Baratoff, A., 1963. Tunneling between superconductors. Physical Review Letters, 10(11), p.486.

[156] Shnirman, A., Schön, G. and Hermon, Z., 1997. Quantum manipulations of small Josephson junctions. Physical Review Letters, 79(12), p.2371.

[157] W. D. Oliver, "Superconducting Qubits," in Quantum Information Processing: Lecture Notes of the 44th IFF Spring School 2013, edited by D. P. DiVincenzo (Forschungszentrum Jülich, 2013) Chap. A4.

[158] Devoret, M.H., Wallraff, A. and Martinis, J.M., 2004. Superconducting qubits: A short review. arXiv preprint cond-mat/0411174.

[159] Baxandall, P.J., 1968. Noise in transistor circuits. Wireless World, 74, pp.388-92.

[160] You, J.Q., Tsai, J.S. and Nori, F., 2006. Hybridized solid-state qubit in the charge-flux regime. Physical Review B, 73(1), p.014510.

[161] Koch, J., Terri, M.Y., Gambetta, J., Houck, A.A., Schuster, D.I., Majer, J., Blais, A., Devoret, M.H., Girvin, S.M. and Schoelkopf, R.J., 2007. Charge-insensitive qubit design derived from the Cooper pair box. Physical Review A, 76(4), p.042319.

[162] Schrödinger, E., 1926. Quantisierung als eigenwertproblem. Annalen der physik, 385(13), pp.437-490.

[163] Bishop, L.S., 2010. Circuit Quantum Electrodynamics. PhD dissertation (Yale University, 2010).

[164] Haroche, S. and Raimond, J.M., 2006. Exploring the quantum: atoms, cavities, and photons. Oxford university press.

[165] Braginsky, V.B., Vorontsov, Y.I. and Thorne, K.S., 1980. Quantum nondemolition measurements. Science, 209(4456), pp.547-557.

[166] Paik, H., Mezzacapo, A., Sandberg, M., McClure, D.T., Abdo, B., Córcoles, A.D., Dial, O., Bogorin, D.F., Plourde, B.L.T., Steffen, M. and Cross, A.W., 2016. Experimental demonstration of a resonator-induced phase gate in a multiqubit circuit-qed system. Physical review letters, 117(25), p.250502.

[167] Jaynes, E.T. and Cummings, F.W., 1963. Comparison of quantum and semiclassical radiation theories with application to the beam maser. Proceedings of the IEEE, 51(1), pp.89-109.

[168] Suri B., 2015. Transmon Qubits Coupled to Superconducting Lumped Element Resonators. PhD dissertation (University of Maryland, 2015).

[169] Griffiths, D.J., 2005. Introduction to quantum mechanics. 2nd, Pearson, Chapter2. The time-independent schrodinger equation, pp.90-91.

[170] Irish, E.K., 2007. Generalized rotating-wave approximation for arbitrarily large coupling. Physical review letters, 99(17), p.173601.

[171] Rabi, I.I., 1937. Space quantization in a gyrating magnetic field. Physical Review, 51(8), p.652.

[172] Bloch, F., 1946. Nuclear induction. Physical review, 70(7-8), p.460.

[173] Padgett, M.J. and Courtial, J., 1999. Poincaré-sphere equivalent for light beams containing orbital angular momentum. Optics letters, 24(7), pp.430-432.

[174] Jaeger, G., 2007. Quantum information (pp. 81-89). Springer New York.

[175] Fano, U., 1957. Description of states in quantum mechanics by density matrix and operator techniques. Reviews of Modern Physics, 29(1), p.74.

[176] Von Neumann, J., 1927. Wahrscheinlichkeitstheoretischer aufbau der quantenmechanik. Nachrichten von der Gesellschaft der Wissenschaften zu Göttingen, Mathematisch-Physikalische Klasse, 1927, pp.245-272.

[177] Schrödinger, E., 1926. An undulatory theory of the mechanics of atoms and molecules. Physical review, 28(6), p.1049.

[178] Breuer, H.P. and Petruccione, F., 2002. The theory of open quantum systems. Oxford University Press on Demand.

[179] Kolovsky, A.R., 2020. Quantum entanglement and the Born-Markov approximation for an open quantum system. Physical Review E, 101(6), p.062116.

[180] Lindblad, G., 1976. On the generators of quantum dynamical semigroups. Communications in Mathematical Physics, 48(2), pp.119-130.

[181] Kossakowski, A., 1972. On quantum statistical mechanics of non-Hamiltonian systems. Reports on Mathematical Physics, 3(4), pp.247-274.

[182] Meystre, P. and Sargent, M., 2007. Elements of quantum optics. Springer Science & Business Media.

[183] Przybysz, A.J., 2010. Reducing decoherence in dc SQUID phase qubits. PhD dissertation (University of Maryland, 2010).

[184] Sears, A.P.,2013. Extending coherence in superconducting qubits: from microseconds to milliseconds. PhD dissertation (Yale University, 2013).

[185] Van Harlingen, D.J., Robertson, T.L., Plourde, B.L.T., Reichardt, P.A., Crane, T.A. and Clarke, J., 2004. Decoherence in Josephson-junction qubits due to critical-current fluctuations. Physical Review B, 70(6), p.064517.

[186] Budoyo, R.P., 2015. Effects of Optical Illumination on Superconducting Quantum Devices. PhD dissertation (University of Maryland, 2015).

[187] O'Malley, P.J.J., 2016. Superconducting Qubits: Dephasing and Quantum Chemistry. PhD dissertation (University of California, Santa Barbara, 2015).

[188] Yeh, J.H., LeFebvre, J., Premaratne, S., Wellstood, F.C. and Palmer, B.S., 2017. Microwave attenuators for use with quantum devices below 100 mK. Journal of Applied Physics, 121(22), p.224501.

[189] Yeh, J.H., Huang, Y., Zhang, R., Premaratne, S., LeFebvre, J., Wellstood, F.C. and Palmer, B.S., 2019. Hot electron heatsinks for microwave attenuators below 100 mK. Applied Physics Letters, 114(15), p.152602.

[190] Reagor, M.J., 2015. Superconducting Cavities for Circuit Quantum Electrodynamics. PhD dissertation (Yale University, 2015).

[191] Clerk, A.A. and Utami, D.W., 2007. Using a qubit to measure photon-number statistics of a driven thermal oscillator. Physical Review A, 75(4), p.042302.

[192] Schoelkopf, R.J., Clerk, A.A., Girvin, S.M., Lehnert, K.W. and Devoret, M.H., 2003. Quantum noise in mesoscopic physics. NATO Science Series in Mathematics.

[193] Houck, A.A., Schreier, J.A., Johnson, B.R., Chow, J.M., Koch, J., Gambetta, J.M., Schuster, D.I., Frunzio, L., Devoret, M.H., Girvin, S.M. and Schoelkopf, R.J., 2008. Controlling the spontaneous emission of a superconducting transmon qubit. Physical review letters, 101(8), p.080502.

[194] Esteve, D., Devoret, M.H. and Martinis, J.M., 1986. Effect of an arbitrary dissipative circuit on the quantum energy levels and tunneling of a Josephson junction. Physical Review B, 34(1), p.158.

[195] Devoret, M.H. and Schoelkopf, R.J., 2013. Superconducting circuits for quantum information: an outlook. Science, 339(6124), pp.1169-1174.

[196] Oliver, W.D. and Welander, P.B., 2013. Materials in superconducting quantum bits. MRS bulletin, 38(10), pp.816-825.

[197] Purcell, E.M., Torrey, H.C. and Pound, R.V., 1946. Resonance absorption by nuclear magnetic moments in a solid. Physical review, 69(1-2), p.37.

[198] Dirac, P.A.M., 1927. The quantum theory of the emission and absorption of radiation. Proceedings of the Royal Society of London. Series A, Containing Papers of a Mathematical and Physical Character, 114(767), pp.243-265.

[199] Sete, E.A., Martinis, J.M. and Korotkov, A.N., 2015. Quantum theory of a bandpass Purcell filter for qubit readout. Physical Review A, 92(1), p.012325.

[200] Martinis, J.M., Cooper, K.B., McDermott, R., Steffen, M., Ansmann, M., Osborn, K.D., Cicak, K., Oh, S., Pappas, D.P., Simmonds, R.W. and Clare, C.Y., 2005. Decoherence in Josephson qubits from dielectric loss. Physical review letters, 95(21), p.210503.

[201] Pappas, D.P., Vissers, M.R., Wisbey, D.S., Kline, J.S. and Gao, J., 2011. Two level system loss in superconducting microwave resonators. IEEE Transactions on Applied Superconductivity, 21(3), pp.871-874.

[202] Oh, S., Cicak, K., Kline, J.S., Sillanpää, M.A., Osborn, K.D., Whittaker, J.D., Simmonds, R.W. and Pappas, D.P., 2006. Elimination of two level fluctuators in superconducting quantum bits by an epitaxial tunnel barrier. Physical Review B, 74(10), p.100502.

[203] Wang, C., Axline, C., Gao, Y.Y., Brecht, T., Chu, Y., Frunzio, L., Devoret, M.H. and Schoelkopf, R.J., 2015. Surface participation and dielectric loss in superconducting qubits. Applied Physics Letters, 107(16), p.162601.

[204] Moridi, A., Ruan, H., Zhang, L.C. and Liu, M., 2013. Residual stresses in thin film systems: Effects of lattice mismatch, thermal mismatch and interface dislocations. International Journal of Solids and Structures, 50(22-23), pp.3562-3569.

[205] Richardson, C.J.K., Siwak, N.P., Hackley, J., Keane, Z.K., Robinson, J.E., Arey, B., Arslan, I. and Palmer, B.S., 2016. Fabrication artifacts and parallel loss channels in metamorphic epitaxial aluminum superconducting resonators. Superconductor Science and Technology, 29(6), p.064003.

[206] Dial, O., McClure, D.T., Poletto, S., Keefe, G.A., Rothwell, M.B., Gambetta, J.M., Abraham, D.W., Chow, J.M. and Steffen, M., 2016. Bulk and surface loss in superconducting transmon qubits. Superconductor Science and Technology, 29(4), p.044001.

[207] Sarabi, B., Ramanayaka, A.N., Burin, A.L., Wellstood, F.C. and Osborn, K.D., 2016. Projected dipole moments of individual two-level defects extracted using circuit quantum electrodynamics. Physical Review Letters, 116(16), p.167002.

[208] Schlör, S., Lisenfeld, J., Müller, C., Bilmes, A., Schneider, A., Pappas, D.P., Ustinov, A.V. and Weides, M., 2019. Correlating decoherence in transmon qubits: Low frequency noise by single fluctuators. Physical review letters, 123(19), p.190502.

[209] Martinis, J.M., Ansmann, M. and Aumentado, J., 2009. Energy decay in superconducting Josephson-junction qubits from nonequilibrium quasiparticle excitations. Physical review letters, 103(9), p.097002.

[210] Gustavsson, S., Yan, F., Catelani, G., Bylander, J., Kamal, A., Birenbaum, J., Hover, D., Rosenberg, D., Samach, G., Sears, A.P. and Weber, S.J., 2016. Suppressing relaxation in superconducting qubits by quasiparticle pumping. Science, 354(6319), pp.1573-1577.

[211] Chen, Y.Y., Zhang, P., Zheng, W., Wu, Z. and Zhai, H., 2020. Many-body echo. Physical Review A, 102(1), p.011301.

[212] Catelani, G., Koch, J., Frunzio, L., Schoelkopf, R.J., Devoret, M.H. and Glazman, L.I., 2011. Quasiparticle relaxation of superconducting qubits in the presence of flux. Physical review letters, 106(7), p.077002.

[213] Joyez, P., Lafarge, P., Filipe, A., Esteve, D. and Devoret, M.H., 1994. Observation of parity-induced suppression of Josephson tunneling in the superconducting single electron transistor. Physical review letters, 72(15), p.2458.

[214] Amar, A., Song, D., Lobb, C.J. and Wellstood, F.C., 1994. 2e to e periodic pair currents in superconducting Coulomb-blockade electrometers. Physical review letters, 72(20), p.3234.

[215] Hergenrother, J.M., Lu, J.G., Tuominen, M.T., Ralph, D.C. and Tinkham, M., 1995. Photon-activated switch behavior in the single-electron transistor with a superconducting island. Physical Review B, 51(14), p.9407.

[216] De Visser, P.J., Baselmans, J.J.A., Diener, P., Yates, S.J.C., Endo, A. and Klapwijk, T.M., 2011. Number fluctuations of sparse quasiparticles in a superconductor. Physical review letters, 106(16), p.167004.

[217] Van Woerkom, D.J., Geresdi, A. and Kouwenhoven, L.P., 2015. One minute parity lifetime of a NbTiN Cooper-pair transistor. Nature Physics, 11(7), pp.547-550.

[218] Yamamoto, T., Nakamura, Y., Pashkin, Y.A., Astafiev, O. and Tsai, J.S., 2006. Parity effect in superconducting aluminum single electron transistors with spatial gap profile controlled by film thickness. Applied physics letters, 88(21), p.212509.

[219] Ferguson, A.J., Hudson, F.E. and Clark, R.G., 2006. Microsecond resolution of quasiparticle tunneling in the single-Cooper-pair transistor. Physical review letters, 97(10), p.106603.

[220] Palmer, B.S., Sanchez, C.A., Naik, A., Manheimer, M.A., Schneiderman, J.F., Echternach, P.M. and Wellstood, F.C., 2007. Steady-state thermodynamics of nonequilibrium quasiparticles in a Cooper-pair box. Physical Review B, 76(5), p.054501.

[221] Shaw, M.D., Lutchyn, R.M., Delsing, P. and Echternach, P.M., 2008. Kinetics of nonequilibrium quasiparticle tunneling in superconducting charge qubits. Physical Review B, 78(2), p.024503.

[222] Moore, D.C., Mazing, B.A., Golwala, S., Bumble, B., Gao, J., Young, B.A., McHugth, S., Day, P.K., LeDuc, H.G. and Zmuidzinas, J., 2009, December. Quasiparticle trapping in microwave kinetic inductance strip detectors. In AIP Conference Proceedings (Vol. 1185, No. 1, pp. 168-171). American Institute of Physics.

[223] Wang, C., Gao, Y.Y., Pop, I.M., Vool, U., Axline, C., Brecht, T., Heeres, R.W., Frunzio, L., Devoret, M.H., Catelani, G. and Glazman, L.I., 2014. Measurement and control of quasiparticle dynamics in a superconducting qubit. Nature communications, 5(1), pp.1-7.

[224] Serniak, K., Hays, M., de Lange, G., Diamond, S., Shankar, S., Burkhart, L.D., Frunzio, L., Houzet, M. and Devoret, M.H., 2018. Hot nonequilibrium quasiparticles in transmon qubits. Physical review letters, 121(15), p.157701.

[225] Rogovin, D. and Scalapino, D.J., 1974. Fluctuation phenomena in tunnel junctions. Annals of Physics, 86(1), pp.1-90.

[226] Day, P.K., LeDuc, H.G., Mazin, B.A., Vayonakis, A. and Zmuidzinas, J., 2003. A broadband superconducting detector suitable for use in large arrays. Nature, 425(6960), pp.817-821.

[227] Wen, C.P., 1969. Coplanar waveguide: A surface strip transmission line suitable for nonreciprocal gyromagnetic device applications. IEEE Transactions on Microwave Theory and Techniques, 17(12), pp.1087-1090.

[228] Simons, R. and Simons, R.N., 2001. Coplanar waveguide circuits, components, and systems (Vol. 15). New York: John Wiley.

[229] Petrakos, S., 1991. Electromagnetic modeling of coplanar waveguide discontinuities (Master's thesis, University of Colorado).

[230] Gao, J., 2008. The Physics of Superconducting Microwave Resonators. PhD thesis (California Institute of Technology, 2008).

[231] Niepce, D., Burnett, J.J., Latorre, M.G. and Bylander, J., 2020. Geometric scaling of two-level-system loss in superconducting resonators. Superconductor Science and Technology, 33(2), p.025013.

[232] COMSOL Multiphysics, general purpose finite element simulation software https://www.comsol.com (visited on 10/01/2020).

[233] Sage, J.M., Bolkhovsky, V., Oliver, W.D., Turek, B. and Welander, P.B., 2011. Study of loss in superconducting coplanar waveguide resonators. Journal of Applied Physics, 109(6), p.063915.

[234] Mazin, B.A., 2004. Microwave Kinetic Inductance Detectors. PhD thesis (California Institute of Technology, 2004).

[235] Calusine, G., Melville, A., Woods, W., Das, R., Stull, C., Bolkhovsky, V., Braje, D., Hover, D., Kim, D.K., Miloshi, X. and Rosenberg, D., 2018. Analysis and mitigation of interface losses in trenched superconducting coplanar waveguide resonators. Applied Physics Letters, 112(6), p.062601.

[236] Melville, A., Calusine, G., Woods, W., Serniak, K., Golden, E., Niedzielski, B.M., Kim, D.K., Sevi, A., Yoder, J.L., Dauler, E.A. and Oliver, W.D., 2020. Comparison of dielectric loss in titanium nitride and aluminum superconducting resonators. Applied Physics Letters, 117(12), p.124004.

[237] Wang, H., Hofheinz, M., Wenner, J., Ansmann, M., Bialczak, R.C., Lenander, M., Lucero, E., Neeley, M., O'Connell, A.D., Sank, D. and Weides, M., 2009. Improving the coherence time of superconducting coplanar resonators. Applied Physics Letters, 95(23), p.233508.

[238] Kumar, S., Gao, J., Zmuidzinas, J., Mazin, B.A., LeDuc, H.G. and Day, P.K., 2008. Temperature dependence of the frequency and noise of superconducting coplanar waveguide resonators. Applied Physics Letters, 92(12), p.123503.

[239] Nsanzineza, I. and Plourde, B.L.T., 2014. Trapping a single vortex and reducing quasiparticles in a superconducting resonator. Physical review letters, 113(11), p.117002.

[240] Budoyo, R.P., Hertzberg, J.B., Ballard, C.J., Voigt, K.D., Kim, Z., Anderson, J.R., Lobb, C.J. and Wellstood, F.C., 2016. Effects of nonequilibrium quasiparticles in a thin-film superconducting microwave resonator under optical illumination. Physical Review B, 93(2), p.024514.

[241] Fulton, T.A. and Dolan, G.J., 1987. Observation of single-electron charging effects in small tunnel junctions. Physical review letters, 59(1), p.109.

[242] Cohen, R.W. and Abeles, B., 1968. Superconductivity in granular aluminum films. Physical Review, 168(2), p.444.

[243] Strongin, M., Thompson, R.S., Kammerer, O.F. and Crow, J.E., 1970. Destruction of superconductivity in disordered near-monolayer films. Physical Review B, 1(3), p.1078.

[244] Chi, C.C. and Clarke, J., 1979. Enhancement of the energy gap in superconducting aluminum by tunneling extraction of quasiparticles. Physical Review B, 20(11), p.4465.

[245] Black, C.T., Ralph, D.C. and Tinkham, M., 1996. Spectroscopy of the superconducting gap in individual nanometer-scale aluminum particles. Physical Review Letters, 76(4), p.688.

[246] Ferguson, A.J. and Clark, R.G., 2007. Energy gap measurement of nanostructured aluminium thin films for single Cooper-pair devices. Superconductor Science and Technology, 21(1), p.015013.

[247] Townsend, P., Gregory, S. and Taylor, R.G., 1972. Superconducting behavior of thin films and small particles of aluminum. Physical Review B, 5(1), p.54.

[248] Vepsäläinen, A., Karamlou, A.H., Orrell, J.L., Dogra, A.S., Loer, B., Vasconcelos, F., Kim, D.K., Melville, A.J., Niedzielski, B.M., Yoder, J.L. and Gustavsson, S., 2020. Impact of ionizing radiation on superconducting qubit coherence. arXiv preprint arXiv:2001.09190.

[249] Premaratne, S.P., 2018. Coherent control of low anharmonicity systems for superconducting quantum computing. PhD dissertation (University of Maryland, 2018).

[250] Novikov, S., 2015. Raman coherence effects in a superconducting Jaynes-Cummings system. PhD thesis (University of Maryland, 2015).

[251] Houck, A.A., Koch, J., Devoret, M.H., Girvin, S.M. and Schoelkopf, R.J., 2009. Life after charge noise: recent results with transmon qubits. Quantum Information Processing, 8(2-3), pp.105-115.

[252] Place, A.P., Rodgers, L.V., Mundada, P., Smitham, B.M., Fitzpatrick, M., Leng, Z., Premkumar, A., Bryon, J., Sussman, S., Cheng, G. and Madhavan, T., 2020. New material platform for superconducting transmon qubits with coherence times exceeding 0.3 milliseconds. arXiv preprint arXiv:2003.00024.

[253] EZ Form, Non-Magnetic Connectors SubMiniature version A (SMA) feedthrough connectors, https://www.ezform.com/docs/Non-Mag.pdf (visited on 10/01/2020).

[254] AutoCAD, computer-aided design (CAD) software, https://www.autodesk.com/products/autocad/overview (visited on 10/01/2020).

[255] ANSYS, 3D Electromagnetic Field Simulator for RF and Wireless Design, https://www.ansys.com/products/electronics/ansys-hfss (visited on 10/01/2020).

[256] Nigg, S.E., Paik, H., Vlastakis, B., Kirchmair, G., Shankar, S., Frunzio, L., Devoret, M.H., Schoelkopf, R.J. and Girvin, S.M., 2012. Black-box superconducting circuit quantization. Physical Review Letters, 108(24), p.240502.

[257] Solgun, F. and DiVincenzo, D.P., 2015. Multiport impedance quantization. Annals of physics, 361, pp.605-669.

[258] Wolfram Mathematica, technical computing software, https://www.wolfram.com/mathematica (visited on 10/01/2020).

[259] Leiden Cryogenics, Cryogen Free CF-CS50, http://www.leiden-cryogenics.com/products/cryogen-free/cf-cs50 (visited on 10/01/2020).

[260] Amuneal, Magnetic Shielding Materials, http://www.amuneal.com/magnetic-shielding/magnetic-shielding-materials (visited on 10/01/2020).

[261] CITCRYO 4-12A amplifier, California Institute of Technology.

[262] Pozar, D.M., 2005. Microwave engineering 3rd ed., ma john wiley & sons.

[263] Graf, R.F., 1999. Modern dictionary of electronics. Elsevier.

[264] Corning, SMF-28 Ultra Optical Fiber, https://www.corning.com/media/worldwide/coc/documents/Fiber/SMF-28%20Ultra.pdf (visited on 10/01/2020).

[265] 1550 nm IR laser Keysight, 81940A Tunable Laser Module, https://www.keysight.com/en/pd-1281761-pn-81940A/compact-tunable-laser-source-with-continuous-sweep-mode-1520nm-to-1630nm?cc=US&lc=eng (visited on 10/01/2020).

[266] Fibertronics, FC/APC optical attenuators, https://www.fibertronics.com/in-line-male-to-female-attenua (visited on 10/01/2020).

[267] Swagelok, vacuum feedthrough, https://www.swagelok.com/en/catalog/Product/Detail?part=SS-6-TA-1-6 (visited on 10/01/2020).

[268] Khalil, M.S., Stoutimore, M.J.A., Wellstood, F.C. and Osborn, K.D., 2012. An analysis method for asymmetric resonator transmission applied to superconducting devices. Journal of Applied Physics, 111(5), p.054510.

[269] Kotz, S., Balakrishnan, N. and Johnson, N.L., 2004. Continuous multivariate distributions, Volume 1: Models and applications. John Wiley & Sons.

[270] Blais, A., Huang, R.S., Wallraff, A., Schoelkopf, R. and Girvin, S., 2004. Entanglement and quantum non-demolition read-out of superconducting qubits in a microwave resonator. APS, 2004, pp.D37-011.

[271] Wallraff, A., Schuster, D.I., Blais, A., Frunzio, L., Huang, R.S., Majer, J., Kumar, S., Girvin, S.M. and Schoelkopf, R.J., 2004. Circuit quantum electrodynamics: Coherent coupling of a single photon to a Cooper pair box. arXiv preprint cond-mat/0407325.

[272] Grangier, P., Levenson, J.A. and Poizat, J.P., 1998. Quantum non-demolition measurements in optics. Nature, 396(6711), pp.537-542.

[273] Lupaşcu, A., Saito, S., Picot, T., De Groot, P.C., Harmans, C.J.P.M. and Mooij, J.E., 2007. Quantum non-demolition measurement of a superconducting two-level system. nature physics, 3(2), pp.119-123.

[274] Macklin, C., O'Brien, K., Hover, D., Schwartz, M.E., Bolkhovsky, V., Zhang, X., Oliver, W.D. and Siddiqi, I., 2015. A near–quantum-limited Josephson traveling-wave parametric amplifier. Science, 350(6258), pp.307-310.

[275] Reed, M.D., DiCarlo, L., Johnson, B.R., Sun, L., Schuster, D.I., Frunzio, L. and Schoelkopf, R.J., 2010. High-fidelity readout in circuit quantum electrodynamics using the Jaynes-Cummings nonlinearity. Physical review letters, 105(17), p.173601.

[276] Babazadeh, A., Erhard, M., Wang, F., Malik, M., Nouroozi, R., Krenn, M. and Zeilinger, A., 2017. High-dimensional single-photon quantum gates: concepts and experiments. Physical review letters, 119(18), p.180510.

[277] Ramsey, N.F., 1950. A molecular beam resonance method with separated oscillating fields. Physical Review, 78(6), p.695.

[278] Houdré, R., Stanley, R.P. and Ilegems, M., 1996. Vacuum-field Rabi splitting in the presence of inhomogeneous broadening: Resolution of a homogeneous linewidth in an inhomogeneously broadened system. Physical Review A, 53(4), p.2711.

[279] Hahn, E.L., 1950. Spin echoes. Physical review, 80(4), p.580.

[280] Kittel, C. and McEuen, P., 1976. Introduction to solid state physics (Vol. 8). New York: Wiley.

[281] Taheriniya, S., Parhizgar, S.S. and Sari, A.H., 2018. Investigating the effect of sputtering conditions on the physical properties of aluminum thin film and the resulting alumina template. Results in Physics, 9, pp.1428-1435.

[282] Dutta, S., Li, K., Zhang, R., Poppert, D., Keshvari, S., Lobb, C. and Wellstood, F., 2020. Temperature Dependence of Relaxation-Time Fluctuations in Transmon Qubits. Bulletin of the American Physical Society, 65.

[283] Vinokur, V.M., Baturina, T.I., Fistul, M.V., Mironov, A.Y., Baklanov, M.R. and Strunk, C., 2008. Superinsulator and quantum synchronization. Nature, 452(7187), pp.613-615.

[284] Gao, J., Vissers, M.R., Sandberg, M.O., Da Silva, F.C.S., Nam, S.W., Pappas, D.P., Wisbey, D.S., Langman, E.C., Meeker, S.R., Mazin, B.A. and Leduc, H.G., 2012. A titanium-nitride near-infrared kinetic inductance photon-counting detector and its anomalous electrodynamics. Applied Physics Letters, 101(14), p.142602.

[285] Woods, W., Calusine, G., Melville, A., Sevi, A., Golden, E., Kim, D.K., Rosenberg, D., Yoder, J.L. and Oliver, W.D., 2019. Determining interface dielectric losses in superconducting coplanar-waveguide resonators. Physical Review Applied, 12(1), p.014012.

[286] Bueno, J., Coumou, P.C.J.J., Zheng, G., De Visser, P.J., Klapwijk, T.M., Driessen, E.F.C., Doyle, S. and Baselmans, J.A., 2014. Anomalous response of superconducting titanium nitride resonators to terahertz radiation. Applied Physics Letters, 105(19), p.192601.

[287] Hsieh, C.F. and Jou, S., 2006. Titanium nitride electrodes for micro-gap discharge. Microelectronics journal, 37(9), pp.867-870.

[288] Liao, W.T., 2019. Investigation of Tunneling in Superconductors using a Millikelvin Scanning Tunneling Microscope. PhD dissertation (University of Maryland, 2019).

[289] Noguchi, T., Dominjon, A. and Sekimoto, Y., 2018. Analysis of characteristics of Al MKID resonators. IEEE Transactions on Applied Superconductivity, 28(4), pp.1-6.